Materials Science in Additive Manufacturing

eISSN: 2810-9635

Volume 4 Issue 3, September 2025

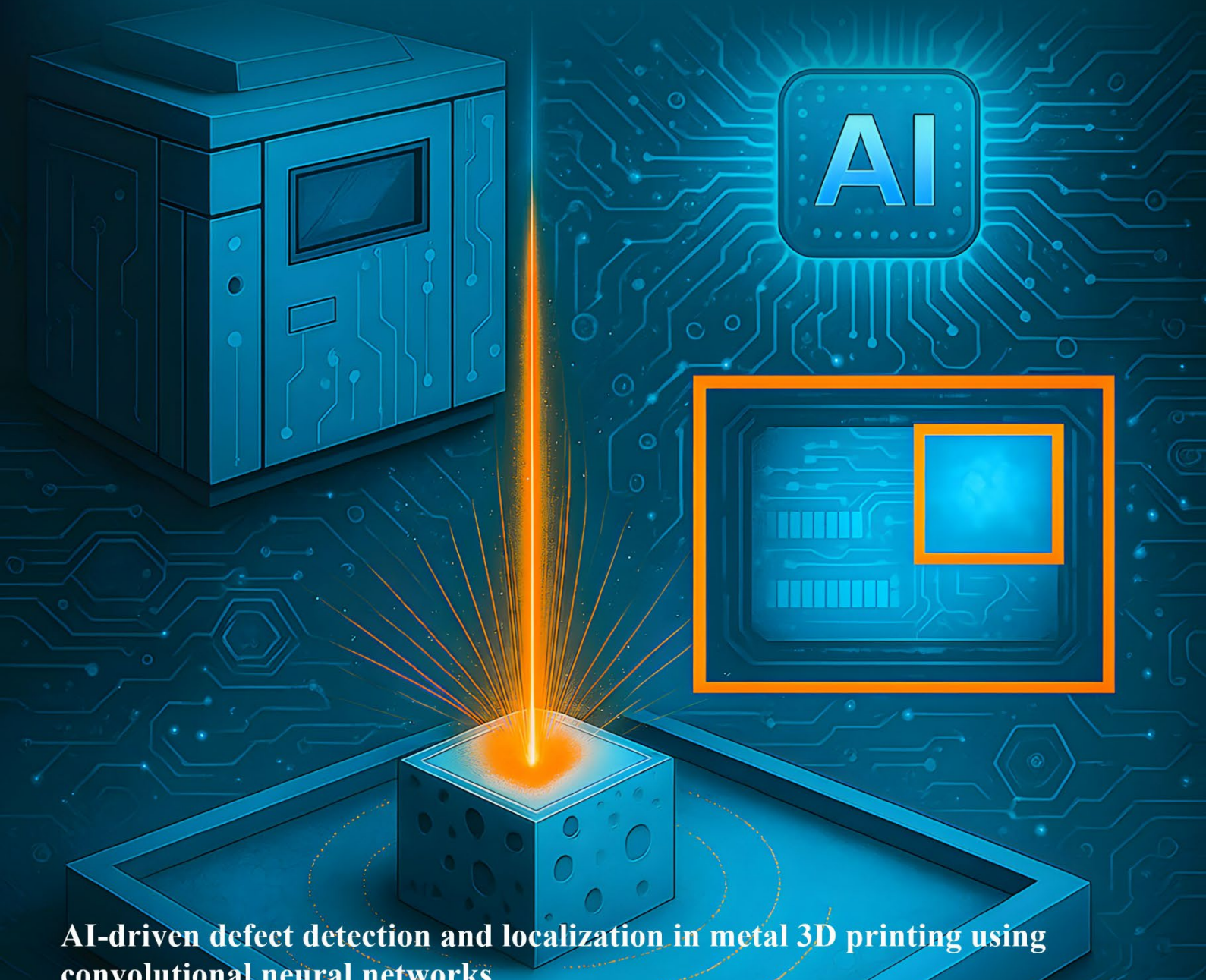

AI-driven defect detection and localization in metal 3D printing using convolutional neural networks

ACCSCIENCE PUBLISHING

ACCSCIENCE PUBLISHING

Materials Science in Additive Manufacturing

Online ISSN: 2810-9635

Materials Science in Additive Manufacturing aims to bridge the cutting-edge research between additive manufacturing and the entire spectrum of materials science. The journal covers all applied and fundamentals of processing, synthesis, structure, composition, properties and performance of materials designed or manipulated for additive manufacturing. The journal covers a wide scope of innovative techniques, processes, methods, and applications.

About the Publisher

AccScience Publishing is a publishing company based in Singapore. We publish a range of high-quality, open-access, peer-reviewed journals and books from a broad spectrum of disciplines.

Contact Us

Managing Editor
msam.office@accscience.sg

AccScience Publishing
9 Raffles Place, Republic Plaza 1 #06-00 Singapore 048619.

Volume 4 • Issue 3 • September 2025
ISSN 2810-9635 (online)

MATERIALS SCIENCE IN ADDITIVE MANUFACTURING

Editor-in-Chief

Chee Kai Chua

Singapore University of Technology and Design, Singapore

ACCSCIENCE PUBLISHING

MATERIALS SCIENCE IN ADDITIVE MANUFACTURING

ISSN: 2810-9635 (online)

Editorial and Production Credits

Publisher: AccScience Publishing
Managing Editor: Wendy Yang
Editorial Assistant: Flora Kang
Production Editor: Puva Ramakrishnan
Article Layout and Typeset: Sinjore Technologies (India)

Supplementary file

Supplementary files of articles can be obtained at https://accscience.com/journal/MSAM/4/3.

Disclaimer

AccScience Publishing is not liable to the statements, perspectives, and opinions contained in the publications. The appearance of advertisements in the journal shall not be construed as a warranty, endorsement, or approval of the products or services advertised and/or the safety thereof. AccScience Publishing disclaims responsibility for any injury to persons or property resulting from any ideas or products referred to in the publications or advertisements. AccScience Publishing remains neutral with regard to jurisdictional claims in published maps and institutional affiliations.

Material Science in Additive Manufacturing

Editorial Board

*Editorial Board Members as of September 15, 2025

ACCSCIENCE PUBLISHING

Volume 4 | Issue 3 | September 2025 |

Materials Science in Additive Manufacturing

https://accscience.com/journal/msam

CONTENTS

ACCSCIENCE PUBLISHING

Materials Science in Additive Manufacturing

REVIEW ARTICLE

Ceramic additive manufacturing via vat photopolymerization

Chongyu Long[1], Zhiyuan Liu[1,2], Changyong Liu[1,2], and Zhangwei Chen[1,2]*

[1]Additive Manufacturing Institute, Shenzhen University, Shenzhen, Guangdong, China

[2]Guangdong Key Laboratory of Electromagnetic Control and Intelligent Robotics, Shenzhen University, Shenzhen, Guangdong, China

(This article belongs to the *Special Issue*: *Additive Manufacturing of High Performance Ceramics*)

Abstract

Vat photopolymerization (VPP) additive manufacturing has emerged as a transformative approach for fabricating high-performance ceramic components with intricate geometries. This review comprehensively examines VPP technologies, including stereolithography, digital light processing, and two-photon polymerization, highlighting their mechanisms, advantages, and limitations. Critical challenges faced by ceramic VPP include light scattering from particles, slurry viscosity control, sedimentation, and post-processing shrinkage. The required optimized characteristics suitable for VPP of ceramic slurries and pre-ceramic polymers are also discussed. The latter offers a promising alternative, enabling the shaping of complex architectures with reduced defects and enhanced thermal stability, supported by active/passive fillers that mitigate shrinkage and improve density. Ceramic VPP applications span biomedical implants, microreactors, aerospace components, and energy devices. Key advancements include the integration of multimaterial systems, hybrid precursors, and nanocomposites. However, challenges persist in achieving uniform curing depths, minimizing anisotropic shrinkage, and scaling production. Future research should focus on material innovation, process parameter optimization, and advanced characterization techniques to unlock the full potential of VPP for next-generation ceramic manufacturing. This technology offers an effective solution for high-value ceramic applications.

Keywords: Ceramics; Vat photopolymerization; Stereolithography; Slurries; Sintering

***Corresponding author:**
Zhangwei Chen
(chen@szu.edu.cn)

Citation: Long C, Liu Z, Liu C, Chen Z. Ceramic additive manufacturing via vat photopolymerization. *Mater Sci Add Manuf*. 2025;4(3):025200031. doi: 10.36922/MSAM025200031

Received: May 13, 2025

Revised: June 3, 2025

Accepted: June 4, 2025

Published online: July 11, 2025

1. Introduction

Additive manufacturing technologies have revolutionized the way we produce complex parts, offering a layer-by-layer approach to creating both two-dimensional (2D) and three-dimensional (3D) components directly from computer-aided design (CAD) models.[1] These advanced techniques have attracted great attention for their capability of producing intricate geometries without the need for additional tooling, making them highly cost-effective for rapid prototyping and final part production. The additive manufacturing landscape is diverse, encompassing seven main categories, including powder bed fusion, binder jetting, material extrusion, and vat photopolymerization (VPP).[2] Among them, VPP technologies stand out for their scalability and ability to produce features ranging from micrometers to full-sized components.[3]

VPP is based on the principle of selectively curing a photosensitive liquid resin contained in a shallow vat through layer-by-layer photo-initiated crosslinking.[3] An automated ultraviolet (UV) light source, guided by a 3D CAD model, is directed across the resin surface to cure it in a precise, controlled manner. This process requires a support structure during the build phase, which is lowered after each layer is cured. The versatility and scalability of VPP techniques make them particularly suitable for creating complex features in various photosensitive polymers. While VPP is commonly associated with stereolithography (SL) for rapid prototyping, its application in ceramic fabrication has also garnered considerable attention.

Ceramics, known for their high hardness, wear resistance, corrosion resistance, and biocompatibility, have been extensively applied in industries such as mechanical engineering, electronics, and biomedical engineering.[4] Traditional ceramic manufacturing methods often involve complex and time-consuming steps, such as casting, injection molding, and pressing, which can limit the production of complex geometries. By offering a promising alternative, VPP enables the direct fabrication of ceramic parts with intricate designs and high precision.[2] This review paper focuses on the various VPP technologies used for ceramic fabrication, their advantages, and applications.

The preparation of ceramic objects using VPP technologies typically involves the use of ceramic slurries, which are composed of ceramic particles, resins, photoinitiators, dispersants, *etc.* These slurries should maintain suitably large solid content and reduced viscosity to ensure good printability and shape retention. The addition of dispersants helps achieve a homogeneous dispersion of ceramic powder in the slurry, which is beneficial to the printing process. However, incorporating ceramic particles into the slurry can pose several challenges, such as dispersion issues, viscosity problems, sedimentation, and stability concerns. These challenges need to be addressed to optimize the printing process and produce high-quality ceramic parts. In recent years, the development of pre-ceramic polymers has opened up new possibilities for ceramic fabrication using VPP technologies. These polymers can be easily shaped and formed and offer exceptional thermal stability, high strength, and fracture toughness compared to traditional ceramic powders. Using pre-ceramic polymers could prevent many of the issues associated with ceramic slurries, such as drying problems, long processing times, and the need for flammable solvents. This review also discusses the use of pre-ceramic polymers in VPP technologies, highlighting their advantages and potential applications in the fabrication of advanced ceramic components.

2. VPP techniques suitable for ceramic fabrication

2.1. Linear scanning SL

SL is regarded as the oldest rapid prototyping process and was invented by Hull in 1986.[5] The process requires the creation of a 3D CAD model and its conversion to an STL file, which is sent to the build station control software. The part is cut into a series of 2D slices of adequate thickness and the model becomes ready to print. A support platform is lowered into a vat of photocurable epoxy acrylate liquid resin so that it rests below a surface of approximately equal to the desired thickness. In linear scanning SL, a UV laser of nearly 100 milliwatts of power of fine beam diameter is directed onto the resin using a series of computer-controlled mirrors.[6] The laser causes the resin to polymerize and solidify it in a precise manner. Now, the platform is moved down with a single layer thickness to ensure that the new level is recoated to the layer of liquid resin. The laser then selectively solidifies the next layer and the overall process is repeated until the final object is built. Upon the completion of the model, the platform is raised up and out of the resin to allow the unsolicited resin to drain away. Further, after removing from the machine any excess resin and support structure are removed and the part is cleaned using suitable organic solvent to remove any uncured resin. The printed part is then cleaned using air and water to remove the solvent and is then placed in a UV oven in order to cure and fully solidify it. Finally, the model can be sanded down using ultra-fine sandpaper to obtain a smooth surface finish. The SL technique is commonly used for creating small-to-medium-sized concept models or prototypes for aerodynamic testing in wind tunnels as well as parts with fine details such as those used in the preparation of scaffolds for tissue engineering, optical, and microelectromechanical system (MEMS)/nanoelectromechanical system devices.

Materials used in SL are normally liquid resins with an appropriate proportion of photoinitiators.[7] SL is not preferred to create chemically functionalized parts due to the fixed composition of the resins and may require post-printing functionalization, if possible in some cases.[8] It is also possible to interchange containers filled with different materials for multimaterial printing of single objects through the SL process.[9] For printing of ceramic parts using SL, ceramic slurries with resins or pre-ceramic precursors are used to create green bodies, and further their processing at high temperatures are performed to obtain high-quality ceramic parts.[10] Light scattering is a challenging factor influencing the printing quality for ceramic powder slurries, while the pre-ceramic precursors are best suited for printing purposes. SL-printed parts are of high resolution due to a laser of fine diameter, which is scanned with high accuracy. The

limitation with SL is the requirement of the build platform, which has to be mechanically removed, necessitating surface finishing. Figure 1A shows the SL working principle. The fundamental mechanism of photopolymerization is that the resin surface is exposed to UV light to trigger polymerization via single-photon absorption by the photoinitiator.

The mechanism of the linear photo-polymerization process involved in linear laser SL is shown in Figure 2B. A single-photon is absorbed by the photoinitiator (Figure 2A) to form free radicals triggering the cross-linking of the monomers. Because of the Gaussian nature of the incident light beam, the number of photons hitting the resin surface will be maximum at the center of the laser spot and will decay away from it. This leads to the parabolic cross-section in the resin during each laser scan. The depth of the parabola, *i.e.*, cure depth (C_d) of the resin is related to the exposure energy and is given by Beer–Lambert law as:

$$C_d = S_d \ln\left(\frac{E}{E_c}\right) \quad \text{(I)}$$

where E is the exposure energy, E_c is the critical exposure energy and S_d is the transmission depth coefficient of the resin. S_d and E_c remain constant for a fixed recipe of resin/slurry.

This cure depth is measured and calibrated to derive a log-linear relationship between the cure depth of the resin and the exposure power. The laser spot size determines the feature size. Further, there must be good adhesion between the lateral lines and the vertical layers of the model to obtain a contiguous full-density part.

In SL, where foreign materials such as ceramic particles are incorporated inside the resin, the polymerization process is influenced significantly by the particle size, and the relationship between the cure depth and the particle size is described as:[11]

$$C_d = \frac{d}{Q}\frac{1}{\varphi}\ln\left(\frac{I_0}{I_{cure}}\right) \quad \text{(II)}$$

where φ = ceramic solid loading, d = ceramic powder size, Q = suspension constant, I_0 = exposure intensity, and I_{cure} = the critical exposure intensity for the suspension. Thus, greater ceramic particles result in larger cure depth as the scattering effect is reduced.[2] Smaller-diameter ceramic particles, which show strong scattering, would lead to lower cure depth. However, small particles are desired for increasing the solid loading printing and lowering the sintering temperature, which is good for the final ceramic products. In terms of the effect of particle shape, the semi-liquid nature of the ceramic slurry is generally favorable in favor of flowability, and there is no specific requirement for particle sphericity and regularity.

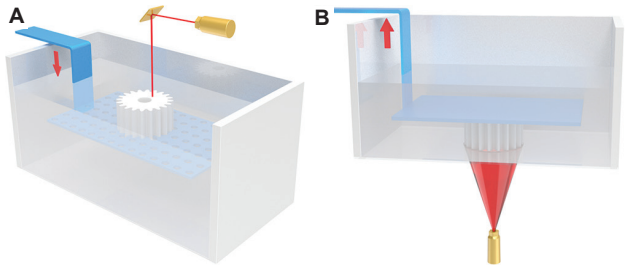

Figure 1. Schematic setup of linear scanning stereolithography technique (A) and image projection digital light processing (DLP) technique (B)[2] (schematics reused under the terms of the Creative Commons CC-BY license)

2.2. Planar photopolymerization based on DLP

DLP photopolymerization technique is based on a similar principle as laser SL, but it uses a conventional UV light source rather than a laser, and the patterns are transferred

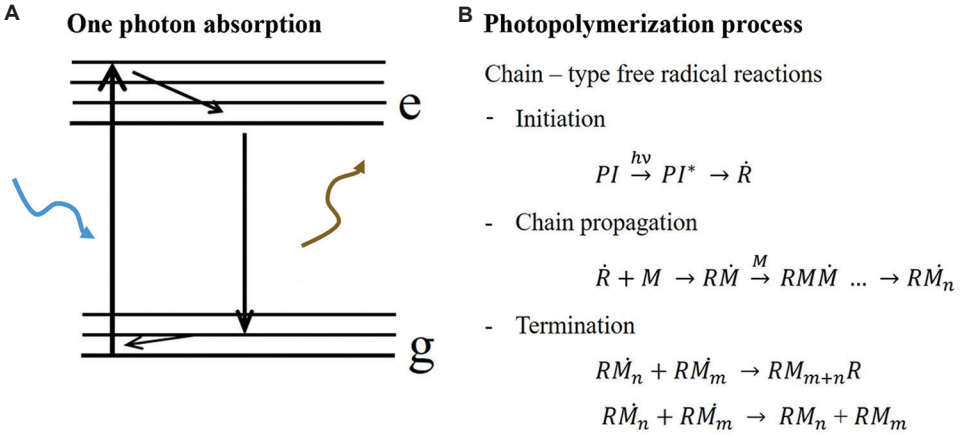

Figure 2. Single-photon absorption mechanism (A) and polymerization mechanism in linear stereolithography and digital light processing (B)

to resin by projecting an entire slice of the 2D model (Figure 1B). For the projection of the slice pattern onto the resin, a digital micromirror device (DMD) panel is used, making the DLP printing process faster than SL and facilitating quick fabrication of highly accurate parts with excellent resolution, resembling the products made with SL. DLP also requires a support platform, and structures need to be removed manually and may require finishing. The concept of DLP was first developed in 1996.[12] Further in 1997, liquid crystal display was replaced by DMDs to create high resolution and contrast in the projected pattern.[13] DMD is an array of microscopic mirrors that are capable of swift rotation within a range of ±10–12°.

2.3. Two-photon polymerization (TPP)

TPP, as illustrated in Figure 3, utilizes the two-photon absorption mechanism, in which molecules transition from ground to excited states through simultaneous absorption of two laser photons – either with identical energy (termed degenerate two-photon absorption [TPA]) or distinct energy levels (non-degenerate TPA). This mechanism demands intense photon flux due to the molecule's extremely brief residence (10^{-18} s) in the transient virtual state, necessitating ultrashort-pulsed infrared lasers to achieve sufficient energy delivery. TPA was theoretically predicted by Göppert-Mayer[14] in 1931 and the experimental observation was confirmed by Kaiser and Garrett[15] in 1961. Nowadays, the TPA process has become extensively important for technological applications, such as multiphoton polymerization, multiphoton optical limiters, and multiphoton fluorescence spectroscopy.

In conventional single-photon absorption (*e.g.*, in SL or DLP printing), excitation occurs when incident photon energy matches the electronic transition energy between ground and excited states, resulting in a linear photon flux dependence. Conversely, TPA requires simultaneous absorption of two lower-energy photons. During TPA, the molecule enters a short-lived virtual intermediate state after the first photon absorption. This mechanism enables UV-sensitive photoinitiators (350 – 400 nm) to be activated by near-infrared Ti: Sapphire lasers (700 – 800 nm) through TPA.

As a third-order nonlinear optical phenomenon,[17] degenerate TPA exhibits an energy absorption rate expressed as:

$$\frac{dW}{dt} = \frac{8\pi^2\omega}{c^2n^2} I^2 \,\mathrm{Im}[\chi^{(3)}] \tag{III}$$

where ω represents the angular frequency, c denotes the speed of light in a vacuum, and n is the refractive index of the medium. The nonlinear optical response arises from the imaginary component of the third-order susceptibility ($\mathrm{Im}[\chi^{(3)}]$), with the TPA process exhibiting a quadratic dependence on laser intensity. Due to this nonlinear intensity dependence, TPA occurs only at extremely high optical intensities, necessitating high-numerical-aperture (NA) microscope objectives for tight laser focusing. The TPA effect rapidly diminishes away from the focal center, resulting in a well-defined 3D voxel that enables intrinsic volumetric fabrication in two-photon lithography. The polymerization threshold is determined by the balance between radical generation (initiated by TPA) and competing deactivation pathways, including quenching, internal conversion, and radical termination.[18] Below this threshold, insufficient crosslinking occurs, while above

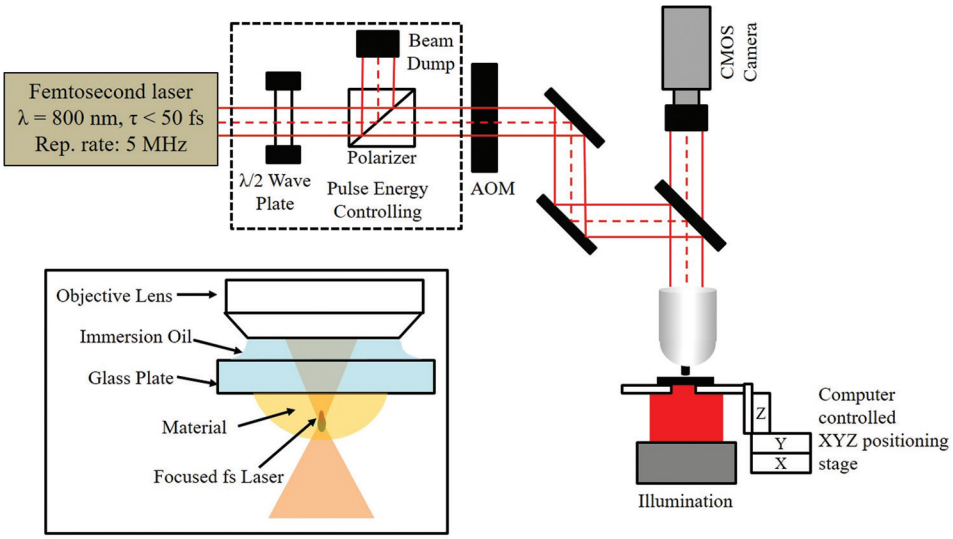

Figure 3. Schematic diagram of two-photon polymerization process[16] (schematic reused under the terms of the Creative Commons CC-BY license)

it, stable solid structures form. The threshold is further influenced by the TPA cross-section (δ) of the photoinitiator, which quantifies the probability of simultaneous photon absorption per unit time (Equation IV):

$$\frac{dn_p}{dt} = \delta N F^2 \quad \text{(IV)}$$

where N denotes the molecular number density (absorbing molecules per unit volume), while $F = I/h\nu$ represents the incident photon flux, where h is Planck's constant and ν is the optical frequency. Since:

$$\frac{dW}{dt} = \frac{dn_p}{dt} h\nu \quad \text{(V)}$$

Hence, δ can be expressed as:

$$\delta = \frac{16\pi^3 h\nu^2}{c^2 n^2 N} \mathrm{Im}[\chi^{(3)}] \quad \text{(VI)}$$

where δ has a unit of 10^{-58} m^4s/photon.[14]

Upon TPA, a portion of the excited initiator undergoes intersystem crossing to the triplet state, followed by bond cleavage to generate reactive radicals or ionic species, thereby initiating TPP. The efficiency of radical formation, termed radical quantum yield (φ), combined with the TPA cross-section (δ), determines the initiator's performance. Optimizing these parameters enables efficient TPP at reduced laser power and higher writing speeds.[17] The lifetime of radicals and polymerization kinetics are influenced by multiple factors, such as radical quenching (*e.g.*, by oxygen or other radicals), intramolecular recombination, and chain transfer reactions with surrounding molecules. These dynamics vary depending on the photoinitiator, monomer, solvent, and environmental conditions (*e.g.*, temperature, atmosphere), ultimately affecting achievable resolution and processing parameters.[19] Although the theoretical resolution limit of TPP is extremely small – determined by the voxel dimensions at the polymerization threshold – practical feature sizes are constrained by laser stability, material composition, and the numerical aperture (NA) of the focusing objective.[20] For high-NA objectives (NA > 0.7), the optical resolution can be estimated using the following equations:[21]

$$r_{xy} = \frac{0.325\lambda}{\sqrt{2} NA^{0.91}} \quad \text{(VII)}$$

$$r_z = \frac{0.532\lambda}{\sqrt{2}} \left[\frac{1}{n - \sqrt{n^2 - NA^2}} \right] \quad \text{(VIII)}$$

where r_{xy} and r_z denote the lateral and axial resolution limits, respectively; λ represents the excitation wavelength; n is the medium's refractive index; and NA corresponds to the objective's NA.

2.4. Continuous liquid interface production

Traditional SL methods employ a layer-by-layer approach, resulting in slow printing speeds unsuitable for mass production. In addition, oxygen inhibition during photopolymerization often leads to incomplete curing by either deactivating photoinitiators or forming peroxides.[22] To address these limitations, Tumbleston *et al.* introduced continuous liquid interface production (CLIP), an advanced SL technique.[22] In CLIP, printing occurs above an oxygen-permeable window, forming a thin "dead zone" (tens of micrometers thick) where oxygen suppresses curing. This uncured layer prevents adhesion between the window and the printed part, enabling continuous fabrication. As illustrated in Figure 4, CLIP operates by projecting UV images through a transparent, oxygen-permeable window into a liquid resin. Unlike conventional SL, which requires intermittent resin renewal and layer repositioning, CLIP continuously draws the cured part upward while fresh resin flows into the dead zone. This eliminates stepwise interruptions, significantly boosting printing speeds – up to 500 mm/h or higher – without compromising resolution. Moreover, print speed remains independent of layer thickness, further enhancing efficiency. Key advantages of CLIP include: (i) elimination of oxygen inhibition via controlled dead zone formation; (ii) continuous printing without pauses for resin replenishment; (iii) high-speed production while maintaining precision; and (iv) flexibility in layer thickness without affecting speed. This innovation overcomes critical drawbacks of conventional SL, making it viable for scalable, high-throughput manufacturing.

The CLIP process critically depends on establishing an oxygen-inhibited dead zone, achieved through an amorphous fluoropolymer window that combines high oxygen permeability with UV transparency and chemical resistance. The dead zone's thickness is determined through differential measurement techniques and varies with both oxygen availability and the window's permeability characteristics. Key observations include: (i) When using ambient air instead of pure oxygen, the dead zone thickness approximately doubles. (ii) Increasing photon flux reduces the dead zone thickness. (iii) Nitrogen environments completely eliminate the dead zone, preventing CLIP operation. For systems operating with ambient air, the dead zone thickness can be calculated as:

$$Dead\ zone\ thickness = C\left(\frac{\varphi_0 \alpha_{PI}}{D_{c0}}\right)^{-0.5} \quad \text{(ix)}$$

where φ_0 is the intensity of incident photons, α_{PI} is the product of photoinitiator concentration and the wavelength-dependent absorptivity, D_{c0} is the resin reactivity, and C is a

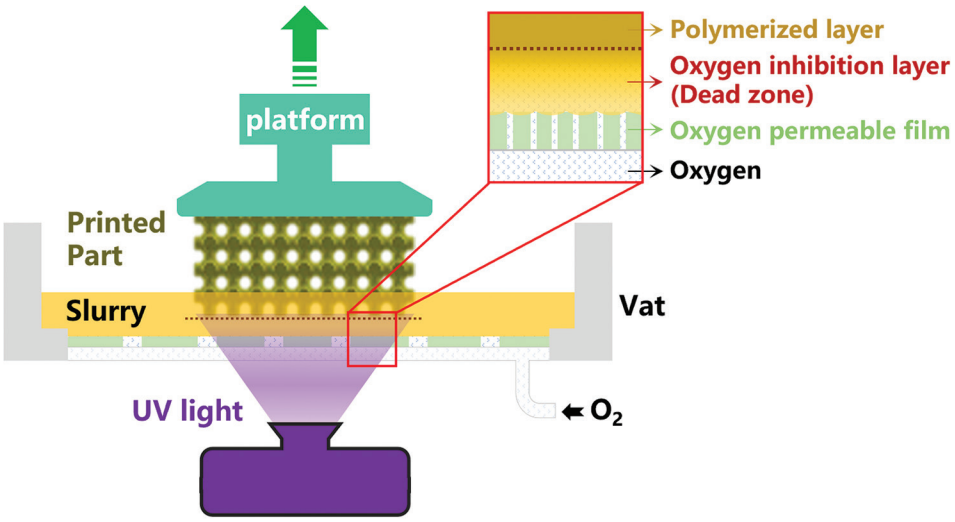

Figure 4. The working principle of continuous liquid interface production technology enables rapid, continuous fabrication without traditional layer-by-layer deposition. The system operates by simultaneously raising the build platform while dynamically updating projected ultraviolet cross-sectional patterns through an oxygen-permeable window. A critical feature is the maintenance of a thin uncured region (dead zone) at the interface between the growing part and the permeable window, allowing for uninterrupted printing.

proportionality constant. An increase in either φ_0 or α_{PI} leads to an increase in free radicals and a decrease in the initial oxygen. The oxygen permeating through the window gradually decreases in concentration as it penetrates deeper into the resin. This creates a concentration gradient where free radicals eventually dominate over oxygen inhibition at a specific penetration depth. The critical polymerization threshold is reached when oxygen depletion occurs while sufficient free radicals remain active. Enhancing the photoinitiation efficiency reduces this threshold distance, consequently decreasing the thickness of the oxygen-rich inhibition layer. The constant C in this system correlates with the square root of the membrane's oxygen diffusion coefficient. Furthermore, maintaining a consistent dead zone requires precise control of oxygen flux, which is determined by the membrane's permeability-to-thickness ratio.[23] The resulting cured layer thickness can be expressed by the following relationship:

$$Cured\ thickness = C\left(\frac{\varphi_0 \alpha_{PI}}{D_{c0}}\right)^{-0.5} \quad \text{(X)}$$

where t is the exposure time and α is the absorption coefficient of the resin. The relation between the print speed, resolution (h_A), and dead zone thickness is given by the following relation:

$$\frac{\text{Speed}}{h_A} = \left(\frac{\varphi_0 \alpha_{PI}}{D_{c0}}\right), \text{where} h_A = 1/\alpha \quad \text{(XI)}$$

The printing speed can be enhanced by optimizing process parameters for a given layer thickness (h_A). However, excessive speed reduction in dead zone thickness may compromise process stability, with critical thresholds typically ranging from 20 μm to 30 μm to avoid adhesion-related defects. When operating at minimal zone thickness, resolution compromises become necessary for further speed improvements. For large solid cross-sections, resin characteristics such as viscosity and pressure gradients require careful optimization. CLIP technology demonstrates versatility across material classes including elastomers, ceramics, and biomaterials, offering advantages in the rapid, cost-effective production of complex geometries. Ongoing research continues to expand its applications, particularly in pre-ceramic material systems. Table 1 summarizes the key characteristics of VPP methods.

3. Materials and process parameters

The VPP technique requires careful formulation of ceramic suspensions to achieve optimal printing performance, mechanical strength, and post-treatment characteristics. The manufacturing sequence involves four key stages: forming, polymerization, thermal decomposition, and ceramic conversion. These ceramic suspensions typically consist of five main components: ceramic particulates, photocurable polymers, light-sensitive initiators, stabilizing agents, and supplementary modifiers. Critical formulation requirements include high ceramic loading with maintained fluidity for successful printing and dimensional stability and effective particle dispersion through stabilization additives to ensure homogeneous microstructures.

Table 1. Comparative analysis of vat photopolymerization methods suitable for ceramic component production

Technology	Features	Power Source	Material type	Shaping method	Requirements	Accuracy
SL	Limited speed, intermediate cost, good efficiency, high surface quality	UV Laser	Slurry	Linear polymerization	UV-polymerizable and solvent-cleavable molecular units	<100 μm
DLP	Fast speed, intermediate cost, good efficiency, high surface quality	UV Source	Slurry	Linear polymerization	UV-polymerizable and solvent-cleavable molecular units	<100 μm
TPP	Limited speed, expensive, superior surface quality, optimal printing precision	IR Laser	Slurry	Nonlinear polymerization	IR-polymerizable and TPA molecular units	<1 μm
CLIP	Faster speed, intermediate cost, high efficiency, high surface quality	UV Source	Slurry	Linear Polymerization	UV-polymerizable and solvent-cleavable molecular units	<100 μm

Abbreviations: CLIP: continuous liquid interface production; DLP: digital light processing; IR: infrared; SL: stereolithography; TPA: two-photon absorption; TPP: two-photon polymerization; UV: ultraviolet.

Common ceramic powders used include oxide ceramics (*e.g.*, alumina [Al_2O_3] and zirconia [ZrO_2]), and non-oxide ceramics (*e.g.*, SiC, Si_3N_4, and AlN). Advanced composites, such as cordierite and Li_4SiO_4 systems, are also employed to enhance mechanical and thermal properties. The addition of ceramic powder into the photopolymers can cause several problems:

(i) *Dispersion issues.* Ceramic particles tend to aggregate due to interparticle forces such as van der Waals forces and electrostatic interactions. This aggregation can lead to an uneven distribution of particles in the slurry, resulting in defects in the printed parts. For example, in the preparation of alumina slurries, if the dispersion is not good, it may cause the formation of pores and cracks in the sintered parts

(ii) *Viscosity problems.* As the amount of ceramic powder increases, the viscosity of the slurry generally increases. High viscosity can affect the flowability of the slurry, making it difficult to fill small features and complex structures during printing

(iii) *Sedimentation and stability.* Ceramic particles are denser than the liquid medium, and they may settle under gravity over time, causing the slurry to become unstable. This sedimentation can lead to a non-uniform distribution of particles in the printed parts, affecting their properties. According to Stokes' sedimentation law, reducing the particle size, increasing the fluid viscosity, and increasing the solid fraction can help stabilize the slurry

(iv) *Shrinkage and deformation.* During the sintering process, the ceramic parts may experience shrinkage and deformation. The lower the solid content in the slurry, the greater the shrinkage rate of the green part. This can influence the structural accuracy and integrity of the final parts

(v) *Binder removal difficulties.* The binder added to the slurry needs to be removed before sintering. If the binder content is high, the debinding process becomes more difficult. The formation of a large amount of gas in the binder removal step can cause stresses, part cracking, and deformation.

More importantly, the addition of ceramic particles would cause absorption and scattering of incident light, which can significantly affect the printing quality in VPP 3D printing.

(i) *Curing depth reduction.* Ceramic particles absorb and scatter light, reducing the intensity of light that reaches deeper layers of the slurry. This leads to a decrease in curing depth. As the solid loading of ceramic particles increased, the light transmittance of the suspension significantly decreased, resulting in a reduction in curing depth. The reduction in curing depth and the increase in curing width can lead to a decrease in the curing ability

(ii) *Curing width increase.* The scattering of light causes the light to spread out, leading to an increase in curing width. This can result in the blurring of the edges of the printed features, reducing the printing resolution and accuracy. The scattering of light in the lateral direction can cause the printed features to be larger than the designed size. This is because the scattered light can cure the resin in the surrounding areas, leading to an increase in the size of the printed features. The scattering of light can also affect the fidelity of the printed features. For example, the edges of the printed features may be blurred or rounded, and the details of the features may be lost, leading to reduced overall quality of the printed parts.

To compensate for the effects of light absorption and scattering, it may be necessary to optimize the printing parameters, such as the light intensity, exposure time, and layer thickness. This can be a complex and time-consuming process and may require extensive experimentation and testing.

For a ceramic slurry to be compatible and printable with VPP, it should have some common features and requirements:

(i) *Composition.* Ceramic slurries consist of ceramic powders (40 – 60 vol.%), UV-curable resins (*e.g.*, acrylates), photoinitiators, and dispersants. For instance, alumina-based slurries with optimized particle size distributions (coarse, medium, and fine powders) improve packing density and reduce defects

(ii) *Rheology.* Low viscosity (<3 Pa·s) is critical for layer uniformity, achieved by balancing solid loading and dispersant content. High solid loading (>50 vol.%) ensures structural stability but risks increased viscosity. Sedimentation and agglomeration of particles can compromise print quality, necessitating continuous agitation

(iii) *Photoreactivity.* Slurries must allow sufficient UV penetration for curing. Nanoparticle additives (*e.g.*, SiC and YAG) can enhance properties but may scatter light, requiring precise formulation.

In recent years, the persistent challenges in formulating ceramic slurries and optimizing VPP processes have prompted the exploration of alternative ceramic feedstock materials. Among these, pre-ceramic polymer-derived ceramics have gained significant research interest due to their superior processability during shaping operations and outstanding material properties. Compared to conventional powder-based ceramic processing, these polymer-derived materials demonstrate remarkable thermal stability along with enhanced mechanical characteristics, including higher strength and improved fracture toughness.

Pre-ceramic polymers can be directly processed through sol-gel methods, offering advantages such as simplified handling, no drying issues, shorter processing times, elimination of flammable solvents, and superior solution stability compared to ceramic powders or pastes. A critical aspect of pre-ceramic polymer processing is crosslinking, which is essential for ceramic formation. Adjusting the molecular weight of these polymers enables precise control over rheological properties, an area of ongoing research.[24] The rheological behavior of pre-ceramic polymers is particularly crucial when they serve as binders for ceramic powders in composite printing applications. Silicon-based pre-ceramic polymers are widely utilized in SL for fabricating intricate structures due to their stability. These photocurable inorganic polymers transform into high-strength, chemically inert ceramics upon pyrolysis in inert atmospheres. The incorporation of active or passive fillers allows for the creation of diverse advanced ceramic phases.[2,25] An optimal pre-ceramic polymer should exhibit high molecular weight, suitable rheological properties, good solubility for shaping, and functional groups that facilitate curing and crosslinking.[26] Table 2 presents a summary of the commonly used organosilicon pre-ceramic polymers, along with their backbone structures, synthesis methods, and resulting ceramics.

In the VPP process, photopolymerizable monomers along with a small amount of photoinitiator and other additives are used to make a slurry/blend of appropriate rheological properties. Ceramic particles of sizes down to micro/nanometers can also be incorporated into it for the fabrication of composite ceramics[44] before printing. The processing and printing steps of pre-ceramic polymers

Table 2. List of commonly used pre-ceramic polymers for vat photopolymerization and ceramization along with their synthesis methods and respective derived ceramics

Pre-ceramic polymer	Derived ceramics	Applications	Ref.
Polysilanes (–R_1R_2Si–)	SiC	Photoresists, semiconductors, precursors to polycarbosilane synthesis	26-28
Polycarbosilane (–R_1R_2Si–C–)	SiC	Electric or photo-conductors, photoresists, nonlinear optical materials	29-33
Polysilazane (–R_1R_2Si–N=)	Si_3N_4 and SiCN	Barrier for heat exchanger, oxidation-resistant	34-36
Polysiloxane (–R_1R_2Si–O–)	SiOC	Biomedical, electronics, textile chemistry	37,38
Poly (organosilylcarbodiimides) (–R_1R_2Si–N=C = N–)	SiCN	High-temperature ceramics, chemically resistant	39,40
Polyborosilazane (–R_1R_2Si–N (R_3R_4B)–) Polyborosilane, (–R_1R_2Si–B (R_3)–) Polyborosiloxane (–R_1R_2Si–O (R_3R_4B)–)	Borosilicate ceramics such as SiCBN, SiBC, etc.	High-temperature ceramics, chemically resistant	41-43

starting from the primary precursors are shown in Figure 5. The final yield, y_c, of the ceramic is given as:

$$y_c = \frac{w_1}{w_0} \quad \text{(XII)}$$

where y_c is the ceramic yield, w_1 is the weight of ceramic residue, and w_0 is the original weight of the specimen before pyrolysis.

The cross-linking of pre-ceramic polymers is a critical step, typically achieved through radiation or catalytic methods at low temperatures. Polymers with a high degree of crosslinking exhibit improved ceramic yield, which is essential for maintaining structural integrity during subsequent processing. Most pre-ceramic polymers feature an inorganic backbone with hydrogen atoms or organic substituents. These components either integrate into the ceramic residue or are released as volatile byproducts during high-temperature pyrolysis. This conversion process involves gas evolution, isotropic shrinkage, and pore formation, often leading to structural defects that compromise the final ceramic density. To mitigate these issues, incorporating fillers has become a primary approach for producing bulk ceramic components with controlled dimensions. A variety of fillers – including polymeric, metallic, and ceramic materials in nano- or micro-scale forms – can be blended into pre-ceramic polymers to enhance their properties. Fillers play multiple functional roles and can be categorized as either reactive or passive. Passive fillers remain chemically stable throughout the entire process, showing no reactivity with the pre-ceramic polymer, ceramic residue, or processing atmosphere. Their primary function involves facilitating gas release during pyrolysis, which helps minimize dimensional shrinkage while preventing crack formation and macroporosity in the final ceramic product.[45] In contrast, active fillers chemically interact with both the gaseous byproducts of ceramization and the processing atmosphere, potentially altering the composition of the resultant ceramic material. These reactive additives enable precise tuning of functional characteristics, including electrical conductivity, thermal expansion behavior, and magnetic properties. Notably, when pre-ceramic polymers contain substantial filler content, the reinforcing effect of these additives may eliminate the need for crosslinking by providing sufficient structural support to maintain dimensional stability during processing.

4. Post-processing and heat treatment

Post-curing represents a critical secondary processing step that enhances the consolidation of incompletely polymerized resin components within fabricated structures. This treatment significantly improves the mechanical performance and structural integrity of printed components. However, substantial dimensional changes occurring during post-processing remain a key challenge in ceramic photopolymerization techniques. Consequently, comprehensive characterization of post-curing behavior is fundamental for minimizing geometric distortion and improving dimensional accuracy in printed ceramic components.

The curing shrinkage is primarily influenced by the curing extent of the green-state material[46] where higher curing degrees result in reduced shrinkage. The curing degree depends on process parameters such as laser power, layer pitch, scan pitch, and scanning speed. Increased laser power enhances crosslinking, improving curing depth and line width. Conversely, larger layers and scan pitches reduce curing by leaving more uncured resin, while faster scanning speeds decrease energy exposure per unit area. Laser power stability and resin photosensitivity (wavelength compatibility) further affect curing efficiency. Among these factors, laser power, layer pitch, and scan pitch play dominant roles in determining the final curing degree.

The curing efficiency demonstrates an inverse correlation with layer thickness, where the reduced spacing between layers promotes greater overlap and minimizes residual uncured resin. This relationship similarly governs scan spacing effects, as wider intervals leave more materials uncured and consequently diminish curing quality. Scanning velocity plays a crucial role, with faster speeds reducing energy deposition per unit area and thus lowering curing effectiveness. Process stability emerges as another critical factor, where fluctuations in laser power lead to inconsistent polymerization. The material's inherent properties, particularly its photosensitivity and spectral

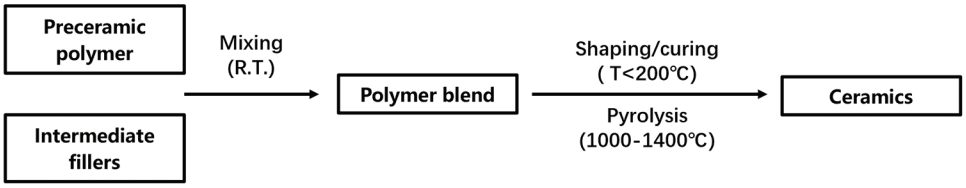

Figure 5. Processing steps involved to obtain ceramics from pre-ceramics
Abbreviations: R.T.: room temperature; T: temperature

compatibility with the irradiation wavelength, significantly influence photon absorption efficiency and curing outcomes. Among these interdependent parameters, laser power output, layer thickness setting, and scan spacing configuration exert the most substantial influence on the final curing performance.

The transformation of cured structures into ceramic components requires controlled thermal treatment, where sintering parameters critically influence the final material characteristics. Key processing variables including heating rate, atmospheric conditions, target temperature, and holding duration collectively govern phase formation and microstructural evolution by modulating crystallization behavior, carbothermal reactions, and filler interactions. During sintering, organic functional groups (methyl, phenyl, vinyl) are progressively removed from the polymer network, enhancing mechanical stability. Sintering defects evolve as the polymer binder burns out, creating initial voids, while simultaneous powder densification drives overall shrinkage. These small voids can coalesce into larger pores driven by capillary forces during particle rearrangement. Differential densification occurs when regions with varying green density (like thick vs. thin sections or near supports) shrink at different rates, generating stress, warping, or cracks propagating from denser areas or large pores. Control strategies include optimizing the polymer resin to pyrolyze cleanly, ensuring high and uniform powder packing in the green part, carefully controlled sintering profiles (temperature, time, atmosphere) for uniform densification, and software-based design compensation for isotropic shrinkage. For example, to minimize crack formation caused by gaseous byproduct evolution, heating rates must be carefully controlled, typically below 2°C/min, particularly within the critical polymer-to-ceramic transition range. Despite such precautions, ceramic products often exhibit residual porosity and microcracks due to inherent shrinkage. These limitations can be effectively mitigated through strategic filler incorporation, where reactive additives interact with either the pre-ceramic matrix or processing atmosphere to produce dense, crack-resistant ceramic composites.[27]

On the other hand, the sustainability of VPP demands attention. Key concerns include the recyclability of uncured resin slurry to minimize hazardous waste, the environmental impact of potentially toxic photoinitiators (driving research into safer alternatives), and the significant energy consumption during high-temperature sintering, a major carbon footprint contributor. Future strategies may focus on closed-loop slurry recycling systems, developing readily biodegradable resin systems and photoinitiators, optimizing sintering profiles, or adopting advanced sintering techniques to drastically reduce energy requirements over the part lifecycle.

5. Performance and applications

VPP enables the fabrication of intricate ceramic components that surpass the geometric capabilities of components generated by traditional additive manufacturing methods. The unique advantages of pre-ceramic polymers – including their processability, formability, and tunable molecular structure – make them particularly suitable for this technique, facilitating the production of specialized ceramic parts. These components demonstrate significant potential across multiple engineering fields, from biomedical implants to electrochemical systems, MEMS, and optical applications. The performance characteristics of the final products are governed by two critical factors: the material composition and the resulting microstructure, both of which are controlled through careful selection of raw materials and optimization of sintering parameters. To meet practical application requirements, the printed ceramic components must satisfy three essential criteria: sufficient mechanical strength, high surface quality, and dimensional accuracy relative to their digital design specifications.[47] To quantitatively validate sintered 3D-printed ceramic part quality, key characterization tools include X-ray diffraction for phase identification and crystallinity assessment, nanoindentation to measure localized hardness and elastic modulus, and X-ray computed tomography for non-destructive 3D visualization and quantification of internal porosity, pore size distribution, and density gradients. These techniques objectively confirm mechanical properties, phase purity, microstructural homogeneity, and the absence of macro-defects such as large voids or cracks resulting from uncontrolled shrinkage or pore coalescence during sintering. Integrating this characterization provides crucial feedback for optimizing printing and sintering parameters to achieve targeted final properties.

The SL has become a widely adopted technique for manufacturing high-performance ceramic components. The preparation of ceramic suspensions represents a critical step in this process, as it directly impacts both printing quality and final part integrity. Optimal ceramic suspensions must exhibit three key characteristics: uniform particle distribution, suitable rheological behavior, and extended colloidal stability. A significant challenge in suspension preparation involves balancing competing requirements. While higher ceramic loading reduces sintering shrinkage and improves densification, excessive solid content increases viscosity and promotes particle sedimentation during storage. This sedimentation phenomenon can cause non-uniform shrinkage during pyrolysis, compromising

dimensional accuracy. Consequently, careful optimization of suspension formulation is essential for achieving the necessary compromise between ceramic content and processing stability for successful stereolithographic fabrication.

The DLP-based 3D printing process has been extensively used to produce ceramic parts. It has been utilized for the fabrication of high-density (97–99 %) complex ceramic parts of zirconia and alumina having Vickers hardness of 13.1 and 17.5 GPa, respectively.[48,49] VPP 3D-printed ceramics have been extensively investigated for biomedical applications.[50-52] A team at Vienna University has developed a commercial DLP-based system, which was named lithography-based ceramic manufacturing (LCM), used for the 3D printing of advanced high-performance ceramics.[53] They have fabricated complex ceramic structures of very fine features ($25 \times 25 \times 25\ \mu m^3$) of alumina and bioglass with relative densities above 90% and good mechanical strength. Other ceramic components of zirconia and β-tricalcium phosphate have also been successfully fabricated with solid loadings of up to 50 vol.%.[54] Cellular ceramic structures of fine feature sizes have been fabricated for applications such as honeycomb catalyst supports,[54] heat exchangers,[55] and metamaterial structures with negative Poisson's ratio.[56] Chen's group at Shenzhen University has also manufactured various porous structural components using DLP-based 3D printing and a number of ceramic slurries, including SiC/SiOC composites, Li_4SiO_4, cordierite, and luminescent ceramics,[57-59] particularly for the fabrication of lattice structures with improved performance, as shown in Figure 6.

Light scattering by ceramic particles presents a fundamental challenge in SL, causing lateral curing resolution degradation and altered interlayer bonding characteristics.[60] The achievable curing depth depends on multiple factors including particle size distribution, solid loading percentage, irradiation intensity, and refractive index properties.[54] Crucially, minimizing the refractive index difference between the ceramic filler and resin matrix is vital for achieving high-resolution features, as significant mismatches can compromise printability.[61,62]

This technology has enabled the production of both dense and porous ceramic components with complex architectures for diverse applications ranging from foundry molds to electronic devices and biomedical implants.[63-66] Recent advancements have focused on three key areas: suspension formulation refinement, printing precision enhancement, and optimized thermal processing protocols.[67-70]

Recently, pre-ceramic polymers instead of ceramic suspensions have received great attention due to their direct

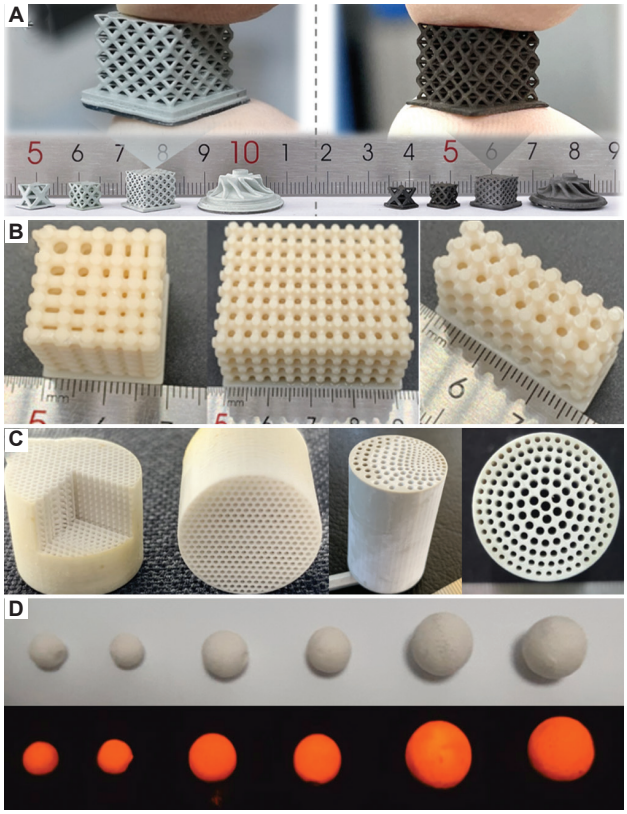

Figure 6. Various components prepared via digital light processing using different ceramic slurries: (A) SiC/SiOC composite lattice structures before and after sintering; (B) Li_4SiO_4 lattice structures; (C) cordierite honeycomb complex structures; (D) luminescent ceramics.

patterning and conversion to ceramic via pyrolysis.[24,71] These advanced ceramics, synthesized through polymer precursor conversion, exhibit superior performance characteristics with tunable functional properties that can be precisely engineered by modifying the pre-ceramic polymer formulation.[72-77] Pre-ceramic polymers offer superior compatibility with printing inks, effectively addressing common challenges related to material non-uniformity and optical interference that typically occur in ceramic particle suspensions. This enhanced formulation enables the fabrication of ceramic components with exceptional surface finish, fine feature resolution, and significant dimensional ratios. Eckel *et al.*[71] developed a UV-curable pre-ceramic polymer system through the combination of mercaptopropyl-methylsiloxane and vinylmethoxysiloxane, incorporating three key additives: a free-radical photoinitiator, radical inhibitor, and UV-absorbing component. The research team successfully employed this resin formulation to produce intricate SiOC ceramic architectures through linear laser SL, followed by pyrolysis at 1000°C under argon protection. Their findings demonstrate that UV-reactive pre-ceramic monomers

suitable for SL can be synthesized by functionalizing organosilicon compounds (siloxanes, silazanes, or carbosilanes) with photopolymerizable groups including thiol, vinyl, acrylate, or methacrylate functionalities.[71] The resin formulation incorporates polymerization inhibitors and UV-absorbing components to precisely control curing depth and reduce light scattering, thereby enhancing feature resolution. This monomer system can be further optimized through the strategic incorporation of metal alkoxides in controlled ratios, enabling the fabrication of advanced composite ceramics. Researchers have successfully extended this methodology to various pre-ceramic polymers, developing efficient production routes for SiCN, silicon nitride, and silicon carbide ceramics that combine dimensional accuracy with cost-effective manufacturing.[61,78-80]

The DLP technique has also been used for printing polymer-derived ceramic (PDC) structures with high resolution and higher efficiency.[81] They prepared dense silicon oxycarbide 3D structures with no cracks and high ceramic yield and micrometer resolution using engineered photosensitive methyl-silsesquioxane pre-ceramic polymer. The printed structures were converted into ceramics in a controlled pyrolysis process, which involves heating to 1000°C for 60 min under nitrogen gas protection with a precisely maintained temperature ramp of 1°C/min.

SiBCN ceramic components have been fabricated with tuned polyborosilazane.[82] A ceramic yield of 58% was obtained after pyrolysis at 1500°C while retaining the shape. The measured weight loss was found to be only 0.35% after pyrolysis, and the highest hardness of 7.8 ± 0.3 GPa with a bulk density of 1.84 ± 0.01 g/cm^3 was achieved. Furthermore, various printable pre-ceramic precursors have been prepared by adding functional groups to the polymer backbones,[80] mixing vinyl/allyl,[61] and physically mixing organosilicones of high ceramic yield with dispersant diluents, monomer, *etc.*[76] An approach different from the free radical polymerization has been proposed by Wang *et al.*,[83] which was introduced with thiol-ene click chemistry-based SL method to produce ceramics upon thermal treatment. The pre-ceramic precursor preparation involves the mixing of polysiloxane and allylhydridopolycarbosilane with phenylbis (2,4,6-trimethylbenzoyl) phosphine oxide (BAPOs) as photoinitiator. Sudan Orange G has been used as a photo-absorber, whereas hydroquinone is a free radical scavenger.[83] After homogenization, the pre-ceramic mixture was functionalized with thiol groups using 1,6-hexanedithiol. The fabricated SiOC ceramic components achieved complete densification without detectable microporosity, demonstrating a remarkable compressive strength of 216 MPa while maintaining a low cellular density of 0.61 g/cm^3. This technique utilizes thiol-ene click chemistry to modify pre-ceramic polymers containing unsaturated bonds (*e.g.*, polysiloxanes, polycarbosilanes, and polycarbosilazanes). During pyrolysis, the printed structures undergo controlled conversion into dimensionally stable thermosets and subsequently into dense glass ceramics with homogeneous shrinkage behavior, maintaining excellent shape retention. The process enables rapid production of pre-ceramic components that yield defect-free, high-density ceramics with superior surface quality after thermal treatment. Brodnik *et al.*[84] demonstrated that pyrolysis behavior varies significantly across different printed geometries, exhibiting structure-dependent shrinkage patterns and mechanical properties – contrasting with earlier assumptions of uniform dimensional changes in pre-ceramic polymer conversion. Fabrication of SiCN ceramic microreactors from polysilazane has been demonstrated by Gyak *et al.*[85] for application in hydrogen generation with ammonia cracking. The researchers developed a novel pre-ceramic processing method involving methacrylate-functionalized polyvinylsilazane combined with a ternary photoinitiator system {2,2-dimethoxy-2-phenylacetophenone, 2-hydroxy-2-methylpropiophenone, diphenyl(2,4,6-trimethylbenzoyl)-phosphine oxide in 3:1:1 ratio} dissolved in toluene. This approach enables the fabrication of advanced functional ceramics with exceptional performance characteristics suitable for extreme operating environments. Researchers have successfully engineered composite ceramic materials by introducing functional additives into pre-ceramic systems. Schmidt *et al.*[86] demonstrated this approach by dispersing alumina particles within a silicone-based pre-ceramic matrix, which upon pyrolysis transformed into porous mullite ceramics with unique rhombicuboctahedral morphology. The resulting 3D-printed mullite components exhibited a compressive strength of 1.8 ± 0.3 MPa, achieving a bulk density of 3.1 g/cm^3 while maintaining an exceptionally high porosity level of 90% by volume.

Chen's group from Shenzhen University has carried out research on the preparation of PDC precursor photosensitive resins and their DLP 3D printing (Figure 7). A low-viscosity and high-curing-strength silicone-based photosensitive resin co-doped with Zr/Ti was synthesized using the sol-gel method.[77] Compact SiOC lattice structures were obtained by pyrolysis at high temperatures in a nitrogen environment. The evolution of phase composition and microstructure was characterized. Their results showed that the compressive strength of lattice structure ceramics was significantly improved as temperature augmented, and the high concentration of metal doping further improved

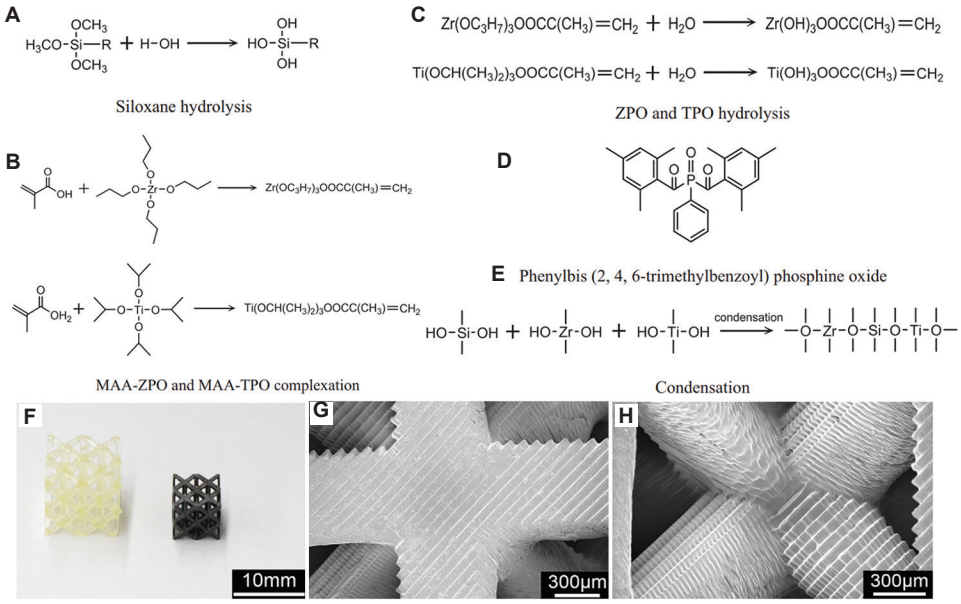

Figure 7. Material synthesis, 3D printed and pyrolyzed SiOC ceramics. The synthesis pathway is illustrated in panel (A-E), showing reagent molecular configurations and the sol-gel transition process that generates the inorganic network. (F) Images displaying the as-printed polymer precursor and its pyrolyzed SiOC ceramic counterpart for comparison purposes. (G and H) Microstructural characterizations revealing surface morphology and fracture patterns of the pyrolyzed octet-truss SiOC ceramic architecture processed at 1000°C.[77] Copyright © 2018 Elsevier. Reprinted with permission of Elsevier

the compressive strength. In addition, zirconium-based photosensitive resin was synthesized with metal alkyls, and a new zirconium-based photosensitive resin suitable for DLP 3D printing was obtained by optimizing the ratio of each component of the resin, and a porous lattice structure ZrOC ceramic with high specific strength was successfully prepared. By comparing the macroscopic photos of the samples treated at different pyrolysis temperatures, it can be found that the product shrank evenly after pyrolysis, showing a smooth surface and no clogging and cracks inside. The shrinkage rate increased continuously with the rise of pyrolysis temperature, concomitant with continuous improvement of the product's mechanical properties. Thus, various metallic precursors such as Fe, Ni, Co, and Pt can be incorporated into pre-ceramics to obtain PDCs for specific applications.

To address the complexity of existing photopolymerizable ceramic precursor material formulations and processes, Chen's group proposed a simplified approach using three commercially available low-cost organic polysiloxane ceramic precursors containing different functional groups/substituents as silicon sources.[76] Through a straightforward physical blending process, they developed photosensitive resin formulations for ceramic precursors. The research focused on investigating key properties and mechanisms including rheological behavior, stability, printability, and pyrolysis-induced ceramic quality of these precursor resins. By optimizing the printing process and sintering parameters to achieve both lightweight strength and structural precision requirements, the group successfully designed and fabricated various lattices. After pyrolysis, fully dense SiOC ceramics with high structural integrity, fine surface finish, and exceptionally high carbon-to-oxygen ratios were formed. Notably, the octagonal lattice-structured SiOC ceramics demonstrated a remarkable apparent density of 0.33 g/cm^3 and a specific strength reaching 5.74 × 10^4 N·m/kg, significantly outperforming previously reported material systems with comparable densities (Figure 8). This study provides robust theoretical and technical support for achieving lightweight yet high-strength complex ceramic precursor components. The breakthrough lies in establishing a material-process-performance framework that enables precise control over structural lightweight and mechanical enhancement in polymer-derived ceramics, opening new possibilities for advanced ceramic applications requiring intricate geometries and superior mechanical properties.

More recently, the research group also developed a novel two-stage folding-assisted pyrolysis strategy for 4D printing of shape-programmable PDCs.[88] A two-step thermal process (300°C pre-pyrolysis followed by 1000°C ceramization) enables controlled deformation and crack mitigation. The first stage fixes folded shapes via partial decomposition of organic components while creating microchannels for gas release, eliminating stress from metal wire fixatives. The second stage achieves

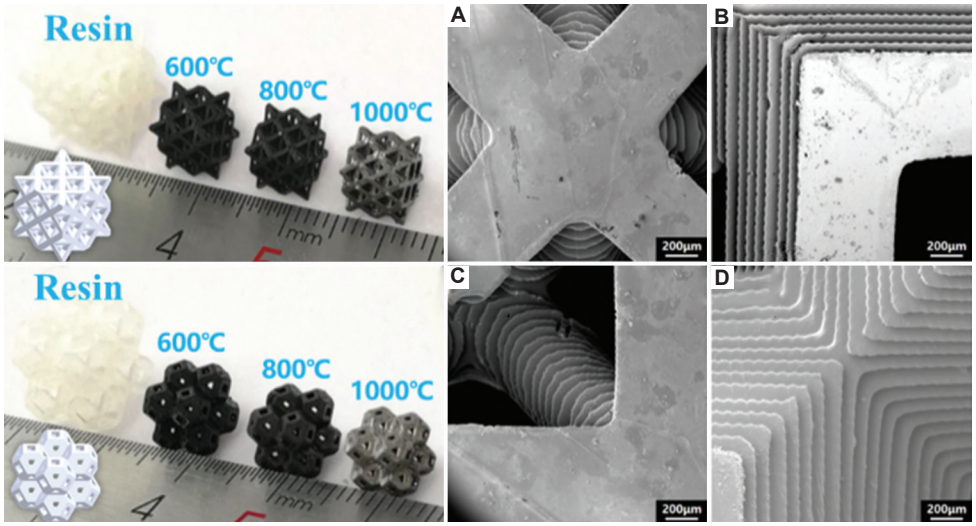

Figure 8. Lattice structures after printing and pyrolysis at different temperatures. Left: digital models and sample photos. Right: (A-D) Microscopic images of the detailed surface features after pyrolysis[76] (diagrams reused under the terms of the Creative Commons CC-BY license) During the pyrolysis of polymer-derived ceramics, the decomposition of organic functional groups generates small molecular gases that continuously and disorderly escape from the structure. This uncontrolled gas release often leads to defects such as cracking, warping, and structural collapse, severely limiting dimensional accuracy, surface morphology, and achievable component size – a critical challenge in precursor-derived ceramic additive manufacturing. To address this issue, Chen's group[87] proposed an innovative approach by introducing low-melting-point additives or specific organic modifiers into the photosensitive resin formulation. These additives create physical microchannels during pyrolysis through their own continuous gas emission, providing organized pathways for the controlled release of macromolecular decomposition gases. This mechanism effectively mitigates internal stress accumulation, thereby suppressing crack formation, minimizing dimensional distortion, and preventing structural collapse. Consequently, precursor-derived ceramic components with enhanced precision, improved surface roughness, reduced warpage, and increased critical thickness (cellular skeleton thickness exceeding 2 mm and bulk body thickness surpassing 5 mm) have been successfully fabricated, as demonstrated in Figure 9. Compared with conventional crack-control techniques such as hot pressing, hot isostatic pressing, and spark plasma sintering, this method offers distinct advantages including simplified processing (ambient pressure operation), reduced cycle time, and cost-effectiveness.

full ceramization into dense SiOC. Despite a low ceramic yield rate (13.5 wt.%) and significant shrinkage (59.91%), the method successfully produces crack-free, geometrically complex ceramics through UV-curable resin design and stress management. Flexible green bodies from photopolymerization allow manual folding into intricate shapes (*e.g.*, spirals, flowers) that retain structural integrity after pyrolysis (Figure 10). Material characterization confirms chemical bond evolution, microchannel formation, and defect-free microstructures, while mechanical testing reveals a compressive strength of 21.31 MPa. This strategy bridges additive manufacturing and ceramic processing, enabling high-precision, defect-resistant PDCs for aerospace and biomedical applications.

TPP has also been explored at a large scale for the fabrication of polymeric materials for optical applications; however, the requirement of complex micro/nanostructures for application in harsh environments has led to the exploration of TPP for the fabrication of advanced ceramic components. Pre-ceramic polymers have been proven to be a suitable candidate for fabricating complex structures using TPP and their direct conversion to ceramic counterparts via pyrolysis. The limitation is the shrinkage of pre-ceramic polymers during pyrolysis and hence various parameters, such as temperature, heating rate, and composition, must be controlled. 3D SiCN nano/microstructures in a resolution of a few hundreds of nanometers were first fabricated by Pham *et al.*[89] using TPP an inorganic pre-ceramic polymer with a linear shrinkage of ~ 41%. Further, they resolved the issue of shrinkage by incorporating 10 nm silica particles into the pre-ceramic polymer and were able to achieve nearly zero shrinkage of the final ceramic component for a solid content of 40 wt.%.

The TPP technique has been employed as a template-based approach for producing hollow ceramic nanolattices. This technique involves three key steps: (i) TPP fabrication of nanoscale polymer molds, (ii) conformal deposition of ceramic materials (TiN, Al_2O_3) via vapor-phase techniques, and (iii) precision opening of the structure using ion-beam milling followed by template removal through chemical or plasma etching.[90] Thus, TPP in conjunction with appropriate photosensitive pre-ceramic polymers enables fabrication of complex 3D structures of extremely high-accuracy sub-wavelength features, which are otherwise not possible with other SL techniques. The challenge associated with this is the difficulty in detaching components from the

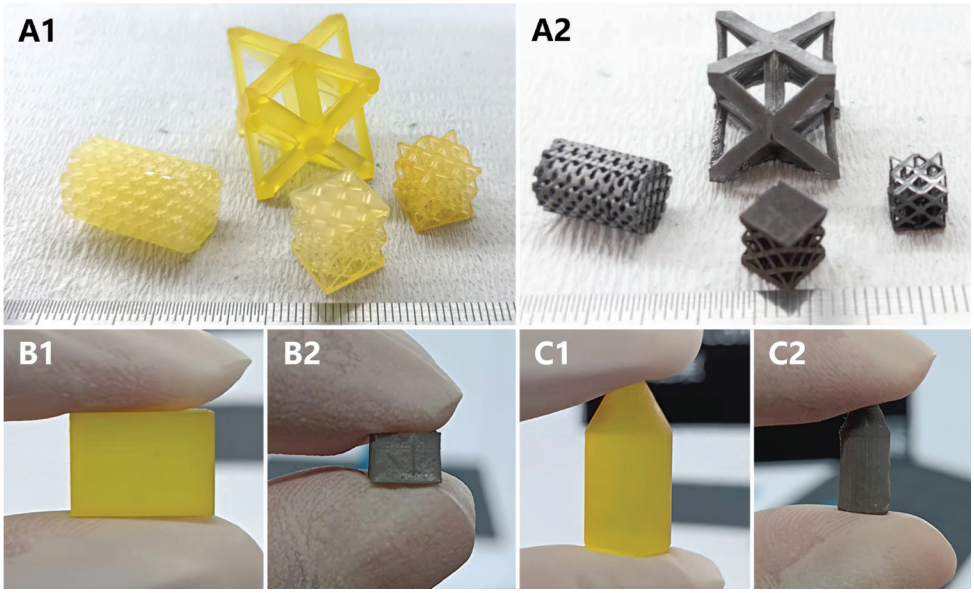

Figure 9. Samples before and after pyrolysis: (A1 and A2) cellular components, (B1 and B2) block, (C1 and C2) bullet

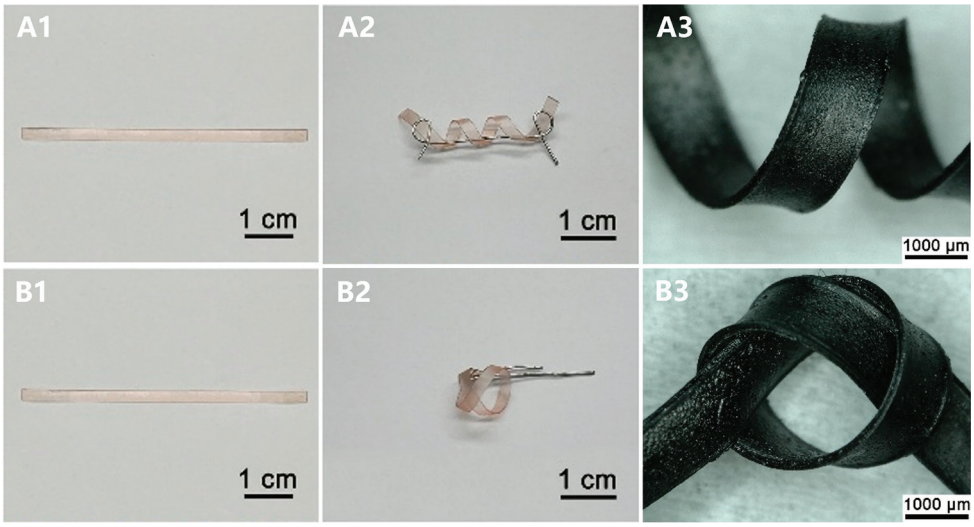

Figure 10. Programmable shapes of printed samples after printing, folding, and folding-assisted two-stage pyrolysis: (A1-A3) shapes of spirals, (B1-B3) shapes of knots

build platform to obtain free-standing components, thereby limiting the pyrolysis temperature to 600°C. The TPP is only applicable to slurries transparent to infrared light and the fabrication of opaque slurries is challenging. In addition, the problem of shrinkage during pyrolysis can be resolved by the incorporation of nanofillers or using a low-shrinkage pre-ceramic polymer.[89] The printed components using TPP are of small sizes and generally require longer production owing to the slow fabrication speed.

The CLIP technique leverages an oxygen-inhibited polymerization zone to enable rapid curing of photopolymer resins. The technology's primary constraints involve resin curing kinetics and flow dynamics within the build area – parameters requiring optimization to fully realize CLIP's revolutionary potential for cost-effective manufacturing of intricate polymer components through additive processes.

These studies showed that the VPP techniques are compatible with producing ceramic parts from pre-ceramic and various ceramic powders together with resins. Micro- to nano-architected ceramic materials of complex shapes can be produced with excellent specific stiffness and strength, which may find application in many areas of science and technology.

Table 3. Application fields for vat photopolymerization 3D-printed ceramics

Application fields	Examples
Biomedicines	Artificial bones, implants, teeth, dental crowns, veneers, orthodontic brackets, etc.
Aerospace	Turbine blades, radomes, combustors, heat insulation tiles, electromagnetic wave shielding components, etc.
Energy	Solid oxide fuel cells, lithium-ion batteries, nuclear fusion tritium breeders, supercapacitors, etc.
Electronics	Smart watch frames, smartphone back panels, delicate components for electronic devices
Cultural products	Jewelry, antique restoration and preservation, customized prototypes and gadgets

6. Conclusion and perspectives

The VPP techniques have emerged as a powerful tool for the additive manufacturing of ceramics, offering unprecedented capabilities in producing complex structures with high precision and resolution. The integration of pre-ceramic polymers and ceramic slurries has significantly expanded the scope of applications, enabling the fabrication of advanced ceramic components with properties tailored for various industries, including biomedical, electronics, aerospace, and energy (Table 3). These techniques have demonstrated the potential to overcome traditional manufacturing limitations, providing a cost-effective and efficient approach to producing high-performance ceramics without the need for additional tooling. The advantages of VPP are multifaceted. The high resolution and fast printing speed make it suitable for creating intricate geometries and microstructures, which are challenging to achieve with conventional manufacturing methods. The ability to produce complex shapes with minimal waste and short production cycles further enhances its appeal. Moreover, the use of pre-ceramic polymers has opened up new possibilities for creating ceramics with exceptional mechanical and thermal properties, as well as multifunctional composites that can be tailored for specific applications. However, despite the significant progress made, several challenges remain. The absorption and scattering of light by ceramic particles can significantly affect the printing quality, leading to issues such as reduced curing depth and increased curing width. This can result in decreased dimensional accuracy and resolution, requiring careful optimization of printing parameters to mitigate these effects. In addition, the ceramic powder dispersion in the slurry, the viscosity, and the stability of the slurry over time are critical factors that need to be addressed to ensure consistent and high-quality prints.

Future work should focus on optimizing the composition and rheology of ceramic slurries and pre-ceramic polymers to enhance printability and reduce defects. The development of new photoinitiators and additives that can improve the photoreactivity of the materials while minimizing light scattering is crucial. Advanced testing techniques, such as *in situ* monitoring and computational modeling, can offer stronger insights into the curing mechanisms and help in the optimization of printing parameters. This will enable more precise control over the manufacturing process, enabling the production of ceramic components with higher quality and stability. Furthermore, the exploration of new applications and materials is essential for the continued growth of VPP in the ceramics field. The fabrication of microreactors, metamaterials, and bioactive scaffolds represents promising areas for future research, with the potential to revolutionize various industries. The development of new ceramic materials with enhanced properties, such as higher strength, improved thermal stability, and advanced functional characteristics, will further expand the scope of applications. In addition, the environmental and economic aspects of VPP should be considered. The use of non-toxic and environmentally friendly materials, as well as the development of more efficient and sustainable manufacturing processes, will be important for the long-term success of this technology. The reduction of waste and energy consumption, along with the optimization of production costs, will make VPP a more viable and attractive option for industrial applications.

As the technology continues to evolve, it is expected to play a pivotal role in the additive manufacturing of high-performance ceramics, contributing to advancements in various scientific and technological fields. The ongoing efforts in this area are likely to induce breakthroughs that will further enhance the capabilities and applications of VPP, making it a valuable tool in the manufacturing of advanced ceramics.

Acknowledgments

None.

Funding

This work was financially supported by the Key Project of the Department of Education of Guangdong Province (2022ZDZX3017), the Special Support Plan of Guangdong Province (2021TQ05Z151), Guangdong Basic and Applied Basic Research Foundation (2024A1515010049), and SZU Research Fund (GFPY-YB-2024-03).

Conflicts of interest

Zhangwei Chen serves as the Editorial Board Member of the journal but was not in any way involved in the

editorial and peer-review process conducted for this paper, directly or indirectly. Other authors declare they have no competing interests.

Author's contributions

Investigation: Chongyu Long
Data curation: Chongyu Long
Formal analysis: Chongyu Long
Funding acquisition: Zhangwei Chen
Investigation: Zhiyuan Liu, Changyong Liu, Zhangwei Chen
Resources: Zhangwei Chen
Supervision: Zhangwei Chen
Visualization: Chongyu Long
Writing–original draft: Chongyu Long, Zhangwei Chen
Writing–review & editing: All authors

Ethics approval and consent to participate

Not applicable.

Consent for publication

Not applicable.

Availability of data

Not applicable.

References

1. Lee JY, An J, Chua CK. Fundamentals and applications of 3D printing for novel materials. *Appl Mater Today*. 2017;7:120-133.

   doi: 10.1016/j.apmt.2017.02.004

2. Chen Z, Li Z, Li J, *et al.* 3D printing of ceramics: A review. *J Eur Ceram Soc*. 2019;39(4):661-687.

   doi: 10.1016/j.jeurceramsoc.2018.11.013

3. Davoudinejad A. Vat photopolymerization methods in additive manufacturing. In: *Additive Manufacturing*. Netherlands: Elsevier; 2021. p. 159-181.

   doi: 10.1016/B978-0-12-818411-0.00007-0

4. Rahaman MN. *Ceramic Processing and Sintering*. United States: CRC Press; 2017.

   doi: 10.1201/9781315274126

5. Hull CW. Inventor; *Methods and Apparatus for Production of Three-dimensional Objects by Stereolithography. USA Patent US5236637*; 1986.

6. Jacobs PF. *Rapid Prototyping & Manufacturing: Fundamentals of Stereolithography*. United States: Society of Manufacturing Engineers; 1992.

7. Parra-Cabrera C, Achille C, Kuhn S, Ameloot R. 3D printing in chemical engineering and catalytic technology: Structured catalysts, mixers and reactors. *Chem Soc Rev*. 2018;47(1):209-230.

   doi: 10.1039/C7CS00631D

8. Choi JW, Kim HC, Wicker R. Multi-material stereolithography. *J Mater Process Technol*. 2011;211(3):318-328.

   doi: 10.1016/j.jmatprotec.2010.10.003

9. Klein J, Stern M, Franchin G, *et al.* Additive manufacturing of optically transparent glass. *3D Print Addit Manuf*. 2015;2(3):92-105.

   doi: 10.1089/3dp.2015.0021

10. Halloran JW. Ceramic stereolithography: Additive manufacturing for ceramics by photopolymerization. *Annu Rev Mater Res*. 2016;46(1):19-40.

    doi: 10.1146/annurev-matsci-070115-031841

11. Griffith ML, Halloran JW. Ultraviolet curable ceramic suspensions for stereolithography of ceramics. In: *Proceedings Solid Freeform Fabrication Symposium;* 1994. p. 529-534.

12. Nakamoto T, Yamaguchi K. *Consideration on the Producing of High Aspect Ratio Micro Parts using UV Sensitive Photopolymer*. United States: IEEE; 1996. p. 53-58.

13. Bertsch A, Zissi S, Jezequel J, Corbel S, Andre J. Microstereophotolithography using a liquid crystal display as dynamic mask-generator. *Microsyst Technol*. 1997;3(2):42-47.

14. Göppert-Mayer M. Elementary processes with two quantum transitions. *Ann Phys*. 2009;521(7-8):466-479.

    doi: 10.1002/andp.200952107-804

15. Kaiser W, Garrett CGB. Two-photon excitation in CaF2:Eu2+. *Phys Rev Lett*. 1961;7(6):229-231.

    doi: 10.1103/PhysRevLett.7.229

16. Paz VF, Emons M, Obata K, *et al.* Development of functional sub-100 nm structures with 3D two-photon polymerization technique and optical methods for characterization. *J Laser Appl*. 2012;24(4):042004.

    doi: 10.2351/1.4712151

17. Bhawalkar JD, He GS, Prasad PN. Nonlinear multiphoton processes in organic and polymeric materials. *Rep Prog Phys*. 1996;59(9):1041.

    doi: 10.1088/0034-4885/59/9/001

18. LaFratta CN, Fourkas JT, Baldacchini T, Farrer RA. Multiphoton fabrication. *Angew Chem Int Ed*. 2007;46(33):6238-6258.

    doi: 10.1002/anie.200603995

19. Fried JR. *Polymer Science and Technology*. United Kingdom: Pearson Education; 2014.

20. Serbin J, Egbert A, Ostendorf A, *et al.* Femtosecond laser-

induced two-photon polymerization of inorganic-organic hybrid materials for applications in photonics. *Opt Lett*. 2003;28(5):301-303.

doi: 10.1364/ol.28.000301

21. Zipfel WR, Williams RM, Webb WW. Nonlinear magic: Multiphoton microscopy in the biosciences. *Nat Biotechnol*. 2003;21(11):1369-1377.

doi: 10.1038/nbt899

22. Tumbleston John R, Shirvanyants D, Ermoshkin N, *et al*. Continuous liquid interface production of 3D objects. *Science*. 2015;347(6228):1349-1352.

doi: 10.1126/science.aaa2397

23. González-Méijome JM, Compañ-Moreno V, Riande E. Determination of oxygen permeability in soft contact lenses using a polarographic method: estimation of relevant physiological parameters. *Ind Eng Chem Res*. 2008;47(10):3619-3629.

24. Wang G, Song Y. Enhancing the yield of polycarbosilane synthesis via recycling of liquid by-product at atmospheric pressure. *Ceram Int*. 2018;44(6):6474-6478.

doi: 10.1016/j.ceramint.2018.01.101

25. Colombo P, Mera G, Riedel R, Sorarù GD. Polymer-derived ceramics: 40 years of research and innovation in advanced ceramics. *J Am Ceram Soc*. 2010;93(7):1805-1837.

doi: 10.1111/j.1551-2916.2010.03876.x

26. Martínez-Crespiera S, Ionescu E, Schlosser M, *et al*. Fabrication of silicon oxycarbide-based microcomponents via photolithographic and soft lithography approaches. *Sens Actuat A Phys*. 2011;169(1):242-249.

doi: 10.1016/j.sna.2011.04.041

27. Kashimura S, Tane Y, Ishifune M, *et al*. Practical method for the synthesis of polysilanes using Mg and Lewis acid system. *Tetrahedron Lett*. 2008;49(2):269-271.

doi: 10.1016/j.tetlet.2007.11.083

28. Jones RG, Holder SJ. High-yield controlled syntheses of polysilanes by the Wurtz-type reductive coupling reaction. *Polym Int*. 2006;55(7):711-718.

doi: 10.1002/pi.1945

29. Krempner C. Polysilane dendrimers. *Polymers*. 2012;4(1):408-447.

doi: 10.3390/polym4010408

30. Chen J, He G, Liao Z, *et al*. Control of structure formation of polycarbosilane synthesized from polydimethylsilane by Kumada rearrangement. *J Appl Polym Sci*. 2008;108(5):3114-3121.

doi: 10.1002/app.27847

31. Cheng X, Xie Z, Song Y, Xiao J, Wang Y. Structure and properties of polycarbosilane synthesized from polydimethylsilane under high pressure. *J Appl Polym Sci*. 2006;99(3):1188-1194.

doi: 10.1002/app.22465

32. Lodhe M, Babu N, Selvam A, Balasubramanian M. Synthesis and characterization of high ceramic yield polycarbosilane precursor for SiC. *J Adv Ceram*. 2015;4:307-311.

doi: 10.1007/s40145-015-0169-8

33. He L, Zhang Z, Yang X, Jiao L, Li Y, Xu C. Liquid polycarbosilanes: synthesis and evaluation as precursors for SiC ceramic. *Polym Int*. 2015;64(8):979-985.

doi: 10.1002/pi.4904

34. Hörz M, Zern A, Berger F, *et al*. Novel polysilazanes as precursors for silicon nitride/silicon carbide composites without "free" carbon. *J Eur Ceram Soc*. 2005;25(2-3):99-110.

doi: 10.1016/j.jeurceramsoc.2004.05.003

35. Blum YD, Schwartz KB, Laine RM. Preceramic polymer pyrolysis: Part 1 Pyrolytic properties of polysilazanes. *J Mater Sci*. 1989;24:1707-1718.

doi: 10.1007/BF01138991

36. Kroke E, Li YL, Konetschny C, Lecomte E, Fasel C, Riedel R. Silazane derived ceramics and related materials. *Mater Sci Eng R Rep.* 2000;26(4-6):97-199.

doi: 10.1016/S0927-796X(00)00013-0

37. Soraru GD. Silicon oxycarbide glasses from gels: Code: H1. *J Sol Gel Sci Technol*. 1994;2:843-848.

doi: 10.1007/BF00489675

38. Schmitt M. Analysis of silanes and of siloxanes formation by Raman spectroscopy. *RSC Adv*. 2014;4(4):1907-1917.

doi: 10.1039/C3RA45816A

39. Mera G, Riedel R, Poli F, Müller K. Carbon-rich SiCN ceramics derived from phenyl-containing poly (silylcarbodiimides). *J Eur Ceram Soc*. 2009;29(13):2873-2883.

doi: 10.1016/j.jeurceramsoc.2009.03.020

40. Widgeon S, Mera G, Gao Y, *et al*. Nanostructure and energetics of carbon-rich SiCN ceramics derived from polysilylcarbodiimides: Role of the nanodomain interfaces. *Chem Mater*. 2012;24(6):1181-1191.

doi: 10.1021/cm3000259

41. Gao Y, Mera G, Nguyen H, Morita K, Kleebe HJ, Riedel R. Processing route dramatically influencing the nanostructure of carbon-rich SiCN and SiBCN polymer-derived ceramics. Part I: Low temperature thermal transformation. *J Eur Ceram Soc*. 2012;32(9):1857-1866.

doi: 10.1016/j.jeurceramsoc.2012.01.022

42. Zhang Z, Zeng F, Han J, Luo Y, Xu C. Synthesis and characterization of a new liquid polymer precursor for Si-B-C-N ceramics. *J Mater Sci*. 2011;46:5940-5947.

doi: 10.1007/s10853-010-4934-1

43. Widgeon S, Mera G, Gao Y, Sen S, Navrotsky A, Riedel R. Effect of precursor on speciation and nanostructure of SiBCN polymer-derived ceramics. *J Am Ceram Soc*. 2013;96(5):1651-1659.

doi: 10.1111/jace.12217

44. Griffith ML, Halloran JW. Freeform fabrication of ceramics via stereolithography. *J Am Ceram Soc*. 1996;79(10):2601-2608.

doi: 10.1111/j.1151-2916.1996.tb09022.x

45. Schwartz KB, Rowcliffe DJ. Modeling density contributions in preceramic polymer/ceramic powder systems. *J Am Ceram Soc*. 1986;69(5):C-106.

doi: 10.1111/j.1151-2916.1986.tb04782.x

46. Wang WL, Cheah CM, Fuh JYH, Lu L. Influence of process parameters on stereolithography part shrinkage. *Mater Design*. 1996;17(4):205-213.

doi: 10.1016/S0261-3069(97)00020-1

47. Travitzky N, Bonet A, Dermeik B, *et al*. Additive manufacturing of ceramic-based materials. *Adv Eng Mater*. 2014;16(6):729-754.

doi: 10.1002/adem.201400097

48. He R, Liu W, Wu Z, *et al*. Fabrication of complex-shaped zirconia ceramic parts via a DLP- stereolithography-based 3D printing method. *Ceram Int*. 2018;44(3):3412-3416.

doi: 10.1016/j.ceramint.2017.11.135

49. Zhou M, Liu W, Wu H, *et al*. Preparation of a defect-free alumina cutting tool via additive manufacturing based on stereolithography - Optimization of the drying and debinding processes. *Ceram Int*. 2016;42(10):11598-11602.

doi: 10.1016/j.ceramint.2016.04.007

50. Li S, Shan Y, Chen J, *et al*. 3D printing and biomedical applications of piezoelectric composites: A critical review. *Adv Mater Technol*. 2025;10(5):2401160.

51. Hamza M, Kanwal Q, Hussain MI, *et al*. Recent progress in 3D printed piezoelectric materials for biomedical applications. *Mater Sci Eng R Rep*. 2025;164:100962.

52. Zhang P, He R. 3D-printed silicon nitride ceramic implants for clinical applications: The state of the art and prospects. *RSC Adv*. 2025;15(1):406-419.

53. Scheithauer U, Schwarzer E, Ganzer G, *et al*. Microhreactors made by lithography-based ceramic manufacturing (LCM). In: *Additive Manufacturing and Strategic Technologies in Advanced Ceramics: Ceramic Transactions*. Vol. 258. United States: Wiley; 2015. p. 31-41.

doi: 10.1002/9781119183860.ch3

54. Schwentenwein M, Homa J. Additive manufacturing of dense alumina ceramics. *Int J Appl Ceram Technol*. 2015;12(1):1-7.

doi: 10.1111/ijac.12324

55. Scheithauer U, Schwarzer E, Moritz T, Michaelis A. Additive manufacturing of ceramic heat exchanger: Opportunities and limits of the lithography-based ceramic manufacturing (LCM). *J Mater Eng Perform*. 2018;27(1):14-20.

doi: 10.1007/s11665-017-3056-1

56. Lantada AD, de Blas Romero A, Schwentenwein M, Jellinek C, Homa J. Lithography-based ceramic manufacture (LCM) of auxetic structures: Present capabilities and challenges. *Smart Mater Struct*. 2016;25(5):054015.

doi: 10.1088/0964-1726/25/5/054015

57. Qu P, Liang G, Hussain MI, *et al*. Low-temperature fabrication of high-specific strength SiC-based ceramics via photopolymerization 3D printing with controllable anisotropy. *Int J Extreme Manuf*. 2025;7(5):055002.

doi: 10.1088/2631-7990/add2e1

58. Luo X, Ren W, Xing H, Hussain MI, Chen Z. Additively manufactured Li4SiO4 ceramic pebbles with radial pores for enhanced performance. *Ceram Int*. 2025.

doi. 10.1016/j.ceramint.2025.01.332

59. Ren W, Liu W, Luo X, Liu Z, Liu C, Chen Z. 3D printing of cordierite glass-ceramics. *Ceram Int*. 2025;51(2):1632-1642.

60. Gentry SP, Halloran JW. Depth and width of cured lines in photopolymerizable ceramic suspensions. *J Eur Ceram Soc*. 2013;33(10):1981-1988.

doi: 10.1016/j.jeurceramsoc.2013.02.012

61. de Hazan Y, Penner D. SiC and SiOC ceramic articles produced by stereolithography of acrylate modified polycarbosilane systems. *J Eur Ceram Soc*. 2017;37(16):5205-5212.

doi: 10.1016/j.jeurceramsoc.2017.03.021

62. Badev A, Abouliatim Y, Chartier T, *et al*. Photopolymerization kinetics of a polyether acrylate in the presence of ceramic fillers used in stereolithography. *J Photochem Photobiol A*. 2011;222(1):117-122.

doi: 10.1016/j.jphotochem.2011.05.010

63. Leigh SJ, Purssell C, Bowen J, Hutchins DA, Covington JA, Billson D. A miniature flow sensor fabricated by micro-stereolithography employing a magnetite/acrylic nanocomposite resin. *Sens Actuat A*. 2011;168(1):66-71.

doi: 10.1016/j.sna.2010.12.007

64. Chen W, Kirihara S, Miyamoto Y. Fabrication and measurement of micro three-dimensional photonic crystals of SiO2 ceramic for terahertz wave applications. *J Am Ceram Soc*. 2007;90(7):2078-2081.

doi: 10.1111/j.1551-2916.2007.01724.x

65. Du D, Asaoka T, Ushida T, Furukawa KS. Fabrication and perfusion culture of anatomically shaped artificial bone using stereolithography. *Biofabrication*. 2014;6(4):045002.

doi: 10.1088/1758-5082/6/4/045002

66. Lian Q, Sui W, Wu X, Yang F, Yang S. Additive manufacturing of ZrO2 ceramic dental bridges by stereolithography. *Rapid Prototyp J*. 2018;24(1):114-119.

doi: 10.1108/RPJ-09-2016-0144

67. Bae CJ, Halloran JW. Influence of residual monomer on cracking in ceramics fabricated by stereolithography. *Int J Appl Ceram Technol*. 2011;8(6):1289-1295.

doi: 10.1111/j.1744-7402.2011.02611.x

68. Bae CJ, Ramachandran A, Halloran JW. Quantifying particle segregation in sequential layers fabricated by additive manufacturing. *J Eur Ceram Soc*. 2018;38:4082-4088.

doi: 10.1016/j.jeurceramsoc.2018.07.040

69. Mitteramskogler G, Gmeiner R, Felzmann R, *et al*. Light curing strategies for lithography-based additive manufacturing of customized ceramics. *Addit Manuf*. 2014;1:110-118.

doi: 10.1016/j.addma.2014.08.004

70. Pfaffinger M, Mitteramskogler G, Gmeiner R, Stampfl J. *Thermal Debinding of Ceramic-filled Photopolymers*. Switzerland: Trans Tech Publ; 2015. p. 75-81.

doi: 10.1002/9781119183860.ch10

71. Eckel ZC, Zhou C, Martin JH, Jacobsen AJ, Carter WB, Schaedler TA. Additive manufacturing of polymer-derived ceramics. *Science*. 2016;351(6268):58-62.

doi: 10.1126/science.aad2688

72. Chaudhary RP, Parameswaran C, Idrees M, *et al*. Additive manufacturing of polymer-derived ceramics: Materials, technologies, properties and potential applications. *Prog Mater Sci*. 2022;128:100969.

doi: 10.1016/j.pmatsci.2022.100969

73. Toma L, Kleebe HJ, Müller MM, *et al*. Correlation between intrinsic microstructure and piezoresistivity in a SiOC polymer-derived ceramic. *J Am Ceram Soc*. 2012; 95(3):1056-1061.

doi: 10.1111/j.1551-2916.2011.05026.x

74. Colombo P, Bernardo E, Parcianello G. Multifunctional advanced ceramics from preceramic polymers and nano-sized active fillers. *J Eur Ceram Soc*. 2013;33(3):453-469.

doi: 10.1016/j.jeurceramsoc.2012.10.006

75. Kim KJ, Eom JH, Kim YW, Seo WS. Electrical conductivity of dense, bulk silicon-oxycarbide ceramics. *J Eur Ceram Soc*. 2015;35(5):1355-1360.

doi: 10.1016/j.jeurceramsoc.2014.12.009

76. Li Z, Chen Z, Liu J, *et al*. Additive manufacturing of lightweight and high-strength polymer-derived SiOC ceramics. *Virtual Phys Prototyp*. 2020;15(2):163-177.

doi: 10.1080/17452759.2019.1710919

77. Fu Y, Xu G, Chen Z, Liu C, Wang D, Lao C. Multiple metals doped polymer-derived SiOC ceramics for 3D printing. *Ceram Int*. 2018;44(10):11030-11038.

doi: 10.1016/j.ceramint.2018.03.075

78. Zocca A, Gomes CM, Staude A, Bernardo E, Günster J, Colombo P. SiOC ceramics with ordered porosity by 3D-printing of a preceramic polymer. *J Mater Res*. 2013;28(17):2243-2252.

doi: 10.1557/jmr.2013.129

79. Zhou S, Mei H, Chang P, Lu M, Cheng L. Molecule editable 3D printed polymer-derived ceramics. *Coord Chem Rev*. 2020;422:213486.

doi: 10.1016/j.ccr.2020.213486

80. Hundley JM, Eckel ZC, Schueller E, *et al*. Geometric characterization of additively manufactured polymer derived ceramics. *Addit Manuf*. 2017;18:95-102.

doi: 10.1016/j.addma.2017.09.005

81. Zanchetta E, Cattaldo M, Franchin G, *et al*. Stereolithography of SiOC ceramic microcomponents. *Adv Mater*. 2016;28(2):370-376.

doi: 10.1002/adma.201503470

82. Li S, Duan W, Zhao T, *et al*. The fabrication of SiBCN ceramic components from preceramic polymers by digital light processing (DLP) 3D printing technology. *J Eur Ceram Soc*. 2018;38(14):4597-4603.

doi: 10.1016/j.jeurceramsoc.2018.05.043

83. Wang X, Schmidt F, Hanaor D, Kamm PH, Li S, Gurlo A. Additive manufacturing of ceramics from preceramic polymers: A versatile stereolithographic approach assisted by thiol-ene click chemistry. *Addit Manuf*. 2019;27:80-90.

doi: 10.1016/j.addma.2019.02.012

84. Brodnik NR, Schmidt J, Colombo P, Faber KT. Analysis of multi-scale mechanical properties of ceramic trusses prepared from preceramic polymers. *Addit Manuf*. 2020;31:100957.

doi: 10.1016/j.addma.2019.100957

85. Gyak KW, Vishwakarma NK, Hwang YH, Kim J, Yun HS, Kim DP. 3D-printed monolithic SiCN ceramic microreactors from a photocurable preceramic resin for the high temperature ammonia cracking process. 10.1039/C9RE00201D. *React Chem Eng*. 2019;4(8):1393-1399.

doi: 10.1039/C9RE00201D

86. Schmidt J, Altun AA, Schwentenwein M, Colombo P. Complex mullite structures fabricated via digital light processing of a preceramic polysiloxane with active alumina fillers. *J Eur Ceram Soc*. 2019;39(4):1336-1343.

doi: 10.1016/j.jeurceramsoc.2018.11.038

87. Xiong SF, Liu J, Cao JW, *et al*. 3D printing of crack-free dense polymer-derived ceramic monoliths and lattice skeletons with improved thickness and mechanical performance. *Addit Manuf*. 2022;57:102964.

doi: 10.1016/j.addma.2022.102964

88. Jiang L, Long C, Xiong S, *et al*. 4D printing of shape-programmable polymer-derived ceramics via two-stage folding-assisted pyrolysis strategy. *Virtual Phys Prototyp*. 2024;19(1):e2406408.

doi: 10.1080/17452759.2024.2406408

89. Pham TA, Kim DP, Lim TW, Park SH, Yang DY, Lee KS. Three-dimensional SiCN ceramic microstructures via nano-stereolithography of inorganic polymer photoresists. 2006;16(9):1235-1241.

doi: 10.1002/adfm.200600009

90. Jang D, Meza LR, Greer F, Greer JR. Fabrication and deformation of three-dimensional hollow ceramic nanostructures. *Nat Mater*. 2013;12(10):893.

doi: 10.1038/nmat3738

ACCSCIENCE PUBLISHING

Materials Science in Additive Manufacturing

ORIGINAL RESEARCH ARTICLE

Numerical simulation and experimental characterization of a single-seam plasma wire arc additive manufacturing process for Ti-6Al-4V

Martin Bielik [1,2*], Erich Neubauer [2], Michael Kitzmantel [2], Ingo Neubauer [3], and Ernst Kozeschnik [1]

[1]Institute of Materials Science and Technology, Faculty for Mechanical and Industrial Engineering, Vienna University of Technology, Vienna, Austria

[2]RHP-Technology GmbH, RHP Group, Research and Technology Center, Seibersdorf, Lower Austria, Austria

[3]Division of Manufacturing Intelligence, Hexagon GmbH, Hamburg, Germany

Abstract

Arc welding processes are increasingly being used in the additive manufacturing of metal components. Physics-based modeling of welding processes enables the study of welding parameter effects on the final weld shape, residual stress state, and distortion, helping to improve weld quality and reduce costs. However, the quality of the process simulation strongly depends on the mathematical description of the heat source. The parameters of the heat source model have a significant influence on the temperature field and, consequently, on the distortion and residual stress fields. This paper presents a trial-and-error method for determining the parameters for Goldak's double-ellipsoidal heat source model. The transient temperature distribution and the size of the melt pool are determined through experimental studies. Numerical models are then set up in Simufact Welding 8.0 with a set of heat source parameters to reproduce the experimental trials. By comparing numerical finite element results with experimental results, the heat source parameters for a multi-pass additive manufacturing process are successfully calibrated and identified.

Keywords: Wire arc additive manufacturing; Finite element method; Heat source model; Melt pool; Ti6Al4V

***Corresponding author:**
Martin Bielik
(martin.bielik@gmx.at)

Citation: Bielik M, Neubauer E, Kitzmantel M, Neubauer I, Kozeschnik E. Numerical simulation and experimental characterization of a single-seam plasma wire arc additive manufacturing process for Ti-6Al-4V. *Mater Sci Add Manuf.* 2025;4(3):025140021
doi: 10.36922/MSAM025140021

Received: April 3, 2025

Revised: April 30, 2025

Accepted: May 2, 2025

Published online: June 17, 2025

1. Introduction

Additive manufacturing (AM) is one of the most innovative and transformative manufacturing processes. According to the International Organization for Standardization/American Society for Testing and Materials 52900, wire arc additive manufacturing (WAAM) is classified as a directed energy deposition process, in which focused thermal energy is used to fuse materials by melting them as they are deposited.[1] Among various AM technologies, WAAM stands out as a novel approach that enables high deposition rates and facilitates the production of large, near-net-shape components at relatively low process costs. In addition, WAAM offers a high buy-to-fly ratio, making it particularly advantageous for aerospace and other high-performance applications.[2-4]

Various arc processes can be used as the energy source in WAAM, including gas metal arc welding, gas tungsten arc welding, and plasma arc welding.[5] A defining characteristic of these welding processes is the localized heat input from a moving high-energy-density heat source, which leads to the formation of transient temperature fields in the material. The evolution of the temperature fields is influenced by the thermo-physical properties of the material, the path strategy, and welding parameters.[6]

Because WAAM is a multi-layer welding process in which the feedstock material is melted and deposited in layers, the previously deposited near-net-shape structure is repeatedly remelted and reheated with each new layer. The cyclic thermal exposure induces non-uniform thermal expansion in both the deposited material and the surrounding base material, leading to the formation of residual stresses and distortion fields.[7] The deformation and residual stresses of WAAM-produced components, particularly those made from titanium and steel, have been studied extensively.[8-11] Residual stresses influence several critical failure mechanisms, including fracture and fatigue properties, stress corrosion cracking, and distortion.[12]

The complex thermal history of parts produced with WAAM poses significant challenges in predicting residual stresses and distortion fields. As a result, numerical process simulation has emerged as a feasible and cost-effective method for predicting temperature distributions, distortions, and stress fields in the parts during the printing process.[13,14] However, the quality of the process simulation strongly depends on the mathematical description of the heat source. The configuration of the heat source, including parameter adjustments and thermal conductivity settings, plays a critical role in determining the accuracy of simulated results, particularly in predicting distortions and residual stresses.[15]

In this study, a trial-and-error approach is used to calibrate the numerical heat source by iteratively adjusting parameters until the simulated temperature fields match the experimental data.[16] Since these parameters are highly dependent on the welding conditions, their accurate determination requires the solution of an inverse optimization problem through appropriate experiments.[17] The calibration process involves refining multiple parameters to achieve a validated temperature field, ensuring consistency with thermal cycles recorded by thermocouples and the weld pool geometry observed in light-optical micrographs.[18] Several variants of Goldak's double-ellipsoid heat source model[19] are tested and compared within Simufact Welding 8.0, allowing for a systematic validation of the numerical model.

2. Materials and methods

2.1. Heat source model

In the arc welding module of Simufact Welding 8.0, the Goldak double-ellipsoid model is implemented as the default heat source (Figure 1). This moving double-ellipsoid model is widely used to simulate various arc welding techniques, including gas metal arc welding, gas tungsten arc welding, shielded metal arc welding, and submerged arc welding.[20]

The thermal analysis of the WAAM process involves solving a heat transfer problem with a moving heat source. The heat source mathematically describes the heat transfer from the arc to the melt pool, characterizing the energy distribution within the weld pool. The goal of this model is to approximate the isothermal surface of the actual melt pool and the heat flow across that surface with high accuracy. The effects of the melt pool are considered indirectly.

The Goldak model describes a Gaussian distributed heat generation per unit volume defined in a moving reference frame. A local Cartesian coordinate system (x, y, and z) is defined at the weld point with the x-axis aligned with the welding direction and the z-axis perpendicular to the welding torch. The heat source moves at a constant velocity v along the x-axis.

To account for the asymmetric nature of the heat distribution in the melt pool, two power distribution functions q_f and q_r (W/m³) are used for the front and rear semi-ellipsoidal regions, respectively.[19] The power density distribution is defined in Equation I:

$$q(x,y,z,t)=\frac{6\sqrt{3}Q}{\pi\sqrt{\pi}bd}\begin{cases}\dfrac{f_{\mathrm{f}}}{a_{\mathrm{f}}}\cdot\exp\left[-\dfrac{3(x-vt)^2}{a_{\mathrm{f}}^2}-\dfrac{3y^2}{b^2}-\dfrac{3z^2}{d^2}\right] & \text{for } x>vt\\ \dfrac{f_{\mathrm{r}}}{a_{\mathrm{r}}}\cdot\exp\left[-\dfrac{3(x-vt)^2}{a_{\mathrm{r}}^2}-\dfrac{3y^2}{b^2}-\dfrac{3z^2}{d^2}\right] & \text{for } x<vt\end{cases} \quad (I)$$

Where Q is the total power (W), a_f and a_r are the front and rear ellipsoid lengths (m), b is the ellipsoid width (m), d is the ellipsoid depth (m), and f_f and f_r are the fractions of heat distributed in the front and rear ellipsoids, respectively. The front and rear fractions satisfy the condition $f_f + f_r = 2$ to ensure continuity of the volumetric heat source. Goldak *et al.*[19] suggest default values that set the front fraction to $f_r = 0.6$ if experimental data are insufficient. These fractions can be computed automatically when the geometric parameters are known (Equation II).[21,22]

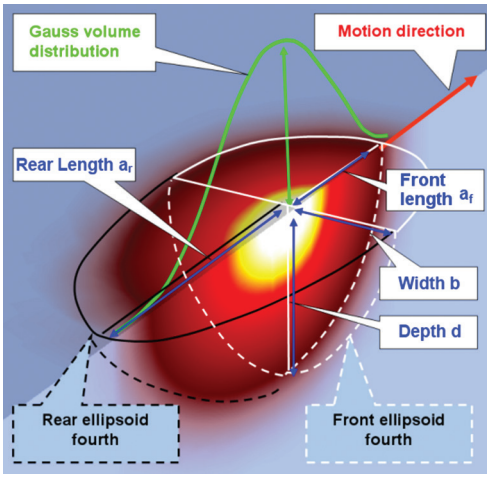

Figure 1. Illustration of Goldak's double-ellipsoid heat source model. Reprinted with permission from Hexagon Manufacturing Intelligence GmbH, Simufact Infosheet Heat Source[20].

$$f_f = 2\frac{a_f}{a_f + a_r}, f_r = 2\frac{a_r}{a_f + a_r} \quad \text{(II)}$$

The heat input during welding plays a critical role in determining the thermal cycles and the properties of the weld. For arc welding, the power input Q (J) by the torch is given in Equation III,

$$Q = \eta\, UI \quad \text{(III)}$$

where I is the current (A), U is the voltage (V), and η is the thermal efficiency (-), linking the gross and net heat inputs.

To calibrate the Goldak double-ellipsoid heat source model, six key parameters must be determined: a_f, a_r, b, d, M, and η. The front length a_f, the rear length a_r, the width b, and the depth d are geometric parameters that define the fusion and heat-affected zone (HAZ). These parameters can be obtained from micrographs of cross-sections of the weld pool shape or *in situ* measurements of the weld pool. The Gaussian parameter M controls the width of the Gaussian bell curve, which affects the energy density over the weld area. The thermal efficiency η defines the fraction of the input energy that is effectively transferred to the workpiece.

Accurate calibration of the double-ellipsoid heat source model is essential for achieving realistic simulation results. The process involves iterative adjustments to fit numerical predictions to experimental data, minimizing discrepancies between simulated and measured temperature fields. However, inherent measurement uncertainties can introduce errors in the calibration process that affect the accuracy of the model.

2.1.1. Governing equations

Finite element (FE) simulations are conducted to compute transient temperature fields, which subsequently serve as input for a thermal elasticplastic mechanical analysis to evaluate deformations and residual stresses of large-scale Ti6Al4V WAAM components. Welding simulations are typically performed as sequential coupled analyses, where the transient temperature field is first computed, followed by structural mechanics calculations. Consequently, the AM process is divided into two primary stages: A heat transfer analysis and a mechanical analysis. These stages are computed separately in a one-way thermo-mechanical coupling approach, meaning that the transient thermal distributions recorded during material deposition are stored at specific time steps and then used as input data for the mechanical analysis.[23] The calibration of the heat source was performed solely based on thermal computations. Therefore, only the governing equations for the thermal model are presented in this study. A complete analysis of the WAAM process requires a fully coupled thermo-mechanical model.

To accurately model the thermal effects of the WAAM process, the total heat input into the component must be determined. The heat flow is derived from the process parameters, considering thermal efficiency and the plasma arc's density distribution function. The thermal behavior is governed by the energy balance equation, which controls temperature evolution and solidification. This equation describes the temporal distribution of heat in a solid medium, incorporating temperature-dependent material properties, and can be expressed as a function of temperature[24] in Equation IV,

$$\frac{\partial T}{\partial t} = \frac{\lambda(T)}{\rho(T)c_p(T)}\vec{\nabla}^2 T + \frac{1}{\rho(T)c_p(T)}\frac{\partial Q_V(x,y,z,t)}{\partial t} \text{ with } T = T(x,y,z,t) \quad \text{(IV)}$$

Where λ is the heat conductivity (W/[m·K]), ρ is the density (kg/m³), c_p is the specific heat capacity (J/[kg·K]), T is the temperature (K), and Q_v is the volumetric heat source (J). The temperature and volumetric heat source are functions of time and spatial coordinates. The general solution of the temperature distribution is obtained by applying the following boundary and initial conditions, which can be written as Equation V.

$$\dot{\vec{q}}_S = -\lambda(T)\frac{\partial T}{\partial \vec{n}}\Big|_S = -\lambda(T)\vec{\nabla}T\Big|_S \quad \text{(V)}$$

$$T(x, y, z, t = 0) = T_0(x, y, z)\big|_{t=0}$$

The heat flux per unit of surface q_s (W/[m²·K]) is computed using Fourier's law. According to Fourier's law, the rate of heat transfer through a material is proportional to the negative temperature gradient and the area through which the heat flows. Heat transfer continues as long as a temperature gradient is present. The proportionality constant λ depends on factors, such as chemical composition, microstructure, and temperature.

Thermal boundary conditions applied on the surface of the computational domain can be described as a Dirichlet (temperature history), Neumann (heat flux history), or Robin boundary condition, which represents a combination of both. In WAAM, the primary heat transfer mechanisms include conduction and surface heat losses, both of which vary depending on the location within the component. In the first layers, the cold baseplate acts as a heat sink, making conduction the dominant heat transfer mechanism. However, as the deposition progresses, the increasing substrate temperature and wall height lead to a greater influence of convective and radiative heat transfer.

Heat radiation is the transfer of internal energy in the form of electromagnetic waves, governed by the Stefan–Boltzmann law, which describes the heat flow rate emitted or absorbed by an object as a function of its temperature. This law applies to all free surfaces, including those of the newly deposited material, and represents the Neumann component of Equation V, as in Equation VI,

$$q_{\mathrm{R}} = \epsilon \sigma \left(T_{\mathrm{S}}^4 - T_{\infty}^4 \right) \tag{VI}$$

where ε is the emissivity (-), σ is the Stefan–Boltzmann constant (W/[m²·K⁴]), T_s is the surface temperature, and T_∞ is the far field temperature. The emissivity can be determined experimentally and numerically as an inverse problem. If the emissivity is known, the temperature of a body can be determined from the heat radiation emitted by the body. However, the emissivity is not only material-dependent but is also influenced by surface conditions of the body, such as oxidation.

Heat convection is a mode of heat transfer driven by the mass motion of a fluid. The movement of a fluid can be forced (forced convection) or free (natural convection). The governing equation of heat convection is Newton's law, expressed as in Equation VII,

$$q_c = h_c \left(T_s - T_\infty \right) \tag{VII}$$

where h_c is the convective heat transfer coefficient in W/(m²·K). The coefficient depends on the type of media (gas or fluid), flow conditions on the surface, surface properties, and temperature, and is typically determined using empirical formulas based on dimensionless parameters.

In addition to radiation and convection, heat transfer between bodies in contact affects thermal behavior. Heat transfer at an interface depends on the temperature of the contacting bodies and the contact heat transfer coefficient a (W/[m²·K]) in Equation VIII.

$$q_a = a \left(T_1 - T_2 \right) \tag{VIII}$$

Due to manufacturing limitations, technically, processed surfaces are not perfectly smooth, and microscopic surface roughness leads to small media-filled gaps at the interface. Consequently, heat transfer across the contact interface occurs through two mechanisms. First, solid-to-solid conduction at points where contact is established, and second, media conduction through the air- or gas-filled gaps. The contact heat transfer coefficient a depends on the materials in contact, the surface conditions of the contacting bodies, contact pressure, and the fluid inside the cavities.

Thermal boundary conditions are modeled by integrating Equations VI to VIII into Equation V, as Equation IX

$$\epsilon \sigma \left(T_{\mathrm{S}}^4 - T_{\infty}^4 \right) + h_{\mathrm{c}} \left(T_{\mathrm{S}} - T_{\infty} \right) + a \left(T_1 - T_2 \right) = -\lambda \vec{\nabla} T \tag{IX}$$

Since the cooling behavior of the model is governed by heat transfer at the boundaries, inaccuracies in defining these mechanisms can significantly impact the simulation results.[25]

2.1.2. Thermal material properties

Structural welding simulations require the specification of temperature-dependent Thermo-physical and thermo-mechanical material parameters. Thermo-physical parameters include thermodynamic quantities, such as thermal conductivity, density, and heat capacity, as well as thermo-metallurgical parameters that characterize solid phase transformations. Thermo-mechanical properties encompass material characteristics, such as thermal expansion, modulus of elasticity, transverse contraction, stress-strain behavior, and transformation plasticity. These parameters are determined experimentally or sourced from literature and material databases, such as JMatPro. Simufact Welding includes an integrated material database that provides relevant parameters for conducting structural welding simulations.

2.2. Experimental setup

Deposition experiments were performed using a custombuilt WAAM system at RHPTechnology GmbH, Austria. The system utilizes plasma metal deposition, a process that uses a plasmatransferred arc energy source in combination with wire feeding to produce three-dimensional parts (Figure 2A). The

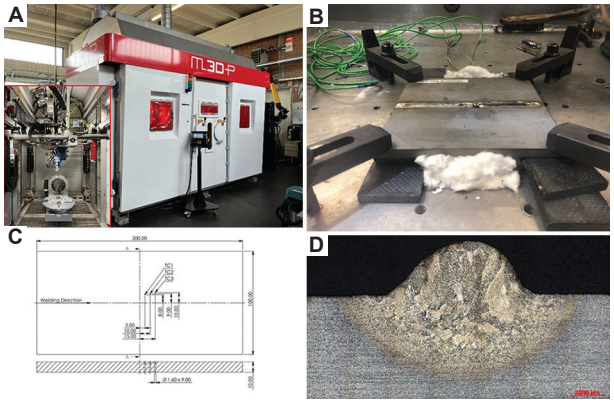

Figure 2. Experimental setup for the heat source calibration. (A) M3DP welding system. (B) Experimental setup for the calibration runs. (C) Thermocouple locations. (D) Micrograph after single bead deposition. Scale bar: 2,000 µm, magnification 5×

deposition process took place within a closed, airtight welding chamber filled with highpurity argon, providing an inert gas atmosphere for adequate shielding. Weldinggrade argon (99.99% purity) was used in both the process and as a shielding gas. Cold Ti6Al4V wire with a diameter of 1.2 mm was continuously fed by an automatic wire feeder. Both base plates and welding wire are commercially available and conform to the American Society for Testing and Materials B265 and American Welding Society A5.16 - 07 standards, respectively.

The experimental setup for the heat source calibration is shown in Figure 2B. To minimize heat loss, the baseplate was supported with carbon fiber composites, and the air gap between the baseplate and the backing plate was filled with alumina wool, which effectively isolated the bottom surface of the baseplate. This design reduced contact heat transfer to the backing plate as well as convective heat loss through the air gap. Weld beads 170 mm in length are deposited to establish a steady thermal process.

To characterize the thermal profiles within the workpiece, thermocouples were positioned at pre-defined measurement locations on the baseplate (Figure 2C), following the methodology described by P. Helbig.[26] These thermocouples recorded peak temperatures and thermal gradients within the workpiece. Insulated type K thermocouples were inserted from the bottom of the baseplate into pre-drilled holes, with direct thermal contact provided by the application of a thermally conductive paste. Temperature was recorded using a PCET 390multi-channel digital thermometer (PCE Instruments GmbH, Germany) with a sampling rate of 1 Hz. In total, three calibration runs were performed: a single pre-heating pass, a single printing pass, and two pre-heating passes with a subsequent printing pass.

To improve adhesion and optimize bead geometry, pre-heating of the baseplate was applied as a process control measure. This strategy effectively reduced thermal stress, minimized cracking, and promoted a more uniform temperature distribution.[27] By increasing the initial temperature of the baseplate, pre-heating prevented the first deposited track from becoming excessively narrow, promoted better metal spreading, and improved metallurgical bonding between the deposited material and the baseplate. Beyond thermal management, pre-heating the baseplate significantly influenced the microstructural evolution of Ti6Al4V in the WAAM process. The first layers experienced relatively high cooling rates due to rapid heat conduction into the cold baseplate, resulting in steeper thermal gradients.[28] Elevated pre-heat temperatures reduced these thermal gradients, slowing cooling rates and consequently modifying the solidification behavior and phase transformation kinetics. According to Tan *et al.*,[29] pre-heating of the baseplate contributed to melt pool stabilization, affected grain growth dynamics, and facilitated microstructural homogenization. These effects are crucial for reducing columnar grain formation, improving part integrity, and enhancing the overall mechanical properties of WAAM-produced components.

The most critical process parameters are the welding current I, the travel speed of the plasma torch, and the wire feed speed, influencing the deposited metal shape.[29] The specific deposition parameters used in the experiments are shown in Table 1.

After the experiments, samples were extracted along the sectional plane A-A (Figure 2C), embedded in bakelite, ground, polished, and etched with Kroll's agent. Metallographic analysis was performed using an optical microscope (Zeiss, Germany) to evaluate the microstructure and measure the dimensions of the weld and HAZ. An example micrograph of single bead deposition is shown in Figure 2D. From these micrographs, the width b, depth d, and cross-sectional area A of the weld bead and HAZ were determined. In this context, the depth d represents the height of the weld seam.

2.3. *FE model*

Wire arc AM can be analyzed at different scales: macro, meso, and micro.[30] At the macro-scale, multi-purpose FE software (Simufact Welding 8.0) was used to simulate the coupled thermo-mechanical behavior of WAAM parts, where a generic heat source model replaces the welding torch and electric arc.

Within Simufact Welding 8.0, the welding process was modeled based on key manufacturing parameters, including the welding process, energy input, welding speed, filler material, metallurgical properties, clamping concept, components of interest, and the FE mesh configuration.

All components were initially designed in SolidWorks 2020 and then meshed in Abaqus CAE 6.14. To optimize computational efficiency, the symmetry properties were exploited by modeling only half of the calibration setup.

To simplify the simulation and facilitate the efficient implementation of thermal interactions, the carbon fiber composites support and the alumina wool insulation were modeled as a single component. This allowed a single effective contact heat transfer coefficient to be applied to the underside of the baseplate. The cross-section profiles of the weld beads were approximated by a second-degree polynomial fitting, expressed as Equation X.

$$f(x) = c_2 x^2 + c_0 \quad \text{(X)}$$

The parabolic representation closely approximates the actual shape of the weld beads, ensuring geometric consistency between the numerical model and the experimental observations. The FE model of the calibration setup is shown in Figure 3.

Figure 3A shows the three-dimensional half-symmetry FE mesh used for the thermal analysis of the calibration experiments. To ensure accurate thermal behavior near the heat source, a refined mesh was applied to the weld bead and surrounding region along the welding line, with element sizes of 1 × 0.5 × 0.5 mm. The mesh became progressively coarser along the *y*-axis, moving away from the weld line (Figure 3B). A total simulation time of 400 s

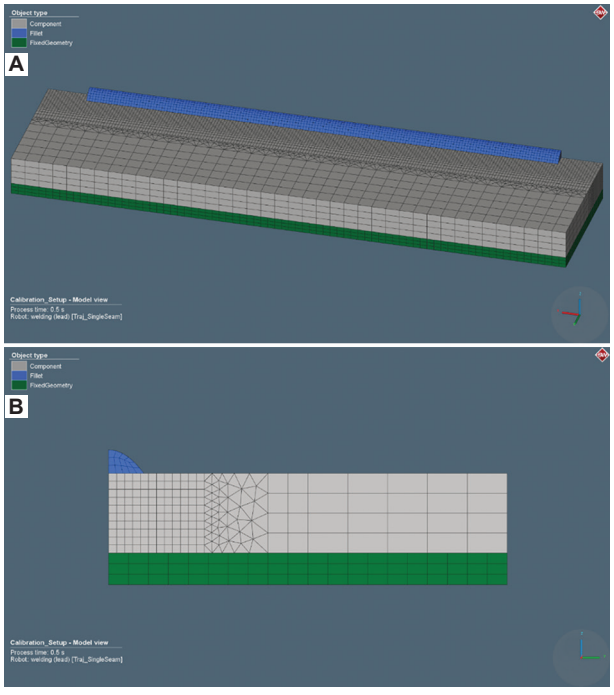

Figure 3. Three-dimensional half-symmetry finite element model. (A) Model view of the calibration setup. (B) Crosssection view of the calibration model.

was set to accurately capture the cooling behavior of the assembly and to precisely define the heat source parameters and cooling parameters.

The moving heat source was calibrated using an iterative trial-and-error approach, where the simulation's fusion zone shape and temperature profiles were matched against experimental results by adjusting the heat source's geometric parameters and thermal boundary conditions.

The melt pool dimensions obtained from the metallurgical analysis were used to define the geometric parameters of the Goldak double-ellipsoid heat source. The width *b* and depth *d* of the fusion zone were measured directly from the micrographs of the weld pool cross-sections. The front and rear ellipsoid lengths, a_f and a_r, were estimated based on the empirical relationships provided by Simufact[20] using Equation XI.

$$a_f = b$$
$$a_r = 2b \quad \text{(XI)}$$

In addition to defining the heat source parameters, thermal boundary conditions were incorporated to simulate the cooling behavior of the component. These included the convective heat transfer coefficient *h*, the contact heat transfer coefficient *a*, and the radiative heat transfer *ε*. The thermal boundary conditions were fine-tuned through an iterative trial-and-error calibration process to ensure that the simulated cooling behavior matched experimental observations.

3. Results

3.1. Weld bead analysis

The shape of the weld bead and its adhesion to the baseplate are critical factors influencing the mechanical performance and structural integrity of welded components. In WAAM, achieving a stable and well-bonded weld bead is essential for ensuring high-quality deposition and minimizing defects. The interaction between the molten metal and the baseplate is governed by the wetting behavior, which is characterized by the wetting angle at the interface of the solid, liquid, and vapor phases. The presence of solid–liquid–vapor interfaces and related interfacial phenomena plays an extremely important role in high-temperature processes, such as welding. A well-attached weld bead exhibits a favorable wetting angle, promoting strong bonding and reducing the risk of defects, such as undercuts, lack of fusion, or delamination from the baseplate.

The deposition of molten metal in WAAM occurs through the formation of liquid metal droplets at the interface between the baseplate and the fed wire. The shape

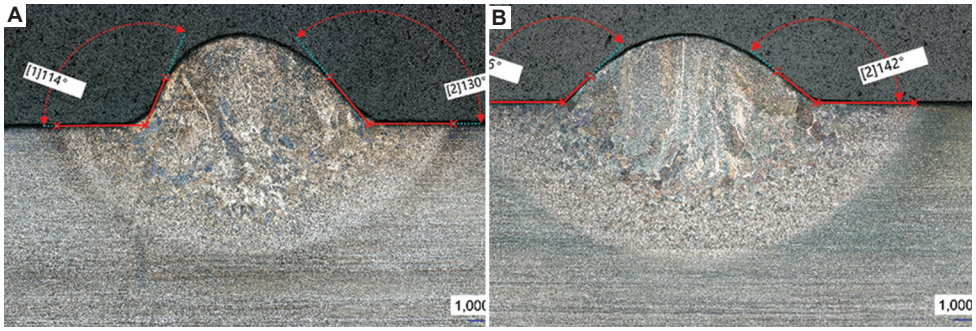

Figure 4. Complementary wetting angles. (A) Single bead. (B) Single bead with two preceding pre-heating passes. Scale bar: 1,000 µm, magnification 5×

and stability of these droplets are governed by process parameters and the interplay between volumetric forces, such as gravity and electromagnetic forces, and interfacial phenomena, such as surface tension and drag forces.[31] These factors, in combination with heat and mass transfer mechanisms, dictate the formation of the weld pool and ultimately influence the overall quality of the welding process. To assess the effects of the wetting behavior of the molten metal on the baseplate, the wetting angles of both the printing pass and the printing pass with pre-heating are analyzed (Figure 4).

The corresponding wetting angles of the left θ_{left} and right θ_{right} side are shown in Table 2.

Asymmetries between the left and right sides of the deposited beads resulted from the transverse feeding direction of the wire. During deposition, the molten droplets are pushed outward on the side opposite to the wire feed direction, leading to steeper wetting angles. Moreover, pre-heating has been observed to reduce wetting angles, thereby enhancing the wettability of the molten material on the baseplate. The formation of various weld-shape defects, such as undercuts (wetting angles exceeding 90°), lack of fusion, and lack of penetration, is closely linked to the wettability of the solid metal by the molten metal.[31] Furthermore, the shape of the deposited bead and the minimum achievable thickness of the deposited material are directly influenced by the wetting angle. Based on these findings, it can be depicted that pre-heating the baseplate, whether by hot plasma gas or heating mats, has a beneficial impact on interlayer bonding, improving the adhesion between the first deposited layer and the baseplate.

3.2. Heat source calibration

The moving heat source is calibrated by fitting the simulated fusion zone and temperature profiles to experimental data through an iterative adjustment of the heat source's geometric parameters and thermal boundary conditions. The calibration process ensures that the prescribed heat input accurately reflects the physical power distribution of the welding arc. Since the heat input directly affects the accuracy of the WAAM process simulations, accurate calibration is essential. The parameters of the Goldak double-ellipsoid heat source for both pre-heating and printing were determined by trial-and-error analysis, as summarized in Table 3.

Cooling behavior and arc efficiency were determined by inverse simulation, ensuring agreement with experimental

Table 1. Deposition parameters

Description	Symbol	Preheating	Deposition	Unit
Wire diameter	d	-	1.2	mm
Welding current	I	130	140	A
Voltage	U	25	25	V
Travel speed	v_{TS}	300	200	mm/min
Feed rate	f	-	0.9	kg/h
Wire feed speed	v_{WFS}	-	2,910	mm/min
Cooling time	t_{cool}	1	30	s
Total dwell time	t_{dwell}	9	38	s
Number of layers	N	2	32	-
Pilot gas		1.5	1.5	l/min
Shielding gas		5	5	l/min

Table 2. Wetting angles

Calibration	θ_{left} (°)	θ_{right} (°)
Single bead	66	50
Single bead plus pre-heating	44	38

Table 3. Goldak double-ellipsoid heat source parameters obtained by trial-and-error

Run	a_f (mm)	a_r (mm)	b (mm)	d (mm)	M (-)	f_f (-)
Preheating	2.85	5.70	2.85	1.4	0	0.66
Deposition	6.72	13.44	6.72	4.41	0	0.66

observations. The final values give an arc efficiency of 0.4, an emissivity of 0.7, a convective heat transfer coefficient of 8 W/(m²·K), and a contact heat transfer coefficient of 10 W/(m²·K). These parameters are assumed to be temperature-independent throughout the simulation.

3.2.1. Double-ellipsoid heat source validation

Accurate modeling of the heat source is critical for realistic simulations of welding processes. The calibration process ensures that the simulated weld pool dimensions match the experimental measurements. During calibration, key parameters such as weld penetration and weld width were systematically fine-tuned to achieve the best agreement with experimental results. A visual comparison of experimental and simulated weld profiles is shown in Figure 5.

The fusion zone boundary in the simulation is defined by the solidification temperature of Ti6Al4V, which is 1,550°C. As shown in Figure 5A, the experimental fusion zone of the single bead is closely reproduced, although the simulated penetration depth is slightly underestimated. However, for the pre-heating pass (Figure 5B), the simulation overestimated the weld pool size compared to the experimental measurements. One possible explanation is the omission of melt pool flow effects in the simulation that affect heat dissipation and melt zone morphology, leading to numerical predictions that are different from those experimentally measured. Visual assessment of the micrograph in Figure 5B reveals that the liquid metal is drawn downward in the peripheral areas while being forced upward toward the center. In contrast, the numerical model for pre-heating does not account for any weld pool geometry; instead, the pre-heating pass is represented as a flat surface, as no wire feedstock is deposited. In addition, arc pressure, which exerts a force on the melt pool, influences the weld pool shape by directing the flow of liquid metal. Thus, melt pool dynamics play a crucial role in the melting process, influencing the weld pool geometry, heat flow, temperature, and temperature gradients.[32] In Figure 5C, the simulation overestimates the penetration depth of the weld pool. This effect is attributed to the larger-than-expected pre-heating fusion zone, which delivers excess energy to the baseplate, causing deeper penetration than experimentally observed.

The ratio of melt width to melt depth $\phi = 2b/d$ is an indicator of the evolution of the weld pool geometry, with higher values corresponding to wider and shallower pools.

Experimental melt pool aspect ratios from Table 4 show that pre-heating results have significantly larger ratios than single beads. Unlike single beads, pre-heating does not involve feedstock material deposition, and melt pool dynamics are primarily governed by forces based on surface tension gradients in the melt. This result in lateral metal transport and the formation of a wide, shallow melt pool (Figure 5B). In contrast, the melt pool ratio of the single bead with preceding pre-heating is slightly lower than that of the single bead alone, indicating greater weld penetration. In this case, the numerical simulation will overestimate the weld penetration, which will affect the calculated aspect ratio. Table 4 confirms that increasing heat input leads to deeper melt zones, which reduces the melt pool aspect ratio.

Overall, the simulated weld pool geometries and corresponding melt pool ratios are in fair agreement with

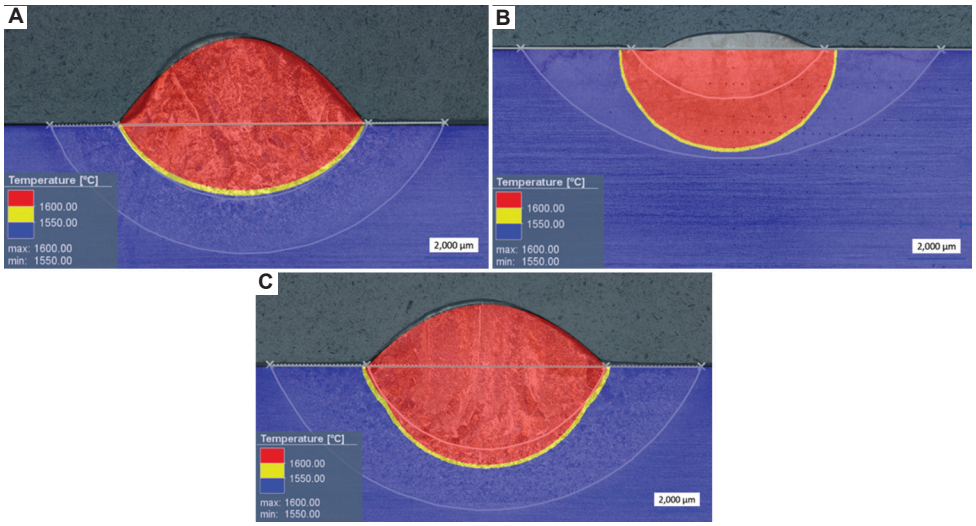

Figure 5. Comparison of calculated and experimental micrographs. (A) Single bead. (B) Pre-heating. (C) Single bead with preceding pre-heating. Scale bar: 2,000 µm

experimental observations. Recent studies, such as Liu *et al.*[33] and Bai *et al.*,[34] have shown that the inclusion of fluid flow dynamics within the melt pool can provide a more comprehensive representation of thermal and fluid behavior.

3.2.2. Thermal profiles

The thermal models are validated by comparing simulated and experimental temperature histories. Figure 6 shows the temperature evolution of single-bead deposition, pre-heating, and single-bead deposition with preceding pre-heating at each thermocouple TC1, TC2, and TC3. Depending on the distance from the heat source, different temperature–time curves are obtained.

For single bead deposition (Figure 6A), the temperature peaks decrease with increasing distance from the weld path, confirming the expected spatial thermal gradients. Once the peak temperature is reached, the heat source moves along its designated path, initiating the cooling phase. Cooling rates are inversely proportional to the distance from the heat source, with temperature profiles flattening as heat dissipation progresses. These observations are consistent with recent experimental and computational studies on WAAM thermal modeling.[16,35]

In particular, the simulated and experimental heating and cooling rates are in good agreement, confirming the accuracy of the FE framework. However, the peak temperatures predicted by the model are slightly higher than the experimental measurements. A possible explanation for this deviation is the measurement lag due to the thermocouple response time (0.9 s) and data acquisition frequency (1 s), which limits the ability of the measurement system to accurately capture rapid thermal transients, especially when the heat source passes through the thermocouple locations. Similar challenges were reported by Aarbogh *et al.*,[16] who observed peak

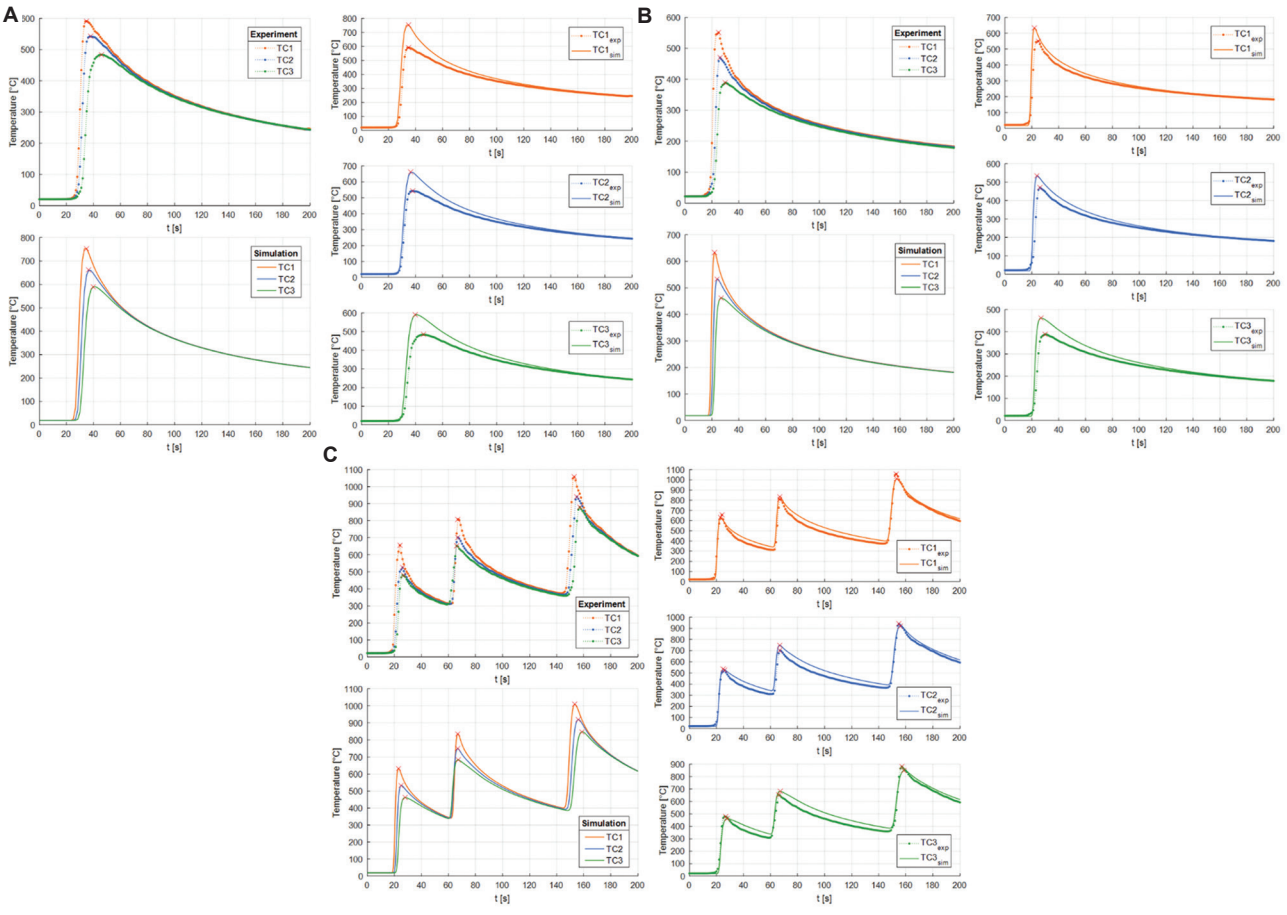

Figure 6. Overview and comparison of experimental (dotted line) and simulated (solid line) temperature profiles at various thermocouple locations obtained during (A) single bead deposition, (B) pre-heating, and (C) single bead deposition plus pre-heating. Thermocouples (TC) were positioned at pre-defined lateral and longitudinal distances relative to the weld track to capture the transient thermal behavior during deposition. Specifically, TC1 was placed at 8 mm, TC2 at 9 mm, and TC3 at 10 mm laterally from the weld centerline. In the welding direction, the thermocouples TC1 to TC3 have an offset of 5 mm.

Table 4. Melt pool ratio

Case	Preheating	Single bead	Single bead+pre-heating
Experiment	4.06	3.31	3.03
Simulation	2.22	3.67	2.45

temperature overestimation in WAAM simulations due to thermocouple placement and data acquisition limitations.

For pre-heating (Figure 6B), lower energy input per unit of length resulted in more moderate temperature peaks. Again, the peak temperatures are overestimated by the simulation, but the cooling behavior of the simulation matches the experimental trends within 100 s of reaching the peak temperatures, confirming the thermal boundary conditions used.

Figure 6C shows the thermal response for single bead deposition with pre-heating, where the simulated and experimental profiles are in good agreement. The pre-heating pass raises the temperature of the weld region to ~400°C, reducing thermal gradients and enabling stable fusion at the weld interface. The highest measured peak temperature at TC1 (~1,000°C) exceeds the β-transus temperature of Ti6Al4V, resulting in microstructural transformation, particularly within the HAZ. In a single weld bead, the final HAZ occurs at the location where the peak temperature rise is approximately equal to the β-transus temperature.[36] This was confirmed by microstructural analysis, where the HAZ half-width of 8.8 mm closely matched the location of TC1 (8 mm from the centerline). The relationship between temperature history and phase transformation is critical in Ti6Al4V processing.[11,37,38]

4. Discussion

4.1. Heat source calibration

In structural welding simulations, an accurate representation of the heat source is paramount. The shape and the heat flux distribution of the heat source must be calibrated against experimental measurements, since the heat source is as a boundary condition rather than a result of the simulation. Accurate heat source definition is essential for reliable simulation results.[18]

Table 5 shows the deviations between measured and simulated fusion zone parameters. The largest deviations occur during pre-heating, with deviations of up to 26% in width and 42% in depth. In contrast, the weld pool shape of the single bead closely matches the experimental measurements. The calculated fusion zone for the single bead with pre-heating matches well in width but deviates by up to 28% in depth. This deviation is primarily attributed to the overestimated depth of the pre-heating pass, which significantly influences the results.

The trial-and-error approach used in this study, which was also used by Aarbogh *et al.*,[16] involves iterative tuning of input parameters to fit experimental data. While common, this method is time-consuming, computationally intensive, and requires considerable expertise. To address these challenges, Gu *et al.*[18] proposed a technique to extract weld pool shape parameters directly from simulations. However, this technique primarily calculates the depth and width, with the length of the front and rear ellipsoids estimated as multiples of the measured width ($a_f = 0.5W_m$ and $a_r = 2W_m$). Aarbogh *et al.*[16] estimated the front and rear ellipsoid lengths with $a_f = W/2$ and $a_r = W$. Unlike width and depth, which can be determined directly from micrographs of the weld cross section, the exact determination of the length of the front and rear ellipsoid is more difficult to determine experimentally and are, thus, often approximated by equations. Chujutalli *et al.*[39] concluded that the parameters of the heat source influence the weld bead size collectively rather than independently.

The numerical model developed in this study for simulating the thermo-mechanical behavior of single-track deposits is distinguished by its use of a fully transient Goldak double-ellipsoid heat source formulation calibrated directly against experimental thermal profiles and melt pool geometries. This contrasts with other modeling strategies presented in the literature that focus on computational efficiency and parametric generalization. Yang *et al.*[40] proposed a semi-analytical model with temporal acceleration to efficiently simulate residual stress and deformation by accelerating heat source movement and adjusting diffusion time, which allowed significant reductions in simulation time while preserving predictive accuracy for large-scale WAAM parts. Strobl *et al.*[41] employed reduced order modeling using proper generalized decomposition to enable fast calibration and parameter estimation through efficient representation of temperature evolution in bead-on-plate welds. This method lays the groundwork for a future digital twin architecture to support real-time process control in WAAM. In contrast, Wang *et al.*[42] developed a purely geometric model for directed energy deposition based on the in-order stacking of primitives. This model approximates the buildup of deposition geometry by stacking idealized bead segments defined by simple mathematical rules. While highly efficient computationally, the model does not simulate heat transfer or mechanical responses, and instead is tailored for rapid predictions of deposition shape and volume, particularly useful for path planning and early-stage process evaluation. Recent studies have highlighted the importance of dynamic

Table 5. Heat source parameters determined by measurement and simulation

Process	Measured values (mm)			Calculated values (mm)			Relative error (%)		
	$2b_{exp}$	d_{exp}	φ_{exp}	$2b_{sim}$	d_{sim}	φ_{sim}	e_r^{2b}	e_r^{d}	e_r^{ϕ}
Preheating	6.34	1.56	4.06	8.00	3.60	2.22	26.18	42.31	-45.32
Single bead	8.88	2.68	3.31	8.80	2.4	3.67	-0.90	-10.45	10.88
Single bead+pre-heating	9.45	3.12	3.03	9.8	4.0	2.45	3.70	28.21	-19.14

Table 6. Computational time comparison between different models

Model	Adaptive mesh refinement	Parallelization	Computational time (h)
Calibration pre-heating	Yes	Yes	~ 1
Calibration single bead	Yes	Yes	~ 4
Calibration single bead+pre-heating	No	Yes	~ 2

calibration techniques for heat source modeling in WAAM. To improve heat source accuracy, in-process measurements, such as high-speed camera monitoring of the weld pool shape, can be incorporated into the calibration procedure.[34] A study by Guo *et al.*[43] introduced a convolutional neural network-based method to identify heat source parameters from the cross-sectional profile of the weld zone, providing a novel approach to heat source calibration. Ilani and Banad[44] presented a data-driven computational approach using Goldak's semi-ellipsoidal heat source model to predict melt pool geometry in metal AM.

This comparative discussion underscores that while reduced-order, semi-analytical, and geometric models provide advantages in computational efficiency or design utility, the present study contributes a robust, experimentally validated framework capable of supporting in-depth analysis of process-induced thermal and structural phenomena in WAAM.

Structural welding simulations are invaluable for predicting and optimizing geometric deviations and accumulated residual stresses before experimentation. Depending on the complexity of the models, simulation times can vary significantly, ranging from a few minutes to several days.[8,45] A comparison of the computational times used for the models is presented in Table 6. Simulations were performed on an eight-core 3.30 GHz i75820K processor with 32 GB of installed random access memory. All models have been computed using parallelization, that is, the computation of a simulation is done in parallel using multiple central processing unit cores.[46]

4.2. Thermal boundary conditions

In this study, the thermal boundary conditions, namely, emissivity ε, convective heat transfer coefficient h_c, and contact heat transfer coefficient a, were assumed to be temperature-independent. This simplification is adopted to reduce both experimental effort and computational complexity. However, it introduces inherent limitations that can affect the accuracy of the thermal model. In practice, these parameters exhibit strong temperature dependence and are affected by the dynamic nature of the heat transfer during the WAAM process. Accurately characterizing their variation over a broad temperature range requires detailed, process-representative measurements, which are often challenging to obtain experimentally. By assuming these parameters as temperature-independent, this simplification can result in localized discrepancies in the predicted temperature fields, particularly in regions with steep thermal gradients or changing surface conditions. Given the wide temperature range inherent in welding and the plasma-based WAAM process, incorporating temperature-dependent boundary conditions becomes essential for enhancing model accuracy. Future work should consider integrating such formulations. As demonstrated by Tröger *et al.*,[47] the inclusion of temperature-dependent boundary conditions significantly improves the reliability of numerical predictions in WAAM simulations.

4.3. Multi-layer welding

While the present study focuses on single-track deposition in plasma-based WAAM, understanding how these conditions evolve in multi-layer builds is essential. In multi-layer WAAM processes, previously deposited layers are subsequently remelted and reheated during the deposition of each new layer, resulting in complex thermal cycles that strongly influence both the material's microstructure and macrostructure. The macrostructure and microstructure are key determinants of the mechanical properties of WAAM-produced components.[48] Understanding these remelting effects is crucial when extrapolating single-bead observations to multi-track, multi-layer components. The evolution of the melt pool geometry, thermal gradients, and cooling rates across successive layers plays a decisive

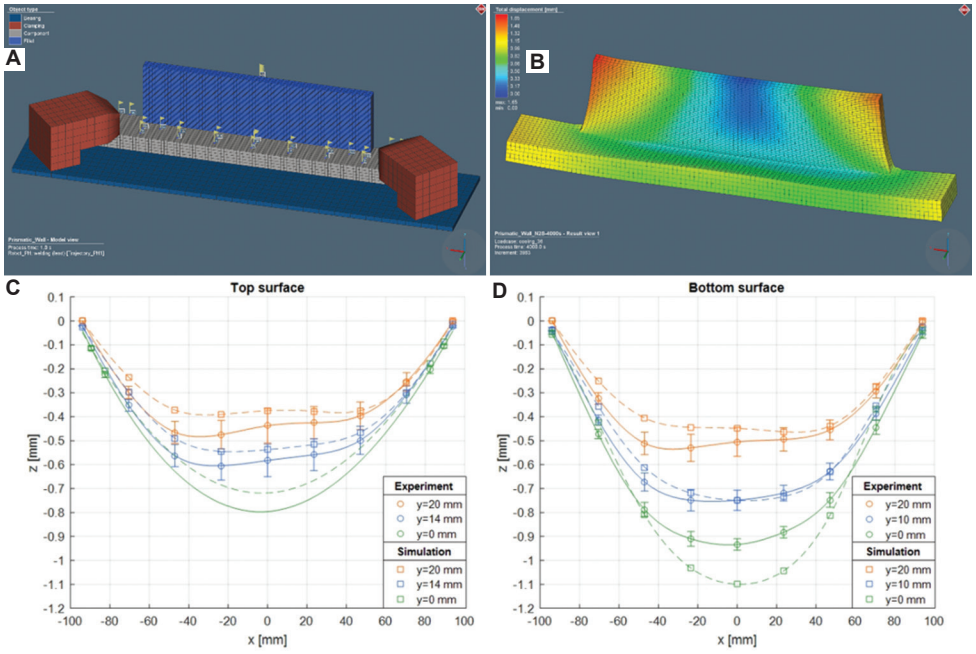

Figure 7. Plasma-based wire arc additive manufacturing simulation and mechanical behavior of a Ti-6Al-4V single-walled structure. (A) Numerical model of the single wall structure. (B) Total displacement of the wall after cooling and unclamping the top surface. (C) Top surface out-of-plane distortion along the longitudinal direction. (D) Bottom surface out-of-plane distortion along the longitudinal direction[49].

role in defining the final part's structural integrity and performance.

To evaluate the applicability of the calibrated single-bead model to more realistic build scenarios, Bielik *et al.*[49] extended the numerical simulation framework to a multi-layer deposition scenario, representative of realistic WAAM components. The thermal model was adapted to simulate the deposition process and to predict the distortion fields for a complete wall structure using Simufact Welding, as shown in Figure 7.[49] The previously derived and calibrated heat source parameters and thermal coefficients remain unchanged, with only the deposition trajectory modified to reflect the multi-pass nature of the wall geometry.

Further studies are needed to assess the correlation between the thermal and geometric evolution of the WAAM parts during multi-layer deposition (aerospace structures,[49] cylindrical, and nonlinear structures[50]). In addition, there is an increasing shift toward material deposition along arbitrary paths, enabling the modeling and fabrication of complex metal structures with greater precision and predictability.

5. Conclusion

This study presents a comprehensive methodology for calibrating the Goldak double-ellipsoid heat source model in plasma-based WAAM of Ti6Al4V single-track welds, integrating FE simulations and experimental validation. A numerical model using Simufact Welding 8.0 was developed to predict the thermal behavior of weld beads, and experimental data were used for model verification and heat source calibration. The results contribute to the optimization of structural welding simulations and the improvement of predictive modeling in AM. The main conclusions of this study are as follows:

(i) The Goldak double-ellipsoid heat source model effectively represents the experimentally determined conditions, demonstrating its suitability for structural welding simulations. However, improved temperature measurement techniques, including shielded thermocouples, advanced mounting methods, higher-frequency data logging, real-time weld pool monitoring, and data-driven algorithms, are required to improve calibration accuracy.

(ii) The simulation results successfully reproduce the temperature distributions, with predictions of the melt zone and HAZ in close agreement with experimental measurements. However, discrepancies arise due to uncertainties in heat source calibration, simplifications in bead geometry modeling, and assumptions in boundary conditions, highlighting the need for further refinement.

(iii) The effectiveness of the trial-and-error method depends on the expertise of the user, which introduces variability in results. This approach to parameter tuning is case-specific and requires recalibration for

different welding conditions, making it inefficient and resource-intensive. Future research should explore data-driven approaches, such as machine learning, regression analysis, or optimization algorithms, to improve calibration efficiency and prediction accuracy.

(iv) Assuming temperature-independent thermal boundary conditions throughout the welding process introduces potential inaccuracies. These parameters are not only temperature-dependent but also influenced by building height and geometry, requiring adaptive calibration approaches to improve model accuracy.

(v) Melt pool dynamics are not explicitly modeled in the present simulation framework, limiting the ability to capture fluid flow effects, temperature gradients, and solidification phenomena. Oversimplified thermal models can misrepresent cooling rates, affecting the microstructure evolution and mechanical properties of the deposited material. Future work should integrate computational fluid dynamics with FE simulations to improve the accuracy of weld pool dynamics, solidification modeling, and heat transfer predictions.

(vi) The results of this study can be extended to multi-pass welding simulations to facilitate the prediction of residual stresses, distortion fields, and thermal cycles in complex AM components. Coupled thermo-mechanical simulations can optimize toolpath strategies and welding parameters, reducing the need for extensive experimental testing. Model enhancements can be tested, and different numerical approaches can be compared to improve computational efficiency and result accuracy.

Acknowledgments

The authors acknowledge TU Wien Bibliothek for financial support through its Open Access Funding Programme.

Funding

Not applicable

Conflict of interest

The authors declare they have no competing interests.

Author contributions

Conceptualization: Martin Bielik, Erich Neubauer, and Ernst Kozeschnik
Investigation: Martin Bielik
Methodology: Martin Bielik
Resources: Erich Neubauer, Michael Kitzmantel, Ingo Neubauer, and Ernst Kozeschnik
Writing – original draft: Martin Bielik
Writing – review and editing: Martin Bielik and Ernst Kozeschnik

Ethics approval and consent to participate

Not applicable.

Consent for publication

Not applicable.

Availability of data

Data will be made available from the corresponding author upon reasonable request.

Further disclosure

The paper is based on the thesis of the first author, Martin Bielik. (https://repositum.tuwien.at/handle/20.500.12708/15047).

References

1. DIN EN ISO/ASTM 52900:2022-03. *Additive Fertigung-Grundlagen-Terminologie Additive Manufacturing-General Principles-Fundamentals and Vocabulary (ISO/ASTM 52900:2021)*; 2022.

   doi: 10.31030/3290011

2. Bielik M. *Thermo-Mechanical Analysis of Plasma-Based Additive Manufacturing of Ti-6Al-4V Components Using Simufact Welding. Master's Thesis*. TU Wien; 2020.

   Available from: https://repositum.tuwien.at/handle/20.500.12708/15047 [Last accessed 2025 Mar 30].

3. Bielik M, Meuthen J, Ariza-Galvan E, *et al. Plasma Metal Deposition in Aerospace Applications Enabling a Cost-Efficient Technology for High Tech Industries. Metal Additive Manufacturing Conference (MAMC), Vienna*; 2020.

4. Wallis C, Neubauer E, Kitzmantel M, *et al.* Investigations of plasma metal deposition (PMD) of 6061 and 7075 aluminum alloys for aerospace and automotive applications. *BHM Berg Hüttenmänn Monats*. 2023;168(5):209-218.

   doi: 10.1007/s00501-023-01345-4

5. Li JZ, Alkahari MR, Rosli NA, Hasan R, Sudin MN, Ramli FR. Review of wire arc additive manufacturing for 3D metal printing. *Int J Autom Technol*. 2019;13(3):346-353.

   doi: 10.20965/ijat.2019.p0346

6. Gierth M, Henckell P, Ali Y, Scholl J, Bergmann JP. Wire arc additive manufacturing (WAAM) of aluminum alloy AlMg5Mn with energy-reduced gas metal arc welding (GMAW). *Materials*. 2020;13(12):2671.

   doi: 10.3390/ma13122671

7. Masubuchi K. Residual stresses and distortion in welds. In: *Encyclopedia of Materials: Science and Technology*. Netherlands: Elsevier; 2005. p. 1-6.

   doi: 10.1016/B0-08-043152-6/01457-1

8. Ding J, Colegrove P, Mehnen J, *et al.* Thermo-mechanical analysis of wire and arc additive layer manufacturing process on large multi-layer parts. *Comput Mater Sci.* 2011;50:3315-3322.

   doi: 10.1016/j.commatsci.2011.06.023

9. Colegrove PA, Coules HE, Fairman J, *et al.* Microstructure and residual stress improvement in wire and arc additively manufactured parts through high-pressure rolling. *J Mater Process Technol*. 2013;213(10):1782-1791.

   doi: 10.1016/j.jmatprotec.2013.04.012

10. Hoye N, Li HJ, Cuiuri D, Paradowska AM. Measurement of residual stresses in titanium aerospace components formed via additive manufacturing. *Mater Sci Forum*. 2014;777:124-129.

    doi: 10.4028/www.scientific.net/MSF.777.124

11. Martina F, Roy MJ, Szost BA, *et al.* Residual stress of as-deposited and rolled wire+arc additive manufacturing Ti-6Al-4V components. *Mater Sci Technol.* 2016;32(14):1439-1448.

    doi: 10.1080/02670836.2016.1142704

12. Coules HE. Contemporary approaches to reducing weld induced residual stress. *Mater Sci Technol*. 2013;29(1):4-18.

    doi: 10.1179/1743284712Y.0000000106

13. Hu X, Chiu LN, Huang A, Liu M, Yan W. Application of melt pool profiles for parameter calibration of Goldak's heat source model. *Addit Manuf*. 2024;92:104379.

    doi: 10.1016/j.addma.2024.104379

14. Bayat M, Dong W, Thorborg J, To AC, Hattel JH. A review of multi-scale and multi-physics simulations of metal additive manufacturing processes with focus on modeling strategies. *Addit Manuf*. 2021;47:102278.

    doi: 10.1016/j.addma.2021.102278

15. Deng D, Murakawa H. Numerical simulation of temperature field and residual stress in multi-pass welds in stainless steel pipe and comparison with experimental measurements. *Comput Mater Sci*. 2006;37(3):269-277.

    doi: 10.1016/j.commatsci.2005.07.007

16. Aarbogh HM, Hamide M, Fjær HG, Mo A, Bellet M. Experimental validation of finite element codes for welding deformations. *J Mater Process Technol.* 2010;210(13):1681-1689.

    doi: 10.1016/j.jmatprotec.2010.05.014

17. Karkhin VA, Pittner A, Schwenk C, Rethmeier M. Simulation of inverse heat conduction problems in fusion welding with extended analytical heat source models. *Front Mater Sci*. 2011;5(2):119-125.

    doi: 10.1007/s11706-011-0137-1

18. Gu Y, Li YD, Yong Y, Xu FL, Su LF. Determination of parameters of double-ellipsoidal heat source model based on optimization method. *Weld World*. 2019;63(2):365-376.

    doi: 10.1007/s40194-018-00678-w

19. Goldak J, Chakravarti A, Bibby M. A new finite element model for welding heat sources. *Metall Trans B*. 1984;15(2):299-305.

    doi: 10.1007/BF02667333

20. *Simufact. Infosheet Heat Source. Simufact Welding Tutorial.* Hamburg, Germany: Simufact Engineering GmbH; 2018.

21. Lundbäck A. *Modelling of Weld Path for Use in Simulations. Master's Thesis*. Sweden: Lulea University of Technology; 2000.

22. Fachinotti VD, Anca AA, Cardona A. Analytical solutions of the thermal field induced by moving double-ellipsoidal and double-elliptical heat sources in a semi-infinite body. *Int J Numer Methods Biomed Eng*. 2011;27(4):595-607.

    doi: 10.1002/cnm.1324

23. Megahed M, Mindt HW, N'Dri N, Duan H, Desmaison O. Metal additive-manufacturing process and residual stress modeling. *Integr Mater Manuf Innov*. 2016;5(1):61-93.

    doi: 10.1186/s40192-016-0047-2

24. Radaj D. *Wärmewirkungen Des Schweißens [Thermal Effects of Welding]*. Berlin, Heidelberg: Springer; 1988.

    doi: 10.1007/978-3-642-52297-0

25. *Simufact. Infosheet Boundary Conditions Thermal.* Simufact Welding Tutorial. Hamburg, Germany: Simufact Engineering GmbH; 2018.

26. Helbig P. *Kalibrierung Von Ersatzwärmequellen Für Die numerische Simulation von Laserschweißprozessen [Calibration of Representative Heat Sources for the Numerical Simulation of Laser Welding Processes]. Master's Thesis.* Kassel: Universität Kassel; 2018.

27. Xiong J, Lei Y, Li R. Finite element analysis and experimental validation of thermal behavior for thin-walled parts in GMAW-based additive manufacturing with various substrate preheating temperatures. *Appl Therm Eng.* 2017;126:43-52.

    doi: 10.1016/j.applthermaleng.2017.07.168

28. Wang J, Lin X, Wang J, *et al.* Grain morphology evolution and texture characterization of wire and arc additive manufactured Ti-6Al-4V. *J Alloys Compd*. 2018;768:97-113.

    doi: 10.1016/j.jallcom.2018.07.235

29. Abe T, Kaneko J, Sasahara H. Thermal sensing and heat input control for thin-walled structure building based on numerical simulation for wire and arc additive manufacturing. *Addit Manuf*. 2020;35:101357.

    doi: 10.1016/j.addma.2020.101357

30. Sampaio RFV, Pragana JPM, Bragança IMF, Silva CMA, Nielsen CV, Martins PAF. Modelling of wire-arc additive manufacturing a review. *Adv Ind Manuf Eng*. 2023;6:100121.

doi: 10.1016/j.aime.2023.100121

31. Deyev G, Deyev D. *Surface Phenomena in Fusion Welding Processes*. 1st ed. United States: CRC Press; 2005.

doi: 10.1201/9781420036299

32. Ou W, Knapp GL, Mukherjee T, Wei Y, DebRoy T. An improved heat transfer and fluid flow model of wire-arc additive manufacturing. *Int J Heat Mass Transf*. 2021;167:120835.

doi: 10.1016/j.ijheatmasstransfer.2020.120835

33. Liu C, Wu Y, Zhou J, Wen Y, Wang L, Xie L. Effect of in situ electromagnetic field manipulation on the microstructure and hardness of titanium alloy during laser melting deposition. *Mater Sci Addit Manuf*. 2025;4(1):8332.

doi: 10.36922/msam.8332

34. Bai X, Colegrove P, Ding J, *et al.* Numerical analysis of heat transfer and fluid flow in multilayer deposition of PAW-based wire and arc additive manufacturing. *Int J Heat Mass Transf*. 2018;124:504-516.

doi: 10.1016/j.ijheatmasstransfer.2018.03.085

35. Belhadj M, Werda S, Belhadj A, Kromer R, Darnis P. *Thermal Analysis of Wire Arc Additive Manufacturing Process*. *ESAFORM 2021*; 2021.

doi: 10.25518/esaform21.4095

36. Liu S, Shin YC. Additive manufacturing of Ti6Al4V alloy: A review. *Mater Des*. 2019;164:107552.

doi: 10.1016/j.matdes.2018.107552

37. Wu B, Pan Z, Ding D, Cuiuri D, Li H. Effects of heat accumulation on microstructure and mechanical properties of Ti6Al4V alloy deposited by wire arc additive manufacturing. *Addit Manuf*. 2018;23:151-160.

doi: 10.1016/j.addma.2018.08.004

38. Hönnige J, Colegrove P, Prangnell P, Ho A, Williams S. The effect of thermal history on microstructural evolution, cold-work refinement and α/β growth in Ti-6Al-4V wire + Arc AM. *Appl Phys [ArXiv Preprint]*; 2018.

doi: 10.48550/ARXIV.1811.02903

39. Chujutalli JH, Lourenço MI, Estefen SF. Experimental-based methodology for the double ellipsoidal heat source parameters in welding simulations. *Mar Syst Ocean Technol*. 2020;15(2):110-123.

doi: 10.1007/s40868-020-00074-4

40. Yang Y, Lin H, Li Q. A computationally efficient thermo-mechanical model with temporal acceleration for prediction of residual stresses and deformations in WAAM. *Virtual Phys Prototyp*. 2024;19(1):e2349683.

doi: 10.1080/17452759.2024.2349683

41. Strobl D, Unger JF, Ghnatios C, *et al.* Efficient bead-on-plate weld model for parameter estimation towards effective wire arc additive manufacturing simulation. *Weld World*. 2024;68(4):969-986.

doi: 10.1007/s40194-024-01700-0

42. Wang X, Meng D, Yi H, Yan Z, Xiao J, Chen S. A novel model for directed energy deposition-arc based on in-order stacking of primitives. *Virtual Phys Prototyp*. 2024;19(1):e2291471.

doi: 10.1080/17452759.2023.2291471

43. Guo Z, Jiang H, He L, Lei Z, Bai R. CNN-empowered identification of heat source parameters from the cross-section profile of laser-welded zone. *Int J Adv Manuf Technol*. 2024;130(11-12):5441-5455.

doi: 10.1007/s00170-024-13054-4

44. Ilani MA, Banad YM. Modeling Melt Pool Geometry in Metal Additive Manufacturing Using Goldak's Semi-Ellipsoidal Heat Source: A Data-Driven Computational Approach. *Numer Anal [ArXiv Preprint]*; 2024.

doi: 10.48550/ARXIV.2404.08834

45. Martukanitz R, Michaleris P, Palmer T, *et al.* Toward an integrated computational system for describing the additive manufacturing process for metallic materials. *Addit Manuf*. 2014;1-4:52-63.

doi: 10.1016/j.addma.2014.09.002

46. *Simufact Infosheet Parallelization*. Simufact Welding Tutorial; 2018.

47. Tröger JA, Hartmann S, Treutler K, Potschka A, Wesling V. Simulation-based process parameter optimization for wire arc additive manufacturing. *Prog Addit Manuf*. 2025;10(1):1-14.

doi: 10.1007/s40964-024-00597-x

48. Wang F, Williams S, Colegrove P, Antonysamy AA. Microstructure and mechanical properties of wire and arc additive manufactured Ti-6Al-4V. *Metall Mater Trans A*. 2013;44(2):968-977.

doi: 10.1007/s11661-012-1444-6

49. Bielik M, Neubauer E, Kitzmantel M, Neubauer I, Kozeschnik E. A simulation approach for series production of plasma-based additive manufacturing of Ti-6Al-4V components. *Math Model Weld Phenomena*. 2022;13:361-393.

doi: 10.3217/978-3-85125-968-1-20

50. Graf M, Hälsig A, Höfer K, Awiszus B, Mayr P. Thermo-mechanical modelling of wire-arc additive manufacturing (WAAM) of semi-finished products. *Metals*. 2018;8(12):1009.

doi: 10.3390/met8121009

ACCSCIENCE PUBLISHING

Materials Science in Additive Manufacturing

ORIGINAL RESEARCH ARTICLE

Artificial intelligence-driven defect detection and localization in metal 3D printing using convolutional neural networks

Xinyi Yin[1]*, Jan Akmal[1,2], and Mika Salmi[1]

[1]Materials to Products Research Group, Department of Energy and Mechanical Engineering, Aalto University, Espoo, Finland

[2]EOS Metal Materials, Electro Optical Systems Finland Oy, Turku, Finland

(This article belongs to the *Special Issue: Smart Additive Manufacturing: Product and Process Qualification through Innovation in Design, Modeling, Monitoring, Machine Learning, Metrology, and Materials Science*)

Abstract

Metal additive manufacturing (AM) has attracted significant interest in high-value industries due to its ability to produce complex parts flexibly, but the reliance on costly manual monitoring remains a major burden for quality control. Artificial intelligence (AI)-driven models for automated defect detection are emerging as promising solutions. This study contributes a new annotated dataset for AI research in AM and evaluates the performance of four widely used convolutional neural network (CNN) models in detecting powder bed morphology defects, based on layer-wise images acquired by the EOSTATE PowderBed system during the metal laser-based powder bed fusion process. The models were trained through transfer learning methods with manually labeled and pre-processed data. Results demonstrated that ResNet50 and EfficientNetV2B0 achieved over 99% accuracy in defect classification, while YOLOv5 outperformed Faster region-based-CNN in defect detection and localization. However, lower average precision values in object detection tasks were attributed to variability in defect scales and annotation quality. This study confirms the potential of AI-based models for defect identification in AM, with YOLOv5 demonstrating clear advantages in managing complex, multi-scale defects. Future improvements will focus on expanding the dataset and refining annotation strategies to further enhance model robustness.

Keywords: Machine learning; Defects detection; Quality control; AI-driven models; Metal additive manufacturing; Image classification; Object detection

***Corresponding author:**
Xinyi Yin
(xinyi.yin@aalto.fi)

Citation: Yin X, Akmal J, Salmi M. Artificial intelligence-driven defect detection and localization in metal 3D printing using convolutional neural networks. *Mater Sci Add Manuf*. 2025;4(3):025150022. doi: 10.36922/MSAM025150022

Received: April 7, 2025

1st revised: May 7, 2025

2nd revised: May 20, 2025

Accepted: May 20, 2025

Published online: June 25, 2025

1. Introduction

Metal additive manufacturing (AM) has attracted significant attention in high-value industries, such as aerospace, automotive, healthcare, and nuclear energy, due to its ability to produce customized, complex parts with excellent mechanical properties while minimizing waste.[1-3] However, a significant challenge in AM is the frequent occurrence of inevitable defects. Even in metal laser-based powder bed fusion (PBF-LB) alone, around 10 typical high-frequency defects may occur, including lack of fusion, keyhole porosity, gas porosity, solidification cracking, solid-state cracking, surface-connected

porosity, and impurity-induced defects, among others.[4-6] In traditional AM processes, product quality is ensured by several hours of manual monitoring of the printing process, leading to low productivity and increased costs.[7,8] Therefore, improving monitoring methods and ensuring product quality to enhance reliability has become a key research focus.[9,10]

In recent years, with the continuous development and maturation of artificial intelligence (AI), machine learning (ML) has been widely discussed and applied in the field of quality control in AM.[1,11-15] Kadam *et al.*[16] employed a series of pre-trained models for feature extraction combined with various ML algorithms to achieve fault detection in the fused deposition modeling (FDM) process, demonstrating the effectiveness of ML algorithms in anomaly detection. In 2024, Herzog *et al.*[1] reviewed the application of various ML methods and *in situ* monitoring technologies in metal AM defect detection. They surveyed 50 independent studies published since 2017, most based on computer vision algorithms to classify defective images. Among image classification-based detection algorithms, over 75% used supervised learning methods that detect anomalous data by labeling the data as "normal" and one or a few "anomalies." These methods reported accurate favorable accuracy rates of approximately 75 – 95%.[1]

Given the effectiveness of AI-based methods, many researchers aim to build AI-based automated quality monitoring systems.[17,18] Khan *et al.*[7] developed a real-time defect detection system based on a convolutional neural network (CNN) model to improve the automation of fused filament fabrication and reduce production losses and labor costs. Although the model achieved an accuracy of 84% in identifying geometric anomalies, it struggled to detect vertical plane defects, and the insufficient dataset led to inconsistencies in the model.[7] Conversely, Cannizzaro *et al.*[19] introduced a real-time defect monitoring and detection system for metal powder bed fusion (PBF) that classifies five different types of powder bed defects and monitors the profile of each printed layer. They also explored using generative adversarial networks to generate synthetic images of powder bed defects to address the scarce labeled data for training and testing ML models.[19] Tamir *et al.*[11] proposed the integration of digital twins and parallel systems into AM for real-time process monitoring to optimize intelligent manufacturing processes through the development of virtual models.

The diversity and size of the dataset directly impact the performance of ML models, and high-quality datasets are crucial for improving prediction and detection accuracy. Nonetheless, researchers often face challenges in finding suitable target datasets.[20,21] Zhang *et al.*[22] emphasized creating a systematic AM database for ML-assisted AM research. Only a few of the six existing AM research databases contain image datasets for quality monitoring, and annotated datasets are almost non-existent.[22] In 2024, Liu *et al.*[23] also identified the scarcity of image-based datasets in the AM field, thereby warranting more open datasets to facilitate quality evaluation and defect detection in AM processes.[23]

Researchers have proposed various methods to address data imbalance and scarcity.[23,24] In the study by Westphal and Seitz,[25] they combined transfer learning with pre-trained VGG16 and Xception models to classify small datasets, with results indicating that VGG16 performed best across multiple performance metrics, validating the effectiveness of CNN-based defect detection for non-destructive quality assurance. Szymanik *et al.*[26] proposed an innovative approach that combines enhanced signal analyses to improve the accuracy and effectiveness of defect detection in materials with low thermal conductivity, enabling precise detection of defects in thermal imaging and automatic identification of their type and size. Ansari *et al.*[27] designed artificial implant defects that simulate various shapes and sizes of pores and combined a CNN model with X-ray tomography data to successfully detect defects as small as 0.2 mm with up to 97% accuracy, demonstrating the potential of CNN models in PBF pore detection. Kozhay *et al.*[28] developed a CNN algorithm for detecting and classifying defects in FDM-printed images, achieving 90% accuracy. However, the system's performance outside specific layouts was limited due to insufficient data, highlighting the importance of defect data diversity for algorithm optimization.[28]

In previous research, CNN models have been widely recognized as the most suitable AI model for defect image classification and detection tasks in the AM field.[12,29] Fu *et al.*[29] systematically summarized ML algorithms for defect detection in PBF-LB processes, noting that supervised learning is the most commonly used ML method. It performs classification and regression by learning the relationship between input and output in labeled datasets, making it widely applied in PBF-LB systems for defect detection and classification. CNNs extract features through convolution layers, reduce dimensions through pooling layers, and output through fully connected layers, showcasing excellent image processing and pattern recognition capabilities. CNNs are the most popular deep learning algorithms for image recognition, image classification, and object detection, making them well-suited for defect detection in Laser-Based AM processes.[29]

As early as 2019, Han *et al.*[30] proposed a deep CNN-based AI technique to effectively monitor surface quality and detect defects by analyzing metal fracture micrographs

and metallographic images in industrial manufacturing. The experimental results demonstrated that a learning rate of 0.01, Adam optimizer, and Inception-ResNet-v2 network achieved the best classification accuracy for image classification tasks in AM.[30] Khan *et al.*[31] used optical tomography data, monitored layer by layer, and combined random forest algorithms to detect porosity and lack of fusion defects. Although an accuracy of 99.98% was achieved, the risk of overfitting existed due to the small training dataset of only 100 images. Their study further proposed that more efficient detection could be achieved with CNNs and larger-scale datasets.[31] Abhilash and Ahmed[32] used the ResNet50 CNN model to classify AM component surface conditions to determine polishing conditions and optimized surface quality while eliminating defects, achieving a prediction accuracy of 96% and significantly reducing manual inspection and material waste. Lee *et al.*[33] proposed a local detection method based on 3D-CNN to perform defect classification and local volume fraction prediction, utilizing data from the melt pool monitoring system and micro-computed tomography. This method could classify porosities caused by the lack of fusion and locked pores in the PBF-LB process.[33] Wen *et al.*[34] combined simple CNN, YOLOv4, and Detectron2 to perform classification, object detection, and segmentation tasks on scanning electron microscopy images of AM parts, achieving excellent accuracy and defect detection capabilities in static and dynamic videos.

These studies demonstrate the significant potential of CNNs for defect detection in AM, warranting further validation of the large-scale image dataset constructed in this work. Previous approaches have primarily focused on binary classification – determining whether defects exist – without providing spatial localization, which increases the burden on manual inspection. The demand for agile, real-time monitoring also exposes the limitations of pixel-level segmentation in practical applications. This study improves detection accuracy based on classification models and further incorporates advanced object detection techniques to enable both identification and localization of defects in metal 3D printing, enhancing model interpretability and applicability. All models are trained and systematically compared on a unified, large-scale dataset to ensure generalizability and provide a comprehensive performance assessment. The workflow includes layer-wise high-resolution image acquisition, data pre-processing and annotation, and model optimization through transfer learning and model evaluation. Results demonstrate that the proposed object detection approach enables accurate and efficient defect localization, significantly reducing manual effort and improving build success rates, thus laying the foundation for smarter real-time monitoring in AM.

2. Methods

2.1. Data collection and model selection

The experiment collected three sets of images from EOSTATE PowderBed (EOS Gmbh, Germany), which consists of a high-resolution (2D bitmap data resolution of 300 – 400 μm) visual wavelength camera on the EOS M290 metal machine. The EOSTATE PowderBed captured layer images of the printing builds, including defects (Table 1). The sets contained 1383, 287, and 1016 images taken layer-by-layer before and after powder bed melting. The feedstock used for test samples was 316L stainless steel. The powder size distribution was Dv(25) = 22 μm, Dv(50) = 37 μm, and Dv(75) = 58 μm, measured using laser diffraction. The recoating speed was set at 80 mm/s.[35]

AM defects differ from typical object detection targets, as they do not have uniform or consistent contours. Instead, they are abstract, mixed, and evolve gradually throughout the printing process. For example, Figure 1 presents grooves formed by debris dragging across the surface, scattered powder, and pits or voids. In the early stages, slight surface irregularities or powder residues caused by recoater vibrations may have low contrast against the background. However, if these defects are not detected and addressed in time, they can escalate into more severe issues. The model is expected to identify these subtle defect patterns early.

In practical industrial settings, the printing of a single AM part can take up to dozens of hours, depending on its size and complexity. On a typical industrial PBF-LB system, such as the EOS M290, printing one layer alone generally takes between 10 and 60 s. Since, it is difficult to predict when and where a defect may occur during the process, operators are often required to monitor the build frequently. This manual monitoring is not only time-consuming

Table 1. Printing parameters

Set	Laser power (W)	Scan speed (mm/s)	Hatch distance (mm)	Layer thickness (μm)	Volumetric energy density (J/mm^3)
1	80 – 250	780 – 3120	0.09	40	8.89, 17.81, 26.71, 35.61
2	215	1083	0.09	40	55.15
3	195	1083	0.09	20	100.03

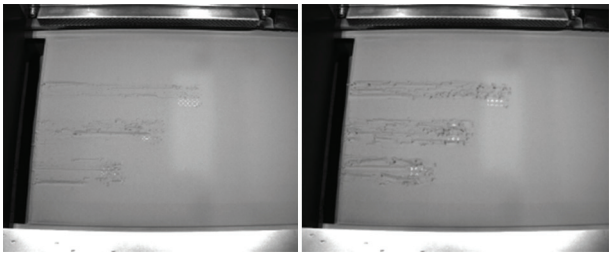

Figure 1. Example of raw powder bed data. Early-stage defects example (left); Late-stage defects example (right)

but also lacks real-time responsiveness. By integrating AI-based models into the process monitoring workflow, it becomes feasible to automatically detect surface defects and pause or stop the build when necessary. Such automated intervention can reduce unnecessary time and material loss, thereby improving overall production efficiency.

To better reflect the practical requirements of quality monitoring in AM, this study defines two task phases, aligned with the hierarchical information needs in industrial production – namely, binary defect detection and spatial localization. In the first phase, the model is designed to rapidly process layer-wise image data from the EOS M290 system and determine whether the current layer contains potential defects, classifying them as "good" or "defects." This phase simulates the industrial demand for fast screening, aiming to identify anomalous layers in real-time and enable timely intervention to minimize material and time waste. ResNet-50 and EfficientNetV2B0 are selected for comparison due to their strong trade-off between accuracy and computational efficiency. ResNet improves model depth and convergence stability through residual connections,[36] while EfficientNet balances model size, computational cost, and accuracy using compound scaling.[37] In the second phase, the model is further required to localize and highlight defect regions with bounding boxes, providing spatial information to support downstream inspection or corrective actions. This phase addresses the industrial need for defect traceability and region-specific analysis while aiming to reduce manual inspection workload. The Faster region-based-CNN (R-CNN) and YOLO Version 5 (YOLOv5; Ultralytics, United Kingdom) models are compared in this phase. Faster R-CNN uses a two-stage approach with a region proposal network, offering higher precision in detecting small or subtle defects, which benefits complex PBF-LB analysis.[38] In contrast, YOLOv5 performs single-stage detection with faster inference and better multi-scale capability, making it more suitable for real-time AM monitoring.[39,40]

All experiments were conducted on a laptop, equipped with Intel Core i7-12700H, 2.30GHz CPU, and 16GB of RAM, and using Python (version 3.10, Python Software Foundation, United Kingdom), PyTorch (version 1.12.1, Meta AI, United States), TensorFlow/Keras (version 2.13.0, Google LLC, United States), OpenCV (version 4.4.0.40, OpenCV.org, United States, Numpy (version 1.24.3, NumPy Developers, United States), and Matplotlib (version 3.7.5, Matplotlib Development Team, United States) for model training and result visualization. All experiments were run in the PyCharm Community Edition (version 2024.1.2, JetBrains s.r.o., Czech Republic) with Anaconda (version 24.3.0, Anaconda, Inc., United States) to ensure dependency isolation and version control.

Table 2. Number of "good" and "defects" powder bed images (*n*=2638)

Classification	Number of PB images, *n*
Good	1108
Defects	1530

2.2. Image classification models

ResNet and EfficientNet offer multiple versions of models, making them well-suited for transfer learning. To balance computational efficiency with performance, this study experimented with and selected ResNet-50 and EfficientNetV2B0 and implemented task-specific adaptations tailored to powder bed image characteristics.

Before training, the image data was pre-processed. First, the three datasets were merged to expand the dataset. The first 8 – 10 images from each print project, which appear overexposed due to high energy and platform reflection, were removed, along with the last few "meaningless" images from the end of the print process. This resulted in a total of 2,638 powder bed images. Data were then manually categorized into "good" and "defects" classes (Table 2). Finally, the dataset was split into training, test, and validation sets at a 70:15:15 ratio.

The default input size for the models was 224 × 224, while the dataset used in this experiment consisted of high-resolution 1280 × 1024 images. Directly inputting the original size would result in insufficient memory, and significantly downsizing the images would risk losing critical features of small defect targets. Therefore, a Python script was used to crop the "defects" images to retain only the defect region and 10% of the surrounding background. To improve the model's generalization, OpenCV was then applied for data augmentation, including normalization, rotation, horizontal flipping, scaling, and shear transformations. Finally, all images were resized to 224 × 224 pixels.

During transfer learning, multiple adjustments were made to optimize training performance. First, ResNet-50

and EfficientNetV2-B0 models pre-trained on ImageNet were imported from the TensorFlow/Keras library. Custom fully connected layers were created for comparison, and after testing Flatten and GlobalAveragePooling2D, the former was selected. Two additional dense layers were added with 256 and 128 neurons, using Rectified Linear Unit (ReLU) as the activation function. Both models included a dropout layer, where ResNet-50 randomly dropped 20% of the neurons to reduce reliance on specific neurons and enhance generalization. Given that EfficientNetV2-B0 converges quickly with a significant accuracy increase in the early epochs, the dropout rate was increased to 0.3 to prevent overfitting. The last 5 – 10 convolutional layers were unfrozen, and the model was recompiled for further training, allowing it to learn the characteristics of the new dataset.

To prevent training stagnation, a learning rate scheduling strategy was applied. The validation loss was monitored, and if no decrease was observed over five epochs, the learning rate was reduced by 20% until 1e-6, with an initial learning rate set to 1e-4. L2 regularization was introduced to improve accuracy and was adjusted from 0.02 to 0.001 to avoid excessive loss. During training, accuracy and loss steadily decreased, indicating good convergence on the training set, but validation loss remained constant, suggesting poor generalization. To address this, the training-to-validation set ratio was adjusted from 70:15:15 to 60:30:10, and the batch size was set to 32.

In addition, an EarlyStopping callback was added to prevent overfitting. EarlyStopping monitors the validation loss, and if it fails to decrease over five epochs, training is stopped, and the model is reverted to the best-performing weights. Epochs were increased to allow the accuracy to stabilize.

Given this study's binary classification problem and class imbalance, the loss function was modified from binary cross-entropy loss to focal loss ($\gamma = 2$; $\alpha = 0.25$) to optimize detection performance. Focal loss is an improved version of cross-entropy loss that introduces a weighting factor α to give weights to the positive and negative classes, focusing on harder-to-classify samples. This method is more effective for handling class imbalance. In this dataset, "good" was treated as the positive class (1) and "defects" as the negative class (0). Although the classes were relatively balanced, due to the nature of defect detection, where missing a defect is undesirable, α was set to 0.25 to encourage the model to focus more on the "defects" class.

These adaptations were designed specifically for the characteristics of AM image data and helped improve model convergence and detection accuracy. The experiment involved training with various parameter combinations, and the final parameter settings are displayed in Table 3.

2.3. Object detection models

In the second phase of the task, manual annotation of the dataset is required to achieve precise localization. In actual powder bed images, 3 – 8 overlapping defects are commonly present, along with interference and noise, making it difficult to distinguish and label specific defect types accurately. Since, in practical scenarios, the goal is only to detect the presence and location of defects to stop printing in time and reduce losses, a simple and general bounding box annotation method is sufficient to meet the requirements. For further research into the causes of defects, pixel-level semantic segmentation methods could be considered. In this study, LabelImg was used to annotate the defect locations in all images as "defects," and the model learns from these annotations to predict potential defect locations in the test images, highlighting them with bounding boxes for inspection.

Before training, approximately 10 – 20% of the images' regions outside the build platform were cropped to maintain a consistent image size, allowing for more detailed information when inputting the images at 600 × 600. The dataset was split using a commonly applied ratio, as displayed in Table 4. In addition to classification loss, Faster R-CNN also uses bounding box regression loss, while the YOLOv5 model incorporates confidence loss.

In this experiment, the YOLOv5 model was selected due to its availability in multiple sizes to meet different task requirements. It is based on PyTorch and features an optimized architecture with reasonable model complexity,

Table 3. Parameter settings of ResNet-50 and EfficientNetV2B0 models

Parameters	Specification	
	ResNet-50	**EfficientNetV2B0**
Batch size	32	32
Learning rate	1e-5	1e-4
Input image size	224×224	224×224
Loss function	Focal loss (γ=2, α=0.25)	Focal loss (γ=2, α=0.25)
Regularization	L2 (0.001)	L2 (0.001)
Layer types	Flatten, Dense (256), Dense (128), Dropout	Flatten, Dense (256), Dense (128), Dropout
Dropout rate	0.2	0.3
Epoch	50	50
Data augmentation settings	• *Normalization:* Rescale=1./255 • *Rotation:* Rotation range=40 • *Horizontal flip:* Horizontal flip=True • *Width shift:* Width shift range=0.2 • *Height shift:* Height shift range=0.2 • *Shear:* Shear range=0.2 • *Zoom:* Zoom range=0.2	

Table 4. Parameter settings for the faster R-CNN model

Parameter	Value	Description
(Training+Validation): Test	9:1	Split of training, validation, and test sets
Training: Validation	9:1	Split of training and validation data
input_shape	(600, 600)	Each input image is resized to 600×600
Backbone	resnet50	Used for feature extraction
anchors_size	(4, 16, 32)	Sets anchor box sizes during training, generating anchor boxes at three different scales to detect objects of varying sizes
Freeze_Epoch	50	End epoch for the frozen stage
Freeze_batch_size	4	Batch size during the frozen stage
Freeze_lr	1e-4	Learning rate during the frozen stage
nFreeze_Epoch	100	End epoch for the unfrozen stage
Unfreeze_batch_size	4	Batch size during the unfrozen stage
Unfreeze_lr	1e-5	Learning rate during the unfrozen stage
Confidence threshold	0.5	Predicted boxes with confidence scores above 0.5 are considered valid detections during object detection
nms_iou threshold	0.3	Intersection Over Union threshold for non-maximum suppression; when the overlap of two predicted boxes exceeds 0.3, the model retains the higher-scoring box and suppresses the other to reduce redundancy
Test anchors_size	(4, 8, 16)	Anchor box sizes used during model evaluation

R-CNN: region-based-Convolutional neural network

faster inference speed, and sound detection performance. YOLOv5 employs mosaic data augmentation, which combines four images into one input image, enhancing the detection of small objects. The model also provides an automated hyperparameter optimization system that searches for the best training configuration for hyperparameters, such as learning rate, weight decay, and mosaic probability.[39]

The model training consists of two stages: Freezing and unfreezing. First, the dataset and pre-trained weights are loaded (to accelerate training and enhance feature extraction capabilities). In the freezing stage, only the detection head parameters are trained, while the backbone network weights remain unchanged to reduce memory usage. In the unfreezing stage, the backbone network parameters are unlocked, allowing the entire model to participate in training and improve performance. During training, loss values are recorded, and model weights are saved after each epoch. A training log is generated to evaluate the model's performance.

The main settings and parameters used for the Faster R-CNN and YOLOv5 models are presented in Tables 4 and 5, respectively.

3. Results

3.1. Loss and accuracy

The loss and accuracy changes for the image classification models, ResNet50 and EfficientNetV2B0, are featured in Figures 2 and 3, respectively. Both training and validation losses for ResNet-50 decrease rapidly in the initial stages and stabilize, with closely aligned trends, indicating good model fitting and effective learning without overfitting. However, its validation accuracy fluctuates, suggesting weaker generalization. In addition, the training accuracy of EfficientNetV2B0 surpasses 90% within the first few batches and remains stable at around 100%, demonstrating superior learning capability and stability compared to ResNet-50. To ensure a fair comparison, both models were trained for 50 epochs, but EfficientNetV2B0 exhibited slight overfitting in the final stages, as indicated by declining training loss, increasing validation loss, and fluctuations in validation accuracy.

The training and validation loss changes during the Faster R-CNN training process are displayed in Figure 4. In the first 50 epochs of the freezing phase, the training and validation losses rapidly decrease in the initial few epochs and then gradually stabilize. The smoothness of the training and validation losses, with a difference of <0.1, indicates that the model did not experience significant overfitting or underfitting. During the following 50 epochs, when the unfreezing phase begins and the model undergoes full parameter updates, fluctuations in the loss are normal. However, after that, the loss decreases but does not fully converge.

One limitation of the Faster R-CNN model is that it selects 256 mini-batches of anchor boxes from the same

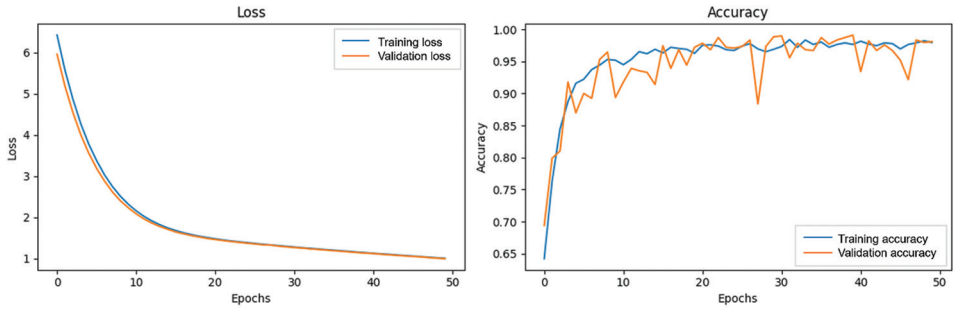

Figure 2. Loss (left) and accuracy plot (right) of the ResNet50 model

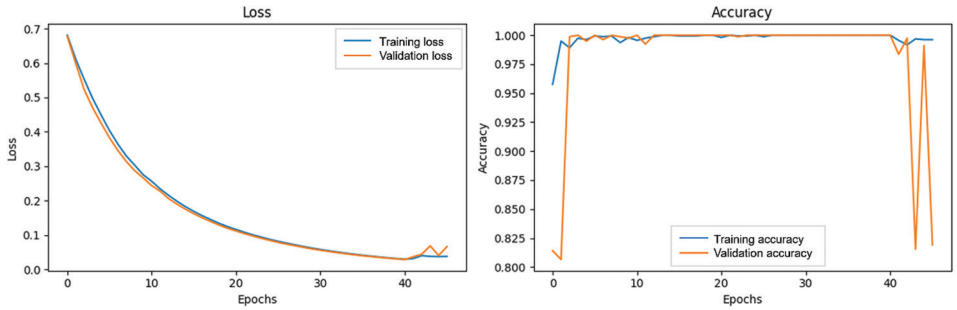

Figure 3. Loss (left) and accuracy plot (right) of the EfficientNetV2B0 model

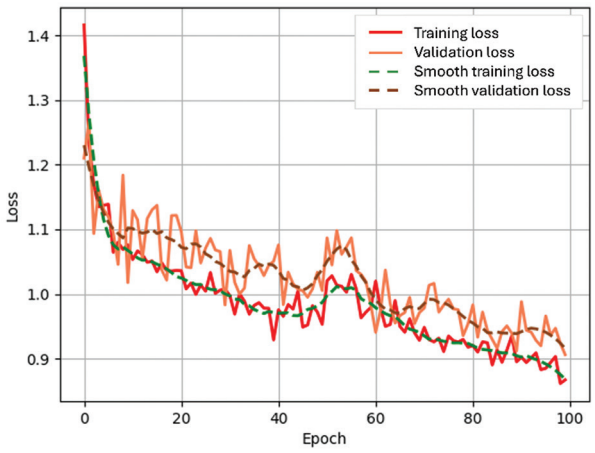

Figure 4. Loss plot of the faster region-based-convolutional neural network model

image for training, and the features of these anchors may be similar, which limits the variety of information the network receives. As a result, the network requires more iteration to learn generalized features, which can lead to longer convergence times.

Figure 5 displays the training and validation losses of the YOLO model over 100 epochs, including box loss, object loss, and classification loss, as well as key metrics, such as precision, recall, and mean average precision (mAP). The bounding box loss (train/box_loss and val/box_loss) and object loss (train/obj_loss and val/obj_loss) both gradually decrease in the training and validation sets, indicating that the model is continuously optimizing and learning. The model demonstrates good adaptability in distinguishing between foreground objects and the background. While the training loss is relatively smooth, the validation loss exhibits some fluctuation, which may be attributed to variations in the validation data. The classification loss remains zero throughout the training process, as the dataset consists of a single-class object detection task. As training progresses, precision and recall steadily increase, with the precision-recall curve stabilizing at a high level of around 0.8. This suggests that most predicted positive samples are correct, with a low false positive rate. The recall increases rapidly in the early stages and stabilizes around 0.6 – 0.7. The loss and evaluation metrics for the validation set fluctuate more significantly, likely due to the dataset's abstract and complex nature of the target features.

3.2. Image classification models comparison

Model validation is a key step in assessing performance, where the trained model is tested on unseen data to evaluate its ability to generalize. This ensures its effectiveness in practical applications. A confusion matrix is commonly used to evaluate model performance in image classification. The diagonal values indicate correct

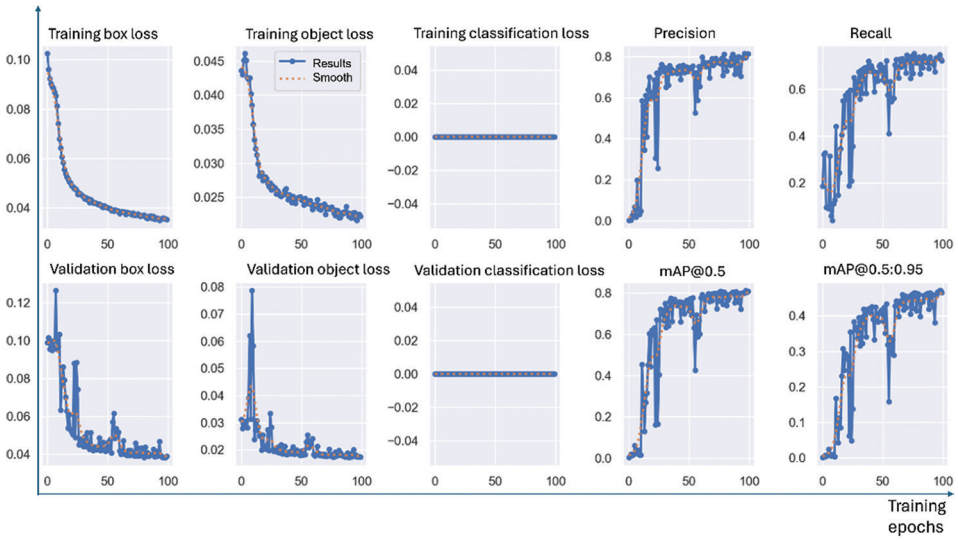

Figure 5. Performance of the YOLOv5 model

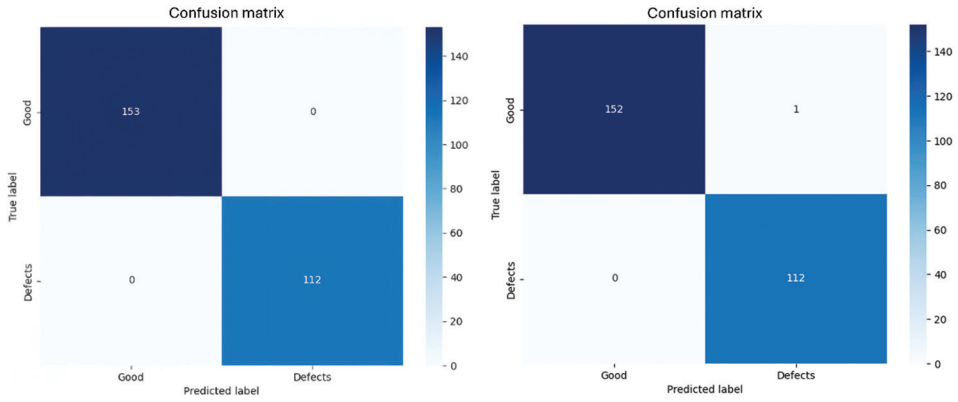

Figure 6. Confusion matrix from the ResNet50 (left) and EfficientNetV2B0 (right) models

predictions, while metrics, including accuracy, precision, and recall, are derived from the matrix to provide a comprehensive assessment (Figure 6).

In the 265 test image samples (Table 6), ResNet50 achieved perfect classification, while EfficientNetV2B0 performed equally well, with only one "good" image misclassified as "defects" and all other samples correctly classified.

After confirming that there was no information leakage, the results (Table 6) demonstrated that the image classification model could always complete the classification task perfectly, with almost no missed or incorrect detections. The choice of different loss functions made little difference since both achieved nearly 100% accuracy. On the test set, both models achieved fast detection, with the EfficientNetV2B0 model demonstrating a faster detection speed. This indicates that these two models found it relatively easy to learn the small- to medium-sized image datasets generated by 3D printers, effectively capturing the key features. This demonstrates good potential for future development and suggests that these models could handle more complex AM image datasets.

For the EfficientNetV2B0 model with deeper networks, the defect classification task appears relatively simple, reaching over 90% accuracy within five iterations and remaining at nearly 100% thereafter. If not overtrained, it outperforms ResNet50 by learning faster and demonstrating excellent stability.

3.3. Object detection models comparison

As displayed in Figure 7, Faster R-CNN achieved an accuracy of 46.25%, which is measured by the area under the precision and recall curves, reflecting the overall detection performance. A higher recall suggests that more

Table 5. Parameter settings for the Yolo-v5 model

Parameter	Value	Description
lr0	0.01	Initial learning rate
lrf	0.01	The learning rate follows a cosine decay schedule, defined as: $lr(x)=\left(1-\cos\left(\frac{x*\pi}{2*step}\right)\right)*(1-lrf)+lrf$ The final learning rate is: $lrfinal=lr0+lrf$
Momentum	0.937	Used in the optimizer to control gradient updates, helping to stabilize convergence
Weight decay	0.0005	Weight decay for regularization helps prevent overfitting by limiting the model's complexity
Warmup epochs	3.0	Several warmup epochs, where the learning rate gradually increases to avoid unstable gradients at the start
Warmup momentum	0.8	During the warmup phase, momentum values gradually increase to the value set by the momentum
Warmup bias lr	0.1	The learning rate for bias terms during the warmup phase
Box	0.05	Weight for the bounding box loss, controlling the contribution of the box regression loss (using CIOU Loss)
cls	0.5	Classification loss weight
cls pw	1.0	Weight coefficient for classification loss
obj	1.0	Weight for object loss uses BCE Loss to measure confidence in object presence
obj pw	1.0	Weight coefficient for object loss
you t	0.25	Intersection Over Union threshold; this defines whether a predicted box matches a ground truth box
anchor t	4.0	Anchor threshold, determining if an anchor box needs adjustment

Abbreviations: BCE: Binary cross-entropy; CIOU: Complete intersection over union.

Table 6. Results of the Resnet50 and EfficientNetV2B0 models

Model	Loss	Accuracy (%)	Precision	Recall	AUC	Time/image (s)
Resnet-50	0.9916	100	1.0000	1.0000	1	0.0272
EfficientNetV2B0	0.0475	99.62	0.9912	1.0000	0.9937	0.0182

Abbreviation: AUC: Area under the ROC curve.

defects are detected but also increases false positives, which lowers precision. The broad coverage of the curve in the figure suggests that the model can maintain a reasonable level of precision at a higher recall, demonstrating better generalization capability in identifying defects.

Figure 8 presents the performance metrics for the YOLOv5 model on the test set. "Images" represents the number of images, while "Instances" denotes the total number of target instances in those images. P (or precision) measures how accurately the model identifies abnormal regions, while R (or recall) indicates the percentage of actual defects detected by the model. The mAP reflects the overall effectiveness of the model. *mAP@0.5* is *mAP at IoU threshold = 0.5*, and *mAP@0.5:0.95* is *mAP averaged over IoU thresholds from 0.5 to 0.95 with a step size of 0.05*. YOLOv5 outperforms Faster R-CNN at mAP50, but its mAP50 – 95 (47.3%) suggests room for improvement in detecting small targets or complex backgrounds.

From Table 7, comparing the two object detection models reveals that YOLOv5 significantly outperforms Faster R-CNN. The YOLOv5 model achieved higher average precision (AP), precision, and recall rates on both datasets. The ground truth objects and detected objects in the Faster R-CNN model display many overlapping detection boxes, which can be adjusted by modifying the threshold. In terms of inference time, YOLOv5 is significantly faster than Faster R-CNN. By directly processing high-resolution images on standard CPU resources, both models achieve detection speeds under 2 s, which is much shorter than the printing time of a single layer on the EOS M290 (typically 10 – 60 s). This ensures that each layer can be monitored in real-time. With more powerful computing hardware, even faster batch processing could be achieved.

As displayed in Figures 9 and 10, although mAP is not exceptionally high, the models can still effectively identify and mark prominent image defects. When the

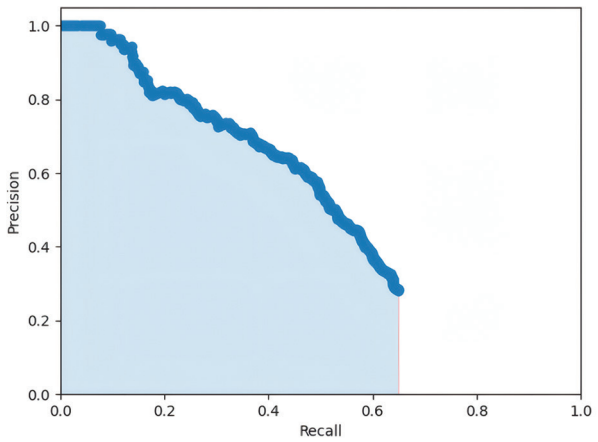

Figure 7. Precision-recall curve of the Faster R-convolutional neural network model. Average precision for the "defects" class is 46.25%

Images	Instances	P	R	mAP50	mAP50-95
153	496	0.797	0.75	0.815	0.473

Figure 8. Metrics of the YOLOv5 model

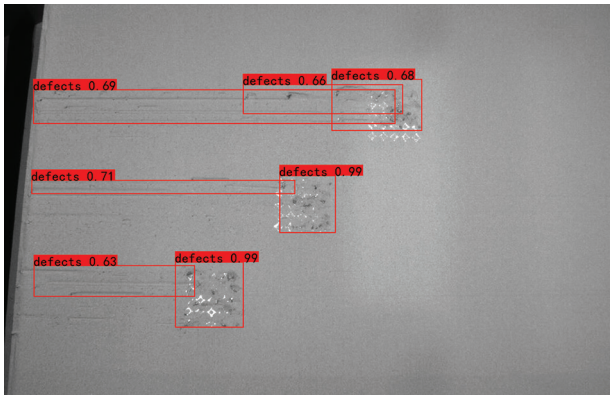

Figure 9. Test result (sample 1) of the object detection model

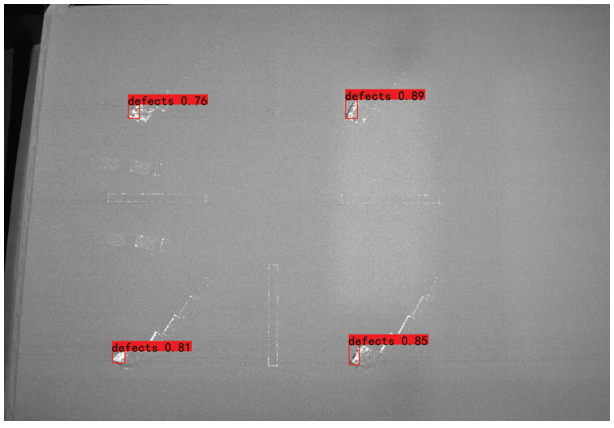

Figure 10. Test result (sample 2) of the object detection model

Table 7. Evaluation results of Faster R-CNN and YOLOv5 models

Parameter	Specification	
	Faster R-CNN	YOLOv5
mAP (%)	46.25	81.5
Test precision (%)	47.68	79.7
Test recall (%)	53.52	75.0
Ground truth objects	482	-
Detected objects	1112	-
Inference time/image (s)	1 – 2	0.5 – 1

Abbreviation: mAP: Mean average precision,
R-CNN: region-based-Convolutional neural network.

defect regions tend to have a relatively uniform shape and size, the model's confidence in predicting defects is high, approaching 1. When the defects to be detected are small, the model struggles to capture the defect's boundaries accurately. Due to the complex and abstract shapes of the defects with varying sizes, the model often produces overlapping detection boxes, which reduces confidence scores. However, the actual detection performance is already satisfactory for supporting manual inspection needs.

4. Discussion

4.1. Analysis of outcome

Based on the experimental results, the ResNet50 and EfficientNetV2B0 models used for image classification performed exceptionally well in distinguishing defective images after transfer learning, with test set accuracy of nearly 100%. However, before training the model, it is crucial to pre-process the raw images by segmenting the defect areas. Without this step, potential subtle defects may be lost during image downscaling, leading to an inability to detect printing issues promptly. Processing high-resolution images requires significant computational power, which can be challenging to access in real-world production settings. Directly feeding raw, unprocessed images into the model may result in suboptimal detection outcomes.

This experiment used three image datasets from defective printing processes. Although the overall data volume is relatively large and the distribution between normal and defective samples is fairly balanced, the nature of AM leads to minimal variation between layer-wise images, and many defects are highly similar and repetitive. This may limit the model's learning capacity. To improve generalization on new data, we applied various data augmentation techniques to increase diversity, aiming

for the model to perform well not only on specific print samples but also on new types of defects caused by different materials in future applications. In future work, we hope to expand the dataset with more experimental data or conduct more detailed classification and detection studies based on different materials and printing builds.

In the object detection phase, the YOLOv5 model achieved an AP of 81.5%, significantly higher than the AP of the Faster R-CNN model (i.e., 46.25%). This suggests that YOLOv5 may be better suited for PBF-LB defect detection tasks, offering stronger adaptability to complex, multi-scale defects with a faster inference speed of under 1 s. Nevertheless, the Faster R-CNN model also demonstrated satisfactory detection results, effectively identifying potential defects and their locations within 2 s, which ensures timely detection of layer-wise changes and confirms its feasibility for real-time monitoring and assisting manual inspection.

The generally lower precision of object detection models compared to image classification models can be attributed to several limitations, including complex defect types, variable object scales, low-contrast backgrounds, and suboptimal annotation quality. These factors often result in false positives or missed detections, reducing precision, recall, and AP. Nevertheless, this approach paves the way for real-time compensation of bounding box-based defective regions. Once the defective regions are detected, it is possible to repair them by recoating the powder bed and/or exposing the defective region to a laser with standard or customized volumetric energy density. More precise mask annotations can be used to further improve model performance. Pixel-level labeling is particularly effective for detecting complex shapes that require accurate localization, as it helps reduce boundary errors and enhances detection accuracy.

4.2. Comparison to previous studies

Most previous studies have adopted image classification methods, and this study followed a similar approach to evaluate model performance (Table 8). The reported accuracies in the literature vary widely (70 – 100%),

Table 8. Previous studies on image classification models

Author, year	Research object	Model (s) used	Accuracy (%)	References
Yin *et al*., 2025	Defect detection in PBF-LB	Resnet50 and EfficientNetV2B0	Resnet 50: 100 EfficientNetV2B0: 99.62	This work
Han *et al*., 2019	Microscopic metal images for AM defect detection	Inception-ResNet-v2	87.5	30
Khan *et al*., 2021	FFF 3D printing defect detection	CNN	84	7
Kadam *et al*., 2021	FDM defect detection	AlexNet+SVM	99.7	16
Westphal and Seitz, 2021	PBF defects in the selective laser sintering process	VGG16 and Xception CNN	VGG16: 95.8 Xception CNN: Not specified	25
Ansari *et al*., 2022	Porosity detection in PBF-LB	Custom CNN	CAD labels: 90 XCT labels: 97	27
Fu *et al*., 2022	Overview of ML-based defect detection in PBF-LB	CNN, SVM, and other ML models	~75 – 95 across studies	29
Abhilash and Ahmed, 2023	Surface quality improvement in metal AM	ResNet-50 CNN	96	32
Akmal *et al*., 2023	Defect detection in PBF-LB	CNN, ANN, MLR	CNN: 100 ANN and MLR: ~99	41
Khan *et al*., 2023	Anomaly detection in PBF-LB using OT imaging	Random forest	99.98	31
Lee *et al*., 2023	Defect detection in PBF-LB	3D-CNN	Recall: 70.47	33
Schmitt *et al*., 2023	Powder bed monitoring in metal AM	Xception-style neural network	~99.15 for large patches	42
Kozhay *et al*., 2024	Defect detection in FDM	Custom CNN with ResNet backbone	97	28
Kuriachen *et al*., 2025	Defect detection in FDM	Custom lightweight CNN	97.77	43

Abbreviations: AM: Additive manufacturing; ANN: Artificial neural network; CAD: Computer-aided design; CNN: Convolutional neural network; FDM: Fused deposition modeling; FFF: Fused filament fabrication; ML: Machine learning; MLR: Multinomial logistic regression; OT: Optical tomography; PBF-LB: Laser-based powder bed fusion; SVM: Support vector machine; XCT: X-ray computed tomography.

Table 9. Previous studies on object detection models

Reference	Research object	Model (s) used	Average precision (%)	References
Yin *et al*., 2025	Defect localization in PBF-LB	Faster R-CNN and YOLOv5	Faster R-CNN: 46.25 YOLOv5: 81.5	This work
Paraskevoudis *et al*., 2020	Detection of stringing defects in FFF 3D printing	SSD with VGG16	44	46
Scime *et al*., 2020	Powder bed anomaly detection	Dynamic Segmentation CNN	Pixel-wise accuracy: >90	49
Cannizzaro *et al*., 2021	PBF defect detection	Computer Vision+U-Net	≥75	19
Wen *et al*., 2021	Detection of cracks and pores in PBF-LB	YOLOv4 (detection) and Detectron2 (segmentation)	~50	34
Wang *et al*., 2024	Small defect detection in metallic AM based on CT images	DC-RCNN	73.3	47
Dong *et al*., 2025	Internal defect detection in AM 6061 aluminum alloy using laser ultrasound	YOLOv5	93.1%	48

Abbreviations: AM: Additive manufacturing; CNN: Convolutional neural network; CT: Computed tomography; DC-R-CNN: Depth-connected region-based convolutional neural network; FFF: Fused filament fabrication; PBF-LB: Laser-based powder bed fusion; SSD: Single shot detector.

depending on factors such as dataset size, defect types, and image quality. Although direct comparisons are not conclusive due to these differences, the cited results provide a general context for interpreting our findings.

Previous studies employed traditional ML algorithms, such as Support Vector Machine (SVM) and random forest,[16,29,31] or simpler deep learning models, such as basic CNNs for image classification tasks.[7,25] In contrast, this study adopts more sophisticated architectures, ResNet50 and EfficientNetV2B0. This study achieved near-perfect accuracy by integrating transfer learning methods to enhance model performance, outperforming many earlier studies. In addition, it was observed that EfficientNetV2B0 not only maintained a very high accuracy rate but also converged faster and demonstrated better stability.

Unlike most existing works that focus solely on image classification, this study systematically evaluated both classification and object detection models using a unified, real-world AM dataset and a consistent training pipeline for the 1st time.[44,45] By integrating recent architectures such as EfficientNetV2B0 and YOLOv5, which offer both accuracy and computational efficiency, the proposed dual-task framework addresses the practical demands of AM process monitoring and provides a valuable reference for future model selection and deployment in industrial defect detection.

Compared to image classification tasks, the application of object detection models for defect localization in AM remains highly underexplored, as illustrated in Table 9. Existing studies demonstrate that models trained with conventional annotations typically achieve AP values in the range of 40 – 50%.[34,46] A recent study by Wang *et al*.[47] proposed a depth-connected region-based (DC-RCNN) model for small defect detection on computed tomography images, but its performance was limited by a small dataset of only C-shaped components (AP up to 73.3%). Dong *et al*.[48] further validated the high accuracy of YOLOv5 (93.1%) on laser ultrasonic data, though the dataset was purely simulated through COMSOL and limited comparisons beyond the YOLO family. In contrast, this study used a larger and more diverse real-world powder bed dataset, demonstrating that optimized YOLOv5 achieves higher AP across multiple defect types. This highlights the broader potential of object detection models for industrial AM applications.

Notably, some studies employed pixel-level annotations and semantic segmentation models, achieving higher AP values (≥75% and ≥90%, respectively).[19,49] These findings suggest that pixel-level annotations can be considered to enhance label quality and improve object detection models' accuracy.[50] Pixel-level annotation in AM requires domain-specific expertise and is prohibitively time-consuming for thousands of images. Consequently, most existing segmentation studies are conducted on relatively small datasets and result in highly task-specific models with limited generalizability. Moreover, segmentation models are computationally intensive, requiring greater computing resources and longer training times, which limits their real-time applicability in edge or online inspection scenarios. Nonetheless, segmentation remains important for deeper analysis of defect formation. Future work will explore advanced segmentation techniques to support root cause investigation and closed-loop quality control in AM.

5. Conclusion

This study comparatively evaluated two image classification models and two object detection models for defect identification and localization on a PBF-LB image dataset. The key findings are summarized below:

- ResNet50 and EfficientNetV2B0 achieved over 99% accuracy in classifying recoating defects with minimal

false predictions. Transfer learning proved effective in accelerating convergence and boosting performance under limited data diversity and computational resources, and appropriate image pre-processing improved the detection of small-scale defects.

- Given the limited exploration of object detection models in AM, this study investigates their potential and demonstrates that both Faster R-CNN and YOLOv5 can effectively localize defect regions to support human inspection. YOLOv5 displays greater robustness to scale variation and complex shapes, significantly outperforming Faster R-CNN.
- To address data imbalance and the scarcity of high-quality AM datasets, this study contributes an annotated image dataset. The high similarity among layer-wise images often limits model generalization across defect types. Public release of the dataset aims to increase data diversity, improve adaptability to novel defects, and support the development of intelligent AM quality monitoring.
- The limited precision of present object detection models is mainly due to the abstract nature of defects, scale variation, low contrast with backgrounds, noise interference, and overlapping bounding boxes. Future improvements may include dataset expansion, refined annotations (e.g., mask labeling), and adoption of advanced detection frameworks to enhance accuracy and generalizability for industrial applications.

Overall, this work provides a comprehensive, task-aligned evaluation of CNN models for AM defect monitoring, supported by a realistic dataset and performance benchmarks. The findings serve as a valuable reference for future research on model selection, deployment strategies, and data standardization in AM quality control.

Acknowledgments

The authors would like to thank Björkstrand Roy, the laboratory manager of ADDLAB at Aalto University, for providing the raw data used in this study.

Funding

This research was financially supported by the Finnish Doctoral Program Network in Artificial Intelligence (AI-DOC, decision number VN/3137/2024-OKM-6) and the Tandem Industry Academia funding from the Finnish Research Impact Foundation.

Conflict of interest

Mika Salmi serves as the Editorial Board Member of the journal but was not in any way involved in the editorial and peer-review process conducted for this paper, directly or indirectly. Other authors declare they have no competing interests.

Author contributions

Conceptualization: Mika Salmi and Xinyi Yin
Data curation: Xinyi Yin
Formal analysis: Xinyi Yin
Methodology: Xinyi Yin and Jan Akmal
Software: Xinyi Yin
Supervision: Mika Salmi and Jan Akmal
Visualization: Xinyi Yin
Writing – original draft: Xinyi Yin
Writing – review and editing: Mika Salmi and Jan Akmal

Ethics approval and consent to participate

Not applicable.

Consent for publication

Not applicable.

Availability of data

The dataset used in this study has been deposited in Zenodo and is publicly available at: https://doi.org/10.5281/zenodo.14996806.

References

1. Herzog T, Brandt M, Trinchi A, Sola A, Molotnikov A. Process monitoring and machine learning for defect detection in laser-based metal additive manufacturing. *J Intell Manuf*. 2024;35(4):1407-1437.

   doi: 10.1007/s10845-023-02119-y

2. Kim H, Lin Y, Tseng TLB. A review on quality control in additive manufacturing. *Rapid Prototyp J*. 2018;24(3):645-669.

   doi: 10.1108/RPJ-03-2017-0048

3. Vasques CMA, Cavadas AMS, Abrantes JCC. Technology overview and investigation of the quality of a 3D-printed maraging steel demonstration part. *MSAM*. 2025;4(2):025040002.

   doi: 10.36922/msam025040002

4. DebRoy T, Wei HL, Zuback JS, *et al*. Additive manufacturing of metallic components-process, structure and properties. *Prog Mater Sci*. 2018;92:112-224.

   doi: 10.1016/j.pmatsci.2017.10.001

5. Tan C, Li R, Su J, *et al*. Review on field assisted metal additive manufacturing. *Int J Mach Tools and Manuf*. 2023;189:104032.

   doi: 10.1016/j.ijmachtools.2023.104032

6. Brennan MC, Keist JS, Palmer TA. Defects in metal additive manufacturing processes. *J Mater Eng Perform*. 2021;30(7):4808-4818.

doi: 10.1007/s11665-021-05919-6

7. Khan MF, Alam A, Siddiqui MA, *et al*. Real-time defect detection in 3D printing using machine learning. *Mater Today Proc*. 2021;42:521-528.

   doi: 10.1016/j.matpr.2020.10.482

8. Gunasegaram DR, Barnard AS, Matthews MJ, *et al*. Machine learning-assisted *in-situ* adaptive strategies for the control of defects and anomalies in metal additive manufacturing. *Addit Manuf*. 2024;81:104013.

   doi: 10.1016/j.addma.2024.104013

9. Cataldo SD, Vinco S, Urgese G, *et al*. Optimizing quality inspection and control in powder bed metal additive manufacturing: Challenges and research directions. *Proc IEEE*. 2021;109(4):326-346.

   doi: 10.1109/JPROC.2021.3054628

10. Xiao Y, Wang X, Yang W, *et al*. Data-driven prediction of future melt pool from built parts during metal additive manufacturing. *Addit Manuf*. 2024;93:104438.

    doi: 10.1016/j.addma.2024.104438

11. Tamir TS, Xiong G, Shen Z, *et al*. 3D printing in materials manufacturing industry: A realm of Industry 4.0. *Heliyon*. 2023;9(9):e19689.

    doi: 10.1016/j.heliyon.2023.e19689

12. Goh GD, Sing SL, Yeong WY. A review on machine learning in 3D printing: Applications, potential, and challenges. *Artif Intell Rev*. 2021;54(1):63-94.

    doi: 10.1007/s10462-020-09876-9

13. Liu Q, Chen W, Yakubov V, Kruzic JJ, Wang CH, Li X. Interpretable machine learning approach for exploring process-structure-property relationships in metal additive manufacturing. *Addit Manuf*. 2024;85:104187.

    doi: 10.1016/j.addma.2024.104187

14. Ng WL, Goh GL, Goh GD, Ten JSJ, Yeong WY. Progress and opportunities for machine learning in materials and processes of additive manufacturing. *Adv Mater*. 2024;36(34):2310006.

    doi: 10.1002/adma.202310006

15. Ukwaththa J, Herath S, Meddage DPP. A review of machine learning (ML) and explainable artificial intelligence (XAI) methods in additive manufacturing (3D printing). *Mater Today Commun*. 2024;41:110294.

    doi: 10.1016/j.mtcomm.2024.110294

16. Kadam V, Kumar S, Bongale A, Wazarkar S, Kamat P, Patil S. Enhancing surface fault detection using machine learning for 3D printed products. *Appl Syst Innov*. 2021;4(2):34.

    doi: 10.3390/asi4020034

17. Chua ZY, Ahn IH, Moon SK. Process monitoring and inspection systems in metal additive manufacturing: Status and applications. *Int J Precis Eng Manuf Green Technol*. 2017;4(2):235-245.

    doi: 10.1007/s40684-017-0029-7

18. Chang LK, Chen RS, Tsai MC, *et al*. Machine learning applied to property prediction of metal additive manufacturing products with textural features extraction. *Int J Adv Manuf Technol*. 2024;132(1):83-98.

    doi: 10.1007/s00170-024-13165-y

19. Cannizzaro D, Varrella AG, Paradiso S, *et al*. *Image Analytics and Machine Learning for In-Situ Defects Detection in Additive Manufacturing*. United States: IEEE; 2021. p. 603-608.

20. Akbari P, Zamani M, Mostafaei A. Machine learning prediction of mechanical properties in metal additive manufacturing. *Addit Manuf*. 2024;91:104320.

    doi: 10.1016/j.addma.2024.104320

21. Tang Y, Rahmani Dehaghani M, Sajadi P, Wang GG. Selecting subsets of source data for transfer learning with applications in metal additive manufacturing. *J Intell Manuf*. 2024;36:3185-3206.

    doi: 10.1007/s10845-024-02402-6

22. Zhang Y, Safdar M, Xie J, Li J, Sage M, Zhao YF. A systematic review on data of additive manufacturing for machine learning applications: The data quality, type, preprocessing, and management. *J Intell Manuf*. 2023;34(8):3305-3340.

    doi: 10.1007/s10845-022-02017-9

23. Liu X, Mileo A, Smeaton AF. *A Systematic Review of Available Datasets in Additive Manufacturing*. [arXiv Preprint]; 2024.

24. Djenouri Y, Srivastava G, Lin JCW. Applied AI in defect detection for additive manufacturing: Current literature, metrics, datasets, and open challenges. *IEEE Instrum Meas Mag*. 2024;27(4):46-53.

    doi: 10.1109/MIM.2024.10540405

25. Westphal E, Seitz H. A machine learning method for defect detection and visualization in selective laser sintering based on convolutional neural networks. *Addit Manuf*. 2021;41:101965.

    doi: 10.1016/j.addma.2021.101965

26. Szymanik B, Psuj G, Hashemi M, Lopato P. Detection and identification of defects in 3D-printed dielectric structures via thermographic inspection and deep neural networks. *Materials*. 2021;14:4168.

    doi: 10.3390/ma14154168

27. Ansari MA, Crampton A, Garrard R, Cai B, Attallah M. A convolutional neural network (CNN) classification to identify the presence of pores in powder bed fusion images. *Int J Adv Manuf Technol*. 2022;120(7):5133-5150.

    doi: 10.1007/s00170-022-08995-7

28. Kozhay K, Turarbek S, Asselbekova T, Ali MH, Shehab E. Convolutional neural network-based defect

detection technique in FDM technology. *Procedia Comput Sci*. 2024;231:119-128.

doi: 10.1016/j.procs.2023.12.183

29. Fu Y, Downey ARJ, Yuan L, Zhang T, Pratt A, Balogun Y. Machine learning algorithms for defect detection in metal laser-based additive manufacturing: A review. *J Manuf Process*. 2022;75:693-710.

doi: 10.1016/j.jmapro.2021.12.061

30. Han F, Zou J, Ai Y, Xu C, Liu S, Liu S. *Image Classification and Analysis During the Additive Manufacturing Process Based on Deep Convolutional Neural Networks*. United States: IEEE; 2019. p. 1-4.

31. Khan IA, Birkhofer H, Kunz D, Lukas D, Ploshikhin V. A random forest classifier for anomaly detection in laser-powder bed fusion using optical monitoring. *Materials (Basel)*. 2023;16(19):6470.

doi: 10.3390/ma16196470

32. Abhilash PM, Ahmed A. Convolutional neural network-based classification for improving the surface quality of metal additive manufactured components. *Int J Adv Manuf Technol*. 2023;126(9):3873-3885.

doi: 10.1007/s00170-023-11388-z

33. Lee KH, Lee HW, Yun GJ. A defect detection framework using three-dimensional convolutional neural network (3D-CNN) with *in-situ* monitoring data in laser powder bed fusion process. *Optics Laser Technol*. 2023;165:109571.

doi: 10.1016/j.optlastec.2023.109571

34. Wen H, Huang C, Guo S. The application of convolutional neural networks (CNNs) to recognize defects in 3D-printed parts. *Materials (Basel)*. 2021;14(10):2575.

doi: 10.3390/ma14102575

35. Yin X, Akmal JS, Salmi M, Björkstrand R. *Data From: Annotated Image Dataset for Defects Detection in Laser Powder Bed Fusion*. Geneva: Zenodo; 2025.

doi: 10.5281/zenodo.14996806

36. He K, Zhang X, Ren S, Sun J. *Deep Residual Learning for Image Recognition*. United States: IEEE; 2016. p. 770-778.

37. Tan M. *Efficientnet: Rethinking Model Scaling for Convolutional Neural Networks*. [arXiv Preprint]; 2019.

38. Ren S. *Faster R-CNN: Towards Real-Time Object Detection with Region Proposal Networks*. [arXiv Preprint]; 2015.

39. Redmon J. *You Only Look Once: Unified, Real-Time Object Detection*. United States: IEEE; 2016.

40. Chen K, Zhang P, Yan H, *et al*. A review of machine learning in additive manufacturing: Design and process. *Int J Adv Manuf Technol*. 2024;135(3):1051-1087.

doi: 10.1007/s00170-024-14543-2

41. Akmal J, Macarie M, Björkstrand R, Minet K, Salmi M. Defect detection in laser-based powder bed fusion process using machine learning classification methods. *IOP Conf Ser Mater Sci Eng*. 2023;1296(1):012013.

doi: 10.1088/1757-899X/1296/1/012013

42. Schmitt AM, Sauer C, Höfflin D, Schiffler A. Powder bed monitoring using semantic image segmentation to detect failures during 3D metal printing. *Sensors (Basel)*. 2023;23(9):4183.

doi: 10.3390/s23094183

43. Kuriachen B, Jeyaraj R, Raphael D, Ashok P, Sundari PS, Paul A. Defect detection in fused deposition modelling using lightweight convolutional neural networks. *Eng Appl Artif Intell*. 2025;141:109802.

doi: 10.1016/j.engappai.2024.109802

44. Sousa J, Brandau B, Darabi R, *et al*. Artificial intelligence for control in laser-based additive manufacturing: A systematic review. *IEEE Access*. 2025;13:30845-30860.

doi: 10.1109/ACCESS.2025.3537859

45. Soori M, Jough FKG, Dastres R, Arezoo B. Additive manufacturing modification by artificial intelligence, machine learning, and deep learning: A review. *Addit Manuf Front*. 2025;4(2):200198.

doi: 10.1016/j.amf.2025.200198

46. Paraskevoudis K, Karayannis P, Koumoulos EP. Real-time 3D printing remote defect detection (stringing) with computer vision and artificial intelligence. *Processes*. 2020;8(11):1464.

doi: 10.3390/pr8111464

47. Wang Y, Wang Z, Liu W, *et al*. A novel depth-connected region-based convolutional neural network for small defect detection in additive manufacturing. *Cognit Comput*. 2024;17(1):36.

doi: 10.1007/s12559-024-10397-8

48. Dong K, Ni M, Liang C, *et al*. Automatic detection and localization of internal defects in additively manufactured aluminum alloy based on deep learning. *Measurement*. 2025;244:116383.

doi: 10.1016/j.measurement.2024.116383

49. Scime L, Siddel D, Baird S, Paquit V. Layer-wise anomaly detection and classification for powder bed additive manufacturing processes: A machine-agnostic algorithm for real-time pixel-wise semantic segmentation. *Addit Manuf*. 2020;36:101453.

doi: 10.1016/j.addma.2020.101453

50. Ferguson M, Ak R, Lee YTT, Law KH. Detection and segmentation of manufacturing defects with convolutional neural networks and transfer learning. *Smart Sustain Manuf Syst*. 2018;2(1):137-164.

doi: 10.1520/SSMS20180033

ACCSCIENCE PUBLISHING

Materials Science in Additive Manufacturing

ORIGINAL RESEARCH ARTICLE

Explainable prediction of bead geometry in laser-arc hybrid additive manufacturing of Al–Cu alloy using a particle swarm optimization-based ensemble model

Runsheng Li[1], Hui Ma[1], Xingwang Bai[2], Boce Xue[1], Changze Li[1], Kui Zeng[1], Youheng Fu[3], Yonghui Liu[4]*, and Yanzhen Zhang[1]*

[1]College of Mechanical and Electronic Engineering, China University of Petroleum (East China), Qingdao, Shandong, China

[2]School of Mechanical Engineering, University of South China, Hengyang, Hunan, China

[3]School of Materials Science and Engineering, Huazhong University of Science and Technology, Wuhan, Hubei, China

[4]Shandong CharmRay Laser Technology Co., Ltd, Yantai, Shandong, China

Abstract

The weld bead is the basic structural unit in metal additive manufacturing, yet the multiphysics coupling inherent to hybrid laser-arc processing greatly complicates the prediction of bead dimensions. Despite the exploration of numerous predictive methods, research on explainable prediction of weld-bead dimensions remains limited. In this work, we developed a particle swarm optimization (PSO)-based ensemble prediction model (PSO-EP) for laser-arc hybrid additive manufacturing, and through SHapley Additive exPlanations (SHAP) analysis, comprehensively uncovered the underlying links between process variables and bead geometry. Experimental evidence indicated that our PSO-EP outperformed individual models and alternative ensembles, delivering superior accuracy, reflected by an R-squared value of 0.9567 for bead width and an R-squared value of 0.9492 for bead height, and markedly lowering prediction errors. The SHAP findings indicated that weld speed is the dominant determinant of bead width, while laser power plays a pivotal role in bead height. Subsequent single-factor dependence analysis showed that different process variables had significantly different impacts on bead size across their respective value intervals. This study provides important theoretical support for the intelligent development of the laser-arc hybrid additive manufacturing process.

Keywords: Additive manufacturing; Ensemble learning; Laser-arc hybrid; Geometry prediction; Aluminum–copper alloys; Explainable analysis

***Corresponding authors:**
Yonghui Liu
(78925411@qq.com)
Yanzhen Zhang
(zhangyanzhen@upc.edu.cn)

Citation: Li R, Ma H, Bai X, *et al*. Explainable prediction of bead geometry in laser-arc hybrid additive manufacturing of Al–Cu alloy using a particle swarm optimization-based ensemble model. *Mater Sci Add Manuf.* 2025;4(3):025220036.
doi: 10.36922/MSAM025220036

Received: May 26, 2025

Revised: June 16, 2025

Accepted: June 17, 2025

Published online: July 17, 2025

1. Introduction

Metal additive manufacturing (MAM), commonly referred to as metal 3D printing, is known for its design versatility and high efficiency, and is therefore extensively employed in aerospace, automotive, shipbuilding, and energy industries.[1] Through

the layer-by-layer deposition and solidification of metal feedstock, MAM creates new possibilities for designing and producing intricate metallic parts,[2-4] significantly enhances manufacturing productivity, propels innovation in product design and processing routes, and expedites the overall evolution of industrial manufacturing.[5,6] Among MAM technologies, powder bed fusion (PBF) and directed energy deposition (DED) are the most widespread;[7] wire-feed DED, in particular, garners interest for its superior deposition rates and material efficiency.[8,9] Wire-feed additive manufacturing utilizes lasers, electron beams, or welding arcs as energy inputs. In comparison with laser-or electron-beam-based AM, wire arc additive manufacturing (WAAM) offers significant benefits in capital expenditure and build rate.[10] The typical deposition rate for laser or electron beam AM lies between 2 and 10 g/min, whereas WAAM attains 50 – 130 g/min;[11,12] its energy efficiency of roughly 90% greatly surpasses the 2 – 5% achieved by laser-based AM.[13,14] Thanks to their favorable welding characteristics, aluminum–copper (Al–Cu) alloys serve as ideal materials for WAAM fabrication.[15-17] The bead geometry, which represents the basic fabrication unit in WAAM, exerts a direct influence on the dimensional fidelity of the manufactured component. Inadequate bead quality requires additional finishing operations, thereby increasing labor expenditure and leading to material wastage.

Recently, the laser-arc hybrid approach to additive manufacturing has come to the forefront of scholarly interest. By steering the arc, the laser decreases its electrical resistance and field strength, which in turn improves arc stability and boosts the build rate.[18] When the two energy sources are coupled, inverse bremsstrahlung further augments laser-energy uptake, and the laser improves melt-pool convection as well as the homogeneity of elemental distribution.[19] Even so, integrating laser and arc complicates the multiphysics interactions, greatly raising the challenge of forecasting weld-bead dimensions. Consequently, the precise prediction of weld-bead geometry in laser-arc hybrid additive manufacturing (LAHAM) emerges as a pivotal problem that demands prompt resolution.

As an essential subdivision of artificial intelligence (AI), machine learning (ML) identifies patterns through data analysis and leverages them for prediction and decision-making tasks.[20] During the past decade, ML has found broad applications across numerous domains, such as medical diagnostics,[21] forecasting material properties,[22] intelligent manufacturing,[23] self-driving vehicles,[24] natural language processing,[25] and object detection.[26] A synopsis of research forecasting the links between process parameters and layer geometry in MAM is provided in Table 1. Using laser power and scan speed as predictors, Le-Hong *et al.*[27] developed random-forest and artificial-neural-network models to estimate layer geometry in laser PBF, reporting validation R^2 values exceeding 90%. With laser power, travel speed, and powder feed rate as variables, Zhu *et al.*[28] employed support vector regression (SVR) to predict the layer height and width of DED, reaching 93% accuracy. Deploying a naïve Bayes approach, Liu and Kuo[29] studied wire-laser DED; by inputting travel velocity, laser power, and wire feed speed, they predicted bead dimensions, yielding R^2 values of 91% and 94%. Xia *et al.*[30] employed a genetic-algorithm-tuned adaptive neuro-fuzzy inference system model to estimate surface roughness from wire feed and welding speeds, achieving validation R^2 values exceeding 90%. Oh *et al.*[31] introduced an SVR model into the WAAM process, using key parameters such as welding current and wire feed rate to accurately predict bead width and height and to identify geometric non-uniformity defects that may arise under different operating conditions. Šket *et al.*[32] used an extreme gradient boosting (XGBoost) regression model, with current and travel speed as the two process parameters, to predict the geometric morphology of the weld bead.

Table 1. Overview of research on data modeling between process parameters and layer geometries in metal additive manufacturing

Process	Models	Inputs	Outputs	Ref.
LPBF	RF and ANN	Laser power and scanning velocity	Layer height, width, and penetration depth	27
Powder-laser DED	SVR	Laser power, travel speed, and powder feed rate	Layer height and width	28
Wire-laser DED	NB	Laser power, travel speed, and wire feed rate	Layer height and width	29
WAAM	ANFIS	Wire feed rate and travel speed	Surface roughness	30
WAAM	SVR	Wire feed rate and travel speed	Layer height and width	31
WAAM	XGBoost	Current and travel speed	Layer height, width, and area	32

Abbreviations: ANFIS: Adaptive neuro-fuzzy inference system; ANN: Artificial neural network; DED: Directed energy deposition; LPBF: Laser powder bed fusion; NB: Naïve Bayes; RF: Random forest; SVR: Support vector regression; WAAM: Wire arc additive manufacturing; XGBoost: Extreme gradient boosting.

Despite these advances in predicting layer geometries of MAM based on process parameters, reliable estimation of bead size in LAHAM still confronts significant challenges. The link between LAHAM processing parameters and

bead dimensions is both intricate and non-linear, calling for further intensive study. Because individual regression models are constrained by their respective hypothesis spaces, no single model can guarantee an optimal result; therefore, ensemble schemes that combine multiple models[33] are generally employed to enhance prediction accuracy. Put differently, simple ML or neural-network approaches alone may not suffice, whereas more elaborate ensemble architectures are able to offer superior predictive accuracy. In addition, incorporating explainable-analysis methods enables researchers to grasp data features more thoroughly and to probe the effect of process parameters on bead-geometry predictions. These analytic approaches, once validated, support investigators in deepening their data understanding and hence in assessing more precisely the impact of process parameters on predictive outcomes.

Herein, we present a particle swarm optimization (PSO)-based ensemble predication (PSO-EP) that combines four base models – Gaussian process regression (GPR), SVR, artificial neural networks (ANN), and extreme learning machines (ELM) – with PSO employed to calibrate their respective weights. The predictive capability of PSO-EP is benchmarked against single base learners and alternative ensemble methods, and the results verify the superiority of the proposed approach. In addition, based on Shapley theory, an interpretability study is carried out in which visual tools, including feature-importance and sample-distribution charts, afford deeper insights into how individual features and samples sway the predictive results.

2. Materials and methods

2.1. Experimental setup

The system utilized in this study is depicted in Figure 1. In the system, the composite heat source is composed of a welding machine (Fronius CMT Advanced 4000R, Austria) and a fiber laser system (Raycus RFL-C3300W, China). The fiber laser system consists of a laser source, an output head, and a cooling unit, with the relative position of the laser output head and the welding gun is illustrated in Figure 1. Line structured light (Gocator 2430, Canada) was utilized to obtain the point cloud data of the weld bead morphology. The procedure of laser-scanning the actual weld bead morphology and generating the point cloud is depicted in Figure 2. The motion platform used is a CNC machine tool (Fana FA2818HG, China). The deposition material is ER2319 aluminum alloy (1.2 mm diameter), and the base material is 2219 aluminum alloy. During the manufacturing process, the welding mode was cold metal transfer pulse advance (CMT-PADV), with the laser CMT process parameters listed in Table 2. Before the experiment, the substrate was processed and cleaned with acetone. The chemical compositions of the substrate and the wire are provided in Table 3.

2.2. Experiment design

Within the WAAM process, the weld bead dimensions are strongly affected by the choice of process parameters. An increase in wire feed speed leads to greater weld bead width and height.[34] A larger arc length adjustment broadens the bead width, whereas a higher pulse correction decreases its height.[35] Within LAHAM, an optimal laser power level supports geometric uniformity, whereas overly high power causes size variability.[36] Accordingly, this study concentrates on the influence of wire feed speed (v_w), welding speed (v_t), arc length correction (l), pulse correction (f), and laser power (p) on weld bead width (W) and height (H).

In Figure 3, the full factorial design with three factors at three levels and the Box–Behnken design are depicted schematically. The Box–Behnken design,[37] as opposed to the full factorial design, prevents extreme condition combinations and efficiently captures second-order effects with a reduced number of experiments, and was therefore employed in this work. First, this study followed the process window recommended in reference[38] and employed single-factor screening experiments to define the valid ranges of each influencing factor, encoding their upper and lower bounds as +1 and −1, respectively; the selected key factors and their symbols are detailed in Table 4. Table 5 displays the 46 coded experimental conditions and outcomes. Table 6 comprises 20 randomly sampled process parameter configurations and associated weld geometry metrics, used as the validation and test datasets. To assess the reproducibility of the experimental dataset, six repeated trials were conducted under the central-point parameter configuration, and the coefficient of variation (CV)[39] was employed for evaluation. The analysis revealed CV values of 3.25% for bead width and 2.74% for bead height – both markedly lower than the commonly accepted 10% benchmark[40] – providing strong evidence of high data consistency. As illustrated in Figure 4, all the weld beads were well-formed and defect-free. The overall experimental count was determined based on Equation I.

$$N = 2q(q-1)+C_0 \quad \text{(I)}$$

where q is the number of experimental parameters, and C_0 denotes the number of repetitions needed to minimize errors arising from environmental and human factors. In this paper, q is 5, and C_0 is 6.

2.3. Particle swarm optimization-based ensemble prediction

In the proposed ensemble forecasting framework, the four base learners – ANN, GPR, SVR, and ELM – are first

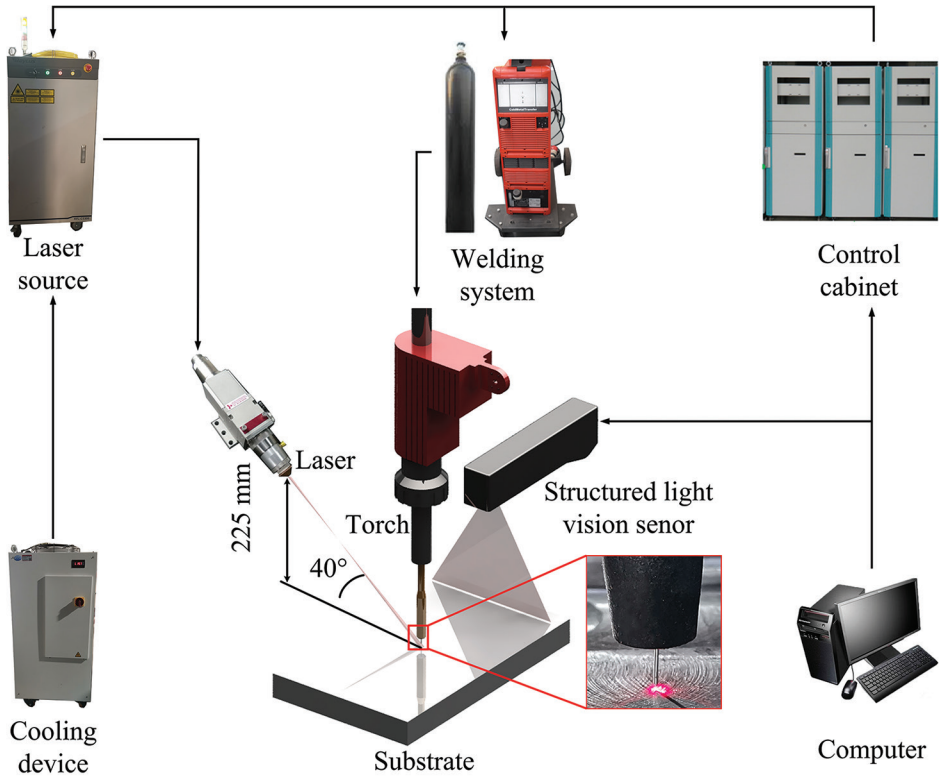

Figure 1. Schematic illustration of the laser-arc hybrid additive manufacturing system

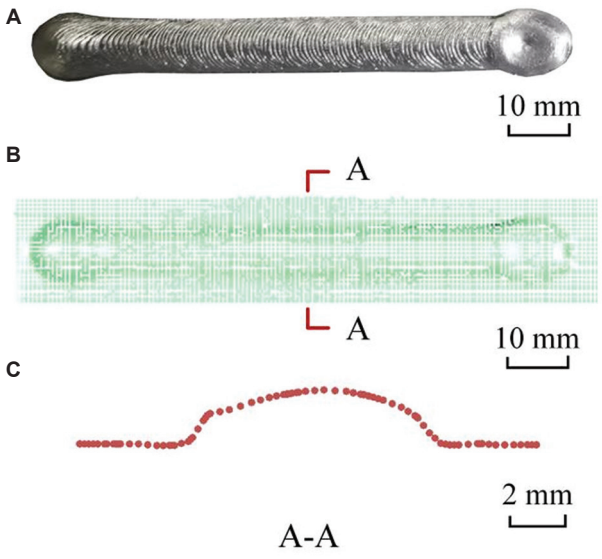

Figure 2. Schematic diagram shows the quantification of weld-bead width and height. (A) Actual morphology of a weld bead in the training set. (B) 3D point cloud obtained through line-laser scanning. (C) Extracted weld-bead contour

subjected to hyperparameter optimization and training on the training and validation datasets. The tuned models are subsequently deployed on the test set, where they each yield their own prediction outputs. Thereafter, particle swarm optimization (PSO) iteratively updates the weights of the models, driving the weighted prediction error downward until convergence and ultimately producing an ensemble prediction that fuses the four models. Finally, in accordance with Equation II, the mean absolute percentage error is calculated for each base model as well as for the ensemble.

$$MAPE = \frac{1}{n}\sum_{i=1}^{n}\frac{\left|y_i - \widehat{y_i}\right|}{y_i} \times 100\% \quad \text{(II)}$$

Particle swarm optimization is a global optimization technique inspired by swarm intelligence, which locates optima by modeling the coordinated, iterative movement of many particles within a multidimensional search domain. Every particle acts as a potential solution; its velocity and position are continually updated with reference to its personal best and the swarm's global best, which hastens convergence and elevates search efficiency.

To simplify the weight optimization for multi-model ensembles, we introduce, under the PSO paradigm, a one-dimensional discrete index encoding (ODIE) that assigns weights to the base regression models with high efficiency.

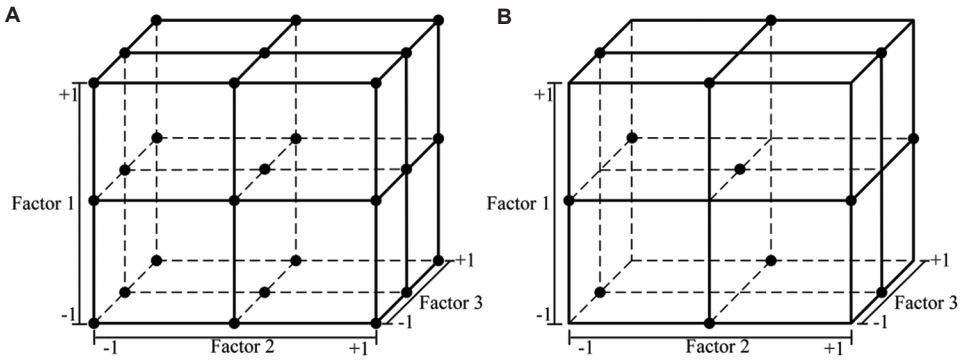

Figure 3. Sketch of three-factor three-level experimental designs. (A) Full factorial design. (B) Box–Behnken design

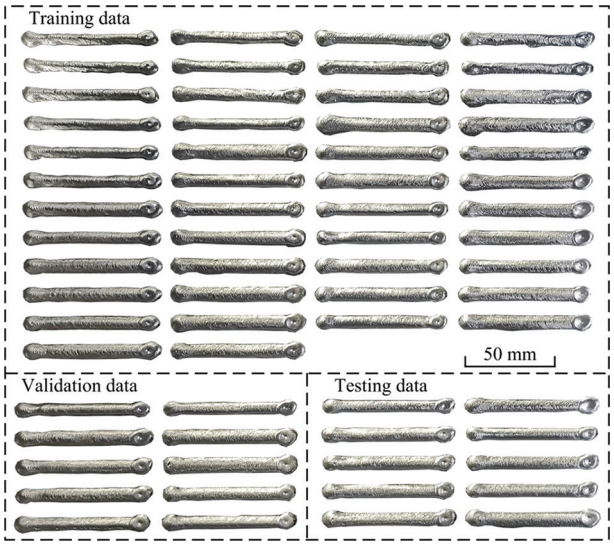

Figure 4. The actual morphology of the 46 weld beads in the training dataset

In traditional methods (Figure 5A), weights are usually expressed as a D-dimensional continuous vector:

$$X = [x_1, x_2, ...x_D], \sum_{i=1}^{D} x_i = 1 \quad \text{(III)}$$

Traditional methods usually encode the weight vector as a D-dimensional continuous variable and perform iterative updates of particle velocities and positions in this high-dimensional space. Nevertheless, this design entails two principal drawbacks: On the one hand, owing to the excessive dimensionality of the search space, PSO tends to converge slowly when optimizing in a D-dimensional continuous domain. On the other hand, to enforce the normalization constraint $\sum_{i=1}^{D} x_i = 1$, the weights must be projected back or a penalty term introduced after every iteration, thereby complicating implementation and further burdening hyperparameter tuning.

Table 2. Process parameters of the laser-CMT process

Heat source	Parameter	Value
CMT	Wire feeding speed (m/min)	6
	Travel speed (mm/min)	600
Laser	Laser power (kW)	3
	Defocusing length (mm)	171.5

Abbreviation: CMT: Cold metal transfer.

Table 3. Wire and substrate chemical compositions

Alloy	Chemical components (wt.%)								
	Si	Fe	Cu	Mn	Mg	Zn	V	Ti	Zr
ER2319 (wire)	0.106	0.156	5.950	0.273	0.009	0.012	0.068	0.104	0.104
2219-T6 (substrate)	0.021	0.100	6.060	0.270	<0.01	0.024	0.092	0.039	0.130

Abbreviations: Si: Silicon; Fe: Iron; Cu: Copper; Mn: Manganese; Mg: Magnesium; Zn: Zinc; V: Vanadium; Ti: Titanium; Zr: Zirconium.

Table 4. Process control parameters and their levels

Parameters	Units	Notation	Factor levels		
			−1	0	1
Wire feed speed	m/min	v_w	6	7	8
Welding speed	mm/min	v_t	500	600	700
Arc length correction	%	l	5	10	15
Pulse correction	%	f	0	1	2
Laser power	kW	p	1	2	3

In the ODIE workflow (Figure 5B), every particle is encoded as an integer sequence of length k:

$$X = [x_1, x_2, .., x_k], x_i \in \{0, 1., D-1\} \quad \text{(IV)}$$

In this setting, D represents the total count of base learners, and x_i indicates the index of the base model chosen at position i. The weight of each base model j can be

Table 5. Design matrix and targets

Experimental run	Design matrix					Results	
	v_w	v_t	l	f	p	W (mm)	H (mm)
1	7	600	5	2	2	8.19	2.78
2	7	600	10	1	2	8.49	2.69
3	8	600	10	1	1	7.66	3.14
4	8	700	10	1	2	7.14	2.54
5	7	600	10	1	2	7.85	2.60
6	7	600	15	0	2	6.70	2.77
7	7	700	5	1	2	7.28	2.56
8	7	500	5	1	2	9.13	2.76
9	6	600	5	1	2	7.52	1.89
10	8	600	5	1	2	8.44	2.92
11	7	600	5	1	3	8.62	2.45
12	7	700	10	1	3	7.09	2.11
13	7	600	10	2	3	9.63	2.12
14	6	600	10	1	3	7.30	2.32
15	6	600	15	1	2	6.86	2.76
16	8	600	10	1	3	9.70	2.35
17	7	600	10	1	2	8.36	2.52
18	7	700	10	1	1	7.53	2.55
19	7	500	10	1	3	10.1	2.56
20	7	600	5	1	1	9.01	2.42
21	6	700	10	1	2	7.25	2.54
22	7	600	15	2	2	8.75	2.72
23	6	500	10	1	2	7.79	2.56
24	7	500	10	2	2	9.44	2.86
25	7	700	10	2	2	7.83	2.38
26	8	600	15	1	2	8.78	2.52
27	7	600	10	2	1	8.14	2.92
28	6	600	10	2	2	7.84	2.48
29	8	600	10	2	2	8.65	2.68
30	7	700	10	0	2	7.02	2.44
31	7	700	15	1	2	7.73	2.40
32	6	600	10	1	1	7.78	2.36
33	7	600	15	1	3	9.20	2.04
34	7	600	10	0	3	8.47	2.24
35	7	600	5	0	2	8.95	2.44
36	7	600	10	1	2	8.49	2.61
37	7	600	15	1	1	7.77	2.93
38	7	500	10	0	2	8.47	2.71
39	8	600	10	0	2	8.98	2.64
40	7	500	10	1	1	8.36	3.00
41	7	600	10	1	2	8.61	2.49
42	7	600	10	0	1	8.15	2.56
43	8	500	10	1	2	10.17	3.02
44	6	600	10	0	2	7.01	2.40
45	7	600	10	1	2	8.49	2.59
46	7	500	15	1	2	9.07	3.12

(Cont'd...)

Table 5. ***(Continued)***

Abbreviations: f: Pulse correction; H: Weld bead height; l: Arc length correction; p: Laser power; v_t: Welding speed; v_w: Wire feed speed; W: Weld bead width.

Table 6. Experimental data for the validation and test sets

Experimental run	Design matrix					Results	
	v_w	v_t	l	f	p	W (mm)	H (mm)
1	6.50	510.00	6.00	1.50	1.20	8.69	2.56
2	6.30	540.00	8.00	1.70	2.70	8.91	2.45
3	6.60	570.00	7.00	0.20	2.20	8.30	2.47
4	7.90	530.00	7.00	0.90	1.80	9.36	3.01
5	7.20	520.00	6.00	0.30	2.90	9.64	2.52
6	7.80	510.00	12.00	0.50	1.50	8.55	3.13
7	7.30	620.00	12.00	1.20	1.60	8.19	2.69
8	6.30	580.00	14.00	1.10	1.00	7.31	2.95
9	7.00	680.00	14.00	1.30	2.00	7.57	2.41
10	8.00	540.00	14.00	1.10	2.80	10.50	2.46
11	6.30	610.00	6.00	0.50	2.30	7.89	2.25
12	6.30	660.00	6.00	0.60	1.50	7.87	2.20
13	6.60	570.00	10.00	0.20	2.00	7.78	2.51
14	6.80	550.00	14.00	1.60	1.20	8.31	3.07
15	7.30	520.00	11.00	1.80	1.30	8.68	3.12
16	6.70	550.00	13.00	0.30	1.20	7.26	2.92
17	7.90	690.00	10.00	0.80	1.20	7.33	2.71
18	7.30	620.00	7.00	1.90	1.00	7.92	2.64
19	6.90	640.00	9.00	1.60	2.70	8.56	2.28
20	7.10	520.00	7.00	1.30	1.80	9.04	2.86

Abbreviations: f: Pulse correction; H: Weld bead height; l: Arc length correction; p: Laser power; v_t: Welding speed; v_w: Wire feed speed; W: Weld bead width.

obtained by tallying its occurrences n_j within the sequence, thus allowing direct decoding:

$$\omega_j = \frac{n_j}{k}, \sum_{j=1}^{D} \omega_j = 1 \quad \text{(V)}$$

The encoding intrinsically meets the normalization requirement without extra projection or penalty terms,

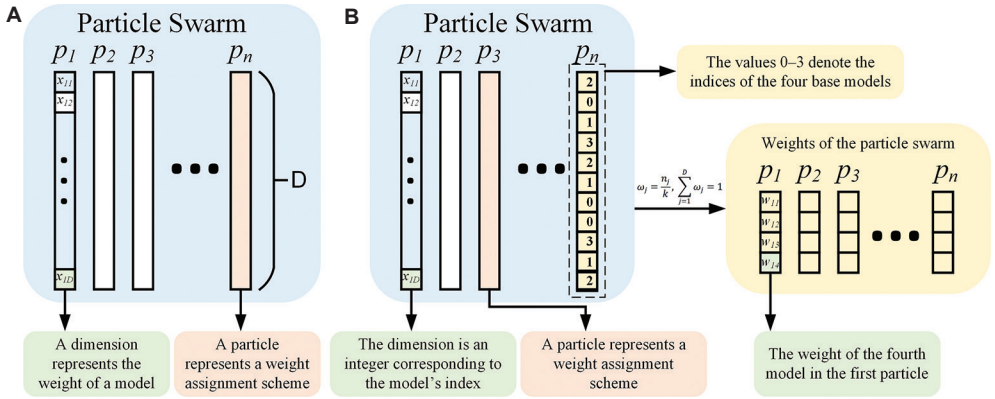

Figure 5. Comparison between traditional particle swarm optimization (PSO) encoding and one-dimensional discrete index encoding: (A) Traditional encoding, and (B) one-dimensional discrete index encoding

and by collapsing the search space from a D-dimensional continuum to a single discrete index, it significantly cuts computational complexity and speeds up convergence.

Figure 6 presents the operational flow of the PSO-driven ensemble learning module. Initially, a swarm of particles is randomly seeded within the one-dimensional discrete index space, where every particle encodes a particular distribution of weights across the base learners. Subsequently, each particle is decoded, the weight of each base model is determined from the index frequencies, and an ensemble prediction is produced accordingly. The error between the predicted and true values is then used as the fitness, driving the velocity and position updates of PSO. During iteration, each particle adjusts its position through a weighted combination of inertia, cognitive, and social components, balancing global exploration and local exploitation. Meanwhile, the historically best particle is retained, and random perturbations are introduced to preserve swarm diversity. Once the termination criterion is met, the global best particle is decoded to yield the optimal weight allocation for the base models.

The specific workflows of the base learners and the PSO iterative optimization are described in detail in the literature.[41-44] Every baseline model was built in a Python environment with the scikit-learn library, and the PSO routine was carried out using the PySwarms toolkit.

2.4. Shapley-based explainable analysis

Despite the widespread use of ML models in pivotal domains such as biomedicine and self-driving technology, their decision paths remain largely inscrutable black boxes, eroding user confidence and hindering real-world implementation. To tackle this challenge, explainable ML has risen to prominence, seeking to illuminate model workings, pinpoint key predictors, and use that knowledge to drive performance improvements. The present work

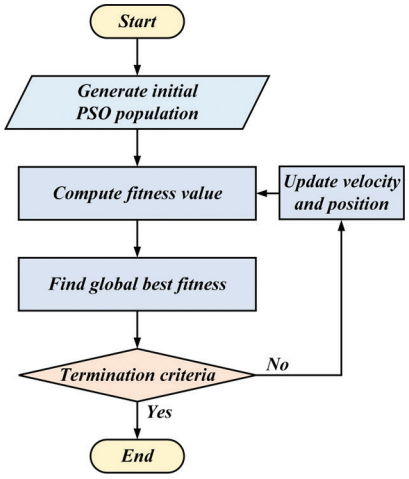

Figure 6. Flow chart of particle swarm optimization-based ensemble module

performed an explainability analysis of the process parameters, isolating the factors that strongly influence bead size and furnishing direction for future model refinement. Proposed by Shapley in 1952,[45] the Shapley value offers a fair way to allocate rewards in cooperative games by measuring every player's marginal contribution. SHapley Additive exPlanations (SHAP), a Python library for *post hoc* model explanation, evaluates the influence of a feature on the output by calculating its marginal contributions over all subset combinations, yielding global importance orders as well as case-specific interpretations. Given the full feature set F, the SHAP value for feature *j* is defined by:

$$\varphi_j^{(i)} = \sum_{S\subseteq\{m_1,\ldots m_o\}\setminus\{m_j\}} \frac{|S|!(o-|S|-1)!}{o!}\left(val(S\cup\{m_j\}) - val(S)\right) \quad \text{(VI)}$$

SHAP represents a paradigmatic *post hoc* interpretability technique, revealing feature–output relationships through

visualization. The study began by calculating SHAP values for every feature, thereby quantifying their influence on the predictions; the original features were then contrasted with newly derived ones to confirm the performance gains attributable to the new attributes. Subsequently, the SHAP visualization toolkit was employed to depict feature importance and the directionality of their effects, affording a deeper dissection of the model's reasoning process.

2.5. Parameter setting of the PSO-EP

The training set trained multiple regression models, while five-fold cross-validation on the validation set tuned their hyperparameters. Once tuning was completed, the model with the best validation performance was chosen to forecast bead size on the test set; these forecasts constituted the response values. Next, the response values together with the models' evaluation indices were fed into the ensemble module, which used the metric of Equation II as a fitness function and applied PSO to derive a weighted fusion of the individual outputs. Within the PSO-EP method, the weight-assignment stage employed up to 50,000 iterations and a swarm of 200 particles. Iterative search ultimately yielded the optimal set of model weights, and a consolidated estimate of bead dimensions was output. The PSO-EP approach was further benchmarked against various alternative techniques to evaluate its efficacy.

2.6. Model evaluation indicators

Once the prediction was complete, the model's performance was assessed by computing the error between the true values and the predicted results for the test data. Smaller errors indicated better model performance. For the regression problem concerning the LAHAM weld bead width and height, this study used mean absolute error (MAE), root mean squared error (RMSE), and coefficient of determination (R^2) as performance metrics. MAE and RMSE assess the deviation between predicted and actual values, with RMSE being more sensitive to larger errors. R^2 reflects the model's ability to explain the variability in the data, with values closer to 1 indicating a better fit. A comprehensive evaluation of model performance can be achieved by integrating these metrics.

$$MAE = \frac{1}{n}\sum_{i=1}^{n} | y_i - \widehat{y_i} | \quad \text{(VII)}$$

$$RMSE = \sqrt{\frac{1}{n}\sum_{i=1}^{n}(y_i - \hat{y}_i)^2} \quad \text{(VIII)}$$

$$R^2 = 1 - \frac{\sum_i \left(\hat{y}_i - y_i\right)^2}{\sum_i \left(y_i - \overline{y}\right)^2} \quad \text{(IX)}$$

3. Results and discussion

In this study, the validity of the proposed PSO-EP method was demonstrated. For performance evaluation, the PSO-EP's predictions were initially benchmarked against each single base model to measure gains in prediction precision. Subsequently, it was assessed alongside other widely used ensemble forecasting approaches to underscore the PSO-EP's overall superiority. Finally, an importance analysis of the process parameters was conducted to uncover their individual impacts on the prediction outcomes.

3.1. Comparison of PSO-EP with base models

To assess the superiority of PSO-EP, the present study conducted a comparison against four baseline models: GPR, SVR, ANN, and ELM. Figures 7 and 8 illustrate the performance of the models in the prediction tasks for weld bead width and height, respectively. To facilitate a clear comparison, the figures display only the test set predictions along with their respective error curves.

Figure 7 illustrates that PSO-EP excels in weld bead width prediction, with an R^2 of 0.9567, markedly outperforming GPR, SVR, ANN, and ELM, which signifies its enhanced capability to accurately capture the overall width variation trend; simultaneously, PSO-EP records the smallest RMSE and MAE values, substantiating its lowest overall prediction error and MAE (Table 7). Nevertheless, the highest relative error observed in extreme samples is 5.6%, which is only superior to ANN's 7.8%, indicating potential for further enhancement in limiting the maximum error. Sample 6 showed a comparatively large error in weld bead width prediction. The feature importance analysis in section 3.3 indicated that wire feed speed and welding speed are the key factors determining width; for this sample, the wire feed speed was 7.80 m/min and the welding speed was 510 mm/min. Figure 9 reveals that this set of parameters is positioned at the boundary of the process window, where their interaction drives an increase in bead width, resulting in an overestimation by the model and a magnified error. This finding suggests, first, that the model's generalization at the boundary of the parameter space can be further enhanced; second, that because this condition approaches the experimental limit, sporadic experimental inaccuracies could also exacerbate the prediction error.

Regarding weld bead height prediction (Figure 8), while all models display comparable overall trend curves, PSO-EP notably excels in fitting regions with pronounced height fluctuations, where its predicted curve almost perfectly overlaps with observed values; by comparison, GPR, SVR, ANN, and ELM show evident discrepancies at

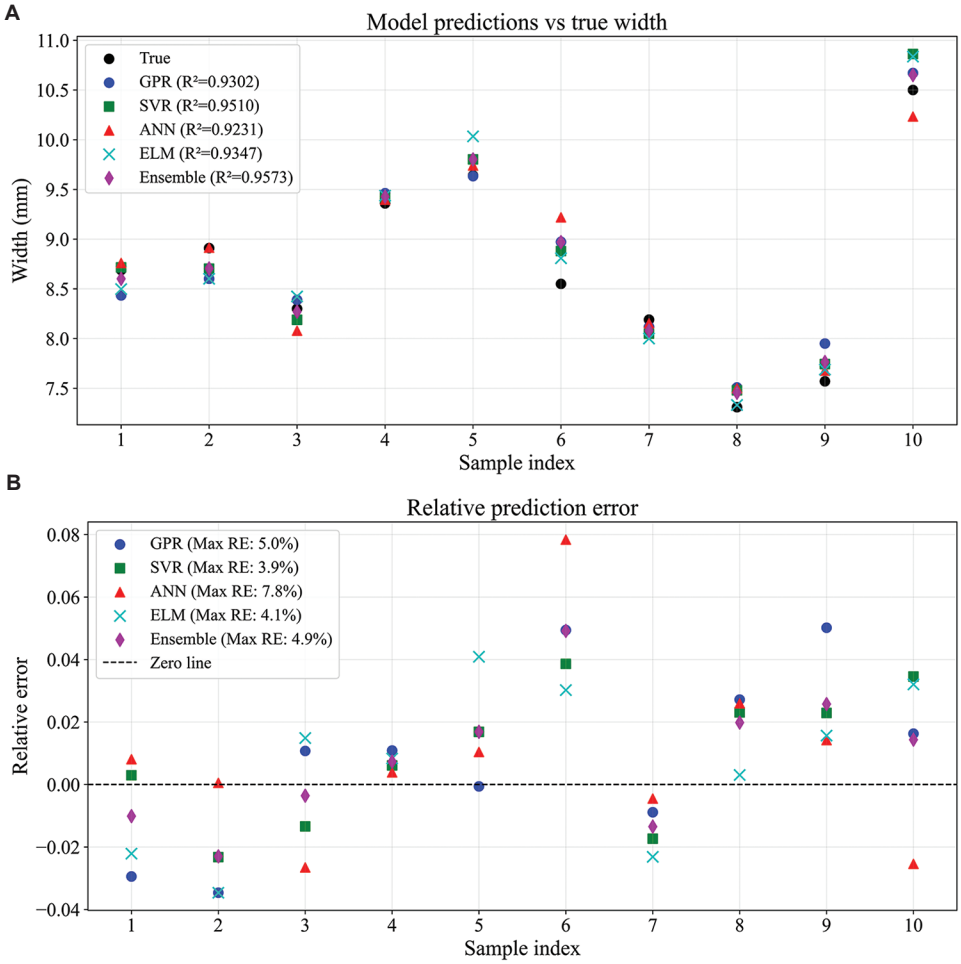

Figure 7. Predicted values (A) and error performance (B) of each model in the width prediction task
Abbreviations: ANN: Artificial neural network; ELM: Extreme learning machines; GPR: Gaussian process regression; SVR: Support vector regression

Table 7. Evaluation metrics of each model in the width prediction task

Model	MAE	RMSE	R^2
GPR	0.2006	0.2400	0.9302
SVR	0.1741	0.2012	0.9510
ANN	0.1704	0.2519	0.9231
ELM	0.2021	0.2322	0.9347
PSO-EP	0.1454	0.1890	0.9567

Abbreviations: ANN: Artificial neural network; ELM: Extreme learning machines; GPR: Gaussian process regression; MAE: Mean absolute error; PSO-EP: Particle swarm optimization-based ensemble prediction model; R^2: Coefficient of determination; RMSE: Root mean squared error; SVR: Support vector regression.

fluctuation points, struggling to precisely represent height changes. Quantitative assessment showed that the PSO-EP achieved an R^2 of 0.9492 (Table 8), again leading all models, with RMSE and MAE metrics below those of competitors; its maximum relative error stood at 4.2%, ranking second to SVR, confirming PSO-EP's outstanding precision and robustness in the weld bead height prediction task.

3.2. Comparison of PSO-EP with other ensemble methods

Figure 10 presents a comparison of four ensemble forecasting approaches: the averaging method,[46] Stacking,[47] ELGA,[48] and the PSO-EP method introduced herein. Results indicated that PSO-EP attained an R^2 of 0.9492 in predicting weld bead height, surpassing the averaging method (0.9387) by 1.12%, stacking (0.9378) by 1.22%, and ELGA (0.9206) by 3.11%. For weld bead width prediction, PSO-EP achieved an R^2 of 0.9567, which is 2.07% higher than the averaging method (0.9373), 3.47% higher than stacking (0.9246), and 2.36% higher than ELGA (0.9346). These notable improvements stem from the PSO algorithm's effective global optimization ability.

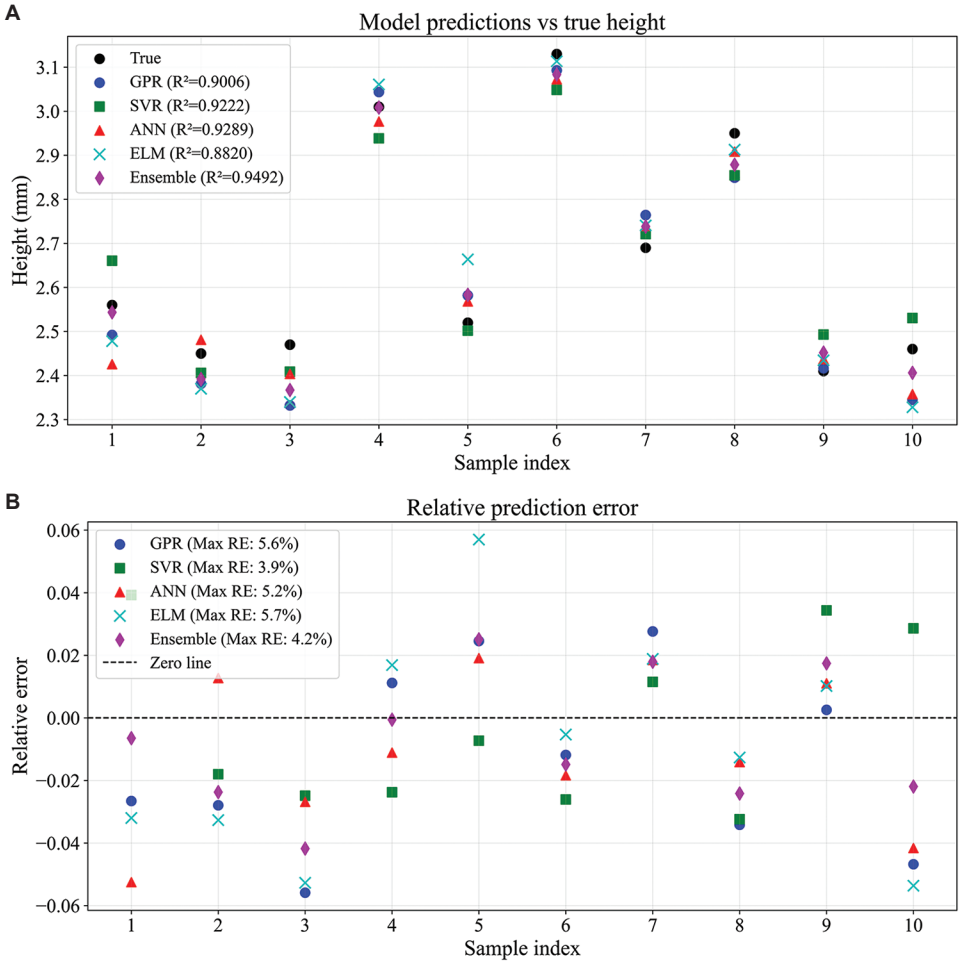

Figure 8. Predicted values (A) and error performance (B) of each model in the width prediction task
Abbreviations: ANN: Artificial neural network; ELM: Extreme learning machines; GPR: Gaussian process regression; SVR: Support vector regression

Table 8. Evaluation metrics of each model in the height prediction task

Model	MAE	RMSE	R^2
GPR	0.0704	0.0798	0.9006
SVR	0.0657	0.0706	0.9222
ANN	0.0591	0.0675	0.9289
ELM	0.0748	0.0869	0.8820
PSO-EP	0.0505	0.0571	0.9492

Abbreviations: ANN: Artificial neural network; ELM: Extreme learning machines; GPR: Gaussian process regression; MAE: Mean absolute error; PSO-EP: Particle swarm optimization-based ensemble prediction model; R^2: Coefficient of determination; RMSE: Root mean squared error; SVR: Support vector regression.

3.3. SHAP analysis

In this section, the association between processing parameters and prediction results is examined through Shapley theory. This theory computes the marginal contribution of each feature within various feature subsets, then derives a weighted average to quantify each feature's impact on the prediction, termed the SHAP value. Figures 11 and 12 illustrate the ranked importance of process parameters within the width and height models, facilitating insight into each parameter's effect on the model. In the figures, each row corresponds to a parameter, the x-axis displays SHAP values, the dot color reflects the feature magnitude, and the order is determined by the average absolute SHAP value over all samples. For predicting weld bead width, welding speed is paramount and inversely correlated with width because increased speed hastens melt pool cooling, reduces metal fill time, and narrows the bead. Wire feeding rate and laser power exhibit positive correlations with width, facilitating bead growth by augmenting metal deposition and raising melt pool temperature, respectively. Arc length and pulse corrections exert limited influence, fine-tuning heat input to modulate width changes. For weld bead height prediction,

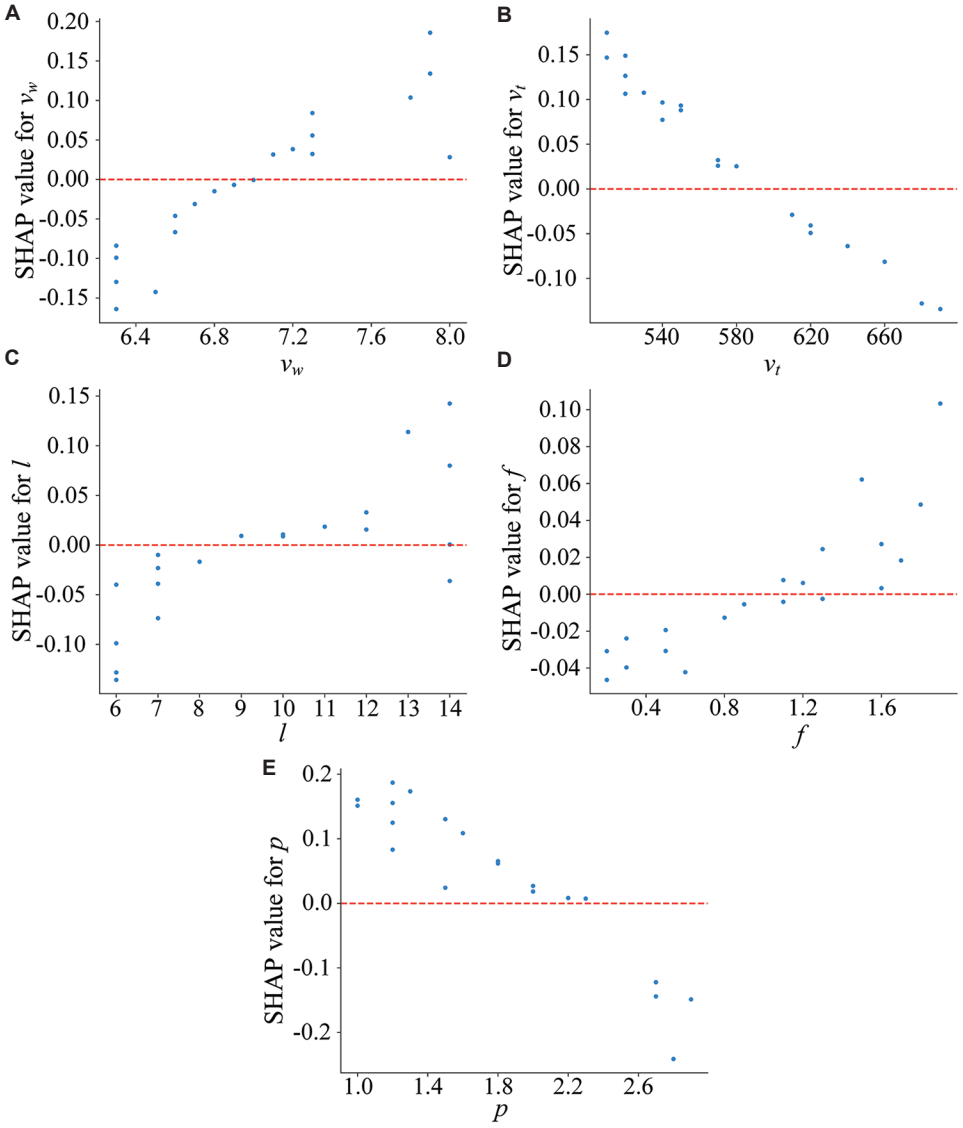

Figure 9. Process parameter dependence plots in the height prediction task: (A) Wire feed speed (v_w), (B) Welding speed (v_t), (C) Arc length correction (l), (D) Pulse correction (f), and (E) Laser power (p)

laser power is the dominant parameter and inversely related to height, since increased lateral expansion restricts vertical accumulation. Welding speed similarly exhibits a negative correlation because increased speed promotes faster cooling, thereby limiting height increase. The wire feed rate shows a positive correlation by promoting vertical deposition. Despite their limited impact, arc length and pulse corrections are positively associated with height, contributing to height enhancement.

Dependence plots serve as crucial instruments to examine how feature values impact prediction results. Figure 13 depicts the relationships between process parameters and weld bead width. With increasing wire feed rate, SHAP values increase markedly, demonstrating positive promotion; below 6.9 m/min, the effect is negative, shifting to positive above this point, resulting in bead width expansion. SHAP values for welding speed are positive under 580 mm/min, fostering width increase, but become negative beyond this threshold, limiting bead expansion. For laser power under 2.3 kW, SHAP values are negative, signifying width limitation at low power; beyond this, the influence turns positive, markedly enhancing bead width. Figure 9 further presents the relationships between process parameters and weld bead height. The influence patterns of wire feed speed, welding speed, and laser power on weld bead height prediction resemble those

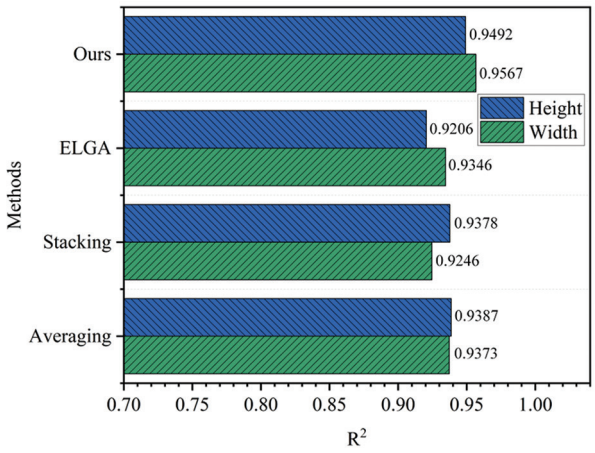

Figure 10. Comparative analysis of various ensemble forecasting approaches

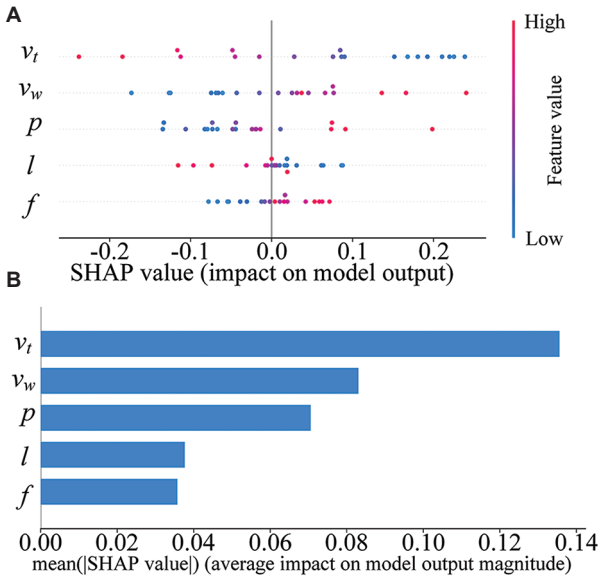

Figure 11. Importance ranking of process parameters in the width prediction task. (A) SHAP summary plot. (B) Importance plot of process parameter
Abbreviations: f: Pulse correction; *l*: Arc length correction; *p*: Laser power; v_t: Welding speed; v_w: Wire feed speed, SHAP: SHapley Additive exPlanations

observed for bead width. Below 7 m/min, wire feed speed has a negative influence, which reverses to positive when exceeding this value, facilitating height growth. Welding speed exhibits a positive correlation under 580 mm/min, shifting to a negative correlation beyond 610 mm/min, thereby inhibiting height increase. Below 2.3 kW, laser power positively correlates with height, but the relationship reverses above this threshold, restricting height growth. In summary, clear thresholds exist for process parameters affecting weld bead width and height, beyond which

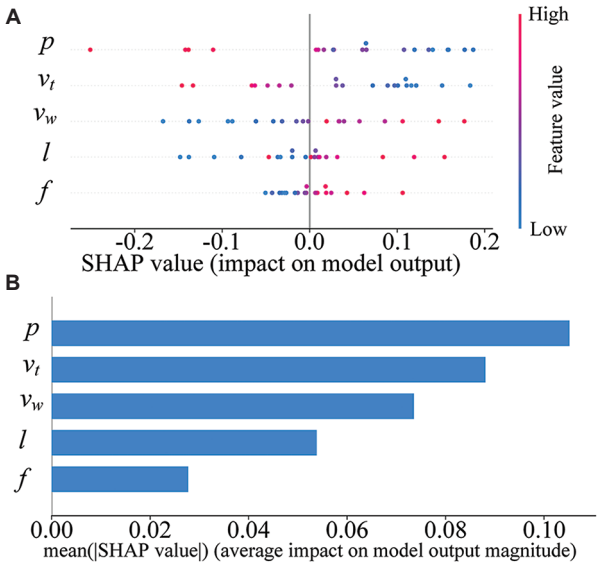

Figure 12. Importance ranking of process parameters in the height prediction task. (A) SHAP summary plot. (B) Importance plot of process parameter
Abbreviations: f: Pulse correction; *l*: Arc length correction; *p*: Laser power; v_t: Welding speed; v_w: Wire feed speed, SHAP: SHapley Additive exPlanations

their effects may invert, thereby affecting the quality of formation.

3.4. Conceptual framework for bead size and shape prediction applied to in-process characterization

Figure 14 depicts the initial stage of the additive manufacturing process, in which the 3D model is first sliced and a deposition path is generated; the slicing operation defines the layer thickness, and the path planning sets the track width and selects the appropriate process settings accordingly. This study concentrates on the high-precision prediction of bead geometry.

Despite the high accuracy achieved in predicting bead morphology, variations in material batches and environmental fluctuations may still prevent the optimized process parameters from faithfully reproducing the target dimensions. Additional dimensional deviations can arise from tool wear, calibration errors, drifts in laser or arc power, and fluctuations in wire-feed rate. To address these issues, we propose embedding the high-precision prediction model within an online quality-monitoring and closed-loop control framework to enable real-time correction and stabilization of bead dimensions.

During printing, a melt-pool camera continuously captures images near the welding torch and feeds them to

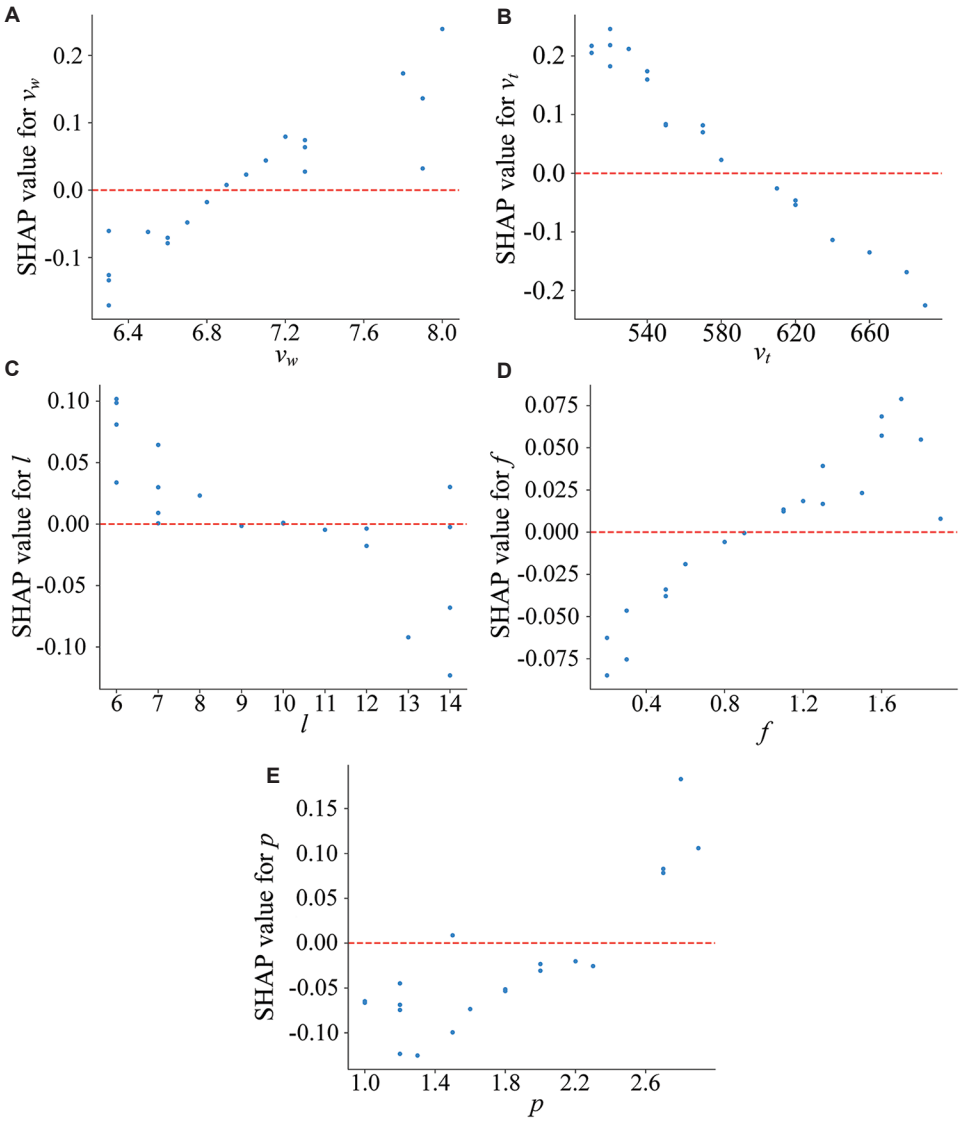

Figure 13. Process parameter dependence plots in the width prediction task: (A) Wire feed speed (v_w), (B) Welding speed (v_t), (C) Arc length correction (l), (D) Pulse correction (f), and (E) Laser power (p)

the trained U-net model, which segments and crops the bead and online extracts the actual bead width W_{real} and height H_{real}. After comparing the measured and desired dimensions, Equations X and XI compute the required correction to obtain new targets W' and H'; these targets feed the accurate bead predictor, which derives revised process parameters and refreshes the G-code. The machine resumes deposition under the updated parameters, the camera repeats image acquisition, and the cycle iterates in a closed loop until the bead size remains inside the specified error band.

$$\Delta W = W - W_{real,} W' = W + \Delta W \quad \text{(X)}$$

$$\Delta H = H - H_{real}, H' = H + \Delta H \quad \text{(XI)}$$

The trajectory of next-generation inspection and monitoring architectures has already been examined in previous works.[49,50] Both studies underscore the considerable potential of AI-driven technologies to deliver more robust defect detection and real-time intervention, thereby substantially enhancing the reliability of additive manufacturing processes. Although these strategies have not yet been implemented in the present study, subsequent work will focus on designing and validating the corresponding control mechanisms with the aim of establishing a fully automated closed-loop quality control system.

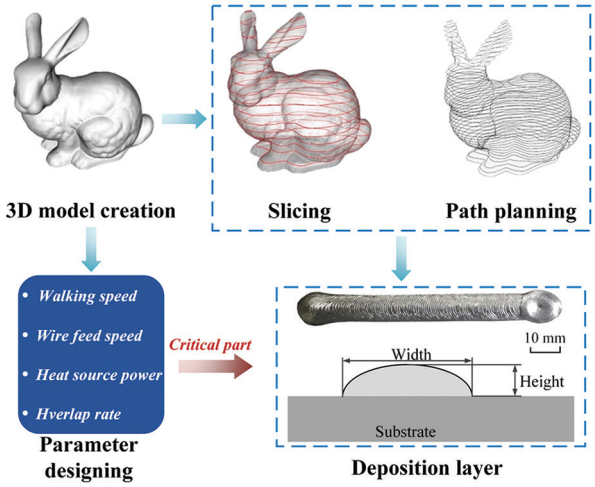

Figure 14. The workflow of path planning

4. Conclusion

In this study, we devised a PSO-driven ensemble regression method, designated PSO-EP, for accurately forecasting weld-bead size in the multiphysics-coupled LAHAM technique. The method leverages PSO to tune the weightings of several base models and, in turn, elevates the aggregate prediction accuracy. The effectiveness of PSO-EP was assessed through extensive comparisons against individual learners (GPR, SVR, ANN, and ELM) and representative ensembles such as averaging, stacking, and ELGA. The findings showed that PSO-EP delivers top-ranked accuracy for predicting both weld-bead width and height.

(1) PSO-EP demonstrated the best performance in weld-bead width prediction, achieving an MAE of 0.1454, an RMSE of 0.1890, and an R^2 of 0.9567; compared with the next-best SVR (R^2 of 0.9510) as well as averaging (R^2 of 0.9373), stacking (R^2 of 0.9246), and ELGA (R^2 of 0.9346), it improved R^2 by 2.07%, 3.47%, and 2.36%, respectively

(2) PSO-EP likewise excelled in predicting weld-bead height, registering an MAE of 0.0505, an RMSE of 0.0571, and an R^2 of 0.9492, substantially surpassing ANN (R^2 of 0.9289), SVR (R^2 of 0.9222), and averaging (R^2 of 0.9387), stacking (R^2 of 0.9378), and ELGA (R^2 of 0.9206), with R^2 gains of 1.12%, 1.22%, and 3.11 %, respectively

(3) SHAP interpretability analysis indicates that weld bead width is primarily influenced by the combined effects of welding speed, wire feed speed, and laser power, whereas weld bead height prediction is driven mainly by laser power and welding speed

(4) Subsequent SHAP threshold analysis uncovered that each process parameter exhibits a threshold above which its influence on weld bead formation can undergo significant shifts in direction or magnitude.

Although the method delivers encouraging results, PSO-EP presently depends on optimizing base model weights within a fixed framework, thereby constraining its flexibility and extensibility. Hence, future studies might explore more self-adaptive or hierarchical ensemble schemes to augment the model's representational capacity and generalization.

Acknowledgments

None.

Funding

This work was financially supported by the CNPC Innovation Foundation (Grant No. 2024DQ02-0306), Innovation and Entrepreneurship Leading Talent Project of Yantai Development Zone in 2022 (Grant No. 2022RC008), Natural Science Foundation of Shandong Province (Grant No. ZR2023QE164), Natural Science Foundation of Qingdao (Grant No. 23-2-1-83-zyyd-jch), and National Natural Science Foundation of China (Grant No. 52405359).

Conflicts of interest

The authors declare no competing interests.

Author's contributions

Conceptualization: Xingwang Bai
Formal analysis: Youheng Fu
Investigation: Boce Xue, Changze Li
Methodology: Kui Zeng
Resource: Yonghui Liu, Yanzhen Zhang
Writing–original draft: Hui Ma, Runsheng Li
Writing–review & editing: Runsheng Li

Ethics approval and consent to participate

Not applicable.

Consent for publication

Not applicable.

Availability of data

Data are available from the corresponding author upon reasonable request.

References

1. Chen X, Fu Y, Kong F, *et al*. An in-process multi-feature data fusion nondestructive testing approach for wire arc additive manufacturing. *Rapid Prototyp J*. 2022;28(3):573-584.

doi: 10.1108/RPJ-02-2021-0034

2. Shi Y, Yan C, Song B, *et al*. Recent advances in additive manufacturing technology: Achievements of the rapid manufacturing center in Huazhong University of science and technology. *Addit Manuf Front*. 2024;3(2):200144.

doi: 10.1016/j.amf.2024.200144

3. Yang Y, Jiang R, Han C, *et al*. Frontiers in laser additive manufacturing technology. *Addit Manuf Front*. 2024;3(4):200160.

doi: 10.1016/j.amf.2024.200160

4. Tan C, Li R, Su J, *et al*. Review on field assisted metal additive manufacturing. *Int J Mach Tools Manuf*. 2023;189:104032.

doi: 10.1016/j.ijmachtools.2023.104032

5. He F, Yuan L, Mu H, *et al*. Research and application of artificial intelligence techniques for wire arc additive manufacturing: A State-of-the-art review. *Robot Comput Integr Manuf*. 2023;82:102525.

doi: 10.1016/j.rcim.2023.102525

6. Qin J, Hu F, Liu Y, *et al*. Research and application of machine learning for additive manufacturing. *Addit Manuf*. 2022;52:102691.

doi: 10.1016/j.addma.2022.102691

7. McNamara K, Ji Y, Lia F, *et al*. Predicting phase transformation kinetics during metal additive manufacturing using non-isothermal Johnson-Mehl-Avrami models: Application to Inconel 718 and Ti-6Al-4V. *Addit Manuf*. 2022;49:102478.

doi: 10.1016/j.addma.2021.102478

8. Kim DO, Lee CM, Kim DH. Determining optimal bead central angle by applying machine learning to wire arc additive manufacturing (WAAM). *Heliyon*. 2024;10(1):e23372.

doi: 10.1016/j.heliyon.2023.e23372

9. Li R, Ju G, Zhao X, *et al*. Simulation of residual stress and distortion evolution in dual-robot collaborative wire-arc additive manufactured Al-Cu alloys. *Virtual Phys Prototyp*. 2024;19(1):e2409390.

doi: 10.1080/17452759.2024.2409390

10. Zhou X, Fang Y, Zhang T, Xiong Z. Retrospective: Advances and opportunities of 3D bioprinting in china over three decades. *Addit Manuf Front*. 2024;3(4):200157.

doi: 10.1016/j.amf.2024.200157

11. Singh S, Sharma SK, Rathod DW. A review on process planning strategies and challenges of WAAM. *Mater Today Proceed*. 2021;47:6564-6575.

doi: 10.1016/j.matpr.2021.02.632

12. Dai F, Zhang S, Li R, Zhang H. Multiaxis wire and arc additive manufacturing for overhangs based on conical substrates. *Rapid Prototy J*. 2022;28(1):126-142.

doi: 10.1108/RPJ-12-2020-0300

13. Sarıkaya M, Başcıl Önler D, Dağlı S, Hartomacıoğlu S, Günay M, Królczyk GM. A review on aluminum alloys produced by wire arc additive manufacturing (WAAM): Applications, benefits, challenges and future trends. *J Mater Res Technol*. 2024;33:5643-5670.

doi: 10.1016/j.jmrt.2024.10.212

14. Tan C, Weng F, Sui S, Chew Y, Bi G. Progress and perspectives in laser additive manufacturing of key aeroengine materials. *Int J Machine Tools Manuf*. 2021;170:103804.

doi: 10.1016/j.ijmachtools.2021.103804

15. Bai JY, Yang CL, Lin SB, Dong BL, Fan CL. Mechanical properties of 2219-Al components produced by additive manufacturing with TIG. *Int J Adv Manuf Technol*. 2016;86(1):479-485.

doi: 10.1007/s00170-015-8168-x

16. Gu J, Ding J, Williams SW, Gu H, Ma P, Zhai Y. The effect of inter-layer cold working and post-deposition heat treatment on porosity in additively manufactured aluminum alloys. *J Mater Process Technol*. 2016;230:26-34.

doi: 10.1016/j.jmatprotec.2015.11.006

17. Wang Z, Xufei L, Xin L, *et al*. Porosity control and properties improvement of Al-Cu alloys via solidification condition optimisation in wire and arc additive manufacturing. *Virtual Phys Prototyp*. 2024;19(1):e2414408.

doi: 10.1080/17452759.2024.2414408

18. Pardal G, Martina F, Williams S. Laser stabilization of GMAW additive manufacturing of Ti-6Al-4V components. *J Mater Process Technol*. 2019;272:1-8.

doi: 10.1016/j.jmatprotec.2019.04.036

19. Li R, Wang R, Zhou X, *et al*. Microstructure and mechanical properties of 2319 aluminum alloy deposited by laser and cold metal transfer hybrid additive manufacturing. *J Mater Res Technol*. 2023;26:6342-6355.

doi: 10.1016/j.jmrt.2023.08.312

20. Yu A, Pan Y, Wan F, Sun G, Zhang J, Lu X. Rapid accomplishment of cost-effective and macro-defect-free LPBF-processed Ti parts based on deep data augmentation. *J Manuf Process*. 2024;120:1023-1034.

doi: 10.1016/j.jmapro.2024.05.003

21. Zhu D, Zhu H, Liu X, *et al*. CREDO: Efficient and privacy-preserving multi-level medical pre-diagnosis based on ML-KNN. *Inform Sci*. 2020;514:244-262.

doi: 10.1016/j.ins.2019.11.041

22. Headley CV, Herrera Del Valle RJ, Ma J, *et al*. The development of an augmented machine learning approach for the additive manufacturing of thermoelectric materials. *J Manuf Process*. 2024;116:165-175.

doi: 10.1016/j.jmapro.2024.02.045

23. Phua A, Cook PS, Davies CHJ, Delaney GW. Smart recoating: A digital twin framework for optimisation and control of powder spreading in metal additive manufacturing. *J Manuf Process*. 2023;99:382-391.

doi: 10.1016/j.jmapro.2023.04.062

24. Kwak J, Lee Y, Choi M, Lee S. Deep learning based approaches to enhance energy efficiency in autonomous driving systems. *Energy*. 2024;307:132625.

doi: 10.1016/j.energy.2024.132625

25. Delhaes JM, Vieira ACL, Oliveira MD. Natural language processing for participatory corporate foresight: The participant input analyzer for identifying biases and fallacies. *Technol Forecast Soc Change*. 2024;209:123652.

doi: 10.1016/j.techfore.2024.123652

26. Ling HB, Huang D, Cui J, Wang CD. HOLT-Net: Detecting smokers via human-object interaction with lite transformer network. *Eng Appl Artif Intell*. 2023;126:106919.

doi: 10.1016/j.engappai.2023.106919

27. Le-Hong T, Lin PC, Chen JZ, Pham TDQ, Van Tran X. Data-driven models for predictions of geometric characteristics of bead fabricated by selective laser melting. *J Intell Manuf*. 2023;34(3):1241-1257.

doi: 10.1007/s10845-021-01845-5

28. Zhu X, Jiang F, Guo C, Wang Z, Dong T, Li H. Prediction of melt pool shape in additive manufacturing based on machine learning methods. *Optics Laser Technol*. 2023;159:108964.

doi: 10.1016/j.optlastec.2022.108964

29. Liu S, Brice C, Zhang X. Interrelated process-geometry-microstructure relationships for wire-feed laser additive manufacturing. *Mater Today Commun*. 2022;31:103794.

doi: 10.1016/j.mtcomm.2022.103794

30. Xia C, Pan Z, Polden J, Li H, Xu Y, Chen S. Modelling and prediction of surface roughness in wire arc additive manufacturing using machine learning. *J Intell Manuf*. 2022;33(5):1467-1482.

doi: 10.1007/s10845-020-01725-4

31. Oh WJ, Lee CM, Kim DH. Prediction of deposition bead geometry in wire arc additive manufacturing using machine learning. *J Mater Res Technol*. 2022;20:4283-4296.

doi: 10.1016/j.jmrt.2022.08.154

32. Šket K, Brezočnik M, Karner T, *et al*. Predictive modelling of weld bead geometry in wire arc additive manufacturing. *J Manuf Mater Process*. 2025;9(2):67.

doi: 10.3390/jmmp9020067

33. Ren Y, Zhang L, Suganthan PN. Ensemble classification and regression-recent developments, applications and future directions [review article]. *IEEE Comput Intell Mag*. 2016;11(1):41-53.

doi: 10.1109/MCI.2015.2471235

34. Huang W, Chen S, Xiao J, Jiang X, Jia Y. Laser wire-feed metal additive manufacturing of the al alloy. *Optics Laser Technol*. 2021;134:106627.

doi: 10.1016/j.optlastec.2020.106627

35. Shukla P, Chitral S, Kumar T, Kiran DV. The influence of GMAW correction parameters on stabilizing the deposition characteristics for wire arc additive manufacturing. *J Manuf Process*. 2023;90:54-68.

doi: 10.1016/j.jmapro.2023.01.075

36. Gong M, Zhang S, Lu Y, Wang D, Gao M. Effects of laser power on texture evolution and mechanical properties of laser-arc hybrid additive manufacturing. *Addit Manuf*. 2021;46:102201.

doi: 10.1016/j.addma.2021.102201

37. Ferreira SLC, Bruns RE, Ferreira HS, *et al*. Box-Behnken design: An alternative for the optimization of analytical methods. *Anal Chim Acta*. 2007;597(2):179-186.

doi: 10.1016/j.aca.2007.07.011

38. Fang X, Ren C, Zhang L, Wang C, Huang K, Lu B. A model of bead size based on the dynamic response of CMT-based wire and arc additive manufacturing process parameters. *Rapid Prototy J*. 2021;27(4):741-753.

doi: 10.1108/RPJ-03-2020-0051

39. Brown CE. Coefficient of variation. In: Brown CE, editor. *Applied Multivariate Statistics in Geohydrology and Related Sciences*. Berlin: Springer Berlin Heidelberg; 1998. p. 155-157.

doi: 10.1007/978-3-642-80328-4

40. Burdick RK, Borror CM, Montgomery DC. A review of methods for measurement systems capability analysis. *J Q Technol*. 2003;35(4):342-354.

doi: 10.1080/00224065.2003.11980232

41. Kennedy J, Eberhart R. *Particle Swarm Optimization*. Vol. 4. United States: IEEE; 1995. p. 1942-1948.

doi: 10.1109/ICNN.1995.488968

42. Huang GB, Zhu QY, Siew CK. Extreme learning machine: Theory and applications. *Neurocomputing*. 2006;70(1): 489-501.

doi: 10.1016/j.neucom.2005.12.126

43. Awad M, Khanna R. Support vector regression. In: Awad M, Khanna R, editors. *Efficient Learning Machines: Theories, Concepts, and Applications for Engineers and System Designers*. New York: Apress; 2015. p. 67-80.

doi: 10.1007/978-1-4302-5990-9

44. Schulz E, Speekenbrink M, Krause A. A tutorial on Gaussian

process regression: Modelling, exploring, and exploiting functions. *J Math Psychol*. 2018;85:1-16.

doi: 10.1016/j.jmp.2018.03.001

45. Shapley LS. Quota solutions of n-person games. In: Harold William K, Albert William T, editors. *Contributions to the Theory of Games*. Vol. 2. United States: Princeton University Press; 1953. p. 343-360.

46. Liu CA, Kuo BS. Model averaging in predictive regressions. *Econom J*. 2016;19(2):203-231.

doi: 10.1111/ectj.12063

47. Mu G, Wei Q, Xu Y, Zhang H, Zhang J, Li Q. Capacity estimation for lithium-ion batteries based on heterogeneous stacking model with feature fusion. *Energy*. 2024;313:133881.

doi: 10.1016/j.energy.2024.133881

48. Wang R, Cheng MN, Loh YM, Wang C, Fai Cheung C. Ensemble learning with a genetic algorithm for surface roughness prediction in multi-jet polishing. *Exp Syst Appl*. 2022;207:118024.

doi: 10.1016/j.eswa.2022.118024

49. Chung J, Shen B, Kong ZJ. Anomaly detection in additive manufacturing processes using supervised classification with imbalanced sensor data based on generative adversarial network. *J Intell Manuf*. 2024;35(5):2387-2406.

doi: 10.1007/s10845-023-02163-8

50. Chua C, Liu Y, Williams RJ, Chua CK, Sing SL. In-process and post-process strategies for part quality assessment in metal powder bed fusion: A review. *J Manuf Syst*. 2024;73:75-105.

doi: 10.1016/j.jmsy.2024.01.004

ACCSCIENCE PUBLISHING

Materials Science in Additive Manufacturing

ORIGINAL RESEARCH ARTICLE

Gaussian process-based interpretable prediction of melt track morphology through melt pool in additive manufacturing

Xin Lin[1], Shilin Liu[1], Haodong Chen[1], Jinrong Mao[1], and Kunpeng Zhu[1,2]*

[1]Precision Manufacturing Institute, Wuhan University of Science and Technology, Wuhan, Hubei, China

[2]Institute of Intelligent Machines, Hefei Institutes of Physical Science, Chinese Academy of Sciences, Hefei, Anhui, China

(This article belongs to the *Special Issue: Smart Additive Manufacturing: Product and Process Qualification through Innovation in Design, Modeling, Monitoring, Machine Learning, Metrology, and Materials Science*)

Abstract

Melt track monitoring in the laser powder bed fusion (LPBF) process is crucial for preventing internal defects in as-printed parts. Uncontrollable melt pool dynamic behavior easily leads to melt track morphology defects. Existing monitoring methods face challenges in balancing modeling accuracy and physical interpretability. Specifically, traditional physics-based models typically require complex monitoring equipment, extensive simulation data, and empirical formulas, resulting in high costs and limited applicability. Meanwhile, conventional data-driven models lack physical constraints, leading to insufficient interpretability, process parameter sensitivity, and poor generalization. To address these challenges, this article proposes a deep Gaussian process-based method for LPBF melt track morphology prediction. The proposed model employs kernel functions in the first layer to learn melt pool evolution patterns and embeds the Rosenthal equation into the second-layer kernel function as a physical constraint, constructing a physically interpretable multilayer Gaussian process framework. Finally, a softmax classifier based on melt track geometric deviation achieves five-category melt track morphology recognition. Multi-condition experimental results demonstrated that the proposed method achieved root mean square errors of 0.069, 0.020, and 0.039 for melt track geometry, outperforming traditional data-driven models in prediction accuracy. The classification accuracy reached 90.76%. Furthermore, the influence of different features on melt track morphology is quantified through time-lagged mutual information analysis and other visualization methods. This study provides an effective solution for achieving quality monitoring and defect prediction in the LPBF process.

Keywords: Laser powder bed fusion; Deep Gaussian process; Morphology prediction; Physical constraint; Melt pool monitoring

***Corresponding author:**
Kunpeng Zhu
(zhukp@iamt.ac.cn)

Citation: Lin X, Liu S, Chen H, Mao J, Zhu K. Gaussian process-based interpretable prediction of melt track morphology through melt pool in additive manufacturing. *Mater Sci Add Manuf.* 2025;4(3):025200030. doi: 10.36922/MSAM025200030

Received: May 12, 2025

Revised: June 5, 2025

Accepted: June 8, 2025

Published online: July 17, 2025

1. Introduction

Additive manufacturing (AM) technology has made remarkable developments in the manufacturing field in recent years and is an innovative approach that surpassed

traditional manufacturing methods. However, the complex changes in the AM process, such as heat transfer, melting, and solidification processes,[1] are prone to cause defects, such as holes, cracks, and unfused parts, limiting the reliability of AM technology in production applications. To address this issue, the introduction of remote and *in situ* monitoring techniques is critical. By continuously monitoring the manufacturing process, tracking key physical phenomena during fusion, and analyzing real-time data from various sensors, this approach enabled the detection of defects before they become hidden beneath subsequent layers.[2-5]

At present, AM process monitoring primarily relies on analyzing in-process sensor data through data modeling, using machine learning and deep learning to detect specific defect occurrences. For example, Khanzadeh *et al.*[6,7] analyzed the thermal distribution characteristics of the melt pool and successfully predicted both pore locations in Ti-6Al-4V alloy parts and geometric deviations in the Fast Fourier Transform process using self-organizing mapping (an unsupervised learning algorithm); they also investigated the influence of process parameters on geometric accuracy. Scime *et al.*[8] classified the types of anomalies in the melt track into six categories and proposed a monitoring algorithm based on machine learning and computer vision, which was successfully used for *post hoc* quality analysis of components. Okaro *et al.*[9] applied binary labels to a small data subset based on defect severity and developed a semi-supervised model using process data with singular value decomposition and Gaussian mixture models. This approach achieved classification performance comparable to fully supervised methods. Yuan *et al.*[10,11] proposed a two-round image processing and height map analysis algorithm to predict and identify laser printing track width and continuity in video datasets. Their approach considered the characteristics of diverse data and addressed labeling difficulties using semi-supervised learning. Mojahed Yazdi *et al.*[12] designed a deep neural network model that utilizes the spatial feature image of regions of interest (ROI) to detect and locate defects. This method achieved significantly higher defect detection rates than traditional machine learning approaches. Lopez *et al.*[13] focused more on quantifying model uncertainty. They explored melt pool width prediction by considering uncertainties arising from thermal modeling assumptions, unknown simulation data, numerical approximations, and calibration data. While these studies leverage the power of machine learning and deep learning to establish complex mapping relationships between monitoring data and melt track geometry, such prediction methods often lack physical interpretability. In addition, they can be highly sensitive to experimental parameters and exhibit limited generalization ability.

In recent years, more researchers explored combining physical models with data models to improve the performance and generalization ability of the models by adding physical constraints. For example, Mahmoudi *et al.*[14] proposed an anomaly detection system that integrated melt pool and phase field models. Utilizing high-speed thermal imaging, spatial statistics, and machine learning, their approach achieved only a 5% average error in melt track width prediction. Gaikwad *et al.*[15] obtained the physical characteristics of the melt pool by utilizing different sensors, such as high-speed cameras and thermocouples, and employed neural networks to predict melt pool patterns, process parameters, melt track width, and melt track continuity. Guo *et al.*[16] established a mathematical melt pool morphology model by fitting key coefficients through extensive experiments. Their model accounts for physical mechanisms, including mass conversion, heat exchange, and temperature fields, thereby controlling average prediction errors for melt pool dimensions (length/width/depth) to 12%. Zhang *et al.*[17] fused melt pool spatial-physical information through coaxial/off-axis dual detection systems. Using long short-term memory networks, they correlated the melt pool temperature with melt track surface morphology, achieving up to 92.87% accuracy. These researchers obtained multimodal data through a large number of experiments and a variety of high-precision sensors and realized the identification of melt pool geometry and anomalous states by combining physical processes.

Based on these findings, traditional physical models incur high experimental costs due to complex monitoring equipment, extensive simulation data, and empirical formulas. Conversely, traditional data-driven models lack physical constraints, exhibit high sensitivity to process parameters, and are susceptible to noise interference. To address these limitations, we propose a melt track morphology prediction model based on deep Gaussian processes (DGPs) with embedded physical constraints. DGPs are a multilayer generalization of Gaussian processes (GPs),[18] where each layer is an independent GP. Compared to single-layer GPs, DGPs overcome the limited expressiveness of the kernel function and also maintain the flexibility, overfitting resistance, and good prediction uncertainty of the GP model. In this study, the experimentally observed melt pool geometric feature data were used as model inputs, with physical model constraints added to the data-driven DGP model to guide physical information to the data model. This approach enables the prediction of geometric features of the melt track and the classification of the morphology of the melt track under different processing conditions using a softmax classification model. The structure of the proposed model is displayed in Figure 1.

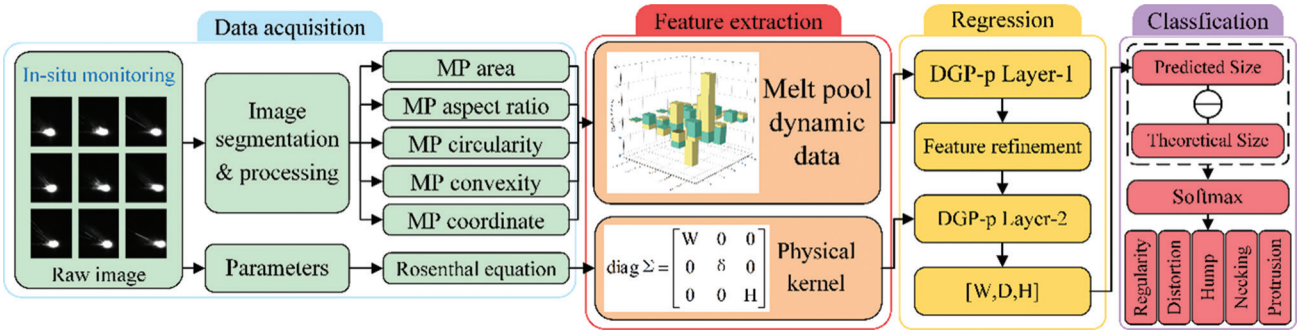

Figure 1. Geometric prediction and morphology classification model of the melt track based on DGP and softmax
Abbreviations: MP: Melt pool; DGP-p: DGP model using physical kernel; W: Melt track width; δ: Small perturbation; H: Melt track height

2. Experiment and methods

2.1. Experimental setup

In this study, the laser powder bed fusion (LPBF) system was set up based on existing LPBF equipment for modification, incorporating high-speed cameras, zoom lenses, and other auxiliary monitoring equipment. The high-speed monitoring system was mounted on the side axis to avoid interference from the laser shielding glass on the molding chamber door, which could affect the imaging results (Figure 2). The laser spot radius of the LPBF equipment was 0.05 mm. The sampling frame rate (FR) of the high-speed camera was calculated to be 10,600 fps using Equation I based on a maximum scanning speed of 1,060 mm/s. The sampling FR was set to 10,000 fps instead of the calculated 10,600 fps for the convenience of calculation.

$$FR = \frac{V}{2r} \quad \text{(I)}$$

Where V denotes the laser scanning speed (mm/s) and r denotes the laser spot radius (mm).

In this experiment, 316L stainless steel powder (particle size: 15 – 45 μm) was uniformly coated on a substrate, whose base material was also 316L stainless steel, using a squeegee, with the layer thickness set to 0.04 mm and the scanning length set to 3 mm. The experimental protocol included five types of laser power (140, 190, 240, 290, and 340 W) and five types of scanning speeds (0.66, 0.76, 0.86, 0.96, and 1.06 m/s), totaling 25 combinations.[19,20] We collected a total of 932 samples.

Figure 3 illustrates the specific distribution of melt track morphology, which was then oversampled by a factor of 2 using the Synthetic Minority Oversampling Technique (SMOTE) during classification prediction due to the significant imbalance in the defect categories.

According to the high-speed camera FR f = 10000 fps and the melt track length L_{total} = 3 mm, for different

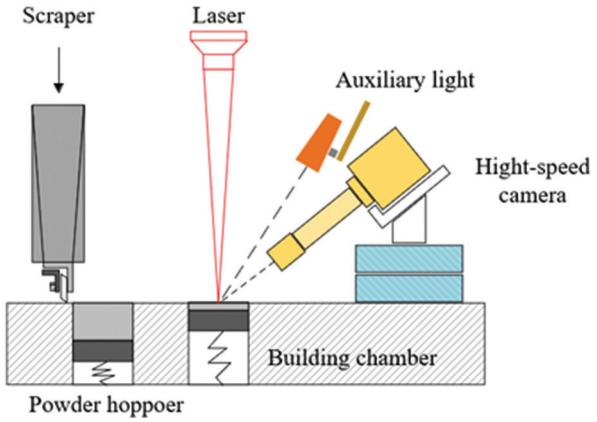

Figure 2. Schematic diagram of the axis monitoring system next to the melt pool

laser scanning speeds v (m/s), the number of melt pool pictures $n = f. L_{total}/v$ was generated, and the corresponding melt track would be sliced in equal portions according to n. The average width of the segment, W_{mean}, average deviation D_{mean}, and average height H_{mean} were obtained by sampling each slice using 7/10n (rounded) points. The schematic diagram for extracting the respective melt track characteristics is presented in Figure 4. The data were retained to two decimal places.

The DGP regression model and softmax classifier were applied to 25 datasets – 3 datasets served as the test set and 22 datasets served as the training set – to establish the relationship between the melt pool geometric features, process parameters, and melt track features, as well as to predict the melt track geometric features and the morphology category. Since a small sample dataset was used, the results of dataset division accounted for a large influence on the model performance. Finally, the dataset was split into an 18:4:3 ratio – 18 datasets were used for model training, 4 datasets served as the validation set, and 3 datasets (240 W-660 mm/s, 290 W-760 mm/s, and 340 W-960 mm/s) were randomly selected as the test sets.

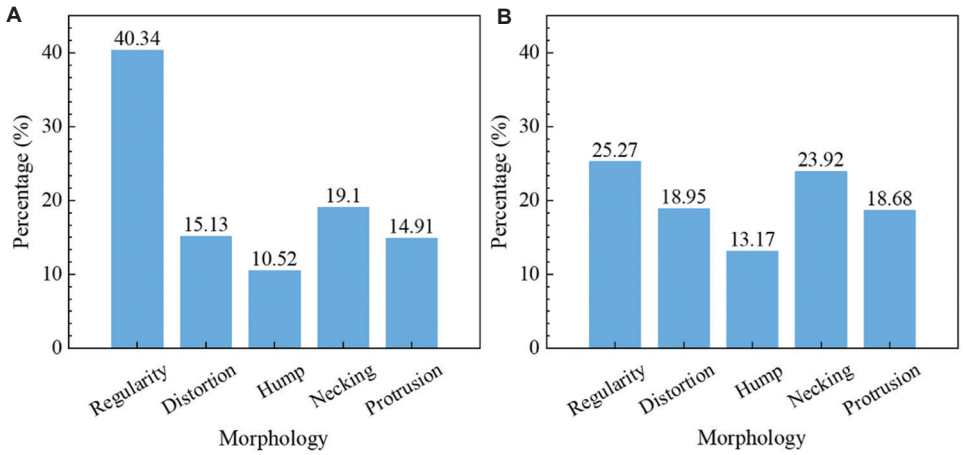

Figure 3. Category distribution: (A) without oversampling, and (B) with oversampling

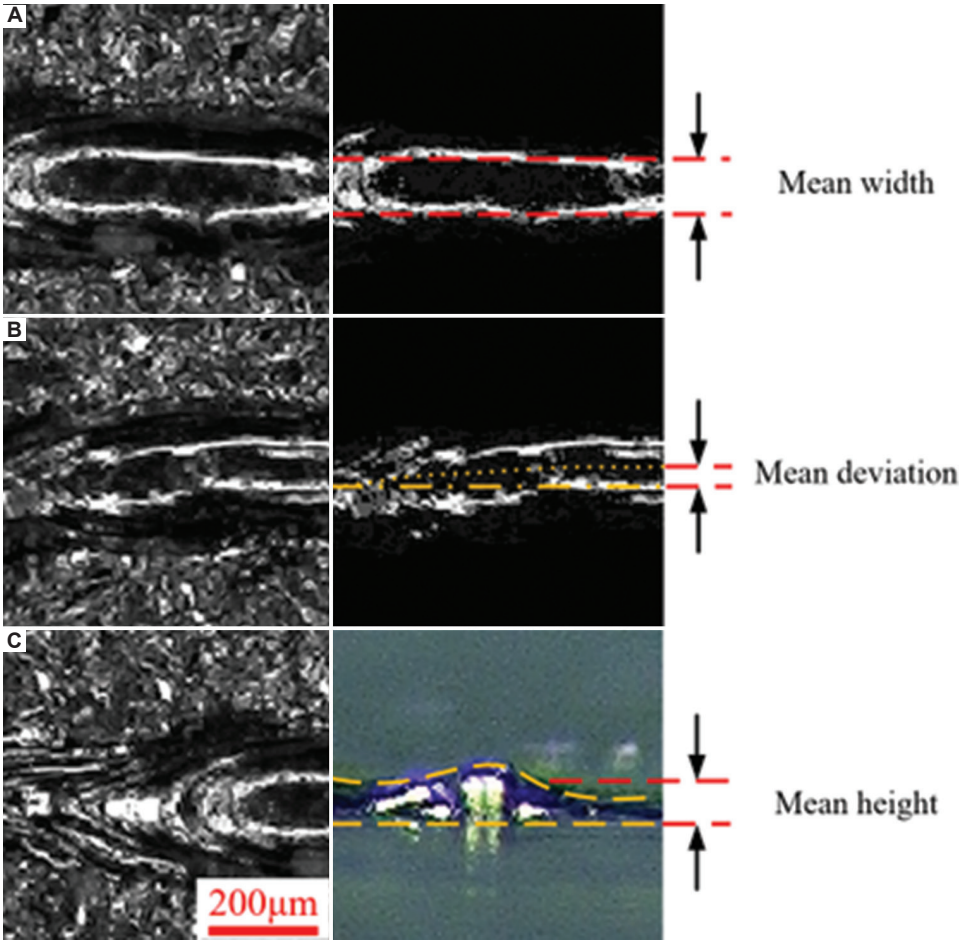

Figure 4. Extraction of melt track features: (A) mean width, (B) mean deviation, and (C) mean height. Scale bar: 200 μm

2.2. Defects in the melt track

In the LPBF process, the flow state of the melt has a great influence on the shape of the melt pool.Numerous studies have established a clear relationship between melt pool characteristics and various types of defects.[21] Drastic changes

in the melt pool can lead to defects in the trajectories. Five types of trajectory characteristics—regularity, distortion, hump, necking, and protrusion—were identified in the experiments, and their morphologies are displayed in Figure 5.

Figure 5A displays a regularity-shaped melt track, characterized by continuous edges that do not deviate from the preset scanning path and are symmetrical along the centerline of the scanning trajectory. Figure 5B features a distortion-shaped melt track,[22] which usually has continuous edges, but the center of the melt track deviates from the pre-defined scanning path, probably due to the Marangoni effect that distorts the trajectory. Figure 5C presents a hump-shaped melt track,[23] which usually has different thicknesses due to bulging. This is associated with the Plateau-Rayleigh (P-R) instability generated by the pressure difference acting on the surface of the melt pool.[24] Figure 5D illustrates a melt track with necking-shaped morphology,[25] characterized by a contraction in width or even the appearance of breakpoints – a phenomenon that is also believed to be caused by cylindrical fluid jets. Figure 5E features a protrusion-shaped melt track,[26] often accompanied by a sudden increase in width, forming an angular lateral bulge – a phenomenon that is usually attributed to high surface tension melt pools and the Marangoni effect.[27]

2.3. Data processing

High surface tension makes the melt pool surface unstable, which can easily lead to melt rupture. The Marangoni effect induces the melt to flow from the high-temperature region to the low-temperature region, leading to metal splashing from the surface of the melt pool. When the surface of the melt pool is disturbed by the expansion, the P-R instability makes the surface of the melt pool protrude, which leads to the splitting of the melt and the splashing of the melt. The combined effect of these factors on the melt pool leads to drastic changes in the morphology of the melt pool, thus increasing the risk of defects.[28,29]

To fully characterize the melt pool geometry, quantitative analysis was performed by extracting geometrical parameters, such as aspect ratio, roundness, and convex defects of the melt pool. During the LPBF process, images captured by the high-speed camera in the side-axis monitoring system are subject to interference from intense metal powder splatter, plasma plumes, and substrate surface reflections. To address this, the ROI method was first applied to identify the maximum connected region (128 × 128 pixels) with grayscale values exceeding 200. This approach effectively eliminates most splatter interference while preserving the integrity of the melt pool morphology. Second, the k-means segmentation method (segmentation category: 7; i.e., the category with the largest sum of pixel values) was used to remove the plume, proximity powder splash, and metal material arc light, among other parameters. The large particle droplet splash and the melt pool were then separated by the kernel operation (kernel size: 5). Connectivity domain analysis was then used to select the largest area to obtain the main body of the melt pool. According to the main body, the area s_m, perimeter p_m, convexity defect t_m, length l_m, width w_m, and center of mass coordinates x,y of the melt pool were calculated, and the flow is displayed in Figure 6. The input features $x_m = [s_m, ar_m, c_m, t_m, y]$ of the melt pool were obtained based on Equations II and III.

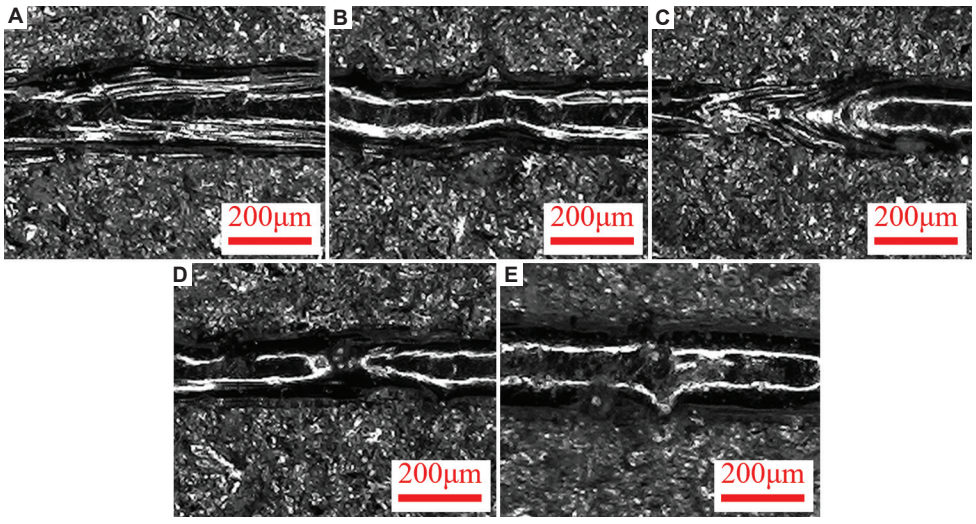

Figure 5. Five different types of melt track morphology in laser powder bed fusion: (A) regularity, (B) distortion, (C) hump, (D) necking, and (E) protrusion. Scale bar: 200 μm

$$ar_m = l_m / w_m \quad \text{(II)}$$

$$c_m = 4\pi s_m / p_m \quad \text{(III)}$$

The oscillatory motion of the melt pool is induced by the combined effects of thermocapillary force, recoil pressure, and surface tension.[30] After extracting the shape characteristics of the melt pool, the characteristic difference between the melt pool at the experimentally observed melt track defects and the neighboring time steps was calculated for the melt pool using Equation IV.

$$\begin{cases} \Delta_m^t = (x_m^t - x_m^{t-1}) / x_m^t \\ \Delta_m^{t+1} = (x_m^t - x_m^{t+1}) / x_m^t \end{cases} \quad \text{(IV)}$$

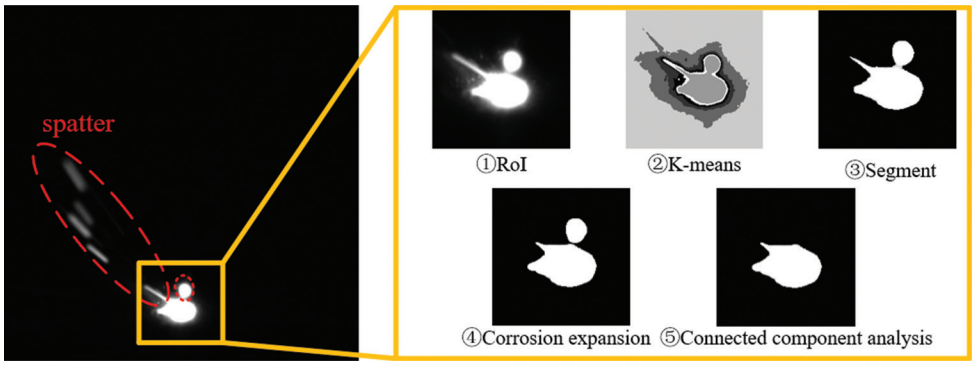

Figure 6. Extraction of melt pool features
Abbreviation: ROI: Region of interest

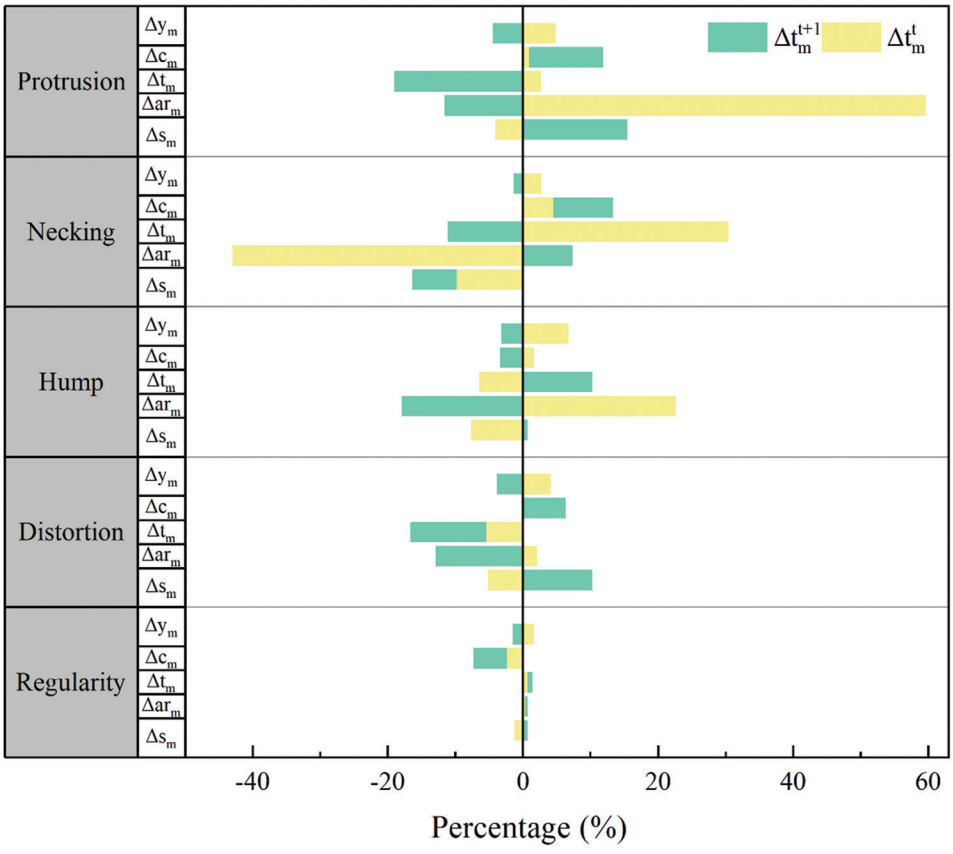

Figure 7. Changes in melt pool characteristics
Abbreviations: y_m: Y-coordinate of the melt pool centroid; c_m: Roundness of the melt pool; t_m: Convex defects in the melt pool; ar_m: The aspect ratio of the melt pool; s_m: The area of the melt pool

The statistical results are presented in Figure 7.

From Figure 8, it can be seen that the regular morphology has stable geometric features, corresponding to a small change in the geometric features of the melt pool. For melt track defects involving width distortion, such as necking and protrusion, the melt pool morphology exhibits distinct changes. During necking, the melt pool area and aspect ratio decrease significantly. Conversely, during protrusion, the melt pool area, aspect ratio, and convexity increase significantly. Therefore, the melt track width may be determined by a combination of the melt pool area, aspect ratio, and convex defects.

For defects in which the melt track deviates from the preset scanning path (i.e., distorted morphology), the area of the melt pool and the y-axis coordinates of the center of mass change significantly, and the extent of the deviation of the melt track may be jointly determined by the area of the melt pool and the y-axis coordinates of the center of mass.

For defects with distortion in the height of the melt track (i.e., hump shape), the area of the melt pool decreases and the aspect ratio increases. The upward shift of the center of mass of the melt pool indicates an increase in the height of the melt track, which may be due to the limitation of the viewing angle of the monitoring equipment. The change in the area and width of the actual melt pool needs to be further verified.

2.4. Melt track theory model

Existing studies[31-34] on 316L, Ti-6Al-4V, and Inconel718 materials have consistently demonstrated that powder bed coverage has no significant effect on melt pool width. Guo *et al.*[16] also verified that, in the case of ignoring the random spattering and flaking of powder, it can be assumed that the powder consumption width and the melt track width are approximately equal. Therefore, this study assumes that the powder consumption width is equal to the theoretical track width.

Assuming that the upper profile curve of the melt track above the substrate surface is bow-shaped (Figure 9A), for points on the curve (x_0,y_0) to meet the center of the circle $(0,y_R)$, the radius R[35,36] can be expressed as Equation V.

$$x_o^2 + (y_o - y_R)^2 = R^2 \quad \text{(V)}$$

Based on the conservation of mass, Equation VI is derived. Similarly, based on the bowing geometry, a relationship can be derived between the width W, radius R, height H, and the bowing area (Equations VII and VIII).

$$\rho_{powder}\, LWL_{track} = \rho LA_{track} \quad \text{(VI)}$$

$$W = 2\sqrt{2RH - H^2} \quad \text{(VII)}$$

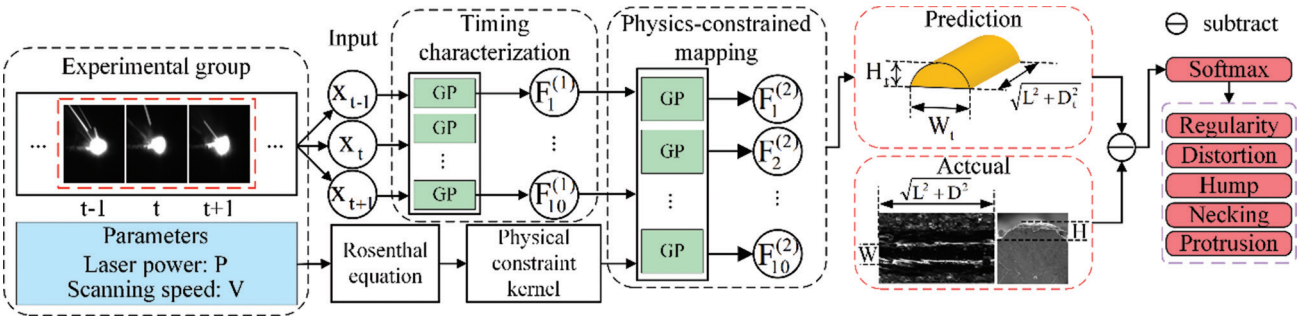

Figure 8. The deep Gaussian process DGP model using the physical kernel (DGP-p) model

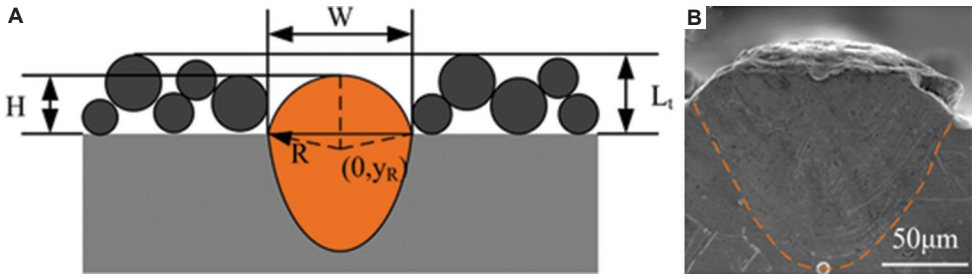

Figure 9. Shape of melt track. (A) Schematic diagram of theoretical melt track. (B) Image of actual melt track
Abbreviations: H: melt track height; W: Melt track width; L_t: Powder layer thickness; R: Radius of the circular contour on the melt track's upper surface; y_R: Y-coordinate of the center point of the melt track's upper surface contour

$$A_{track} = R^2 \arccos\left(\frac{R-H}{R}\right) - (R-H)\sqrt{2RH-H^2} \quad \text{(VIII)}$$

Where W and H denote the width and height of the melt track; R denotes the radius of the bowls; A_{track} denotes the area of the upper half of the melt track; ρ_{powder} and ρ denote the powder material density and single-pass material density, respectively; L_{track} denotes the layer thickness; and L, W, and H denote the length, width, and height of the upper partial melt track.

In this study, the powder's stacking density was assumed to be 50%; that is, ρ_{powder} = 50% ρ, where ρ is the material density, which is taken as 7,800 kg/m^3.

By substituting Equation VII into Equation VI and associating it with Equation VIII, Equation IX is obtained.

$$0.5WL_{track} = \left(\frac{W^2+4H^2}{8H}\right)^2 \arccos\left(1-\frac{8H^2}{W^2+4H^2}\right) - \left(\frac{W^2+4H^2}{8H}-H\right)\frac{W}{2} \quad \text{(IX)}$$

Using Halley's iterative method, the melt track height H can be solved. However, for the melt track width W, it has been indicated that the effect of laser radius on the melt track width is negligible.[16] The width of the melt track based on the formation of the melt track by the steady-state melt pool can be expressed as Equation X.

$$\xi P = 2\pi k(T_f - T_0)W + 0.1 \bullet e\pi\rho C\,(T_f - T_0)\,VW^2 \quad \text{(X)}$$

Where the powder absorption rate ξ is taken as 0.35; P is the laser power; π is the circumference; the thermal conductivity k is taken as 14 W/m K; the initial temperature T_0 is taken as 300 K; the melting temperature T_f of the powder is taken as 1700 K; e is a natural constant; the specific heat capacity C is taken as 683 J/kg K; and V is the laser scanning speed.

Similarly, the theoretical volume of the melt track *Vol* is expressed in Equation XI.

$$Vol = \left(\frac{\pi W^2}{4} - \frac{1}{2}WH\right)L \quad \text{(XI)}$$

2.5. DGP-p-based melt track size prediction and morphology classification

DGPs have a powerful non-linear learning capability, with a network structure that consists of an input layer, a hidden layer, and an output layer (Figure 8).

For the melt pool, the geometric feature vector $x_m = [s_m, ar_m, c_m, t_m, y]$ at time t is normalized based on the melt pool features of the neighboring moments. The feature matrix $X_t = [x_m^{t-1}, x_m^t, x_m^{t+1}]^T$ is formed as the input, while the hidden layer is defined by the melt track features $Y_t = [W_t, D_t, H_t]$. The process flow is displayed in Figure 8. Due to the general complexity of the experimental data in this study, a two-layer DGP model was used, containing the following core layers:

(i) Melt pool periodic feature extraction layer (first layer): For the melt pool data of the same test set, 10 independent GPs – each using the Gaussian cosine composite kernel function – were used two-by-two to learn the characteristic fluctuations of different frequencies. For the input of melt pool time series data X_t, the output $F_i^{(1)}(X_t)$ of the ith GP obeys the following distribution (Equation XII).

$$F_i^{(1)} \sim GP\left(\mu_i^{(1)}(X_t), K^{(1)}(X_t, X_t')\right),\ i = 1,\ldots,10 \quad \text{(XII)}$$

The work of Salimbeni *et al.*[37] also indicated that the linear mean function predicts better than the constant mean function, and the computational overhead is less than that of the non-linear mean function; hence, each GP mean function $\mu_i^{(j)}(X)$ is in linear form (Equation XIII).

$$\mu_i^{(1)}(x_m) = a_i^T x_m,\ i = 1,\ldots,10 \quad \text{(XIII)}$$

Where $K^{(1)}(X_t, X_t')$ is expressed as in Equation XIV.

$$K^{(1)}(X_t, X_t') = \sigma_i^2 exp\left(-\frac{X_t - X_t'^2}{2l_i^2}\right) \cdot cos\left(\frac{2\pi X_t - X_t'}{T_i}\right),\ i = 1,\ldots,10\# \quad \text{(XIV)}$$

Where σ_i^2 is used to control the amplitude of the output of the kernel function, l_i^2 is used to control the smoothness of the kernel, and T_i defines the periodicity of the function.

(ii) Melt track geometric feature mapping layer (second layer): This layer maps the periodic feature $F^{(1)}$ output from the first layer to the melt track geometric feature $F^{(2)}$ through six GPs. Each GP uses the Matérn kernel employing physical constraints, and for the jth GP, the output $F_j^{(2)}(x)$ obeys the following distribution (Equations XV and XVI).

$$F_j^{(2)} \sim GP\left(\mu_j^{(2)}(F^{(1)}), K^{(2)}(F^{(1)}, F^{(1)'})\right),\ j = 1,\ldots,6 \quad \text{(XV)}$$

$$K^{(2)}(F^{(1)}, F^{(1)'}) = \sigma_m^2 \exp(-\frac{1}{2}(F^{(1)} - F^{(1)'})^T £^{-1}(F^{(1)} - F^{(1)'})) \quad \text{(XVI)}$$

Where σ_m^2 is the magnitude, Σ = diag ([W^2, δ, H^2]), and δ is a small perturbation term to prevent the theory from deviating from 0 and causing numerical instability.

Finally, the geometrical parameter $Y_t = \sum_{j=1}^{6} w_j K_j^{(2)}\left(F^{(1)}, F^{(1)'}\right)$ of the output melt track of the second layer.

The DGP-p model in this study was trained using variational inference combined with stochastic gradient descent. Unlike traditional GP, the multilayer structure of DGP limits the direct computation of the exact posterior distribution. Hence, the variational inference was used to approximate the posterior distribution. The objective function of the model is the evidence lower bound (ELBO).

$$L(\theta) = E_q\left[logp(y \mid F^{(2)})\right] - KL\left[q\left(F^{(1)}\right) \| p(F^{(1)} \mid X_t)\right] - KL\left[q\left(F^{(2)} \mid F^{(1)}\right) \| p(F^{(2)} \mid F^{(1)})\right] \quad \text{(XVII)}$$

Where θ denotes the model learnable parameter.

θ is all learnable parameters.

E_q $[logp(y|F^{(2)})]$ is the expected log-likelihood of y with given $F^{(2)}$.

$q(F^{(1)})$ isthe variational distribution of hidden variables in the first layer.

$q(F^{(2)}/F^{(1)})$ is the conditional variational distribution of second-layer hidden variables given $F^{(1)}$.

$p(F^{(1)}|X_t)$ is the conditional prior distribution of the first-layer latent variable given the input X_t

$p(F^{(2)}|F^{(1)})$ is the conditional prior distribution of the second-layer latent variable given $F^{(1)}$.

KL(·): This function means kullback-leibler divergence.

We using Equation XVII as the loss equation to train the model.

In the optimization process, the Adam optimizer was used for gradient updating. The initial learning rate was set to 0.01, and an exponential decay strategy was used, where the learning rate was decayed to 0.9 times the original rate at every 50 rounds of iterations. To avoid local optima, an early stopping strategy was implemented during training, halting the process when the validation loss fails to improve over 10 consecutive epochs.

After obtaining the predicted melt track geometric features [W_t, D_t, H_t] from the melt pool features, the deviation of the predicted melt track volume Vol_t from the ideal volume V was calculated using Equation XVIII.

$$\Delta V = Vol_t - Vol = \left(\frac{\pi W_t^2}{4} - \frac{1}{2} W_t H_t\right)\sqrt{L^2 + (D_t - D_{t-1})^2} - V \quad \text{(XVIII)}$$

Where L_v is the corresponding track length of the melt pool under different laser scanning speeds.

The deviation characteristics were determined by synthesizing the predicted deviations of track width, height, and position (Equations XIX-XXII).

$$\Delta = [\Delta V, \Delta W, \Delta D, \Delta H] \quad \text{(XIX)}$$

$$\Delta W = W_t - W \quad \text{(XX)}$$

$$\Delta D = D_t - D \quad \text{(XXI)}$$

$$\Delta H = H_t - h \quad \text{(XXII)}$$

Where ΔW, ΔD, and ΔH denote the deviations in melt track width, deviation, and height, respectively.

Based on the deviation features and melt track category labels, a simple and efficient softmax classifier was utilized to classify the melt track categories.

2.6. Model training

During training, the root mean square error (RMSE) (Equation XXIII) was used to evaluate model performance.

$$RMSE = \left(\frac{1}{n}\sum_{i=1}^{n}\left(\bar{f}_i - f_i\right)^2\right)^{0.5} \quad \text{(XXIII)}$$

Where n is the number of samples, $\bar{f}_i$ is the true value, and f_i is the predicted value.

The training effect of the proposed model using RMSE loss in 70 epochs is displayed in Figure 10. During the first 10 epochs, both training and validation losses decreased rapidly in parallel, indicating efficient initial model learning. Between epochs 10 – 40, convergence decreased without oscillation. Beyond epoch 40, while training loss continued to decline, validation loss exhibited slow fluctuations with a gradually widening divergence between them, suggesting mild overfitting.

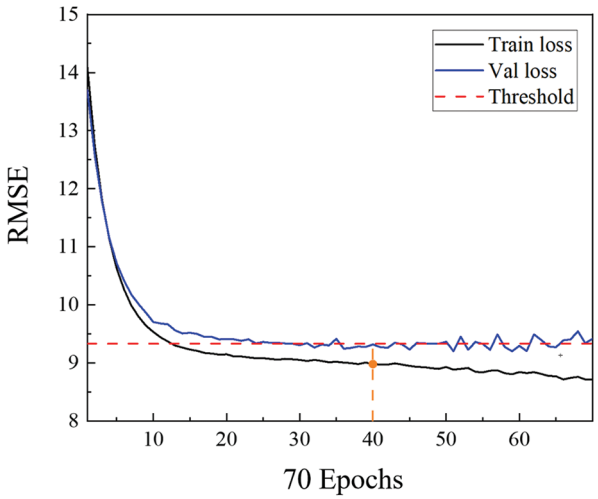

Figure 10. Root mean square error loss of the DGP-p model
Abbreviations: DGP-p: DGP model using physical kernel; Val: Validation datasets; Train: Training datasets

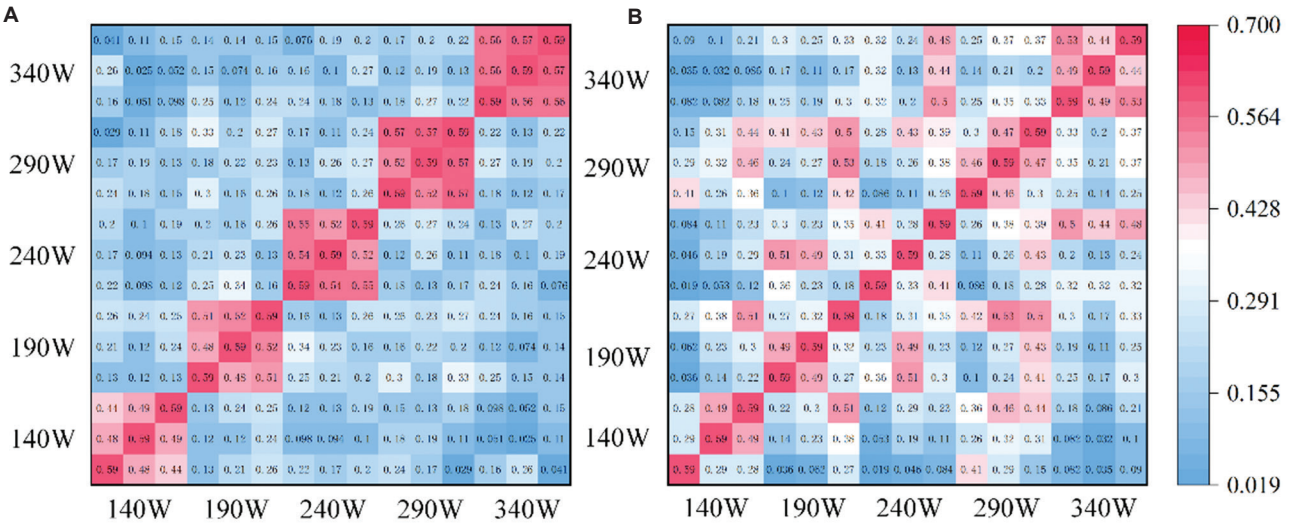

Figure 11. Covariance matrix heat map: (A) DGP-p, and (B) DGP-b
Abbreviations: DGP-p: DGP model using physical kernel; DGP-b: DGP model using basic mahalanobis kernel

Therefore, the model in the 40th epoch was selected as the optimal training model, and the generalization gap of the model at this point was 3.76%, which is within a reasonable range.

To verify the guiding effect of the physical constraint kernel function on the training process, we first selected a test group with a scanning speed of 860 mm/s. We then randomly selected three samples from this test group that had different powers. Next, we compared these three samples using two models: (i) the DGP-b model, which uses an ordinary martensitic kernel, and (ii) the DPG-p model, which employs a physical constraint kernel. Thereafter, we calculated the kernel covariance matrix for each of the comparisons and generated heat maps based on the calculated kernel covariance matrices. The results of this analysis are presented in Figure 11.

Due to data normalization, the constant diagonal values equal 0.59. It can be observed that for the same power group, a high covariance value was obtained; at different power groups, the covariance values were lower; and the intra-group similarity increased with increasing power (Figure 11A). In Figure 11B, the inter-group similarity (0.533) significantly exceeded the intra-group similarity (0.281), with a more dispersed distribution pattern. This indicates that the relationship is governed by data distribution rather than physical laws, failing to reflect the power increment effect.

In addition, the stability of working conditions was improved, and some of the cross-group covariance values were high, with noise interference. This result indicates that the physical kernel effectively suppresses unphysical fluctuations – resulting in high similarity within the same power group and low similarity across groups – and noise interference.

Table 1. Ablation experimental prediction results

Prediction set	Geometric features	Root mean square error	
		DGP-p	DGP-b
240 W-660 mm/s	Width	0.060	0.068
	Deviation	0.020	0.023
	Height	0.043	0.047
290 W-760 mm/s	Width	0.065	0.090
	Deviation	0.017	0.023
	Height	0.036	0.039
340 W-960 mm/s	Width	0.083	0.121
	Deviation	0.024	0.031
	Height	0.038	0.040

Note: The geometric features were evaluated based on the root mean square error.
Abbreviation: DGP: Deep Gaussian processes

3. Results and discussion

3.1. Interpretability based on physical constraints

To verify the effectiveness of the proposed physically constrained martensitic kernel, the results of the DGP-b and DGP-p models on the prediction set were compared (Table 1).

As observed from Table 1, the DGP-p model – using a physically constrained martensitic kernel—has a lower average relative error than the DGP-b model – using the

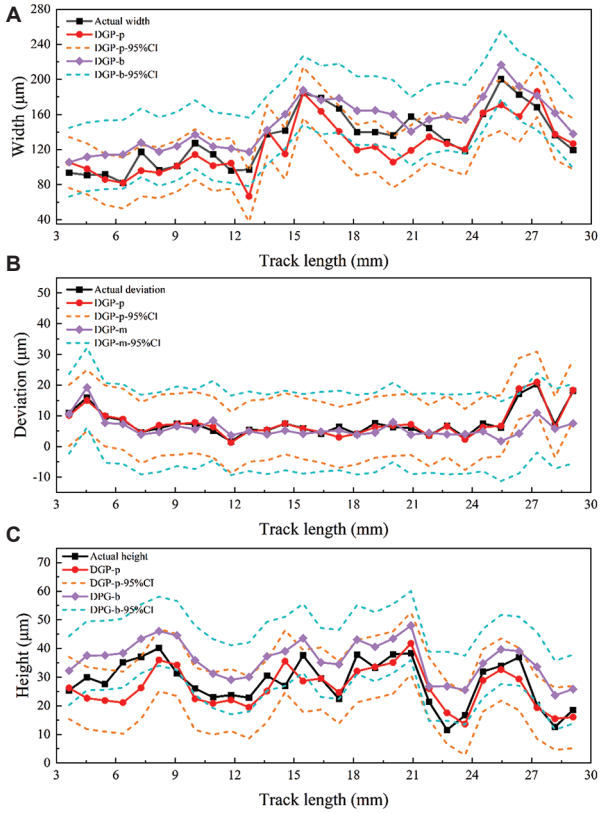

Figure 12. Ablation experiment: (A) width, (B) deviation, and (C) height Abbreviations: DGP-p: DGP model using physical kernel; DGP-b: DGP model using basic mahalanobis kernel; CI: Confidence interval

standard martensitic kernel. The average improvement in width, deviation, and height are 23.65%, 20.57%, and 7.07%, respectively. The prediction curves of the ablation test are presented in Figure 12. Further analysis of the width of the confidence intervals revealed a smaller confidence interval for the DGP-p model compared to the DGP-b model; the mean widths of the confidence intervals (width, deviation, and height) for the DGP-p model decreased from 39.170 μm, 12.970 μm, and 12.051 μm to 37.579 μm, 9.957 μm, and 10.858 μm, respectively. This result indicates that the physical constraints reduced the prediction uncertainty.

The prediction mean of the DGP-b model is generally higher than that of the DGP-p model, as the ordinary martensitic kernel relies on training data statistics, which may maintain a statistically positive correlation between power and track size. However, due to complex non-linear relationships in actual processing, such as melt pool mode shifts under high power conditions,[16] the real track size grows slowly. The martensitic kernel fails to constrain this non-linear decoupling, resulting in overprediction.

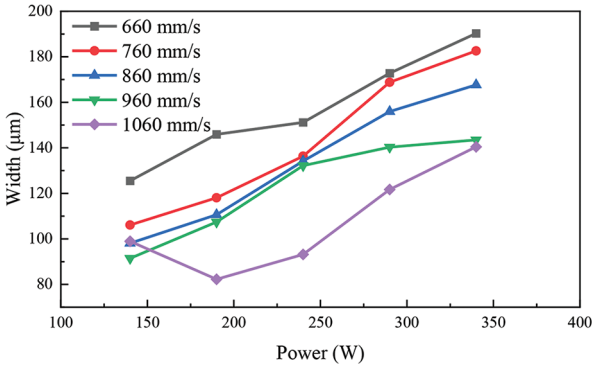

Figure 13. Width of the melt track

The physical kernel forces the model to follow the non-linear equilibrium between power, velocity, and track size through Rosenthal's equation, effectively limiting excessive growth of the predicted width and height. The specific widths of each group of tracks under this test are displayed in Figure 13. At a fixed scanning speed, the track width growth rate decreased with increasing laser power.

3.2. Comparison of melt track size prediction

We evaluated the prediction performance using four models, namely, the elasticity regression model (ENR), GP regression model, support vector machines (SVR), and Kolmogorov-Arnold Networks (KAN). ENR is a classical linear regression model and was used in this study to compare the applicability of the linear model with the non-linear model in predicting the melt track geometric features. GP was used to verify whether this experiment required a DGP model with multiple layers and multiple parallel GPs per layer to manage the complex non-linear relationship between melt pool geometric features and melt track geometric features. SVR is an algorithm that solves non-linear problems using kernel functions. KAN is a model proposed in recent years that implements non-linear modeling using the Kolmogorov-Arnold theorem. The selection of DGP is justified by comparing these algorithms, each with different characteristics.

Both ENR and SVR were implemented based on the Sklearn framework, while GP, KAN, and DGP were implemented based on the Pytorch framework. The basic parameters of the model were set as follows:

(i) ENR: The L1 regularization ratio was set at 45%; the L2 regularization ratio was set at 55%; the learning rate adopted the auto-tuning strategy; and the number of iterations was set to 50.

(ii) GP: The Matérn kernel was used; the smoothing parameter was set to 2.5; the remaining hyperparameters were set to 1; and the mean function was constant.

(iii) SVR: The radial basis kernel function was used and the regular term coefficient was set to 1.
(iv) KAN: Three hidden layers were used; the number of neurons was 36, 24, and 12, respectively, connected by fully connected form; the number of iterations was 100; the optimizer used Adam; and the learning rate was set to 0.001.
(v) DGP-p: The first layer used a Gaussian cosine composite kernel, with a smoothing parameter set to 2.5 and the period set to 1; the second layer used a physically constrained Matérn kernel.

Table 2 presents the average RMSE of the model predictions for the three sets of experiments computed using MinMax-normalized data.

Table 2. Experimental prediction results

Experimental set	Geometric features	Root mean square error				
		DGP	GP	KAN	SVR	ENR
240 W-660 mm/s	Width	0.060	0.288	0.268	0.236	0.234
	Deviation	0.020	0.097	0.057	0.124	0.150
	Height	0.043	0.053	0.047	0.048	0.048
290 W-760 mm/s	Width	0.065	0.170	0.157	0.136	0.141
	Deviation	0.017	0.121	0.032	0.044	0.045
	Height	0.036	0.062	0.050	0.054	0.044
340 W-960 mm/s	Width	0.083	0.201	0.174	0.136	0.151
	Deviation	0.024	0.041	0.055	0.049	0.045
	Height	0.038	0.067	0.069	0.052	0.061

Note: The geometric features were evaluated based on the root mean square error.
Abbreviations: DGP: Deep Gaussian processes; GP: Gaussian processes; KAN: Kolmogorov-Arnold Networks; SVR: Support vector machines; ENR: Elasticity regression model.

From the model RMSE results, the DGP – optimized based on the physical model – significantly outperformed the GP, KAN, SVR, and ENR models in the prediction of melt track geometric features. To further elucidate the rationale for selecting the DGP model, the 340 W-960 m/s experimental set with the largest RMSE index was further analyzed. Figures 14-16 demonstrate that when back-normalizing true values to predicted values, the RMSE differences between models in the experimental set are minimal. However, the melt track exhibits reduced widths in initial segments and increased fluctuation amplitudes during mid-to-late stages.

In the width prediction of the melt track (Figure 14), there were some gaps between the SVR model and the actual melt track width at the beginning, with notable hysteresis at width value fluctuations. There was a bigger gap between the KAN model and the actual melt track width at the beginning, and there were fluctuations in the width value. The prediction result of the ENR model was relatively smooth, which does not conform to the fluctuation of the actual width. The prediction result of the GP model was relatively good in the initial stage, with a decent width in the tail section. While the GP model achieved precise front-section width predictions, its tail-section predictions diverged substantially from experimental data. This discrepancy correlates with observed hysteresis in tracking time-dependent width variations, indicating limited dynamic response capability.

In the deviation prediction of the melt track (Figure 15), the SVR model displayed better prediction results in the middle and end sections and appeared to be more sensitive to the sudden fluctuation of the melt track deviation. The KAN and ENR models demonstrated relatively smooth

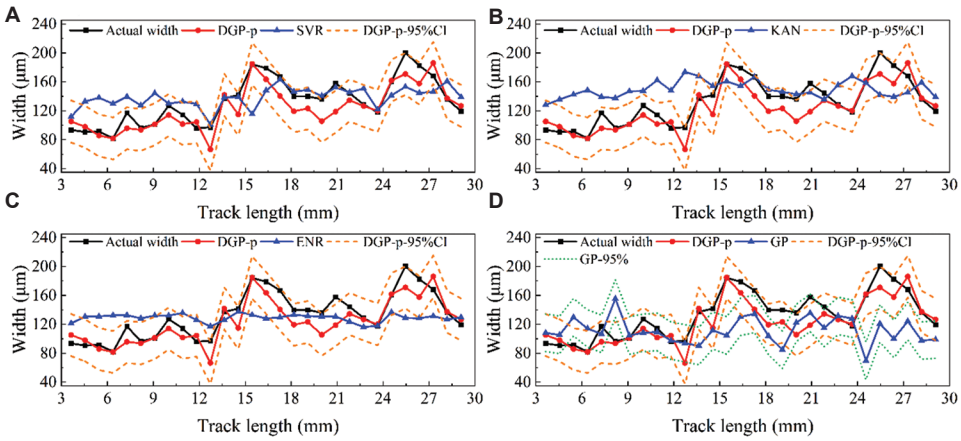

Figure 14. Comparison of validation results between the proposed DGP model and various other models in width prediction: (A) SVR, (B) KAN, (C) ENR, and (D) GP
Abbreviations: DGP-p: DGP model using physical kernel; ENR: Elasticity regression model; GP: Gaussian process regression model; SVR: Support vector machines

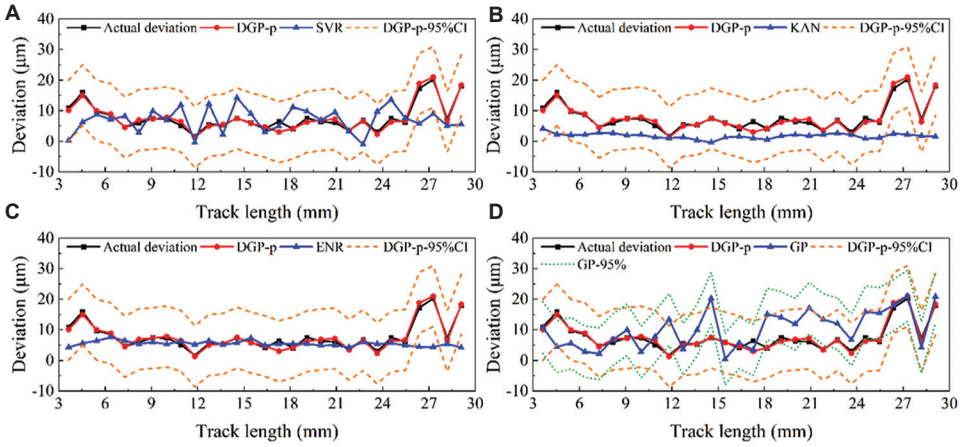

Figure 15. Comparison of validation results between the proposed DGP model and various other models in deviation prediction: (A) SVR, (B) KAN, (C) ENR, and (D) GP
Abbreviations: DGP-p: DGP model using physical kernel; ENR: Elasticity regression model; GP: Gaussian process regression model; SVR: Support vector machines

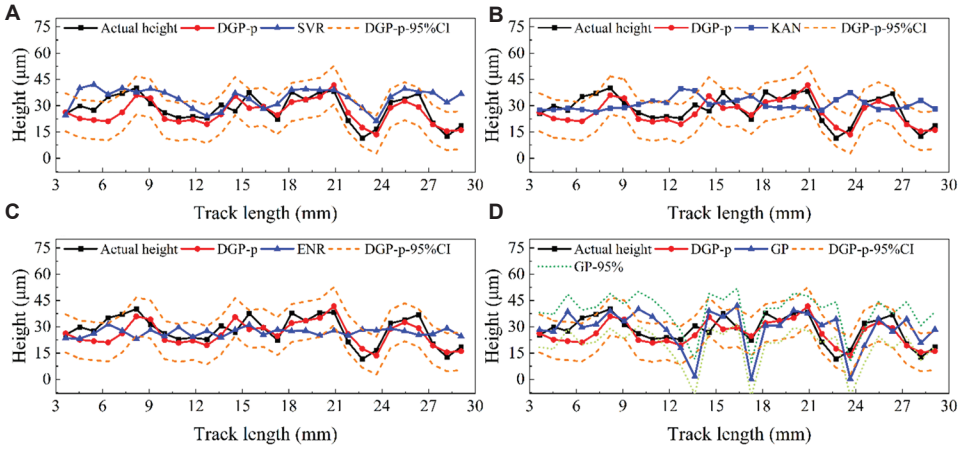

Figure 16. Comparison of validation results between the proposed DGP model and various other models in height prediction: (A) SVR, (B) KAN, (C) ENR, and (D) GP
Abbreviations: DGP-p: DGP model using physical kernel; ENR: Elasticity regression model; GP: Gaussian process regression model; SVR: Support vector machines

deviation fluctuations and were not sensitive to the sudden fluctuation of the melt track deviation. The GP model presented a stronger fluctuation and appeared to be more sensitive to the fluctuation of the melt track deviation.

In the height prediction of the melt track (Figure 16), the SVR model predicted changes that aligned with the changes in the real value. The KAN and ENR models displayed relatively smooth height fluctuations and were not sensitive to the sudden fluctuation of the melt track height. The GP model demonstrated strong volatility and was more sensitive to the fluctuation of the melt track height.

Overall, in predicting the geometric characteristics of the melt track, the linear ENR model demonstrates fundamental limitations by capturing only global linear relationships while failing to model non-linear melt pool dynamics. Comparatively, non-linear models reveal critical constraints. For instance, the KAN model – bound by the univariate superposition principle of Kolmogorov-Arnold's theorem – inadequately represents higher-order non-linear coupling that is inherent in melt track feature interdependencies. This theoretical limitation, combined with poor local mutation modeling capacity, results in KAN's inferior performance among the non-linear models.

The GP model directly models data distributions through covariance, but risks performance degradation from kernel overfitting noise and sensitivity to data

sparsity. In contrast, the SVR model achieves superior performance by balancing global trend capture with moderate local mutation sensitivity. The DGP-based melt track geometric feature prediction model is guided by multilayer non-linear hidden variable transfer and physical principles, ensuring the capability to accommodate sudden local offsets while predicting global trends. This approach mitigates purely data-driven overfitting risks, enforces physical law compliance in predictions, and enhances model interpretability. Due to its multilayer architecture, uncertainty propagates layer-wise through kernel functions from initially hidden variables, resulting in marginally expanded confidence intervals compared to traditional GP models.

However, the impact of the transmission of uncertain hidden variables is significantly reduced through the introduction of physical constraints. The predicted average width of the melt track was 123.55 μm and the average height was 28.29 μm, comparable to the actual geometry of the melt track by 9.89% and 16.03%, respectively, with a relative error of 10.21% in the average deviation. The relative errors in the width, height, and deviation predictions for the other groups were 8.06%, 14.45%, and 9.59% (for 240 W-660 mm/s) and 8.13%, 11.60%, and 9.39% (for 290 W-760 mm/s), with average relative errors of 8.69%, 14.02%, and 9.73%, respectively.

The DGP model demonstrates the highest accuracy in melt track width prediction. However, deviation predictions deteriorate significantly, while height predictions display the poorest performance. Notably, under higher energy density, the 24th group (refers to 340 W-960 mm/s) exhibited larger average relative errors than the other two groups. This degradation may be attributable to three factors: (i) the melt pool behavioral pattern changes under high power, invalidating Equation X to this process parameter; (ii) the assumption of Equation IX on the height is relatively simple and does not sufficiently take into account the actual physical process; and (iii) the height of the melt track is sensitive to changes in the melt pool aspect ratio, and the optimal time lag value of the melt pool aspect ratio is 2, resulting in deterioration in the prediction effect.

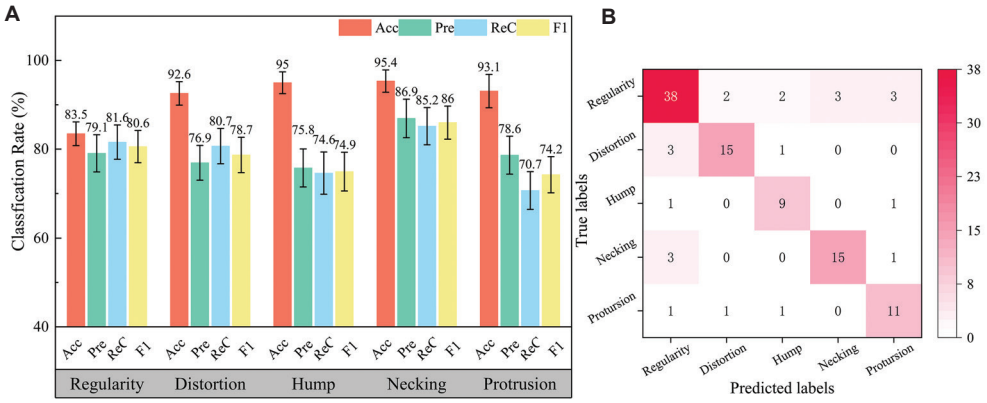

Figure 17. Classification results without oversampling: (A) evaluation metrics; and (B) confusion matrix

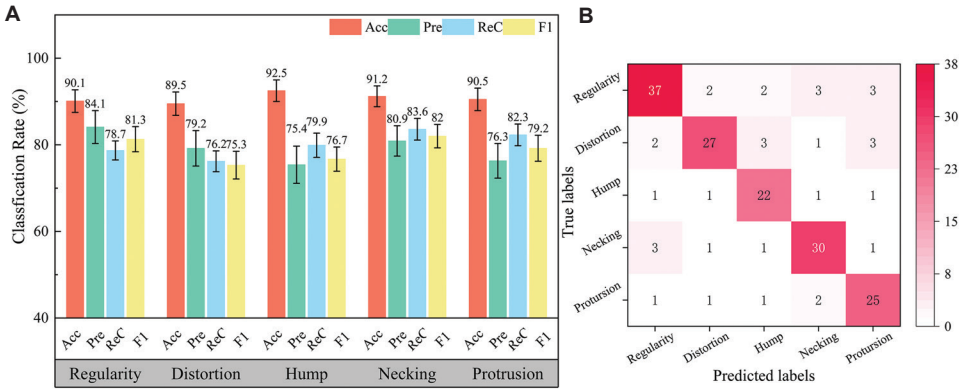

Figure 18. Classification results with oversampling: (A) evaluation metrics, and (B) confusion matrix

3.3. Morphological prediction

Following physical constraint-guided DGP model predictions of melt track dimensions, the deviation feature (Equation XIX) was used to predict the melt track morphology (Figure 17). This approach demonstrates robust predictive performance based on quantification by accuracy (91.89%), precision, recall, and F1-score metrics.

Analysis of evaluation metrics (Figure 17A) and the confusion matrix (Figure 17B) revealed sample imbalance across defect categories. To address this, two-stage SMOTE oversampling was applied to the five defect classes, consequently generating improved predictions (Figure 18).

A comparison between Figures 17A and 18A reveals significant recall improvements of 5.3% and 11.6% in the hump and protrusion categories, respectively. In addition, the standard deviation decreased across all categories, while the model's predictive consistency improved. Although the model exhibited reduced precision and fluctuations in accuracy, its substantial enhancement in defect detection recall demonstrates satisfactory overall performance.[38]

Similarly, a comparison between Figures 17B and 18B reveals a notably high leakage rate (exceeding 16%) in the regularity category, which is prone to confusion with other defect types, and may also affect other defect categories. The issue could be due to the presence of composite defect morphologies within the melt tracks, as exemplified by the three typical cases displayed in Figure 19. Specifically, the composite necking-protrusion morphology can produce an average melt track width similar to that of the regularity category in the final sampling results. Since the classifier relies primarily on global features and overlooks local feature mutations, classification boundaries become blurred, leading to misses (leakage) and false positives. Consequently, enhancing the classifier's ability to accurately recognize multiple co-occurring defects within a single melt track remains a significant challenge.

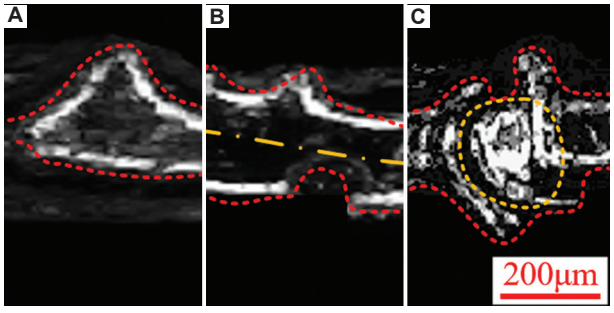

Figure 19. Composite morphology. (A) necking-protrusion. (B) distortion-necking-protrusion. (C) hump-protrusion. Scale bar: 200 μm

These findings further indicate that samples from different morphology categories occupy overlapping regions in the feature space, leading to confusion and ambiguous classification boundaries.

To understand the importance of different deviations for the class prediction of melt tracks, a feature importance analysis method based on permutation importance was used to verify whether the physical model of the theoretical deviations of melt tracks can effectively distinguish the classes of different melt track morphologies. Figure 20A demonstrates the importance of different deviations in the prediction of categories, and Figure 20B demonstrates the volumetric deviations on the upper surface of the melt track for different categories. These findings indicate distributional overlap among different morphology categories in the feature space, resulting in ambiguous classification boundaries and misclassifications. However, volumetric deviation demonstrates the discriminative capability for melt track morphology to some extent, with its high feature importance confirming its role as a critical classifier for morphology differentiation. The corresponding melt track deviation and height deviation values become particularly important for distortion and

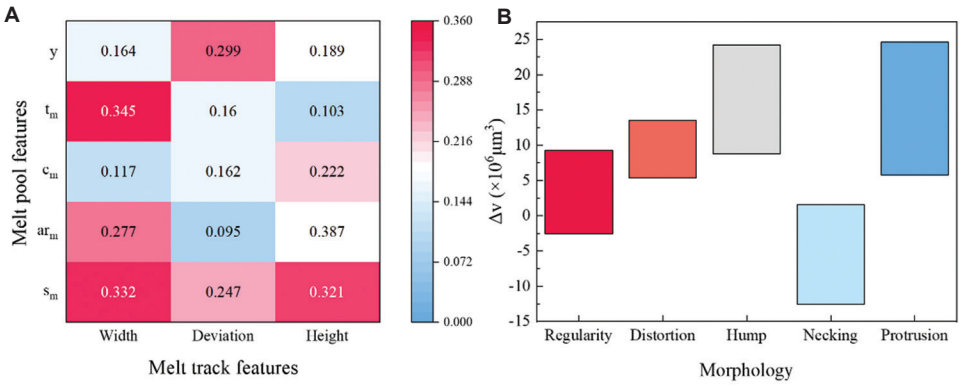

Figure 20. Analysis of classification results: (A) importance of features, and (B) melt track volume deviation

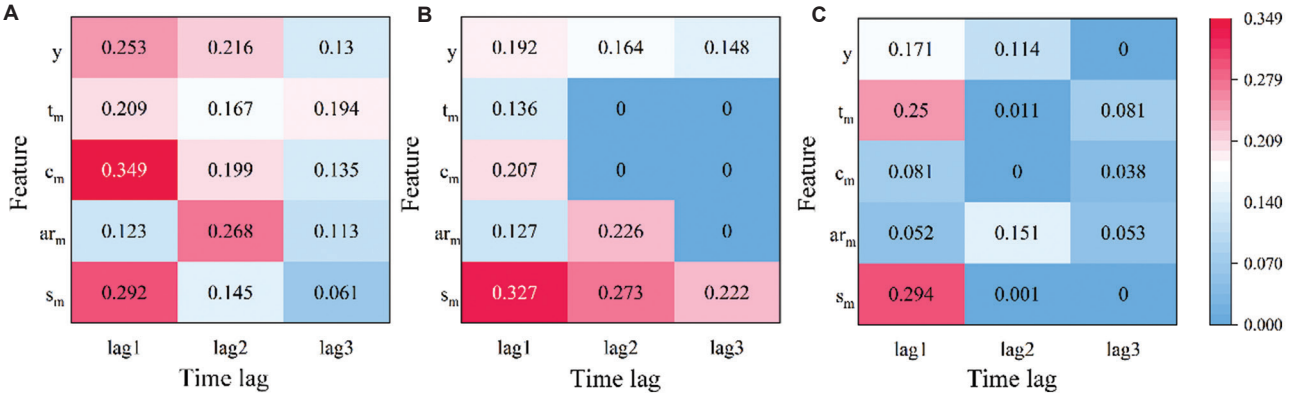

Figure 21. Delay mutual information matrix: (A) melt track width, (B) melt track deviation, and (C) melt track height

hump, which are two defective morphologies mainly caused by melt track deviation and height variation.

3.4. Analysis of the correlation between the melt pool and melt track

To test the hypotheses established in Section 2.3 and further clarify the type of melt pool fluctuations most likely to cause specific defects, the feature-defect causality needs to be quantified. However, Granger's causality analysis[39] is a parametric-based causality analysis method and does not apply to the non-parametric DGP model in this study. Hence, time-lagged mutual information was used instead of the Granger method to evaluate the feature-to-feature non-linear correlations, avoiding the limitations of the linearity assumption and quantifying the dynamic sensitivity.

$$I\left(X_t;Y_{t+\tau}\right)=\sum_{X,Y}p(X_t,Y_{t+\tau})log\frac{p\left(X_t,Y_{t+\tau}\right)}{p\left(X_t\right)p\left(Y_{t+\tau}\right)} \quad \text{(XXIV)}$$

$$S(X_t \to Y_{t+\tau}) = I(X_t; Y_{t+\tau}) - I(X_{t-1}; Y_{t+\tau}) \quad \text{(XXV)}$$

$I(X_t; Y_{t+\tau})$ is the time lag mutual information value between X_t and $Y_{t+\tau}$.

X_t is the eigenvector of the melt pool at time t.

$X_t = \left[s_m^t, ar_m^t, c_m^t, t_m^t, y^t\right]$, The upper right label of the eigenvalue represents the corresponding time t

Y_t is the eigenvector of the melt track at time t, $Y_t = [W_t, D_t, H_t]$

τ is the time lag, $p(X_t, Y_{t+\tau})$ is the joint probability distribution. $p(X_t)$ and $p(Y_{t+\tau})$ are the marginal probability distributions.

$S(X_t \to Y_{t+\tau})$ is the amount of information transmitted from X_t to $Y_{t+\tau}$.

Based on Equation XXIV and Equation XXV, the specific values in each matrix of Figure 21 can be calculated.

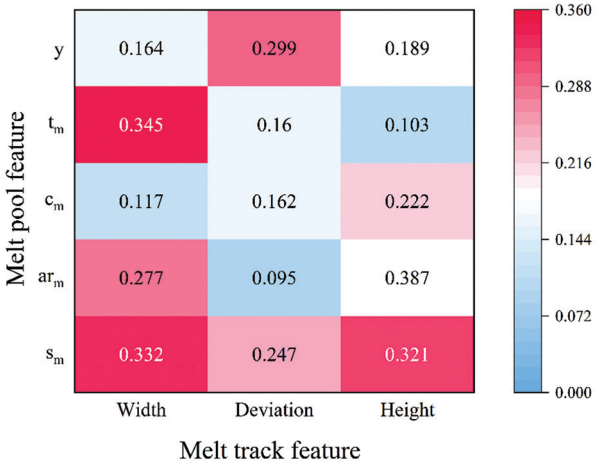

Figure 22. Feature sensitivity matrix

For the melt track geometric features, the time-lag information of the melt pool (melt track width, deviation, and height) is presented in Figure 17, where a larger mutual information value indicates a stronger correlation between the features. Figure 21A demonstrates that the mutual information values of melt track width exhibited a smoother time-lag decay characteristic, and there is a continuous influence of melt pool features on melt track width. Figure 21B highlights that the mutual information values of melt track deviation featured a steep decay trend – especially the mutual information values for c_m and t_m dropping to 0 at lag2 and lag3 – thereby indicating that the effect is limited to the short term. Figure 21C demonstrates that the mutual information value of melt track height is lower than the other two features as a whole, and the s_m and t_m features of the melt pool displayed a strong correlation at lag1, while the values of most features increased at lag3. Most of the features have the highest mutual information value at lag1, while only the ar_m feature of the melt pool has the highest mutual information value at lag2. These results validate the short-term changes of the melt pool feature through the neighboring time series.

Figure 22 displays the sensitivity of the melt track characteristics to changes in the characteristics of the melt pool. Changes in the convexity of the melt pool and the roundness of the melt track are strongly correlated with variations in melt track width, while melt track offset primarily responds to shifts in the melt pool's centroid position and area. In addition, melt track height fluctuations are dependent on alterations to the melt pool's aspect ratio and area. This observation validates the defect-causation hypothesis proposed in Section 2.3. Analysis of the time-lag mutual information matrix further reveals near-synchronized responses between melt track width and deviation changes, whereas height adjustments exhibit a measurable temporal lag.

4. Conclusion

The proposed DGP-p model establishes an interpretable feature-mapping mechanism. Experimental results demonstrate that the physical kernel function enhances intra-group sample variance within the same power category (from 0.456 to 0.547, an improvement of 19.9%) while reducing inter-group covariance across different power categories (from 0.256 to 0.176, a reduction of 31.3%), thereby validating its effectiveness in filtering non-physical feature correlations.

The model demonstrated superior performance under single-sensor conditions, with average relative errors of 9.89% (width), 10.21% (deviation), and 16.03% (height), outperforming traditional machine learning methods. With a 9.8 ms inference time (GPU: 4070super) – slightly slower than the GP model's 7.5 ms – it achieved 65.57% higher prediction accuracy. The melt track defect classifier – combining volumetric deviation (weight = 0.39) and geometric features – attained 90.76% classification accuracy.

This study employed feature-sensitive analysis and time-lag mutual information quantification. Notably, there is a continuous effect of the dynamic behavior of the melt pool on the geometrical characteristics of the melt track: the melt track width is affected by the convexity characteristics of the melt pool and the area. The deviation of the melt track is affected by the position of the center of mass and the area of the melt pool, while the height of the melt track is affected by the length-to-width ratio of the melt pool and the area.

Overall, this study highlights that there is a continuous effect on the changes induced by these features, with a significant lag effect on the changes induced by the melt pool aspect. Based on these findings, an effective early warning mechanism can be established at the early stages of defect formation by monitoring changes in the geometric features of the melt pool in real time. This study provides a reference for AM process monitoring and defect prevention and control. Future research will further investigate how single-track defects propagate through multilayer and multi-track interactions.

Acknowledgments

The authors would like to acknowledge financial support from the National Natural Science Foundation of China under Grant Number 52175481 and the China Post-doctoral Science Foundation under Grant Number 2023M743539.

Funding

This work was supported in part by the National Natural Science Foundation of China (grant no. 52175481) and in part by the China Post-doctoral Science Foundation (grant no. 2023M743539).

Conflict of interest

Xin Lin serves as the Editorial Board Member of the journal but was not in any way involved in the editorial and peer-review process conducted for this paper, directly or indirectly. Other authors declare they have no competing interests.

Author contributions

Conceptualization: Xin Lin and Kunpeng Zhu
Formal analysis: Xin Lin
Investigation: Xin Lin, Kunpeng Zhu, and Haodong Chen
Methodology: Shilin Liu, Xin Lin, Kunpeng Zhu, and Jinrong Mao
Writing – original draft: Shilin Liu, Haodong Chen, and Xin Lin
Writing – review and editing: Xin Lin

Ethics approval and consent to participate

Not applicable.

Consent for publication

Not applicable.

Availability of data

The raw/processed data required to reproduce these findings cannot be shared at the time of publication, as the data also forms part of an ongoing study.

References

1. Khairallah SA, Martin AA, Lee JR, *et al.* Controlling interdependent meso-nanosecond dynamics and defect generation in metal 3D printing. *Science.*

2020;368(6491):660-665.

doi: 10.1126/science.aay7830

2. Fang Q, Tan Z, Li H, *et al*. *In-situ* capture of melt pool signature in selective laser melting using U-Net-based convolutional neural network. *J Manuf Process*. 2021;68:347-355.

doi: 10.1016/j.jmapro.2021.05.052

3. Yang L, Lo L, Ding S, Özel T. Monitoring and detection of meltpool and spatter regions in laser powder bed fusion of super alloy Inconel 625. *Prog Addit Manuf*. 2020;5(4):367-378.

doi: 10.1007/s40964-020-00140-8

4. Liu J, Wei B, Chang H, Li J, Yang G. Review of visual measurement methods for metal vaporization processes in laser powder bed fusion. *Micromachines (Basel)*. 2023;14(7):1351.

doi: 10.3390/mi14071351

5. Forien JB, Calta NP, DePond PJ, Guss GM, Roehling TT, Matthews MJ. Detecting keyhole pore defects and monitoring process signatures during laser powder bed fusion: A correlation between *in situ* pyrometry and *ex situ* X-ray radiography. *Addit Manuf*. 2020;35:101336.

doi: 10.1016/j.addma.2020.101336

6. Khanzadeh M, Chowdhury S, Tschopp MA, Doude HR, Marufuzzaman M, Bian L. *In-situ* monitoring of melt pool images for porosity prediction in directed energy deposition processes. *IISE Trans*. 2018;51(5):437-455.

doi: 10.1080/24725854.2017.1417656

7. Khanzadeh M, Dantin M, Tian W, Priddy MW, Doude H, Bian L. Fast prediction of thermal data stream for direct laser deposition processes using network-based tensor regression. *J Manuf Sci Eng*. 2021;144(4):041004.

doi: 10.1115/1.4052207

8. Scime L, Beuth J. Anomaly detection and classification in a laser powder bed additive manufacturing process using a trained computer vision algorithm. *Addit Manuf*. 2018;19:114-126.

doi: 10.1016/j.addma.2017.11.009

9. Okaro IA, Jayasinghe S, Sutcliffe C, Black K, Paoletti P, Green PL. Automatic fault detection for laser powder-bed fusion using semi-supervised machine learning. *Addit Manuf*. 2019;27:42-53.

doi: 10.1016/j.addma.2019.01.006

10. Yuan B, Giera B, Guss G, Matthews M, McMains S. Semi-supervised convolutional neural networks for *in-situ* video monitoring of selective laser melting. In: *2019 IEEE Winter Conference on Applications of Computer Vision (WACV)*. United States: IEEE; 2019. p. 744-753.

doi: 10.1109/WACV.2019.00084

11. Yuan B, Guss GM, Wilson AC, *et al*. Machine-learning-based monitoring of laser powder bed fusion. *Adv Mater Technol*. 2018;3(12):1800136.

doi: 10.1002/admt.201800136

12. Mojahed Yazdi R, Imani F, Yang H. A hybrid deep learning model of process-build interactions in additive manufacturing. *J Manuf Syst*. 2020;57:460-468.

doi: 10.1016/j.jmsy.2020.11.001

13. Lopez F, Witherell P, Lane B. Identifying uncertainty in laser powder bed fusion additive manufacturing models. *J Mech Des*. 2016;138(11):114502.

doi: 10.1115/1.4034103

14. Mahmoudi M, Ezzat A, Elwany A. Layerwise anomaly detection in laser powder-bed fusion metal additive manufacturing. *J Manuf Sci Eng*. 2019;141(3):031002.

doi: 10.1115/1.4042108

15. Gaikwad A, Giera B, Guss GM, Forien JB, Matthews MJ, Rao P. Heterogeneous sensing and scientific machine learning for quality assurance in laser powder bed fusion - a single-track study. *Addit Manuf*. 2020;36:101659.

doi: 10.1016/j.addma.2020.101659

16. Guo K, Qiao L, Huang Z, Anwer N, Cao Y. A computational model of melt pool morphology for selective laser melting process. *Int J Adv Manuf Technol*. 2022;121(3-4):1651-1673.

doi: 10.1007/s00170-022-09366-y

17. Zhang H, Vallabh CK, Zhao X. Registration and fusion of large-scale melt pool temperature and morphology monitoring data demonstrated for surface topography prediction in LPBF. *Addit Manuf*. 2022;58:103075.

doi: 10.1016/j.addma.2022.103075

18. Biggio L, Wieland A, Chao MA, Kastanis I, Fink O. Uncertainty-aware prognosis via deep gaussian process. *IEEE Access*. 2021;9:123517-123527.

doi: 10.1109/ACCESS.2021.3110049

19. Fan Z, Lu M, Huang H. Selective laser melting of alumina: A single track study. *Ceram Int*. 2018;44(8):9484-9493.

doi: 10.1016/j.ceramint.2018.02.166

20. Yadroitsev I, Krakhmalev P, Yadroitsava I, Johansson S, Smurov I. Energy input effect on morphology and microstructure of selective laser melting single track from metallic powder. *J Mater Process Technol*. 2013;213(4):606-613.

doi: 10.1016/j.jmatprotec.2012.11.014

21. Yang J, Liu G, Zhu W, *et al*. High-precision and ultraspeed monitoring of melt-pool morphology in laser-directed energy deposition using deep learning. *Addit Manuf Front*. 2025;4(2):200199.

doi: 10.1016/j.amf.2025.200199

22. Xiang Y, Zhang S, Wei Z, *et al*. Forming and defect analysis for single track scanning in selective laser melting of Ti6Al4V. *Appl Phys A*. 2018;124(10):685.

doi: 10.1007/s00339-018-2056-9

23. Hu Z, Nagarajan B, Song X, Huang R, Zhai W, Wei J. Formation of SS316L single tracks in micro selective laser melting: Surface, geometry, and defects. *Adv Mater Sci Eng*. 2019;2019:9451406.

doi: 10.1155/2019/9451406

24. Zhou H, Su H, Guo Y, *et al*. Formation and evolution of surface morphology in overhang structure of IN718 superalloy fabricated by laser powder bed fusion. *Acta Metall Sin*. 2023;36(9):1433-1453.

doi: 10.1007/s40195-023-01546-3

25. Li C, Guo YB, Zhao JB. Interfacial phenomena and characteristics between the deposited material and substrate in selective laser melting Inconel 625. *J Mater Process Technol*. 2017;243:269-281.

doi: 10.1016/j.jmatprotec.2016.12.033

26. Khairallah SA, Anderson AT, Rubenchik A, King WE. Laser powder-bed fusion additive manufacturing: Physics of complex melt flow and formation mechanisms of pores, spatter, and denudation zones. *Acta Mater*. 2016;108:36-45.

doi: 10.1016/j.actamat.2016.02.014

27. Chen H, Lin X, Sun Y, Wang S, Zhu K, Dan B. Revealing formation mechanism of end of process depression in laser powder bed fusion by multi-physics meso-scale simulation. *Virtual Phys Prototyp.* 2024;19(1):e2326599.

doi: 10.1080/17452759.2024.2326599

28. Yuan P, Gu D. Molten pool behaviour and its physical mechanism during selective laser melting of TiC/AlSi10Mg nanocomposites: Simulation and experiments. *J Phys D Appl Phys.* 2015;48(3):035303.

doi: 10.1088/0022-3727/48/3/035303

29. Yuan W, Chen H, Cheng T, Wei Q. Effects of laser scanning speeds on different states of the molten pool during selective laser melting: Simulation and experiment. *Mater Des*. 2020;189:108542.

doi: 10.1016/j.matdes.2020.108542

30. Caprio L, Demir A, Previtali B. Observing molten pool surface oscillations during keyhole processing in laser powder bed fusion as a novel method to estimate the penetration depth. *Addit Manuf*. 2020;36:101470.

doi: 10.1016/j.addma.2020.101470

31. Tang M, Pistorius PC, Beuth JL. Prediction of lack-of-fusion porosity for powder bed fusion. *Addit Manuf*. 2017;14:39-48.

doi: 10.1016/j.addma.2016.12.001

32. Ning J, Mirkoohi E, Dong Y, Sievers DE, Garmestani H, Liang SY. Analytical modeling of 3D temperature distribution in selective laser melting of Ti-6Al-4V considering part boundary conditions. *J Manuf Process*. 2019;44:319-326.

doi: 10.1016/j.jmapro.2019.06.013

33. Promoppatum P, Yao SC, Pistorius PC, Rollett AD. A comprehensive comparison of the analytical and numerical prediction of the thermal history and solidification microstructure of inconel 718 products made by laser powder-bed fusion. *Engineering*. 2017;3(5):685-694.

doi: 10.1016/J.ENG.2017.05.023

34. Wang W, Liang SY. A 3D analytical modeling method for keyhole porosity prediction in laser powder bed fusion. *Int J Adv Manuf Technol*. 2022;120(5-6):3017-3025.

doi: 10.1007/s00170-022-08898-7

35. Yang J, Han J, Yu H, *et al*. Role of molten pool mode on formability, microstructure and mechanical properties of selective laser melted Ti-6Al-4V alloy. *Mater Des*. 2016;110:558-570.

doi: 10.1016/j.matdes.2016.08.036

36. Kamath C, El-dasher B, Gallegos GF, King WE, Sisto A. Density of additively-manufactured, 316L SS parts using laser powder-bed fusion at powers up to 400 W. *Int J Adv Manuf Technol*. 2014;74(1-4):65-78.

doi: 10.1007/s00170-014-5954-9

37. Salimbeni H, Deisenroth M. Doubly stochastic variational inference for deep Gaussian processes. In: *Advances in Neural Information Processing Systems*. United States: Morgan Kaufmann Publishers Inc.; 2017. p. 30.

doi: 10.48550/arXiv.1705.08933

38. Roth K, Pemula L, Zepeda J, Scholkopf B, Brox T, Gehler P. Towards total recall in industrial anomaly detection. In: *IEEE/CVF Conference on Computer Vision and Pattern Recognition (CVPR)*. United States: IEEE; 2022. p. 14298-14308.

doi: 10.1109/cvpr52688.2022.01392

39. Shojaie A, Fox EB. Granger causality: A review and recent advances. *Annu Rev Stat Appl.* 2022;9(1):289-319.

doi: 10.1146/annurev-statistics-040120-010930

ACCSCIENCE PUBLISHING

Materials Science in Additive Manufacturing

ORIGINAL RESEARCH ARTICLE

Enhanced strength of A131 steel via heterostructures induced by laser-directed energy deposition

Yuchao Bai[1,2,3], Silu Zhang[1,2,3], Qi Yan[1,2,3]*, Cuiling Zhao[1,2,3]*, and Jiaming Zhan[4]

[1]Guangdong Provincial Key Laboratory of Intelligent Morphing Mechanisms and Adaptive Robots, Harbin Institute of Technology, Shenzhen, Guangdong, China

[2]Key University Laboratory of Mechanism and Machine Theory and Intelligent Unmanned Systems of Guangdong, Harbin Institute of Technology, Shenzhen, Guangdong, China

[3]School of Robotics and Advanced Manufacture, Harbin Institute of Technology, Shenzhen, Guangdong, China

[4]School of Advanced Manufacturing, Sun Yat-sen University, Shenzhen, Guangdong, China

(This article belongs to the *Special Issue: Metallic Additive Manufacturing*)

Abstract

The trade-off between strength and plasticity has posed a challenge to the broader application of conventional metallic structural materials in high-speed, heavy-load, and extreme service environments. Heterogeneous structure designs could potentially overcome these limitations with their inherent superior combination of strength and plasticity. To harness this potential, this study employed a directed energy deposition additive manufacturing (AM) technology to fabricate a novel heterostructure in as-built (AB) A131 steel, consisting of alternating coarse and fine-grain layers along the building direction. In addition, a heat treatment process was applied to fabricate a near-homogeneous microstructure, allowing for the investigation of the role of crystal misorientation in tensile anisotropy. Compared to the performance of commercial hot-rolled ASTM A131 steel (yield strength [σ_{YS}]: 346.5 MPa; ultimate tensile strength [σ_{UTS}]: 545.0 MPa), the AB A131 steel achieved significant enhancements of 168.3% and 78.0% in σ_{YS} and σ_{UTS}, respectively, when maintaining a comparable elongation of 24.6% along the deposition direction similar to the ASTM A131 standard. Comprehensive experimental characterizations, combined with molecular dynamics simulations, were conducted to investigate the underlying formation mechanism of the heterostructure and the origins of mechanical anisotropy. It was found that single-pass deposition produced three distinct microstructure regions with different grain sizes owing to dendrite growth. With repeated thermal cycles, these evolved into a layered heterostructure consisting of alternating fine crystals and coarse-columnar grains. This heterostructure remarkably contributed to an exceptional improvement in strength, accompanied by only a minor reduction in plasticity. These findings present an efficacious avenue for substantially augmenting the mechanical properties of conventional iron-based alloys, offering useful references for overcoming the strength-plasticity trade-off in other alloys fabricated by AM.

Keywords: Additive manufacturing; A131 steel; Heterostructure; Mechanical performance; Molecular dynamics

***Corresponding authors:**
Qi Yan
(galaxy.yanqi@gmail.com)
Cuiling Zhao
(zhaocuiling@hit.edu.cn)

Citation: Bai Y, Zhang S, Yan Q, Zhao C, Zhan J. Enhanced strength of A131 steel via heterostructures induced by laser-directed energy deposition. *Mater Sci Add Manuf*. 2025;4(3):025220038. doi: 10.36922/MSAM025220038

Received: May 27, 2025

Revised: June 14, 2025

Accepted: June 16, 2025

Published online: July 21, 2025

1. Introduction

Additive manufacturing (AM) has demonstrated ultra-high efficiency in producing heavy-load, complex-geometry, and large-volume equipment, exemplified by the successful launch of Terran 1, a launch vehicle entirely manufactured by 3D printing, primarily using directed energy deposition (DED) technology.[1] The 2-month production cycle of the 3D-printed rocket set a new record for the fastest rocket fabrication in history. Large-format metallic structural components developed using the DED method have been widely employed in alloys, such as titanium,[2] aluminum,[3] copper,[4] iron,[5] and their matrix composites.[6] Since the rapid commercialization and development of the aviation industry, difficult-to-machine alloys (*e.g.*, titanium alloys) have struggled to meet the demands of resource-efficient manufacturing. The outstanding performance of the Falcon[7] heavy-launch vehicle outlined that conventional high-strength steel could also be used in space equipment with remarkable economic effects. As a result, conventional iron materials are gaining increasing attention for future applications in the commercial aerospace industry.

A131 steel, a distinctive low-carbon structural steel developed over the past century, typically exhibits a standard yield strength of 235~390 MPa and an elongation of 19~23%, occupying a significant share in the steel market due to its comprehensive applications in both civilian and defensive industries, especially in marine vessels.[5,8,9] However, the structural strength of conventional A131 steel lacks the strength of conventional aerospace titanium alloy (*e.g.*, 800~1200 MPa for Ti-6Al-4V [Ti64]).[10,11] Leveraging the rapid cooling rates associated with laser melting to introduce the formation of martensite phases offers a promising route to enhancing the strength of the A131 steel.[5,12,13] Wu *et al.*[14,15] employed a selective laser melting method, combined with post-treatment, to fabricate A131 steel. Their results demonstrated a significant enhancement in strength, with the as-built (AB) A131 steel achieving a tensile strength of 1030 MPa, comparable to that of Ti64 alloy. However, this enhancement was accompanied by a reduction in plasticity, as the elongation of the A131 steel dropped sharply to just 3%. Post-process heat treatment led to a partial recovery of elongation, albeit with a notable decrement in strength. Similarly, Wang *et al.*[16-18] also manufactured A131 steels using a selective laser melting method with various scanning strategies. The results revealed the formation of substantial martensite microstructures, with an improved tensile strength of 937 MPa and a notable reduction in elongation (*i.e.*, <6%). Although steel strength can be significantly improved through selective laser melting methods, it is often accompanied by a considerable loss in elongation, rendering the mechanical performance insufficient to match that of commercial aerospace alloys.

Constructing a heterogeneous microstructure with a dual-phase or dual-grain-size structure offers a promising strategy for enhancing the strength of A131 steel without reducing plasticity.[19,20] Due to the high freedom and the ability to deposit multimaterial parts with different powders,[21-23] the DED technique enables the development of special heterostructures to improve the performance of the materials.[24-26] For example, Dan *et al.*[27] developed heterogeneous TiAl alloys by alternately depositing Ti and TiAl layers using DED methods, achieving a significant improvement in plasticity compared to that of the heterogeneous TiAl alloy in a submicron scale. However, the heterogeneous structure still exhibited the inherent trade-off between strength and plasticity. Wu *et al.*[28] successfully fabricated a heterogeneous structure in lamella-structured titanium alloys, consisting of alternating coarse and fine-grain regions, through post-treatment processes. This design led to a remarkable improvement in tensile strength with a limited reduction in elongation. Similarly, Li *et al.*[29] reported the fabrication of heterostructures in titanium alloys composed of alternating coarse and fine grains via a heat-treatment (HT) process. The results demonstrated a noticeable improvement in strength when maintaining elongation comparable to that of the control group. Gao *et al.*[20,30] fabricated heterostructures in SS316L steel via selective laser melting using an alternating remelting method. Their resulting heterostructure comprised nanoscale alternating layers of recrystallized and non-recrystallized regions, achieving a notable improvement in ultimate tensile strength with a limited decrement in elongation. Su *et al.*[26] designed DED processes incorporating interlayer pauses to fabricate maraging steels with heterogeneous layers composed of multiple phases in alternating layers, achieving a super-high strength of 1.5 GPa in maraging steel. These findings suggest that if a heterogeneous structure consisting of alternating coarse and fine-grain layers could be controlled by an AM method, the A131 steel could also potentially overcome the trade-off effects of strength and plasticity in a cost-effective manner. Although selective laser melting has demonstrated the feasibility of constructing nanoscale heterogeneous structures to overcome the trade-off effects, it has limited capabilities in fabricating complex geometries on a large scale. Therefore, developing DED methods to construct a submicron heterostructure with varied grain sizes is a promising strategy for achieving simultaneous improvements in both strength and plasticity, particularly for future applications in large-scale engineering equipment.

In this study, A131 steel with heterostructures, comprising alternating layers of coarse and fine grains, was successfully developed using a DED method that utilizes the dendritic growth features of melt pools and thermal cycle behavior. An HT and commercial hot-rolled (HR) A131 steel was also employed in this study as the control group. The tensile strength of the AB A131 steel exhibited an exceptional combination of strength, approaching that of Ti64 alloy, and plasticity within the range specified by the ductile ASTM A131 standard. To understand the formation mechanism of the heterostructure, multitype microstructure characterization and single-pass deposition experiments were employed to elucidate the model of the alternating layer of fine and coarse grains with crystal misorientation. In addition, molecular dynamics (MD) was employed to reconstruct the model of the heterogeneous microstructure according to the observed microstructure. The model was stretched in the same direction as the experimental process to reveal the anisotropy of the tensile behavior of the AB A131 steel. This innovative structural design strategy presents a promising insight into crafting traditional iron with a remarkable strength-plasticity combination free from trade-off effects, with broader implications for other conventional alloys in the industries.

2. Materials and methods

2.1. Materials

In this study, commercial gas-atomized mild steel powders (A131 EH36; particle size: 45 – 90 μm; Zhongyuan Advanced Materials Technology Co., Ltd, China) were utilized (Figure 1A). The powder was approximately spherical, with a low-carbon equivalent value (0.3%) (Figure 1B; Table S1). For comparison, commercial HR A131 steel bulk (ThyssenKrupp Material Services GmbH Co., Ltd., Germany) was used as the control group. All materials were used in the as-received state.

2.2. Fabrication process

The AB A131 EH36 steel used in this study was fabricated using a DED AM machine (Figure 2A) equipped with a fiber laser (wavelength: 1070 nm; laser beam spot diameter: 2.5 mm) under an argon atmosphere (1 bar pressure). The DED settings were: 1.23 kW laser power, 0.5 mm layer thickness, 1200 mm/min moving speed, 1.25 mm track space, and 722.2 mm/min powder feeding speed with Gaussian distribution. The orthogonal strategy was used, where the moving direction rotated by 90° for each alternating layer alongside the building direction (Figure 2B). To distinguish the building direction, a 3D axis was constructed with normal direction (ND; parallel to the laser deposition), transverse direction (TD), and rolling direction (RD).

In the HT process, the AB A131 EH36 steel was quenched and subsequently tempered using a box-type furnace (MXQ1600-40, MICRO-X Ltd Co., China) (Figure 2C). The cleaned AB A131 EH36 bulk was heated (10 K/min) at 910°C for 0.5 h, followed by water quenching, subsequent tempering at 500°C for 2 h (Figure 2D), and air-cooling. To investigate the formation mechanism of the microstructure, single-pass deposition of A131 steel was carried out using the DED method with the same parameters.

2.3. Material characterization

The starting raw materials and bulks were characterized using a scanning electron microscope (SEM) (JEOL JSM-5500LV; JEOL Ltd., Japan) equipped with an energy-dispersive X-ray spectrometer (EDS). The microstructure of the bulks was also examined using an SEM system (Apreo 2 SEM; Thermo Fisher Scientific, United States of America [USA]) equipped with EDS and an electron backscatter diffraction (EBSD) detector. The microstructure was also observed using a laser confocal

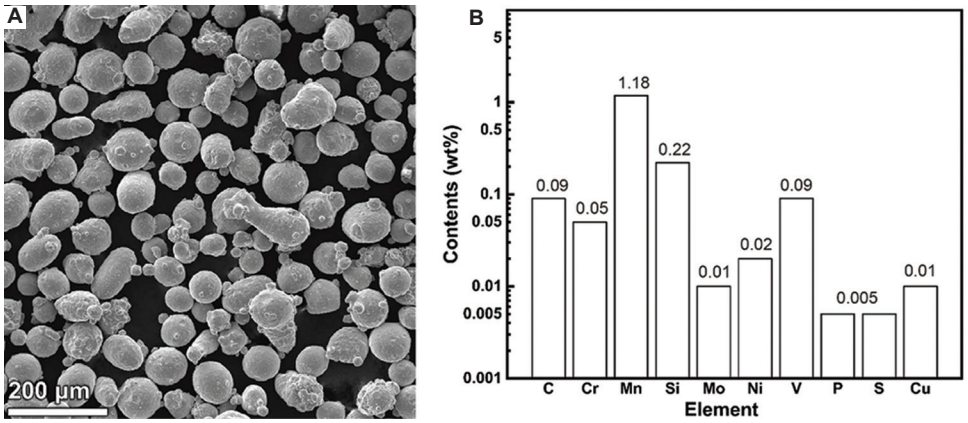

Figure 1. Steel powder morphology (A) and elemental composition (B)

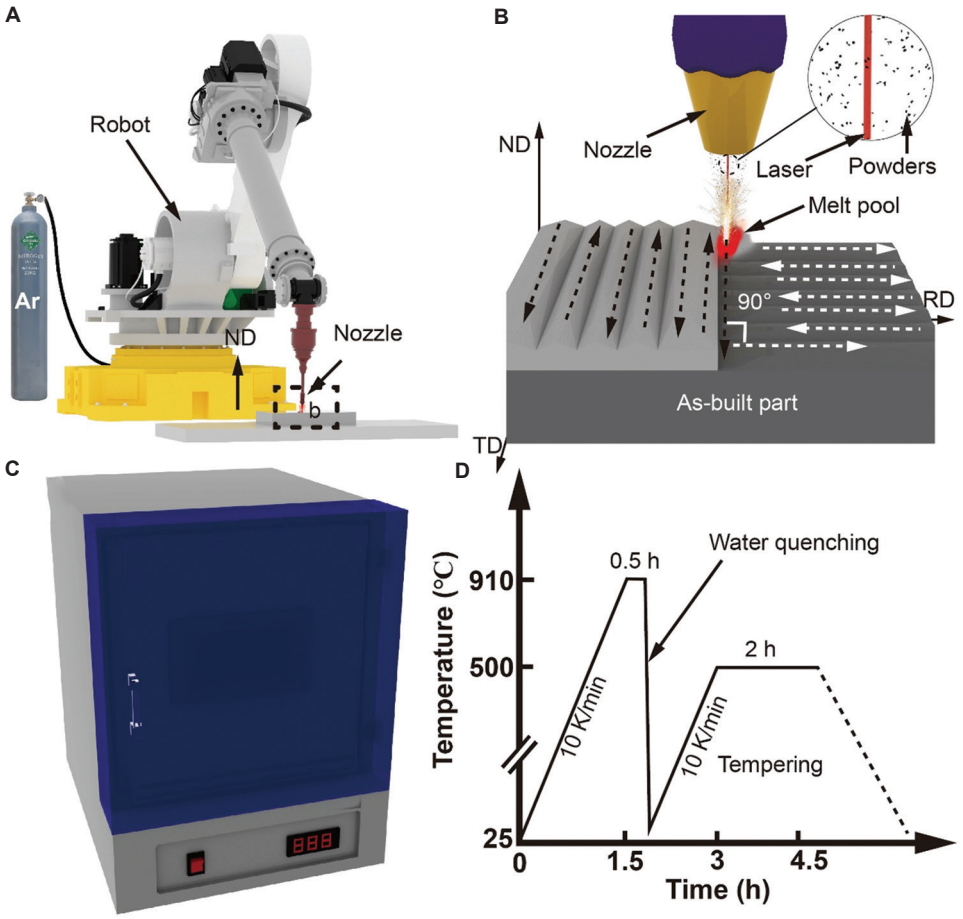

Figure 2. Diagrams of material fabrication and post-treatment process: (A) Schematics of the L-DED process; (B) manufacturing strategy; (C) oven used for heat treatment; and (D) heat treatment parameters
Abbreviations: L-DED: Laser-directed energy deposition; ND: Nominal direction; TD: Transverse direction; RD: Rolling direction

microscope (Olympus LEXT OLS5000; Alpha Co., USA). For SEM observation, the surface of the bulk was ground and polished in accordance with ASTM E3-2011 standards, followed by etching with an ethylene nitrate mixture (4 mL HNO_3 and 100 mL C_2H_5OH). For EBSD examination, the surface of the bulk was electrolytically polished in accordance with ASTM E1558 standards using a 1 μm step referring to GB/T 36165-2018.[31]

Phase analysis was performed using X-ray diffraction (XRD) (SmartLab SE; Rigaku Co., Ltd., Japan) with the CoKa wavelength (λ_{Co} Ka) of 1.79 Å, over a rotation-diffraction angle of 30° – 120° and a scanning speed of 5°/min. The density of all AB bulks was measured using the Archimedes method (ISO 1183-2017) in an analytical reagent grade alcohol solution.

2.4. Material property testing

The uniaxial tensile (ISO 6892-1: 2009) and Vicker hardness test (ISO 6507-1-2018) were carried out at room temperature to evaluate the material mechanical properties. The uniaxial tensile performance was examined using a microcomputer-controlled electronic universal testing machine (Instron 8501; INSTRON Co., USA) at a strain rate of 0.5 mm/min. The AB bulks were machined into a dog bone-shaped specimen, with a total length of 40 mm, thickness of 3 mm, gauge width of 4 mm, and gauge length of 12 mm. The hardness test was carried out using a Vickers hardness tester (HV-1000Z; HUAYIN Ltd., China) with a load of 200 gf and a dwell time of 15 s.

2.5. Models and computation

The model construction and analysis of deformation behavior during tensile loading were performed using MD simulations with the LAMMPS package.[32,33] This method has been successfully applied in assessing the mechanical performance of metals with body-centered cubic (BCC) crystal structures,[34,35] especially in iron-based materials.[36] The corresponding directions of the model along ND,

TD, and RD corresponded to the x-, y-, and z-axes, respectively. The entire configuration was box-shaped (43 × 11 × 43 nm), packed with two kinds of grains with the same lattice parameter of 2.86 Å. These two types of grains formed a sandwich structure: Fine equiaxed crystals with an average diameter of 2.86 nm at the edges, and coarse columnar grains in the center, measuring approximately 2.86 nm in diameter and 7 nm in length.

The entire system was first thermalized and equilibrated to zero pressure using the isothermal-isobaric ensemble (NPT) under 3D periodic boundary conditions. For the uniaxial tension simulation, all the samples were deformed either along the ND and TD axes at a constant strain rate of 1×10^9 s^{-1}. Periodic boundary conditions were applied along RD. For ND and TD, the tensile direction was set as "periodic," while the non-loading direction was assigned as "surface." In addition, zero normal stress was maintained along RD during deformation. Virial stresses in the tensile direction were calculated at each strain level. The engineering strain at each time step was calculated as:

$$\frac{l-l_0}{l} \quad \text{(I)}$$

where l and l_0 represent the length of the present and initial box along the tensile direction, respectively. The interaction between individual atoms in the Fe matrix was modeled using a many-body embedded-atom method based on the interatomic potential, which can be expressed as:

$$E_{tot} = \frac{1}{2}\sum_{ij} \mathrm{V}(r_{ij}) + \sum F(\bar{\rho}_i)$$
$$\bar{\rho}_i = \sum_{j \neq i} \rho(r_{ij}) \quad \text{(II)}$$

where $V(r_{ij})$ is the pair potential, r_{ij} is the atomic separation between j and i, F is the embedded energy as a function of $\bar{\rho}_i$, and $\rho(r_{ij})$ is the atomic function.

3. Results

3.1. Phase configuration and microstructure

Figure 3A displays the measured density and the relative density for the AB samples and control group, with the corresponding data summarized in Table S2. The measured density of all the steel bulks exceeded 7.7 g/cm^3 with minor variation, and the values of the AB steels were slightly higher than those of the control group. Compared to the theoretical density of A131 steel (7.85 g/cm^3), all the relative densities were above 98%, illustrating that both AB and HT steels were well-consolidated with minimal defects.

Figure 3B displays the XRD patterns of the steels, with similar peak profiles across A131 steels subjected to different post-processing treatments. This suggests that the crystal structure for the primary phase remained largely unchanged, consisting mainly of the ferrite (α-Fe) and/or martensite (α′), both of which possessed a BCC crystal structure.[17] The α′-phase was preferentially formed in the AB A131 steel due to non-equilibrium consolidation and rapid cooling rates (10^4 – 10^6 K/s) in the melt pool.[30] Subsequent treatments (HT or HR) facilitated the transformation of the α′-phase into α-Fe.[5] In addition, the most prominent diffraction peak corresponded to the crystal plane in all bulks, indicating a preferred crystallographic orientation, which might contribute to anisotropic mechanical performance.

Figure 4 displays the 3D-reconstructed optical microscope (OM) image of the AB bulk microstructure in an orthographic view. Figure 4A features the microstructure of AB A131 steel, revealing minor visible defects, such as holes and unfused particles, further confirming that the AB A131 steel was well-consolidated with full density. The grain size and grain profile were significantly different along ND and TD, which is due to dendritic growth during the consolidation of the melt pool.[37,38] In addition, there was a significant sandwich structure for the grain size in the TD section, a novel heterogeneous structure was formed layer-by-layer, consisting of coarse columnar grains and fine crystals, alongside the laser deposition direction. The layer thickness of columnar grains was ~300 μm, and fine acicular martensite and equiaxed crystals were observed, likely resulting from the high cooling rate and thermal cycles[30] induced by alternating laser deposition layers. Therefore, the imbalanced consolidation provided insufficient kinetics for the phase transformation from γ-Fe to α-Fe and pearlite, when promoting the formation of fine martensite.[39] In addition, the thermal cycle offered necessary thermodynamic advantages for the grain growth of fine crystals alongside ND, where a sandwich-heterostructure was formed, consisting of columnar grains and fine crystals. This heterostructure contributed to the anisotropy in grain orientation, consistent with the XRD results, and eventually induced variations in mechanical performance.

Following tempering, Figure 4B displays the microstructure of HT A131 steel, with significant variations observed for grain sizes and crystal profiles. The sandwich heterostructure was visible but disappeared when the grain size increased. The microstructure of HT A131 steel consisted of equiaxed grains with a typical ferrite-pearlite structure, indicating negligible variation in grain profiles alongside ND and TD. This

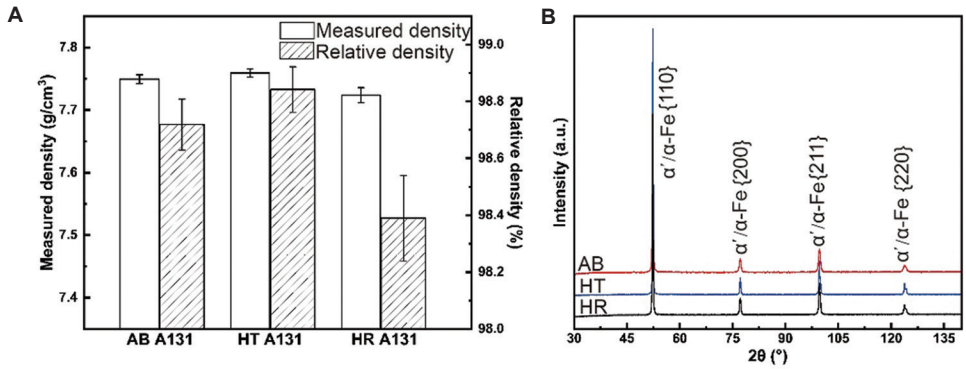

Figure 3. The density (n = 5) (A) and XRD patterns (B) of A131 samples subjected to different processes
Abbreviations: AB: As-built; HT: Heat treatment; HR: Hot rolling

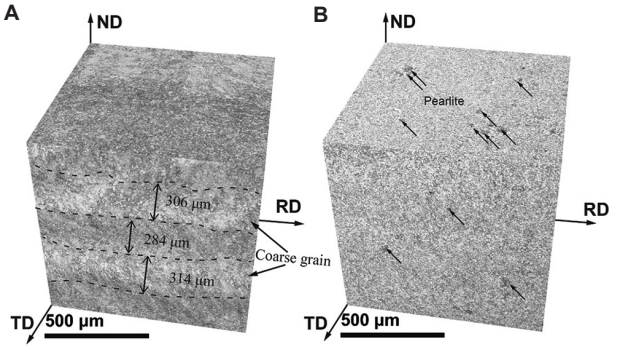

Figure 4. 3D-reconstructed microstructure of A131 steel: (A) AB; and (B) HT. Black arrows in (B) indicate pearlite
Abbreviations: AB: As-built; HT: Heat treatment; ND: Nominal direction; TD: Transverse direction; RD: Rolling direction

is most likely due to the HT process, which provided sufficient kinetic and thermodynamic conditions for both phase transformation and grain growth. In addition, the anisotropy of the microstructure was significantly reduced, which could be beneficial to the isotropic mechanical properties.

Figure 5A-C displays the magnified image of the AB A131 steel microstructure in the ND section. Figure 5A presents an OM image of the fine acicular martensite structure predominated with some coarse equiaxed grains (black arrows), and the acicular martensite possessed a submicron size without specific orientation (Figure 5A, inset). Figure 5B presents an SEM image of the acicular martensite-equiaxed grain structure with notable particle defects (white arrows). These particles (300~800 nm) were randomly distributed (Figure 5B, inset), most likely due to oxidation during the deposition process. As these particles were relatively small (<1 μm), their influence on density is negligible. The magnified SEM image (Figure 5C) highlights the submicron equiaxed grains (~2 μm) and acicular martensite blocks (~5 μm).

Figure 5D-F displays the AB A131 steel microstructure along the TD section at different magnifications. Figure 5D presents the transitional interface between the fine and coarse grains, where the boundary is not distinctive. The coarse-grain part mainly consisted of three types of grains: Coarse columnar grain, middle-size equiaxed crystal, and fine acicular martensite. The maximum length of the continued columnar reached 83.4 μm, surrounded by other small-sized grains. The dimension of equiaxed grains was measured as 16.5 μm, smaller than that of columnar grains (Figure 5D, inset). The size of the fine acicular martensite was the same as the grains in the fine grain region (Figure 5E). The boundary between the coarse- and fine-grain regions depended on the distribution of the columnar grains, and the fine grains primarily consisted of equiaxed grains and acicular martensite (Figure 5E, inset) in a submicron size. The magnified image (Figure 5F) reveals randomly distributed submicron defects and columnar grains as discontinuous lamellae along ND. This observation suggested that the heterogeneous structure was related to dendritic growth in the melt pools, resulting in partial grain coarsening.

To observe the AB A131 steel heterostructure, EBSD analysis was performed on the TD section. Figure 6A features an inverse pole figure (IPF) with grain orientations in different colors, revealing a non-uniform distribution and an optimal grain orientation consistent with the XRD results. According to grain size and grain profiles, the IPF image was divided into three parts (resembling a sandwich structure): Fine grain region (#1), coarse grain region (#2), and fine grain region (#3). The distribution of equivalent circle diameter for the relative regions is displayed in Figure 6B. The fine-grain region (#1) primarily consisted of acicular martensite and small equiaxed grains (average diameter: 6.91 μm), and the maximum diameter was <20 μm. Compared to region #1, grains in coarse grain

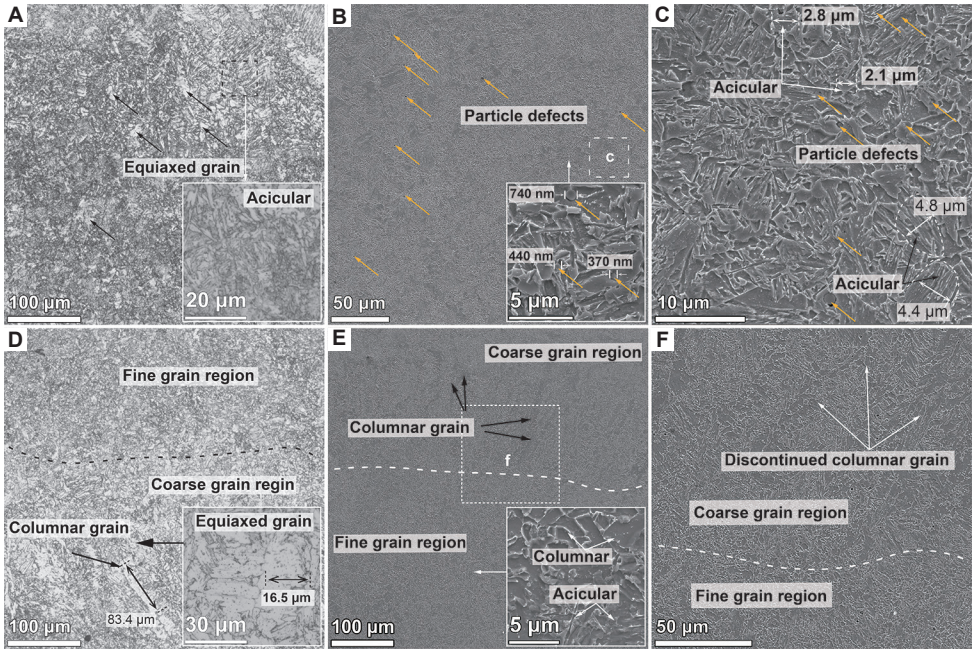

Figure 5. Microstructure of AB A131 along ND (A-C) and TD (D-F). Yellow arrow (B-C): Particle defects. Scale bars: 100 μm (A, D and E); 50 μm (B and F); 10 μm (C)
Abbreviations: AB: As-built; ND: Nominal direction; TD: Transverse direction

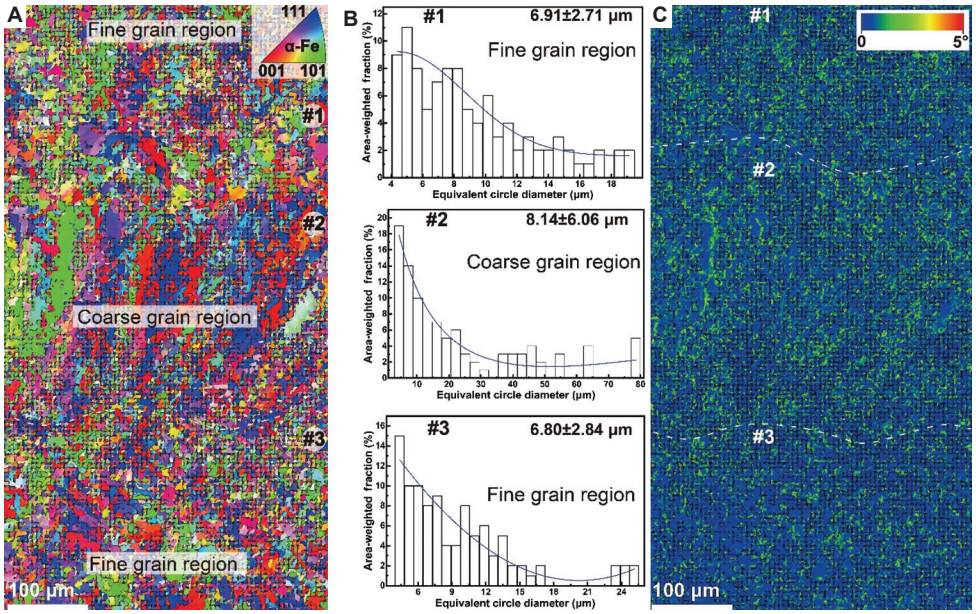

Figure 6. AB A131 steel heterostructure along TD: (A) IPF image; (B) grain size distribution, and (C) KAM mappings alongside the TD direction of AB A131 steel. Scale bars: 100 μm (A and C)
Abbreviations: AB: As-built; IPF: Inverse pole figures; TD: Transverse direction; KAM: Kernel average misorientation

region #2 have a larger average diameter of 8.14 μm and a maximum diameter of up to 80 μm, the increase in both parameters is likely due to the columnar grains. This further confirmed that the coarse-grain region primarily consisted of discontinued columnar grains formed by dendritic growth. In region #3, the average diameter of the grains was 6.8 μm (relatively similar to that of region #1), and the maximum diameter was <25 μm. This indicated that the fine-grain region mainly consisted of fine acicular martensite and small equiaxed grains.

Figure 6C displays the Kernel average misorientation (KAM) mappings, revealing the misorientation angle of the grains related to the lattice distortion. It can be observed that the misorientation was related to the grain size, with smaller grains exhibiting larger misorientation angles. A large misorientation angle corresponds to higher stress within the crystal, most likely due to the martensite phase and rapid cooling rates.

After tempering, the IPF mappings (Figure 7A) display equiaxed grains in HT A131 steel with uniformly distributed colors, suggesting reduced crystal misorientation compared to AB A131 steel. The corresponding pole figures (Figures S1 and S2) further confirmed that the HT process contributed to reducing the maximum orientation density of the grain (from 2.01° to 1.59°). In addition, the heterostructure disappeared, and both grain size and grain profiles became identical (average grain size: 7.93 μm), similar to that of the coarse grain region. This indicated that the HT process led to recrystallization, resulting in different orientations and the formation of equiaxed grains. Compared to AB A131 steel, the KAM mappings (Figure 7B) of HT A131 steel displayed smaller misorientation angles within the grains, likely due to reduced martensite content and grain growth, which helped reduce lattice distortion.

3.2. Mechanical properties

To further investigate the effects of A131 steel microstructure on mechanical performance, uniaxial tensile and hardness tests were performed along ND and TD, respectively. From the stress-strain curves (Figure 8A), AB A131 steel exhibited outstanding tensile strength compared to the other groups, while elongation significantly decreased compared to that of commercial steel along TD (HR-TD). In addition, AB A131 steel exhibited strong anisotropy in tensile strength, with both tensile strength and elongation of AB A131 steel along ND (AB-ND) surpassing those along TD (AB-TD). After the HT process, the performance of HT A131 steel tested along ND (HT-ND) also exceeded that along TD (HT-TD), suggesting that the HT process played a limited role in reducing anisotropy in mechanical performance. Moreover, an interesting Portevin-Le Chandelier (PLC) phenomenon[40,41] was observed in the curves of both AB-TD and HT-TD, leading to stress serrations in the curves. This observation is likely due to the negative strain rate sensitivity induced by dynamic strain aging effects,[42,43] where crystal misorientation of the grains led to increased dislocation interactions along TD under the given strain rate.

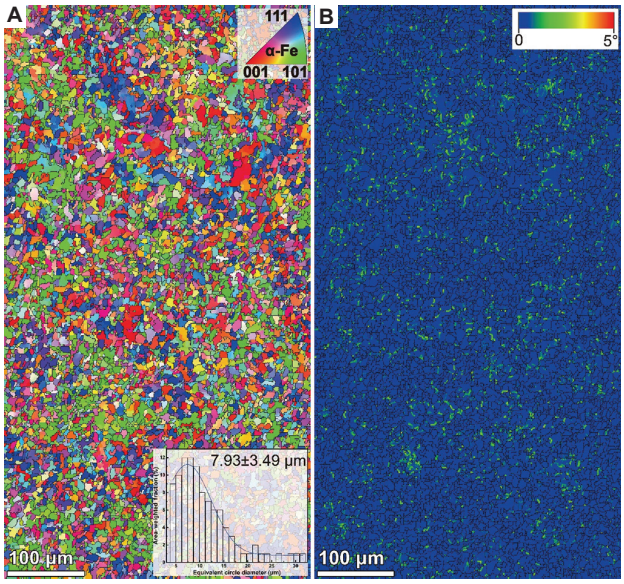

Figure 7. HT A131 steel heterostructure along TD: (A) IPF image; and (B) KAM mappings. (A, inset) a bar chart of the grainsize distribution. Scale bars: 100 μm

Abbreviations: HT: Heat treatment; IPF: Inverse pole figures; KAM: Kernel average misorientation; TD: Transverse direction

Figure 8B displays true stress-strain curves and corresponding work-hardening behavior based on Figure 8A, indicating that the work-hardening curve of HR-TD gradually decreases after the yield strength (σ_{YS}) point, with the rate of work-hardening declining gradually as elongation increases. The work-hardening rates of AB A131 steel decreased dramatically against the increasing rates of strains, especially for the AB-TD curve, likely due to limited elongation. Moreover, significant stress serrations were observed in the work-hardening curves along TD for both AB and HT A131 steel, attributed to the PLC effects, leading to notable stress fluctuations. This suggested that work hardening was limited in resisting deformation during the tensile test along TD at the given strain rate.

The corresponding σ_{YS}, ultimate tensile strength (σ_{UTS}), and elongation are displayed in Figure 8C, and the corresponding data are summarized in Table S3. Compared to the σ_{YS} (346.5 MPa) and σ_{UTS} (545.0 MPa) of HR-TD, the σ_{YS} and σ_{UTS} of AB-ND dramatically improved by 168.3% and 78.0%, respectively, with the strain of 24.6% meets the definition of the EH A131 standard (19~26% in strain). The performance of AB A131 steel decreased slightly in TD but reported enhanced σ_{YS} and σ_{UTS} of 132.2% and 46.6%, respectively, with a 65.5% reduction in elongation. This was attributed to the predominant acicular martensite and fine equiaxed grain (Figures 4-6), resulting in notable improvements in strength. After the HT process, HT A131 steel reported reduced strength, with enhancements of 70.0% and 24.1% in σ_{YS} and σ_{UTS}, respectively, for HT-ND, while HT-ND exhibited a 4.6% decrease in σ_{UTS}.

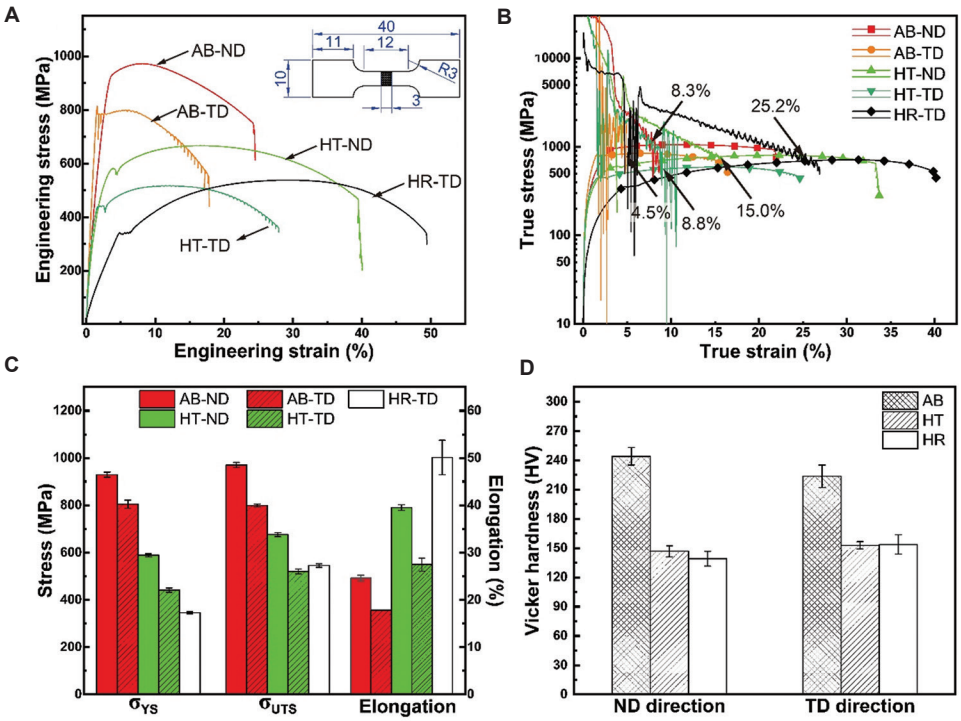

Figure 8. Room-temperature mechanism performances of A131 steel. (A) Room-temperature uniaxial strain-stress tensile curves. (B) True strain-stress tensile curves. (C) Tensile properties (n = 3). (D) Hardness (n = 10)
Abbreviations: AB: As-built; HR: Hot rolling; HT: Heat treatment; ND: Nominal direction; TD: Transverse direction

This observation was attributed to the elimination of fine martensite and the misorientation of the grains (Figure 7), leading to significant anisotropy in resistance deformation along the TD orientation.

Figure 8D displays the Vicker hardness of A131 steels along ND and TD, with corresponding values summarized in Table S4. All steels exhibited notable hardness anisotropy, with strength and elongation anisotropy ratios estimated in Table S5. In both AB and HT A131 steels, hardness was higher in ND compared to TD, whereas HR A131 steel displayed the opposite trend. Similar to the tensile results, AB A131 steel displayed the highest hardness, achieving a 75.5% increase over HR A131 steel in ND (139 HV). After HT, HT A131 steel exhibited a notable decrement in hardness in both directions, likely due to the formation of equiaxed grains with reduced misorientation. While HT A131 steel had a similar phase composition to HR A131, it offered only a marginal hardness advantage, though both retained higher anisotropy ratios than A131 steel fabricated using other DED methods[17] or wire-arc AM.[44]

Figure 9 presents the fracture morphologies of AB A131 steel along ND. Figure 9A displays the fracture surface at the edge close to the necking section, with numerous internal defects (white arrows). A magnified view (Figure 9B) reveals submicron holes (~20 μm) (Figure 9B, inset) surrounded by abundant dimples. These defects likely originated from small closed pores and inclusions inside the melt pools, which enlarged under tensile stress. Figure 9C highlights broken, spherical inclusions surrounded by dimples. EDS analysis (Figure 9C, inset) verified that these inclusions were rich in oxygen (> 50 at%), identifying them as oxide inclusions. Figure 9D features the middle of the fracture surface, also revealing visible holes (Figure 9E) and oxide inclusions (Figure 9F). These defects likely contributed to a significant decrease in elongation and a rapid decline in work-hardening rates. However, the prevalence of dimples indicates that plastic deformation remained predominant under tensile loading.

4. Discussion

In this experiment, AB A131 steel exhibited a unique heterogeneous structure composed of alternating coarse- and fine-grain regions, leading to significantly enhanced mechanical performance. To reveal the formation mechanism of the heterostructure, a single-pass deposition was carried out with the same DED parameters.

The overall cross-sectional microstructure is displayed in Figure S3, with high-magnification images presented in Figure 10. Figure 10A displays an OM image of the top region, revealing a notable orientation of the crystals

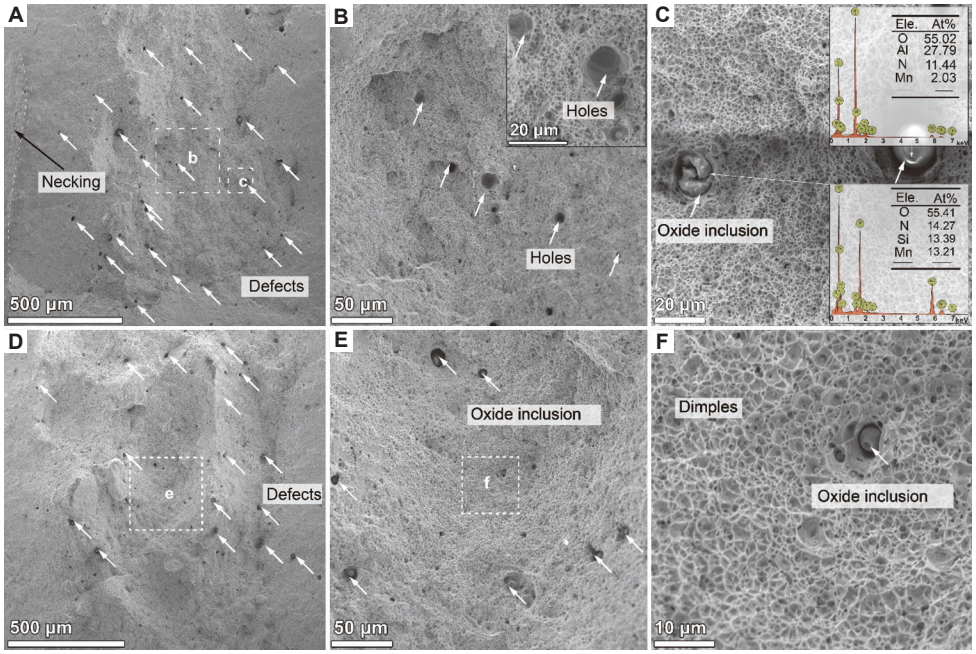

Figure 9. Broken surface of the tensile sample of AB A131 steel: (A-C) SEM images of defects at the edge; and (D-F) SEM images of defects in the middle. (C, inset) EDS spectrums of the particle defect. Scale bars: 500 μm (A and D); 50 μm (B and E); 20 μm (C); 10 μm (F)
Abbreviations: AB: As-built; SEM: Scanning electron microstructure; EDS: Energy dispersive spectrometer; O: Oxygen; Al: Aluminum; N: Nitrogen; Mn: Manganese

along ND. The grains were relatively small and comprised columnar grains, fine acicular martensite, and some equiaxed grains, attributed to dendritic growth during the consolidation of the melt pool under rapid cooling rates.[45] Discontinuous columnar crystals were formed along ND and surrounded by fine martensite. The IPF mappings (Figure 10B) further confirmed dendritic crystal formation along the build direction, consisting of columnar and fine-equiaxed grains with a weak (101) crystal orientation and a huge misorientation angle of 5.24° (Figure S4). The average equivalent grain size was 6.33 μm, with a maximum of 83.6 μm due to dendritic growth of the columnar grains.

Figure 10D displays the microstructure of the single-pass track in the middle region, featuring coarse columnar grains and acicular martensite. Compared to the top region (Figure 10A-C), the columnar grains are more evident (Figure 10E), indicating significant coarsening due to limited thermal conduction and a lower temperature gradient at the center of the melt pool.[46] This results in a discrepancy in grain size from the center to the edge, accompanied by increased crystal misorientation of 6.03° (Figure S5). The average grain size slightly decreased to 5.93 μm, but the maximum grain size significantly increased to 146.8 μm with a high area ratio (Figure 10F), substantially greater than in AB A131 steel (Figure 6). This suggests that alternating remelting and cyclic thermal effects helped refine the coarse columnar grains.

Figure 10G displays the microstructure at the interface between the single-pass track and the 304L steel substrate, consisting of equiaxed grains and acicular martensite. A distinctive interface could be observed, where fine A131 steel grains are deposited on the top of coarse 304L substrate grains. Compared to the microstructure of the single-pass track at the top (Figure 10A-C) and middle (Figure 10D-F) regions, the grains near the substrate (Figure 10H) resemble the fine-grained regions (Figures 4A; 5D and E; and 6), and the misorientation significantly decreased (Figure S6). The average grain size is approximately 5.45 μm (Figure 10I), slightly smaller than that of AB A131 steel (6.8 μm), with a maximum diameter of 31.6 μm. This suggests that laser thermal cycling promotes submicron-scale grain growth, leading to a slight increase in the average size. Such effects facilitate the formation of alternating fine- and coarse-grain regions during one-pass deposition. Subsequent passes remelt the surface with similar thermal gradients to those near the 304L substrate, promoting the formation of fined equiaxed crystals. These repeated thermal cycles contributed to the uniform distribution of heterogeneous structures at alternating layers.

To further investigate the heterostructure on anisotropic mechanical performance, an MD model of the sandwich structure was built, consisting of the fine- and columnar-grain regions with a similar volume ratio

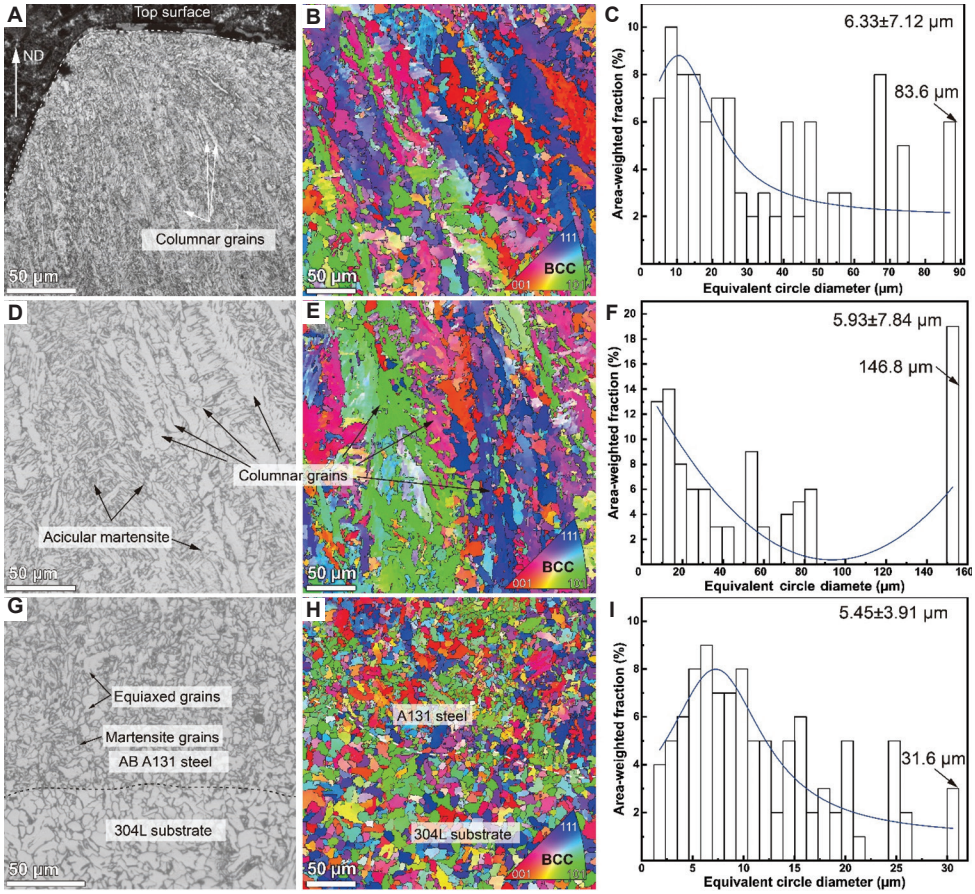

Figure 10. A131 steel microstructure from single-pass deposition: (A-C) top section; (D-E) middle region; and (G-I) bottom section. (A, D, G) OM image; (B, E, H) IPF image with corresponding grainsize distribution (C, F, I). Scale bars: 50 μm
Abbreviations: AB: As-built; BCC: Body centered cubic; IPF: Inverse pole figure; ND: Nominal direction; OM: Optical microscope

(Figure 11A). Tensile tests were simulated along ND and TD at room temperature, and the resulting stress-strain curves are depicted in Figure 11B. The AB A131 steel exhibited optimal tensile strength and elongation along ND. Assuming the fine-grain regions possess isotropy in mechanical performance with a constant elastic modulus (E_0), the coarse columnar grain was considered anisotropic, with distinct elastic moduli along ND (E_{ND}) and TD (E_{TD}). The relationship of the modulus is:

$$E_{ND} > E_{TD} \approx E_0 \quad \text{(III)}$$

When applying the load on the model along ND, according to the parallel connection principle, the relationship of the stress (σ_{ND}) and strain (ε) could be estimated as:

$$\sigma_{ND} = \frac{2E_0 E_{ND}}{E_0 + E_{ND}}\varepsilon \quad \text{(IV)}$$

When the load was only applied along TD, the σ_{ND}-ε could be assessed as:

$$\sigma_{TD} = \frac{E_0 + E_{TD}}{2}\varepsilon \quad \text{(V)}$$

Uniaxial deformation also induces shear stresses in other directions. To simplify the stress model, the ratio of the stresses along TD and ND can be expressed as:

$$n = \frac{\sigma_{TD}}{\sigma_{ND}} = \frac{(E_0 + E_{ND})(E_0 + E_{TD})}{4E_0 E_{ND}}\varepsilon \quad \text{(VI)}$$

Ideally, since $E_{TD} \approx E_0$, n is generally <1, the tensile stress along ND is expected to be higher than that along TD at the same strain level, suggesting a greater tensile strength in the ND orientation.

After applying the load in ND, the tensile results (Figure 11C) reveal an elliptical deformation profile within the coarse-grain region, attributed to strain-induced boundary migration. The fine-grain region was largely consumed, exhibiting minimal misorientation along TD. Strain mappings indicated a high density of localized shear strain at both ends, suggesting that strain

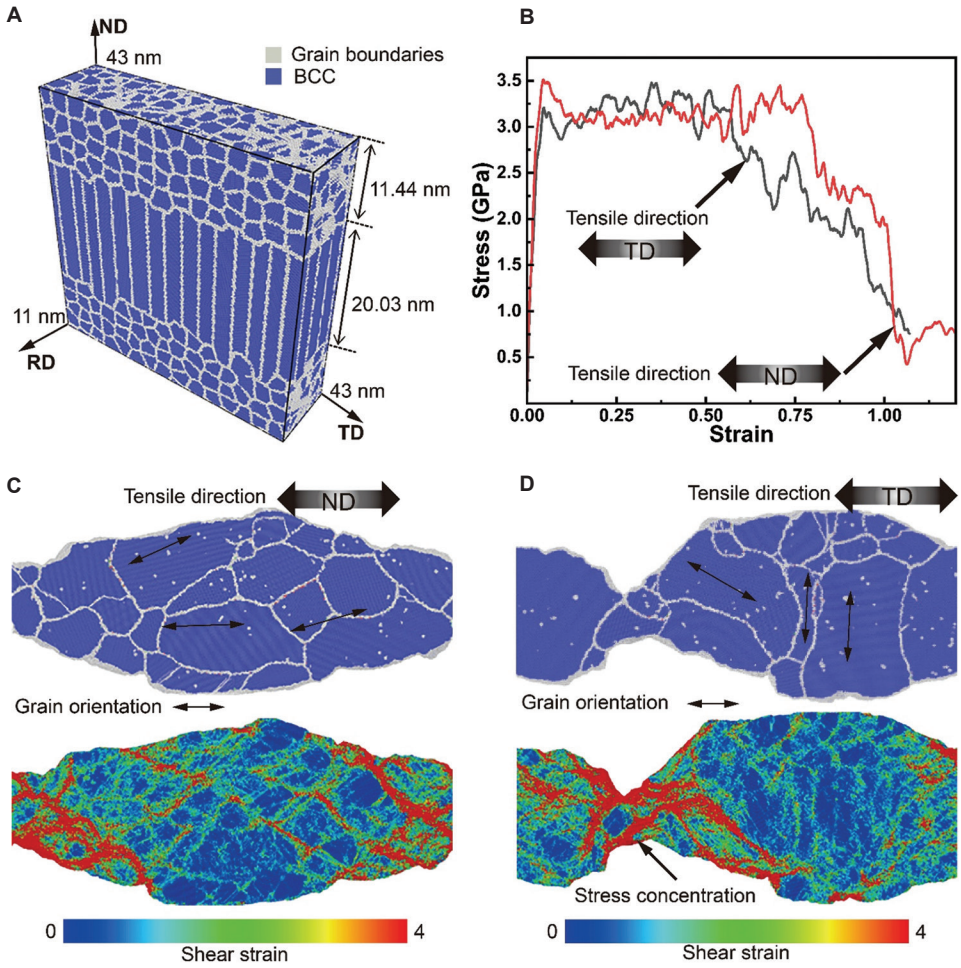

Figure 11. Molecular dynamics (MD) simulation of the heterogeneous structure in AB A131 steel. (A) Model of the heterostructure. (B) Stress-strain curve of the simulation. (C and D) Deformed model and strain mappings along (C) ND and (D) TD
Abbreviations: AB: As-built; ND: Nominal direction; TD: Transverse direction; BCC: Body centered cubic; RD: Roling direction

deformation primarily occurred in the fine-grain region. This behavior contributed to the enhanced tensile strength and high plasticity, consistent with the experiment results of AB-ND.

Under tensile loading in TD, the deformed model (Figure 11D) exhibited an irregular grain profile with notable misorientation along TD. A significant necking phenomenon occurred, characterized by a narrow region where the primary shear strain was concentrated. This suggests uneven deformation and notable stress concentration, which facilitated premature crack initiation and propagation, ultimately reducing tensile strength and elongation. Moreover, the stress concentration also limited the work-hardening capacity under constant loading, consistent with the experimental AB-TD results. Even after HT, HT A131 steel retained the anisotropy performance as tested along different directions, though the heterostructure disappeared. This can be attributed to the optimal crystal orientation along ND (Figures 3B and 7A), which also resulted in significant grain disorientation (Figure S2) and maintained tensile strength differences along different orientations.

5. Conclusion

This study demonstrated the formation of a heterostructure comprising alternative layers of coarse and fine grains in A131 steel fabricated using the DED technique and post-treatment processes. The structure featured notable improvement in strength without the plasticity trade-off. The phase configuration, heterogeneous microstructure, and anisotropy in mechanical performance were thoroughly investigated, with comparisons made to commercial A131 steel. Finally, the formation of the heterostructure and the tensile performance were discussed based on the single-pass deposition and MD simulation, respectively. The main conclusions were summarized as follows:

(i) The AB A131 steel exhibited a high σ_{YS} of 929.5 MPa and σ_{UTS} of 970.4 MPa, approximately 168% and 78% enhancement compared to those of commercial A131 steel (σ_{YS}: 346.5 MPa; σ_{UTS}: 545.0 MPa), with an elongation of 24.5%. After HT, the strength of A131 steel was significantly reduced compared to that before tempering, when retaining 70% enhancement in σ_{YS} compared to commercial A131 steel.

(ii) The A131 steel fabricated by DED methods possesses a significant heterostructure comprising alternating layers of coarse- and fine-grain sections (~300 μm thick), formed due to dendritic growth and thermal cycling. The coarse-grain region mainly consisted of fine columnar grains and acicular martensite, while the fine-grain region featured small equiaxed crystals and fine martensite.

(iii) Tempering treatment of AB A131 steel induced martensite-to-ferrite phase transformation and grain growth into equiaxed structures, reducing crystal misorientation and anisotropy in the microstructure but significantly decreasing mechanical strength.

(iv) The heterostructure induced notable anisotropy in tensile performance, where the tensile properties and hardness of the A131 steel along ND significantly exceeded those in TD. HD had limited impact on reducing anisotropy, even resulting in a 4.6% decrease in σ_{UTS} along TD compared to commercial A131 steel.

(v) MD simulations demonstrated that uniaxial load at ND promoted uniform deformation, enhancing strength and elongation. In contrast, applied load along TD could induce partial stress concentration and necking, reducing both tensile strength and plasticity.

Acknowledgments

None.

Funding

This study was funded by the Guangdong Basic and Applied Basic Research Foundation (2023A1515110594; 2024A1515012049), Shenzhen Science and Technology Program (JCYJ20241202123701003; QTD20210811090146075), and Shenzhen Natural Science Fund (Stable Support Plan Program; GXWD20231129161359002).

Conflict of interest

Yuchao Bai serves as the Guest Editor of the Special Issue, but was not in any way involved in the editorial and peer-review process conducted for this paper, directly or indirectly. Other authors declare they have no competing interests.

Author contributions

Conceptualization: Yuchao Bai
Formal analysis: Jiaming Zhan, Silu Zhang
Investigation: Yuchao Bai, Qi Yan
Methodology: Yuchao Bai, Silu Zhang
Data Curation and Visualization: Qi Yan, Cuiling Zhao
Writing – original draft: Yuchao Bai
Writing – review & editing: Qi Yan, Cuiling Zhao
Funding acquisition: Yuchao Bai

Ethics approval and consent to participate

Not applicable.

Consent for publication

Not applicable.

Availability of data

Data is available from the corresponding author upon reasonable request.

References

1. Kuntanapreeda S, Hess D. Opening access to space by maximizing utilization of 3D printing in launch vehicle design and production. *Appl Sci Eng Prog*. 2021;14(2):143-145.

doi: 10.13316/j.asep/2020/12.002

2. Liu S, Shin YC. Additive manufacturing of Ti6Al4V alloy: A review. *Mater Des*. 2019;164:107552.

doi: 10.1016/j.matdes.2018.107552

3. Liu TS, Chen P, Qiu F, *et al*. Review on laser directed energy deposited aluminum alloys. *Int J Extreme Manuf*. 2024;6(2):022004.

doi: 10.1088/2631-7990/ad16bb

4. Zhang B, Gao Z, Xiao H, Yang X, Li Y, Zhu H. Size effects and optimization during laser directed energy deposition on high thermal conductivity copper alloys. *J Mater Res Technol*. 2024;33:4389-4399.

doi: 10.1016/j.jmrt.2024.10.104

5. Bai Y, Chaudhari A, Wang H. Investigation on the microstructure and machinability of ASTM A131 steel manufactured by directed energy deposition. *J Mater Process Technol*. 2020;276:116410.

doi: 10.1016/j.jmatprotec.2019.116410

6. Gu D, Shi X, Poprawe R, Bourell DL, Setchi R, Zhu J. Material-structure-performance integrated laser-metal additive manufacturing. *Science*. 2021;372(6545):eabg1487.

doi: 10.1126/science.abg1487

7. Seedhouse E, editor. Falcon 9 and falcon heavy. In: *SpaceX: Starship to Mars The First 20 Years*. New York: Springer

International Publishing; 2022. p. 71-93.

8. Materials ASfTa. *ASTM A131/A 131M-04. Standard Specification for Structural Steel for Ships*. Commonwealth of Pennsylvania: ASTM International; 2004.

9. Sirisatien T, Mahabunphachai S, Sojiphan K. Effect of submerged arc welding process with one-side one-pass welding technique on distortion behavior of shipbuilding steel plate ASTM A131 grade A. *Mater Today Proc*. 2018;5(3, Part 2):9543-9551.

   doi: 10.1016/j.matpr.2017.10.136

10. Yan Q, Chen B, Kang N, *et al*. Comparison study on microstructure and mechanical properties of Ti-6Al-4V alloys fabricated by powder-based selective-laser-melting and sintering methods. *Mater Charact*. 2020;164:110358.

    doi: 10.1016/j.matchar.2020.110358

11. Yan Q, Chen B, Jia Z, *et al*. Formation of dual quasi-continuous networked structure and its strengthening effect in Ti-6Al-4V alloy reinforced with graphene via powder bed fusion. *Add Manuf*. 2024;92:104364.

    doi: 10.1016/j.addma.2024.104364

12. Bai Y, Yan Y, Chen J, Liang C, Bi G, Zhao C. Microstructure and mechanical property evolution of 316L/18Ni300 bimetallic structure manufactured by laser powder bed fusion. *Mater Sci Eng A*. 2025;929:148141.

    doi: 10.1016/j.msea.2025.148141

13. Ang LJJ, Huang J, Nai MLS, Wang P. Additive manufacturing techniques for EH36 steels: Challenges and future directions. *ESAM*. 2025;1(1):025060005.

    doi: 10.36922/esam025060005

14. Wenjin W, Beng TS, Kai CC, *et al*. Preliminary investigation on SLM of ASTM A131 EH36 high tensile strength steel for shipbuilding applications. *Proceedings of the 2nd International Conference on Progress in Additive Manufacturing*; 2014.

    doi: 10.3850/978-981-09-0446-3_083

15. Wu W, Tor SB, Merchant AA. Tensile properties of ASTM A131 EH36 shipbuilding steel processed by selective laser melting. *Proceedings of the 3rd International Conference on Progress in Additive Manufacturing*; 2018.

16. Wang J, Wu WJ, Jing W, *et al*. Improvement of densification and microstructure of ASTM A131 EH36 steel samples additively manufactured via selective laser melting with varying laser scanning speed and hatch spacing. *Mater Sci Eng A*. 2019;746:300-313.

    doi: 10.1016/j.msea.2019.01.019

17. Wang J, Chew YX, Wu WJ, *et al*. Microstructure and mechanical properties of ASTM A131 EH36 steel fabricated by laser aided additive manufacturing. *Mater Charact*. 2021;174:110949.

    doi: 10.1016/j.matchar.2021.110949

18. Wang J, Zhang M, Wang B, *et al*. Influence of surface porosity on fatigue life of additively manufactured ASTM A131 EH36 steel. *Int J Fatigue*. 2021;142:105894.

    doi: 10.1016/j.ijfatigue.2020.105894

19. Liu L, Li S, Pan D, *et al*. Loss-free tensile ductility of dual-structure titanium composites via an interdiffusion and self-organization strategy. *Proc Natl Acad Sci U S A*. 2023;120(28):e2302234120.

    doi: 10.1073/pnas.2302234120

20. Gao S, Li Z, Van Petegem S, *et al*. Additive manufacturing of alloys with programmable microstructure and properties. *Nat Commun*. 2023;14(1):6752.

    doi: 10.1038/s41467-023-42326-y

21. Tan C, Li R, Su J, *et al*. Review on field assisted metal additive manufacturing. *Int J Mach Tools Manuf*. 2023;189:104032.

    doi: 10.1016/j.ijmachtools.2023.104032

22. Svetlizky D, Das M, Zheng B, *et al*. Directed energy deposition (DED) additive manufacturing: Physical characteristics, defects, challenges and applications. *Mater Today*. 2021;49:271-295.

    doi: 10.1016/j.mattod.2021.03.020

23. Kong H, Yibo L, Fuxiang L, *et al*. *In situ* fabrication of martensitic stainless steel via heterogeneous double-wire arc-directed energy deposition. *Virt Phys Prototyp*. 2024;19(1):e2350610.

    doi: 10.1080/17452759.2024.2350610

24. Myers MB, Bandyopadhyay A. Understanding the antibacterial efficacy of additively manufactured copper-added 316L stainless steel. *MSAM*. 2025;4(1):7357.

    doi: 10.36922/msam.7357

25. Zuckschwerdt NW, Bandyopadhyay A. Multi-material structures of Ti6Al4V and Ti6Al4V-B4C through directed energy deposition-based additive manufacturing. *MSAM*. 2024;3(3):3571.

    doi: 10.36922/msam.3571

26. Su J, Li Q, Teng J, *et al*. Programmable mechanical properties of additively manufactured novel steel. *Int J Extreme Manuf*. 2025;7(1):015001.

    doi: 10.1088/2631-7990/ad88bc

27. Dan X, Ren C, Song Z, *et al*. Exceptional strength and ductility in heterogeneous multi-gradient TiAl alloys through additive manufacturing. *Acta Mater*. 2024;281:120395.

    doi: 10.1016/j.actamat.2024.120395

28. Wu X, Yang M, Yuan F, *et al*. Heterogeneous lamella structure unites ultrafine-grain strength with coarse-grain ductility. *Proc Natl Acad Sci U S A*. 2015;112(47):14501-14505.

    doi: 10.1073/pnas.1517193112

29. Li D, Fan G, Huang X, *et al*. Enhanced strength in pure Ti via design of alternating coarse- and fine-grain layers. *Acta Mater*. 2021;206:116627.

    doi: 10.1016/j.actamat.2021.116627

30. Tan C, Li Q, Yao X, *et al*. Machine learning customized novel material for energy-efficient 4D printing. *Adv Sci*. 2023;10(10):2206607.

    doi: 10.1002/advs.202206607

31. National Standardization Administration of the People's Republic of China. *GB/T 36165-2018. Determination of Average Grain Size of Metal -- Electron Backscatter Dirffraction (EBSD) Method*. Beijing: National Standardization Administration of the People's Republic of China; 2018.

32. Plimpton S. Fast parallel algorithms for short-range molecular dynamics. *J Comput Phys*. 1995;117(1):1-19.

    doi: 10.1006/jcph.1995.1039

33. Zhan JM, Yao XH, Han F. An approach of peridynamic modeling associated with molecular dynamics for fracture simulation of particle reinforced metal matrix composites. *Compos Struct*. 2020;250:112613.

    doi: 10.1016/j.compstruct.2020.112613

34. Proville L, Choudhury A. Unravelling the jerky glide of dislocations in body-centred cubic crystals. *Nat Mater*. 2024;23(1):47-51.

    doi: 10.1038/s41563-023-01728-5

35. Etesami SA, Asadi E. Molecular dynamics for near melting temperatures simulations of metals using modified embedded-atom method. *J Phys Chem Solids*. 2018;112:61-72.

    doi: 10.1016/j.jpcs.2017.09.001

36. Lim H, Hale LM, Zimmerman JA, Battaile CC, Weinberger CR. A multi-scale model of dislocation plasticity in α-Fe: Incorporating temperature, strain rate and non-schmid effects. *Int J Plastic*. 2015;73:100-118.

    doi: 10.1016/j.ijplas.2014.12.005

37. Vasques CMA, Cavadas AMS, Abrantes JCC. Technology overview and investigation of the quality of a 3D-printed maraging steel demonstration part. *MSAM*. 2025;4(2):025040002.

    doi: 10.36922/msam025040002

38. Li W, Yan L, Chen X, Zhang J, Zhang X, Liou F. Directed energy depositing a new Fe-Cr-Ni alloy with gradually changing composition with elemental powder mixes and particle size' effect in fabrication process. *J Mater Proc Technol*. 2018;255:96-104.

    doi: 10.1016/j.jmatprotec.2017.12.010

39. Donizete Borba TM, Wagner DF, Leonardo DOT, Cardoso R Jr. Assessment of the weldability of EH36 TMCP shipbuilding steel welded by high heat input submerged arc welding. *Weld Int*. 2017;31(3):184-195.

    doi: 10.1080/09507116.2016.1218619

40. Potez L, Lapasset G, Kubin L. Jerky flow (the PLC effect) in Ll2 Al3Ti-based alloys. *Scr Metallurgica Mater*. 1992; 26(5):841-846.

    doi: 10.1016/0956-716X(92)90449-O

41. Hsu WC, Shen TE, Liang YC, Yeh JW, Tsai CW. *In situ* analysis of the portevin-le chatelier effect from low to high-entropy alloy in equal HfNbTaTiZr system. *Acta Mater*. 2023;253:118981.

    doi: 10.1016/j.actamat.2023.118981

42. Ananthakrishna G. Current theoretical approaches to collective behavior of dislocations. *Phys Rep*. 2007; 440(4-6):113-259.

    doi: 10.1016/j.physrep.2006.10.003

43. Sarkar A, Maloy SA, Murty KL. Investigation of portevin-le chatelier effect in HT-9 steel. *Mater Sci Eng A*. 2015;631:120-125.

    doi: 10.1016/j.msea.2015.02.022

44. Vahedi Nemani A, Ghaffari M, Nasiri A. Comparison of microstructural characteristics and mechanical properties of shipbuilding steel plates fabricated by conventional rolling versus wire arc additive manufacturing. *Add Manuf*. 2020;32:101086.

    doi: 10.1016/j.addma.2020.101086

45. Chen ZW, Phan MAL, Darvish K. Grain growth during selective laser melting of a co-cr-mo alloy. *J Mater Sci*. 2017;52(12):7415-7427.

    doi: 10.1007/s10853-017-0975-z

46. Kok Y, Tan XP, Wang P, *et al*. Anisotropy and heterogeneity of microstructure and mechanical properties in metal additive manufacturing: A critical review. *Mater Des*. 2018;139:565-586.

    doi: 10.1016/j.matdes.2017.11.021

ACCSCIENCE PUBLISHING

Materials Science in Additive Manufacturing

ORIGINAL RESEARCH ARTICLE

Sustainable manufacturing of FDM-manufactured composite impellers using hybrid machine learning and simulation-based optimization

Subramani Raja[1], Ahamed Jalaludeen Mohammad Iliyas[1], Paneer Selvam Vishnu[1], Amaladas John Rajan[2], Maher Ali Rusho[3], Mohamad Reda Refaai[4]*, and Oluseye Adewale Adebimpe[5]

[1]Center for Advanced Multidisciplinary Research and Innovation, Chennai Institute of Technology, Chennai, Tamil Nadu, India

[2]Department of Mechanical Engineering, School of Mechanical Engineering, Vellore Institute of Technology, Chennai, Tamil Nadu, India

[3]Research and Development Unit, Mr.R BUSINESS CORPORATION, Karur, Tamil Nadu, India

[4]Department of Mechanical Engineering, College of Engineering, Prince Sattam bin Abdulaziz University, Al-Kharj 11942, Saudi Arabia

[5]Department of Industrial and Production Engineering, Faculty of Technology, University of Ibadan, Ibadan, Oyo, Nigeria

***Corresponding author:**
Mohamad Reda Refaai
(m.rifaee@psau.edu.sa)

Citation: Raja S, Mohammad Iliyas AJ, Vishnu PS, *et al*. Sustainable manufacturing of FDM-manufactured composite impellers using hybrid machine learning and simulation-based optimization. *Mater Sci Add Manuf*. 2025;4(3):025200033. doi: 10.36922/MSAM025200033

Received: May 14, 2025

Revised: June 24, 2025

Accepted: July 4, 2025

Published online: July 28, 2025

Abstract

Conventional optimization of fused deposition modeling (FDM) often relies on trial-and-error or heuristic approaches, which lack scalability and precision, especially for complex geometries such as impellers. While prior studies have integrated artificial intelligence (AI) or multi-criteria decision-making (MCDM) techniques for process optimization, their combined application remains limited, particularly in scenarios that prioritize energy-efficient and sustainable manufacturing. This study introduces a novel hybrid AI-MCDM framework for the multi-objective optimization of FDM-printed composite impellers, integrating mechanical performance, energy consumption, and material utilization within a unified decision-making model. A key feature of the approach is the real-time tracking of energy usage, enabling dynamic evaluation of process efficiency. Experimental validation demonstrates a 7% enhancement in tensile strength, a 25% reduction in energy consumption, and a 30% decrease in material wastage compared to baseline configurations. These results underscore the potential of AI-driven simulation and optimization frameworks to support sustainable additive manufacturing, with significant implications for aerospace, biomedical, and energy sector applications.

Keywords: Fused deposition modeling; Rapid prototyping; Machine learning; Multi-criteria decision-making; Sustainable manufacturing; Optimization algorithms; Mechanical characterization; SDG Goals

1. Introduction

Fused deposition modeling (FDM) is the most commonly used additive manufacturing (AM) technology, due to its ease of operation, affordability, capability to produce

intricate geometries, and low material waste. FDM entails passing a thermoplastic filament through a heated extruder nozzle, where it is melted and pushed layer-wise onto a build platform. As every new layer is deposited, it melts into the one below it, building up gradually to the shape of the desired 3D part. Important process parameters, including layer thickness, infill density, printing speed, and nozzle temperature, significantly influence the mechanical performance, surface finish, and energy efficiency of the printed object. FDM is widely applied in multiple industries, such as aerospace, automotive, biomedical, consumer products, and rapid prototyping, due to its capability to produce light, personalized, and functionally graded parts. Regardless of its extensive utilization, maintaining uniform mechanical quality and energy-efficient production remains a challenge, especially for geometrically complex components such as impellers.[1,2] The efficiency of an impeller is a key factor influencing energy consumption and operational performance; therefore, optimizing its manufacturing processes to enhance mechanical strength, minimize material wastage, and improve energy efficiency is of significant interest. However, the optimization of FDM process parameters is typically conducted using trial-and-error methods, which are inefficient with complex trade-offs in mechanical performance, energy consumption, and sustainability. This limitation underscores the need for artificial intelligence (AI) and machine learning (ML)-based methods in optimizing FDM-based manufacturing of impellers. These advances have facilitated data-driven process optimization, allowing real-time decision-making and predictive modeling of AM. Studies have demonstrated that mechanical properties can be predicted with reasonable accuracy using ML algorithms based on process parameters, thereby improving print quality and minimizing defects.[3-5]

In addition, MCDM techniques, such as fuzzy analytic hierarchy process (AHP) and the Technique for Order of Preference by Similarity to Ideal Solution (TOPSIS), have been used extensively to compare and rank various process conditions based on different performance measures, such as mechanical integrity, energy efficiency, and material efficiency.[6-8] While AI and ML have made considerable advances, limited research works have utilized AI-based MCDM platforms to optimize FDM processing for the production of impellers. With the increasing demand for sustainable, lightweight, and high-performance impellers, there is a need for a holistic AI-based optimization strategy to address the United Nations' Sustainable Development Goals (SDGs). Minimizing energy consumption during printing is a critical aspect of sustainability in the FDM-based production of impellers. In this study, a power meter was utilized to record real-time energy consumption of the FDM printer, providing valuable insights into energy efficiency across various process parameters. This approach facilitates the identification of optimal printing conditions that minimize power consumption while maintaining structural integrity and mechanical performance. Although AI has been utilized extensively for process automation and defect prediction, limited research has utilized real-time monitoring of energy consumption within AI-MCDM platforms for sustainable impeller production.

This study proposes a theoretical AI-assisted MCDM approach of FDM process parameter optimization in the production of composite impellers. This approach systematically analyzes the effect of significant FDM parameters – including layer thickness, infill density, nozzle temperature, and print speed – on mechanical properties, energy efficiency, and material usage. ML algorithms, combined with fuzzy AHP and TOPSIS, were employed to support multi-objective decision-making. Mechanical characterization through tensile, flexural, wear, and compression testing, along with scanning electron microscopy analysis, validates the optimized parameters. Real-time power monitoring enables quantitative assessment of energy consumption, reinforcing the sustainability dimension of the process. The results could benefit sustainable AM practices, optimizing production performance and environmental footprint in fluid-handling applications.

1.1. AI-driven optimization of FDM

The convergence of ML and AI with AM has significantly advanced process optimization, in-process monitoring, and defect detection, especially for FDM, the most common AM process. FDM is valued for its cost-effectiveness, simplicity, and ability to create complex geometries with minimal material wastage.[9] However, optimizing FDM-produced parts remains challenging due to the interdependencies between different process parameters, such as infill density, cooling rate, nozzle temperature, print speed, and layer thickness. These parameters collectively influence mechanical strength, surface finish, energy utilization, and material consumption. Conventional optimization methods, including empirical modeling and trial-and-error, are non-adaptive,[10] making it even more challenging to balance sustainability, production efficiency, and quality. AI optimization techniques – such as artificial neural networks (ANNs), convolutional neural networks (CNNs), decision tree algorithms, support vector machines (SVMs), and reinforcement learning (RL) – have demonstrated significant promise in optimizing FDM processes by enabling predictive modeling, real-time monitoring, and adaptive control.[11-13] Zhou *et al.*[14] provided a comprehensive review of AI applications in

AM, highlighting how ML algorithms can simplify FDM processes by offering data-driven insights and automation. Interestingly, ML models trained on extensive process and mechanical testing data have achieved high accuracy in predicting material behavior and performance outcomes. ANNs have been widely employed to develop surrogate models capable of replacing computationally intensive finite element analysis (FEA), thus accelerating design iterations. Gaussian process regression (GPR) and deep neural networks (DNNs) have been employed to optimize input parameters for desired output qualities, including tensile strength, impact resistance, and dimensional accuracy.[15] CNNs have demonstrated potential in detecting surface defects in FDM-printed parts through image-based inspection, enabling real-time feedback and automatic quality control.[16] AI-powered computer vision systems have been employed to develop closed-loop control systems that dynamically adjust FDM parameters during printing, effectively minimizing defects such as warping, delamination, and stringing. Another significant use of AI-enhanced FDM optimization involves integrating MCDM methods, such as Fuzzy AHP and TOPSIS. These methods systematically examine trade-offs among mechanical performance, energy consumption, and material usage, supporting the development of more sustainable printing setups.[17-19]

One of the critical challenges related to FDM is its variable energy consumption, which is heavily influenced by print parameters, material types, and machine efficiency. To address this issue, researchers have applied real-time power monitoring using power meters and AI algorithms to forecast and minimize energy consumption without compromising the structural integrity of the printed parts.[20-22] Empirical studies have demonstrated that AI-augmented energy modeling can reduce FDM power consumption by dynamically adjusting nozzle temperature and print speed, thereby maximizing energy efficiency without compromising part quality. In addition, RL methodologies have also been explored for self-adaptive parameter tuning, where AI agents learn optimal print settings iteratively by trial and error, improving decision-making capabilities with real-time feedback.[23] The application of generative adversarial networks (GANs) in topology optimization represents a novel approach, enabling the generation of mechanically efficient yet lightweight FDM-printed structures that support material conservation and sustainability.[24] Furthermore, AI-driven defect detection systems have advanced significantly, allowing early detection of print failures. Consequently, this approach reduces material waste and production downtime. The integration of AI with Internet of Things (IoT) sensors has also assisted in smart manufacturing. For instance, FDM machines equipped with real-time temperature, vibration, and humidity sensors can feed process data to AI models for predicting potential failures and recommending corrective actions before defects occur.[25]

Predictive maintenance has been most advantageous in industrial manufacturing, where machine reliability directly impacts the success of mass production operations. Hybrid AI approaches, combining ML with physics-based simulation, have proven to enhance the accuracy of forecasting thermal distortion and residual stress in FDM-printed components, addressing a significant gap in AM process validation. Another vital research area is AI-driven toolpath optimization. AI models analyze and generate optimal extrusion paths that minimize travel time, material consumption, and stress formation in printed components. The technique is particularly useful in impeller production, where highly curved geometries demand careful control of extrusion direction and layer adhesion to provide fluid dynamic performance and structural integrity. Finally, AI-driven part orientation algorithms have been developed to determine the optimal positioning of FDM-printed parts on the build platform. These algorithms reduce the need for support structures and post-processing while simultaneously enhancing surface finish quality. In biomedical applications, AI-assisted bioinspired design optimization enables the production of patient-specific prosthetics and implants. ML algorithms process patient scan data to generate personalized FDM-printable models with optimized mechanics.[26] In aerospace and automotive applications, AI-facilitated design of lightweight structures has resulted in significant material savings by leveraging lattice and honeycomb infill patterns optimized by deep learning algorithms.[27]

Despite these advancements, challenges remain regarding the generalizability and interpretability of AI models due to the inherent variability in FDM processes, which arise from different material properties, machine inconsistencies, and environmental factors. Existing work has focused on enhancing AI robustness by employing transfer learning schemes, whereby pre-trained models from similar AM processes are adapted to new materials and machine setups with minimal retraining sample sizes. Another promising direction is the integration of AI with digital twin technologies, which synchronizes real-time data from FDM printers with digital simulations to enable predictive process optimization and adaptive process control. Further evolution of AI in FDM is expected to be driven by edge computing and cloud-based facilities, enabling real-time, multi-party optimization of AM processes within distributed manufacturing networks.

In addition, AI-powered sustainability frameworks are being created to minimize the carbon footprint of FDM printing. These frameworks support the alignment of AI-enabled manufacturing with the circular economy. With AI capabilities under development, its potential in FDM will shift from parameter optimization to end-to-end process automation, where intelligent autonomous systems automate the entire AM process, thereby enabling a new paradigm of green, high-performance, and fully autonomous additive manufacturing.

1.2. MCDM in FDM process optimization in impeller production

The application of MCDM methods has gained significant attention in optimizing the FDM process for fabricating impellers, likely due to challenges in identifying an optimal set of process parameters that balance mechanical performance, energy efficacy, and material utilization. Impellers, which are critical components in pumps, turbines, and compressors, demand high precision in terms of geometric accuracy, structural integrity, and fluid flow dynamics.[28-30] The most significant concern in the FDM-based production of impellers is the intrinsic trade-offs amongst conflicting objectives, such as maximizing mechanical strength and surface finish while simultaneously minimizing printing time and energy utilization. Conventional optimization methods, such as trial-and-error and single-objective optimization models, proved inadequate in portraying these multi-dimensional interactions, warranting the implementation of advanced MCDM paradigms. Recent studies have demonstrated the effectiveness of hybrid MCDM methods that combine the application of Fuzzy AHP, TOPSIS, and genetic algorithms (GA) to systematically select and rank the best process parameters for FDM-fabricated impellers.[31-33]

Mechanical integrity is one of the most critical performance parameters for impellers, and it is influenced by a dynamic set of process parameters, including extrusion temperature, layer thickness, infill density, and print speed. Prior research has demonstrated that higher infill density and lower layer thickness can significantly improve mechanical strength and surface finish, but these adjustments typically result in higher energy consumption and a longer print time.[34] Conversely, a higher print speed reduces production time but compromises interlayer adhesion and structural integrity.[35] To avoid such trade-offs, Fuzzy AHP has been utilized to assign weights to performance criteria based on expert evaluations. These weights are then incorporated into TOPSIS to rank various parameter sets in terms of closeness to an ideal solution.[35,36] This hybrid approach enables the selection of optimal process parameters that simultaneously maximize tensile strength, flexural strength, impact resistance, and surface roughness, all of which are key attributes for impeller performance in high-speed fluid applications.

Beyond mechanical performance, energy efficiency has emerged as a pivotal consideration in FDM-based impeller manufacturing. The integration of power meters into FDM machines has enabled real-time monitoring of actual energy consumption, providing valuable data for process optimization. Empirical studies have demonstrated that higher extrusion temperatures enhance interlayer adhesion but significantly increase power consumption, while lower extrusion temperatures reduce energy usage at the expense of weakened interlayer bonding.[37-39] In response to these trade-offs, researchers have developed AI-assisted MCDM frameworks that incorporate real-time energy data into the decision-making process. These intelligent systems enable dynamic optimization of parameters such as extrusion temperature, print speed, and cooling settings, aiming to minimize power consumption while preserving mechanical integrity.

Surface roughness is another critical performance determinant for impellers, as it directly affects fluid efficiency and resistance to cavitation. Elevated surface roughness promotes turbulent flow and energy losses, ultimately diminishing the impeller's overall efficiency. Conventionally, improving surface finish requires post-processing techniques such as sanding or chemical smoothing – methods that are both time-consuming and costly. Recent MCDM-based studies, however, have focused on in-process optimization by tuning parameters such as layer height, nozzle temperature, and print speed, which naturally influence surface quality. Hybrid optimization frameworks that integrate GA with MCDM approaches have demonstrated success in automating the selection of process parameters to achieve low surface roughness. These methods reduce or eliminate the need for post-processing, thereby enhancing manufacturing efficiency and cost-effectiveness in FDM-based impeller production.[40-42]

The integration of MCDM methods with AI has further advanced impeller optimization by enabling predictive modeling and real-time process control. Leveraging ML algorithms trained on historical print data, researchers have developed adaptive MCDM models capable of predicting defects and dynamically adjusting process parameters during fabrication.[42] This approach has led to significantly higher first-print success rates, thereby minimizing material waste and improving overall production efficiency. In addition, the incorporation of metaheuristic optimization techniques, such as the Non-dominated Sorting Genetic Algorithm II (NSGA-II) and

Gray Relational Analysis (GRA), has yielded superior multi-objective optimization outcomes. These methods have proven effective in identifying process parameter sets that offer an optimal balance among mechanical strength, energy efficiency, and surface finish – key factors in high-performance impeller fabrication.

Recent advancements have also seen the application of MCDM techniques in the production of composite impellers, particularly those fabricated using high-performance thermoplastics such as carbon fiber-reinforced polyether-ether-ketone (CF-PEEK). These materials are highly valued for their exceptional strength-to-weight ratios and thermal resistance, making them suitable for demanding applications. Optimization studies employing a hybrid Fuzzy AHP-TOPSIS framework have identified an optimal combination of process parameters for CF-PEEK impeller production, including a 70% infill density, 0.15 mm layer height, 60 mm/s print speed, and an extrusion temperature of 445°C. This parameter set has been ported to deliver superior mechanical strength while maintaining energy efficiency. These findings underscore the growing relevance of MCDM-based optimization models in the development of next-generation impellers for aerospace, marine, and advanced industrial fluid systems.[43]

Despite significant progress, a key challenge that persists is the limited generalizability of current MCDM-based models to diverse impeller geometries and material compositions. Future research must focus on further advancing AI-enhanced MCDM frameworks through the integration of real-time sensor data, enabling adaptive control of printing parameters based on in-situ mechanical and thermal feedback. This would allow for dynamic process optimization tailored to varying design and material requirements. Furthermore, the incorporation of sustainability metrics – such as carbon footprint assessments and life cycle analysis (LCA) – into MCDM models will be essential in steering FDM-based impeller manufacturing toward circular economy principles. With continuous advancements in AI, the IoT, and decision-making algorithms, the future of impeller production is poised to become more sustainable, intelligent, and autonomous, supporting the creation of high-performance, energy-efficient components for industrial fluid systems.

1.3. AI-based waste reduction and energy optimization in 3D printing

The integration of AI and ML into AM has become a driving force in minimizing material and energy waste, thereby advancing the sustainability of 3D printing. Conventional AM techniques, particularly FDM, often suffer from inefficiencies, such as excessive material usage, high-energy consumption, and limited control over process parameters. AI-driven approaches address these challenges through predictive modeling, real-time process optimization, and adaptive control mechanisms. By leveraging AI-based systems, research institutions and industrial entities can significantly reduce material wastage, enhance energy efficiency, and maximize overall process performance, aligning 3D printing practices with circular economy principles. A major source of inefficiency in AM is failed prints, which often result from over-supporting structures, suboptimal parameter settings, warping, or poor interlayer adhesion. Studies have demonstrated that defective prints account for approximately 10 – 30% of material waste in FDM processes.[44] To mitigate these losses, AI-based real-time defect detection systems utilizing computer vision and CNNs have been developed. These systems continuously monitor the printing process and detect potential defects as they emerge, enabling real-time corrective actions such as adjusting extrusion temperature, print speed, or feed rate to prevent print failure. Furthermore, ML-based predictive models trained on historical print data have achieved defect detection accuracies of up to 90%, offering a proactive means of minimizing material loss and enhancing process reliability.

Another major sustainability challenge in 3D printing is the overuse of support structures, which not only leads to significant material wastage but also increases post-processing time and costs. To address this, AI-enabled topology optimization and generative design techniques have been employed to minimize support requirements without compromising part strength or manufacturability. Combined with lattice structure optimization algorithms, these approaches allow for the design of mechanically robust and lightweight parts, resulting in substantial raw material savings. Empirical studies have demonstrated material reductions of 20 – 40% through AI-driven topology optimization, while maintaining mechanical performance.[45] Beyond waste minimization, AI also plays a pivotal role in optimizing energy consumption in AM processes. Energy usage in FDM systems is highly sensitive to parameters such as print speed, nozzle temperature, layer thickness, and infill density. AI-powered energy simulation systems – leveraging deep learning architectures such as long short-term memory (LSTM) networks and RL – enable real-time parameter prediction and adjustment to lower energy usage while preserving print quality. Coupled with real-time power monitoring through smart meters and intelligent sensors, these systems enable adaptive energy management strategies, achieving energy savings of 15 – 30% during production.[46] Recent advances in AI-based production scheduling further enhance energy

efficiency. By analyzing historical energy usage, print job complexity, and machine utilization patterns, AI algorithms can schedule prints during off-peak hours, capitalizing on cheaper and cleaner energy sources. In industrial AM settings, multi-objective AI optimization frameworks are increasingly employed to simultaneously reduce material consumption, energy demand, and build time, ensuring both environmental and economic viability.[47] AI-integrated MCDM tools, such as Fuzzy AHP and TOPSIS, enable manufacturers to make informed decisions based on trade-offs between mechanical properties, material usage, and energy efficiency. These AI-enhanced systems have been reported to reduce failed prints by 25%, lower energy costs by 30%, and improve production efficiency by up to 15%.[48] Moreover, AI is increasingly powering circular economy practices in AM, particularly in the recycling and reuse of materials. ML algorithms are used to sort and process waste filaments, ensuring that recycled materials maintain optimal printability and mechanical integrity. Predictive models are also used to assess the degradation of recycled polymers, allowing adaptive print settings to compensate for material inconsistencies. As a result, companies have reported 30 – 50% reductions in the consumption of new materials through AI-enhanced recycling systems. In addition to energy and material efficiency, AI has significantly contributed to process parameter automation, enabling closed-loop control systems that dynamically adjust variables such as extrusion pressure, cooling rates, and print speed. These feedback-based systems enhance print consistency while minimizing waste. AI-based predictive maintenance also helps anticipate machine failures, thus reducing unplanned downtime and resource loss.[49] Despite these advancements, several challenges remain. Many current AI models are tailored to specific machines or materials, limiting their scalability across diverse AM platforms. Furthermore, the computational intensity of real-time monitoring and optimization remains a barrier to widespread industrial deployment. Future efforts should focus on developing hybrid AI approaches that integrate data-driven learning with physics-based simulations to achieve broader applicability and more accurate, scalable optimizations. In summary, AI technologies have revolutionized sustainable 3D printing by reducing failure rates, optimizing material usage, and lowering energy consumption. AI-powered predictive modeling, in-process defect detection, and adaptive control mechanisms are significantly improving the environmental sustainability of AM processes. As AI continues to evolve, its role in promoting environmentally and economically sustainable manufacturing within Industry 4.0 and circular manufacturing frameworks is set to grow even more prominent.

2. Methods

2.1. Experimental workflow for sustainable FDM printing of thermoplastic polyurethane (TPU) 95A components

In this study, we focused on the fabrication, optimization, and mechanical characterization of TPU 95A specimens produced through FDM, with particular focus on analyzing energy consumption throughout each stage of the process. The objective is to assess the efficiency, mechanical performance, and sustainability of TPU 95A components by integrating twin-screw extrusion-based filament production, AM using a Bambu Lab A1 3D printer, and stress-controlled mechanical testing. Energy usage is continuously monitored using power meters across the entire workflow – from raw material preparation to final product – to evaluate the energy footprint associated with extrusion, printing, and testing.

The first stage of the study involved the preparation of TPU 95A filaments using a twin-screw extruder, a critical process that determines the quality and homogeneity of the feedstock for FDM printing. TPU 95A pellets (Dream Shapes Printing, India) were loaded into the extruder hopper and melted at 200°C within the extrusion chamber. The screw speed was regulated between 30 – 50 rpm to ensure uniform mixing and homogenized extrusion of the thermoplastic material. The molten TPU was extruded through a 1.75 mm diameter die to form a continuous filament, which was immediately quenched in a water bath to achieve dimensional stability, prevent defects, and enhance material properties. The solidified filament was then wound using a puller system with consistent tension. Real-time energy consumption during filament extrusion was measured using a power meter, enabling detailed analysis of the process efficiency and contributing to an assessment of TPU 95A's viability as a sustainable FDM material. After filament preparation, the extruded TPU 95A filament was processed using the Bambu Lab A1 FDM 3D printer (China) to generate test specimens for mechanical testing. The processing parameters for FDM were optimized to balance mechanical performance, print accuracy, and energy efficiency. The print speed of 70 mm/s was selected to facilitate rapid printing and support structural integrity. Nozzle temperature was maintained at 230°C for optimal flow and interlayer adhesion to prevent warping or delamination defects, while the bed temperature was maintained at 50°C to provide optimal first-layer adhesion and reduce shrinkage. A layer height of 0.2 mm was used to enhance surface finish without compromising geometric accuracy, and the infill density was set at 50% with a hexagonal infill pattern, chosen for its high strength-to-weight ratio and effective load distribution. Cooling fan

speed was held constant at 30% to regulate solidification of the extruded material, thereby preventing overheating and supporting interlayer bonding. The test specimens were printed in the XY-plane to ensure mechanical stability and were subjected to compression, flexural, and tensile testing. Real-time power consumption during printing was also monitored using a power meter, providing real-time data on the energy demands of TPU 95A processing. This energy analysis is essential for evaluating the sustainability of FDM printing with TPU, particularly in comparison to conventional manufacturing techniques.

Following the printing process, the mechanical properties of printed TPU 95A specimens were evaluated in accordance with standardized test procedures. The samples were conditioned and tested based on ASTM D638 Type V for tensile strength, ASTM D790 for flexural properties, ASTM D695 for compression, and ASTM E99 for wear resistance using a pin-on-disc tribometer. Tensile, flexural, and compressive tests were conducted using a Tinius Olsen Universal Testing Machine (UTM) (Norway). The experiments were conducted at a strain rate of 5 mm/min to ensure consistent stress application and precise mechanical response. In addition, a 10 kN unit load was used to determine the tensile strength, Young's modulus, flexural strength, and compressive strength of the TPU 95A specimen. Wear resistance was assessed using a pin-on-disc tribometer, evaluating the adhesive and abrasive resistance of the material when subjected to regulated friction conditions. Each mechanical test was replicated three times to ensure statistical validity and reduce experimental variability. Energy consumption during the testing process was monitored continuously, providing insights into the power consumption of the tribometer and UTM during mechanical characterization. This continuous monitoring enabled the identification of energy-intensive stages and supports the development of more energy-efficient testing and printing processes. To normalize energy usage across specimens of varying infill densities and print durations, energy consumption was reported per unit mass of printed material (Wh/g).

Figure 1 illustrates the complete fabrication and characterization of TPU 95A specimens by FDM. Experimental data, including mechanical characteristics, energy consumption, and process efficiency, were analyzed accordingly. By integrating AI-assisted process optimization, real-time energy monitoring, and mechanistic testing, this study aimed to establish a sustainable and high-performance system for the AM of TPU-based components.

2.2. ANN implementation

In this study, an ANN was developed to predict key mechanical properties, namely, tensile strength, flexural strength, compression strength, and wear resistance, based on FDM process parameters. The ANN model also served as a decision-support system within the broader AI-MCDM optimization framework.[18,50-53]

2.2.1. Model architecture and setup

The ANN architecture consisted of the following components:

(i) Input layer: Four neurons representing the main FDM parameters – layer thickness, infill density, shell thickness, and print speed.

(ii) Hidden layers: Two hidden layers were employed: the first consisted of 16 neurons, and the second had eight neurons; both layers used the Rectified Linear Unit (ReLU) activation function to introduce non-linearity.

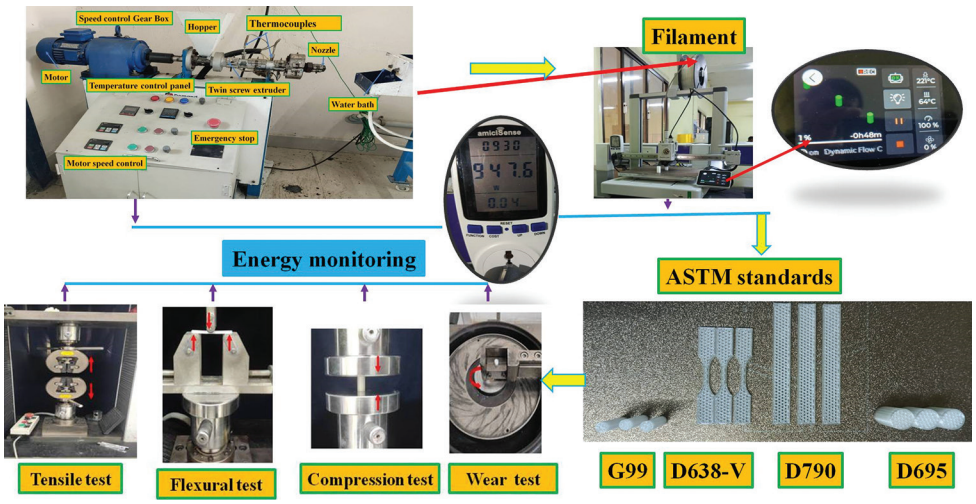

Figure 1. Experimental workflow for sustainable fuse deposition modeling (FDM)-based printing of TPU 95A components. India

(iii) Output layer: Four neurons corresponding to predicted values of tensile strength, flexural strength, compression strength, and wear rate; a linear activation function was applied to accommodate the continuous nature of the output values.

2.2.2. Dataset and training strategy

The model was trained on a dataset of over 500, comprising both experimentally generated data and literature-reported FDM process records. Each record included different parameter combinations along with corresponding mechanical test results. The dataset was divided into 80% for training and 20% for testing to ensure unbiased performance evaluation. Input and output values were normalized to enhance convergence.

2.2.3. Training parameters and tools

Training was performed using the mean squared error (MSE) loss function and the Adam optimizer, with a learning rate of 0.001. The model was trained over 100 epochs with a batch size of 32, implemented in a Python-based TensorFlow/Keras environment.

2.2.4. Model performance and validation

The performance of the trained ANN was assessed using several metrics:

(i) Root MSE (RMSE) ranged between 0.85 – 2.57 for different mechanical properties.
(ii) Mean absolute error (MAE) and mean absolute percentage error (MAPE) indicated consistent and reliable prediction consistency,
(iii) R^2 reached up to 0.95 for compression strength, reflecting an excellent model fit.

Scatter plots of experimental and predicted outcomes (Figures 2-5) further support the accuracy and aptness of the model for optimizing FDM parameters in impeller production.

2.3. MCDM framework

The MCDM framework serves as the backbone for FDM process optimization in impeller production, aiming to balance mechanical performance, energy consumption, and sustainability. This framework utilized Fuzzy AHP and TOPSIS for the sequential weighing and ranking of different process parameters, such as layer height, infill density, nozzle temperature, print speed, and cooling rate – each of which influences the quality and strength of the 3D-printed impellers.[33] Given the intricate trade-offs involved in impeller design – where mechanical strength and durability must be maximized while minimizing material usage and energy consumption – a hybrid Fuzzy AHP-TOPSIS model was employed to enable intelligent

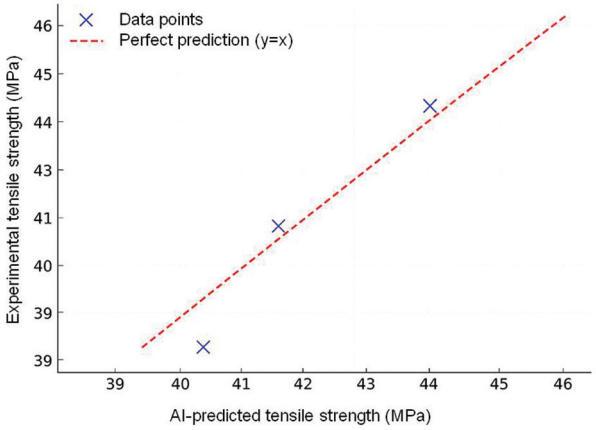

Figure 2. Scatter plot comparing artificial intelligence (AI)-predicted and experimentally measured tensile strength. The blue "×" mark represents an individual data point comparing predicted and actual results. The red dashed line (y = x) denotes perfect prediction; data points aligning with this line indicate accurate AI estimations, while deviations reflect prediction errors. This comparison illustrates the effectiveness of the AI model in estimating mechanical performance

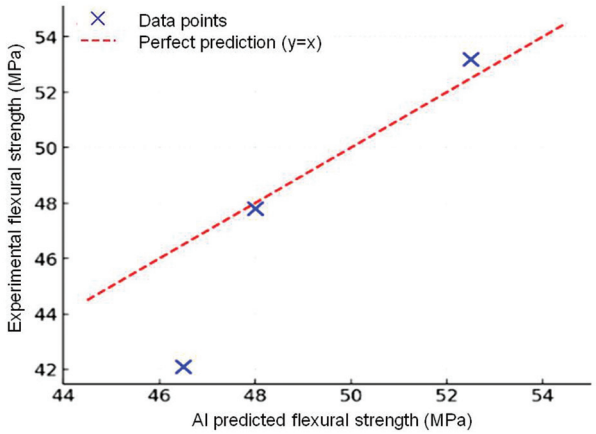

Figure 3. Scatter plot comparing artificial intelligence-predicted and experimentally measured flexural strength

decision-making. Fuzzy AHP was used to determine the relative weights of various criteria based on expert opinion and historical data. By integrating linguistic variables and fuzzy logic, it mitigates uncertainty in the decision-making process and facilitates prioritization of key attributes, such as tensile strength, flexural modulus, wear resistance, and surface roughness, to ensure a holistic evaluation of impeller performance. After the weighting phase, TOPSIS was used to rank different printing parameter settings based on closeness to the ideal solution that optimizes performance and energy efficiency. The implementation of AI-based MCDM models significantly enhances the system's predictive capabilities and supports real-time adjustments to the FDM setup through sensor feedback

and process monitoring. In this study, a twin-screw extruder was utilized to manufacture TPU 95A filaments, with real-time energy consumption tracked using a power meter. This allows sustainability measures to be closely tied into the MCDM framework. Experimental data from mechanical testing and energy monitoring served as inputs to the Fuzzy AHP-TOPSIS model, with each metric carefully analyzed to determine the optimum process conditions. By applying the hybrid MCDM approach, optimal trade-offs among mechanical strength, energy efficiency, and print accuracy were achieved, facilitating high-performance, sustainable manufacturing of impellers. The Fuzzy AHP-TOPSIS model was integrated with AI regression techniques, making it more appropriate for handling a vast array of impeller geometries and materials. The model incorporates real-time sensor feedback from the 3D printer to dynamically optimize process parameters, thereby minimizing the need for manual parameter tuning. By combining data-driven AI models and expert-driven MCDM techniques, this study presents a logical and sustainable decision-making approach for FDM-based impeller production, with enhanced process efficacy, material utilization, productivity, and environmental performance. The architecture of the implemented ANN model is illustrated in Figure 6, illustrating the data flow from FDM parameters to predicted mechanical and energy-related outputs.

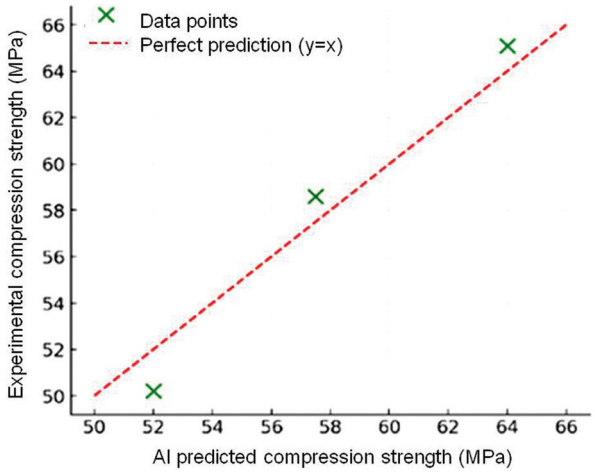

Figure 4. Scatter plot comparing artificial intelligence-predicted and experimentally measured compression strength

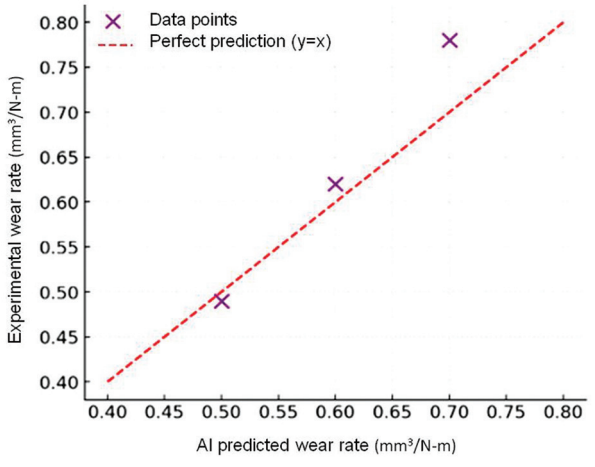

Figure 5. Scatter plot comparing artificial intelligence-predicted and experimentally measured wear rates

3. Results and discussion

Mechanical performance, energy consumption, and AI-MCDM optimization of FDM-based 3D-printed TPU 95A impellers were comprehensively examined. All aspects of the process, from filament extrusion to 3D printing and mechanical testing, were meticulously monitored for energy consumption to evaluate overall sustainability. Optimization of FDM printing parameters, such as layer thickness, infill density, shell thickness, and print speed, was performed using AI-based predictive modeling and MCDM methods, namely, Fuzzy AHP and TOPSIS. The mechanical properties of the impellers were evaluated through tensile, flexural, and compressive tests, while wear resistance was assessed using a pin-on-disc tribometer. The findings indicate that increasing shell thickness and infill density enhances wear resistance and mechanical strength, but also increases energy consumption. Therefore, an optimal trade-off strategy must be identified to achieve sustainable manufacturing. The test results are presented in Table 1.

The mechanical characteristics of TPU 95A impellers were determined based on the infill density and shell thickness from the tensile, flexural, and compression strength tests. Sample S1, with a layer thickness of 0.1 mm, infill density of 20%, and a shell thickness of 0.8 mm, exhibited poor mechanical properties, characterized by

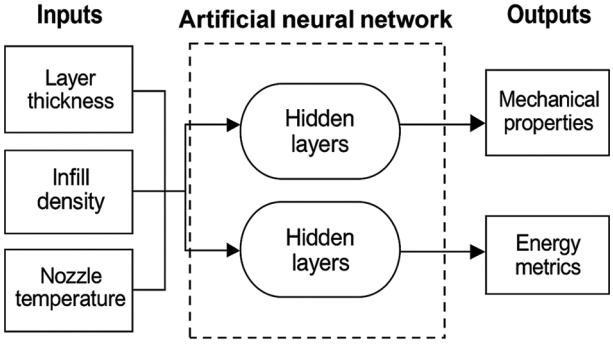

Figure 6. Architecture of the artificial neural network model used in this study

tensile strength of 32.5 MPa, flexural strength of 42.1 MPa, and compression strength of 50.2 MPa. In comparison, sample S2, with 50% higher infill density and a shell thickness of 1.2 mm, exhibited higher tensile strength (38.7 MPa), flexural strength (47.8 MPa), and compression strength (58.6 MPa). The highest mechanical response was observed for sample S3 (80% infill density and 1.6 mm shell thickness), with tensile strength of 44.2 MPa, flexural strength of 53.2 MPa, and compression strength of 65.1 MPa. This trend indicates that higher infill densities and thicker shells enhance load distribution and structural integrity, making them suitable for high-performance impeller applications. However, these improvements come at the cost of increased material usage, longer print times, and higher energy consumption. As such, data-driven optimization becomes essential to balance mechanical performance with sustainability. Table 2 presents energy consumption at each stage of TPU 95A impeller manufacturing, including variations in power consumption during filament extrusion, 3D printing, and mechanical testing.

Power consumption recorded at each stage of the production process revealed that filament extrusion required 85 Wh, indicating a significant contribution to total energy demand. During the 3D printing process, energy usage increased with higher infill density and shell thickness, as these required greater material deposition and longer print times. In particular, sample S1 used 110 Wh, sample S2 used 140 Wh, and sample S3 (having the highest infill density) used 180 Wh. The mechanical testing phase, which includes tensile, flexural, and compression tests, used an additional 50 Wh, while the pin-on-disc wear test contributed a further 30 Wh. These findings highlight the importance of implementing effective energy control to avoid unnecessary power usage during FDM-based impeller manufacturing. The total energy utilized by each sample for testing, 3D printing, and filament preparation ranged from 275 Wh for sample S1 to 345 Wh for sample S3, demonstrating the strong correlation between process parameters and the overall energy footprint.

The wear resistance test revealed a clear inverse relationship between infill density and wear rate. Sample S1, with 20% infill density, exhibited the highest wear rate of 0.78 mm^3/N·m, confirming that low-density structures are more prone to surface degradation under frictional loads. Sample S2, with 50% infill density, displayed improved wear resistance with a wear rate of 0.62 mm^3/N·m, while sample S3, with 80% infill density, reported the lowest wear rate of 0.49 mm^3/N·m. These results confirm that higher infill density enhances impeller durability by reducing surface wear. However, the energy consumption results indicate that achieving high wear resistance comes at the cost of increased power consumption, reiterating the need for AI-driven optimization to attain a balance between durability and energy efficiency.

Prediction accuracy of the AI model for tensile strength was quantified using RMSE, R^2, MAE, and MAPE. The RMSE was 1.05 MPa, indicating that the AI model's tensile strength predictions deviated by ±1.05 MPa from experimental values – an error margin acceptable within general engineering tolerances but still warranting further refinement. The R^2 of 0.78 suggests that 78% of the variance in tensile strength was captured by the model,

Table 1. Mechanical properties of fused deposition modeling (FDM)-printed TPU 95A impellers

Sample ID	Layer thickness (mm)	Infill density (%)	Shell thickness (mm)	Tensile strength (MPa)	Flexural strength (MPa)	Compression strength (MPa)	Wear rate (mm^3/N·m)
S1	0.1	20	0.8	32.5	42.1	50.2	0.78
S2	0.2	50	1.2	38.7	47.8	58.6	0.62
S3	0.3	80	1.6	44.2	53.2	65.1	0.49

Table 2. Energy consumption at each stage of TPU 95A impeller production

Process stage	Sample ID	Layer thickness (mm)	Infill density (%)	Shell thickness (mm)	Energy consumption (Wh)
Filament extrusion	-	-	-	-	85
3D printing	S1	0.1	20	0.8	110
	S2	0.2	50	1.2	140
	S3	0.3	80	1.6	180
Mechanical testing (tensile, flexural, and compression)	All samples	-	-	-	50
Wear test (pin-on-disc)	All samples	-	-	-	30

while the remaining 22% may be attributed to factors such as microstructural inconsistency, filament quality variation, or limitations in the modeling process. The MAE was 0.87 MPa, indicating that predictions by AI models differed from experimental results by an average of 0.87 MPa. The MAPE was 2.1%, indicating a relatively low average percentage error and demonstrating the model's strong predictive performance. These results highlight the potential of the AI model in predicting mechanical properties within FDM, while also highlighting that additional training data, sensor feedback, and parameter tuning for RL could further reduce prediction errors and enhance the overall optimization accuracy toward real-time adaptive control of FDM process parameters.

The precision of AI model predictions for flexural strength, compression strength, and wear resistance was determined using scatter plots and standard error metrics. For flexural strength, the model demonstrated moderate accuracy with an RMSE of 2.57 MPa, R^2 of 0.68, MAE of 1.77 MPa, and MAPE of 4.06%. These results indicate that while the model generally followed experimental trends, small variations were present, likely due to material anisotropy and interlayer bonding differences in FDM (Figure 3). In contrast, the prediction of compression strength displayed high accuracy, with an RMSE of 1.37 MPa, R^2 of 0.95, MAE of 1.33 MPa, and MAPE of 2.38%. These values suggest that the trained model closely replicated the load-carrying behavior of the material under compression (Figure 4). For wear resistance, the model had slightly lower predictive accuracy, with an RMSE of 0.048 $mm^3/N{\cdot}m$, R^2 of 0.84, MAE of 0.037 $mm^3/N{\cdot}m$, and MAPE of 5.17%. This decrease in performance may be attributed to the complex nature of tribological interactions and surface wear mechanisms (Figure 5). Across all tests, scatter plots revealed that AI-optimized parameter selection effectively predicted mechanical properties, reducing reliance on trial-and-error methods in FDM-based impeller production. However, further improvements, such as incorporating real-time sensor feedback, enlarging the training dataset, and applying RL for adaptive control, can enhance the model's accuracy, particularly in wear resistance predictions where surface roughness and frictional force introduce high variability.

To address the trade-off between mechanical performance and energy consumption, an AI-MCDM approach using Fuzzy AHP-TOPSIS was employed to identify the optimal printing parameters. The AI model utilized historical FDM process data to predict the optimal layer thickness, infill density, and shell thickness, prioritizing mechanical strength over energy efficiency based on predefined objective weightings. Table 3 presents the AI-MCDM-optimized parameters of FDM for impeller production, balancing mechanical performance and energy efficiency under different objective weightings. The Fuzzy AHP method was used to determine the relative importance of criteria under two optimization scenarios: (i) mechanical performance (60%) versus energy efficiency (40%); and (ii) energy efficiency (60%) versus mechanical performance (40%). In (i), where mechanical performance was prioritized, the optimal parameters were 0.2 mm layer thickness, 70% infill density, and 1.2 mm shell thickness, resulting in a tensile strength of 41.5 MPa and energy consumption of 145 Wh. In (ii), where energy efficiency was emphasized, the model suggested 0.3 mm layer thickness, 50% infill density, and 1.0 mm shell thickness, with a resultant tensile strength of 38.0 MPa and reduced energy consumption of 125 Wh. These results demonstrate the capability of the AI-MCDM approach to effectively balance strength, wear resistance, and sustainability in FDM-based impeller production.

Table 4 presents a comparison between AI-MCDM-optimized parameter selection and conventional FDM parameter selection. The analysis revealed that the AI-based approach outperformed manually selected parameters. Specifically, AI-optimized parameters improved tensile strength by 7% and wear resistance by 11%, while maintaining only a moderate increase in energy consumption of 3.5%. In contrast, conventional parameter selection, in accordance with standard FDM protocols, resulted in suboptimal mechanical performance and inefficient material deposition, resulting in unnecessary energy consumption. The use of the Fuzzy AHP-TOPSIS ranking technique enabled optimal selection of process parameters from real-time measurements, effectively reducing the need for trial-and-error experimentation. In addition, the AI model continuously refined its predictions based on sensor feedback from the 3D printer, thereby

Table 3. AI-MCDM-optimized FDM parameters for impeller production

Objective weighting (%)	Layer thickness (mm)	Infill density (%)	Shell thickness (mm)	Tensile strength (MPa)	Energy consumption (Wh)	Wear rate ($mm^3/N{\cdot}m$)
Mechanical (60); energy (40)	0.2	70	1.2	41.5	145	0.55
Mechanical (40); energy (60)	0.3	50	1.0	38.0	125	0.61

Abbreviations: AI-MCDM: Artificial Intelligence–multicriteria decision-making; FDM: Fused deposition modeling.

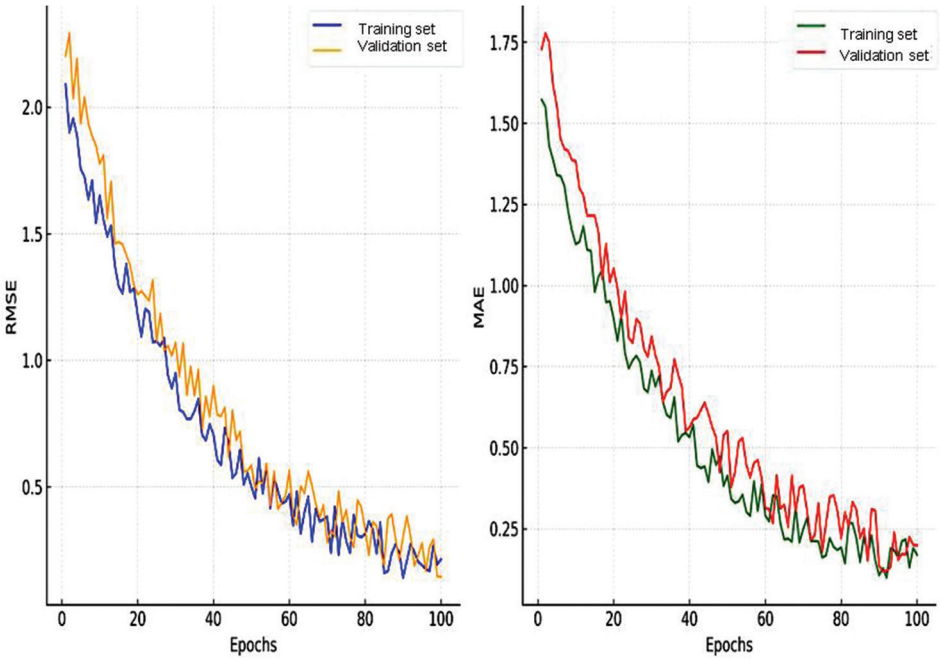

Figure 7. Root mean squared error (left) and mean absolute error (right) values over training epochs for both training and validation sets

Table 4. Comparative analysis of AI-MCDM and conventional parameter selection

Parameter selection method	Tensile strength (MPa)	Energy consumption (Wh)	Wear rate ($mm^3/N·m$)
Conventional approach	38.7	140	0.62
AI-MCDM-optimized	41.5	145	0.55

Abbreviation: AI-MCDM: Artificial Intelligence–multi-criteria decision-making.

enabling real-time adaptive control in the manufacturing process.

Figure 7 demonstrates stable convergence behavior of the ANN model, with decreasing error trends and no indication of overfitting, thereby confirming the reliability and generalization capability of the predictive model. These results demonstrate the potential of AI-MCDM-based optimization in FDM impeller manufacturing. The AI-MCDM-based approach enables data-driven enhancement of material efficiency, mechanical performance, and energy consumption. The integration of real-time sensors in the AI system enables dynamic adjustment of print parameters, ensuring high process reliability and sustainability.

Collectively, the results of this study suggest that future research should focus on extending AI-MCDM frameworks to additional objectives, such as optimization of surface roughness, thermal distortion compensation, and real-time defect detection, to further automate FDM-based impeller manufacturing. Other hybrid AI methods, including RL and digital twin models, hold promise for predicting machine-specific variations in FDM performance. Such advancements would contribute to the development of next-generation smart manufacturing platforms, where AI systems continually learn and evolve FDM processes in real-time to optimize efficiency, reduce waste, and improve product quality.

4. Conclusion

The findings of this study validated the performance of AI-based optimization and MCDM methods in optimizing the mechanical characteristics and sustainability of FDM-based impeller fabrication. The combination of Fuzzy AHP and TOPSIS with AI predictive modeling enabled the identification of optimal trade-offs among tensile, flexural, and compressive strengths, wear resistance, and energy efficiency. Higher infill densities and shell thicknesses led to notable improvements in mechanical properties and wear resistance; however, these gains were accompanied by increased energy consumption, highlighting the importance of AI-driven, eco-friendly parameter optimization. The AI-optimized process yielded 7% higher tensile strength and 11% lower wear rate, while maintaining energy consumption within 3.5% of baseline FDM parameters. Overall, the results highlighted the superiority

of AI-supported decision models over conventional trial-and-error approaches, offering a better, more efficient, and sustainable method for AM process optimization.

The industrial applications of AI-optimized FDM span multiple sectors that employ high-performance impellers and complex fluid-handling components. Various industries, such as automotive, aerospace, marine, and energy, stand to benefit from AI-driven FDM processes capable of producing lightweight, wear-resistant, and aerodynamically optimized impellers. AI-based multi-objective optimization can also be applied in biomedical engineering, where patient-specific implants and prosthetics fabrication require accurate fabrication with minimal material loss. Furthermore, real-time AI monitoring and adaptive learning algorithms in FDM can improve production efficiency by reducing cycle times and operational costs, while maintaining consistent print quality, particularly advantageous in mass manufacturing settings. These developments align closely with the United Nations' SDGs, suggesting that AI-driven sustainability frameworks in AM can promote more environmentally responsible industrial practices. Future research directions include the implementation of real-time AI monitoring systems with IoT-enabled sensors to facilitate adaptive process control and *in situ* defect detection, ensuring optimal layer adhesion, extrusion flow, and energy consumption. The LCA of AI-optimized FDM processes will also be essential to evaluate their long-term environmental and economic advantages. Moreover, the integration of digital twin simulations and RL algorithms could further evolve FDM into a fully autonomous, smart manufacturing platform. These technologies would enable dynamic parameter tuning based on real-time data and sustainability metrics, paving the way for energy-efficient, scalable, and high-quality additive manufacturing solutions. In future work, we aim to expand the experimental dataset by fabricating and testing a broader range of parameter combinations. This will help validate the consistency and generalizability of the AI-MCDM optimization framework. Additional mechanical characterization and real-time energy monitoring across different geometries and materials will be performed to enhance the robustness of the model.

Acknowledgments

Not applicable.

Funding

This project is sponsored by Prince Sattam Bin Abdulaziz University (PSAU) as part of funding for its SDG Roadmap Research Funding Programme project number PSAU-2023-SDG-2023/SDG/74.

Conflicts of interest

The authors declare no conflicts of interest.

Authors' contributions

Conceptualization: S. Raja, Mohamad Reda Refaai
Data curation: Vishnu PS, Maher Ali Rusho
Formal analysis: Mohamad Reda Refaai, Oluseye Adewale Adebimpe
Investigation: Maher Ali Rusho, Ahamed Jalaudeen M, Vishnu PS
Methodology: S. Raja, Ahamed Jalaudeen M, Vishnu PS, John Rajan A
Project administration: S. Raja
Resources: John Rajan A, Maher Ali Rusho
Software: Ahamed Jalaudeen M, Vishnu PS
Supervision: S. Raja, Mohamad Reda Refaai
Validation: John Rajan A, Oluseye Adewale Adebimpe
Visualization: Ahamed Jalaudeen M, Vishnu PS
Writing – original draft: S. Raja, Ahamed Jalaudeen M
Writing – review and editing: Mohamad Reda Refaai, John Rajan A, Oluseye Adewale Adebimpe

Ethics approval and consent to participate

Not applicable.

Consent for publication

Not applicable.

Availability of data

The datasets used and/or analyzed during the present study are available from the corresponding author on reasonable request.

References

1. Roozkhosh P, Pooya A, Soleimani Fard O, Bagheri R. Revolutionizing supply chain sustainability: An additive manufacturing-enabled optimization model for minimizing waste and costs. *Process Integr Optim Sustain*. 2024;8(1):285-300.

   doi: 10.1007/s41660-023-00368-1

2. Subramani R. Optimizing process parameters for enhanced mechanical performance in 3D printed impellers using graphene-reinforced polylactic acid (G-PLA) filament. *J Mech Sci Technol*. 2025;39:1387-1397.

   doi: 10.1007/s12206-025-0231-4

3. Panesar A, Brackett D, Ashcroft I, Wildman R, Hague R. *Design Optimization Strategy for Multifunctional 3D Printing*; 2014. Available from: https://www.com hdl.handle.net/2152/89261 [Last accessed on 2025 Jul 22].

4. Hussain S, Lee CKM, Tsang YP, Waqar S. A machine

learning-based recommendation framework for material extrusion fabricated triply periodic minimal surface lattice structures. *J Mater Sci Mater Eng.* 2025;20(1);27.

doi: 10.1186/s40712-025-00229-4

5. Goh GD, Sing SL, Lim YF, *et al*. Machine learning for 3D printed multi-materials tissue-mimicking anatomical models. *Mater Design*. 2021;211:110125.

doi: 10.1016/j.matdes.2021.110125

6. Yadav R. Analytic hierarchy process-technique for order preference by similarity to ideal solution: A multi criteria decision-making technique to select the best dental restorative composite materials. *Polym Compos.* 2021;42(12):6867-6877.

doi: 10.1002/pc.26346

7. Gyani J, Ahmed A, Haq MA. MCDM and various prioritization methods in AHP for CSS: A comprehensive review. *IEEE Access*. 2022;10:33492-33511.

doi: 10.1109/ACCESS.2022.3161742

8. Tran NT, Trinh VL, Chung CK. An integrated approach of fuzzy AHP-TOPSIS for multi-criteria decision-making in industrial robot selection. *Processes*. 2024;12(8):1723.

doi: 10.3390/pr12081723

9. Kantaros A, Katsantoni M, Ganetsos T, Petrescu N. The evolution of thermoplastic raw materials in high-speed FFF/FDM 3D printing Era: Challenges and opportunities. *Materials (Basel)*. 2025;18(6):1220.

doi: 10.3390/ma18061220

10. Achite M, Nasiri H, Katipoğlu OM, Abdallah M, Moazenzadeh R, Mohammadi B. A coupled extreme gradient boosting-MPA approach for estimating daily reference evapotranspiration. *Theor Appl Climatol.* 2025;156(2):113.

doi: 10.1007/s00704-024-05313-x

11. Nandipati M, Fatoki O, Desai S. Bridging nanomanufacturing and artificial intelligence-a comprehensive review. *Materials (Basel)*. 2024;17(7):1621.

doi: 10.3390/ma17071621

12. Batu T, Lemu HG, Shimels H. Application of artificial intelligence for surface roughness prediction of additively manufactured components. *Materials (Basel)*. 2023;16(18):6266.

doi: 10.3390/ma16186266

13. Elahi M, Afolaranmi SO, Lastra JLM, Garcia JAP. A comprehensive literature review of the applications of AI techniques through the lifecycle of industrial equipment. *Discov Artif Intell*. 2023;3:43.

doi: 10.1007/s44163-023-00089-x

14. Zhou L, Miller J, Vezza J, *et al*. Additive manufacturing: A comprehensive review. *Sensors (Basel)*. 2024;24(9):2668.

doi: 10.3390/s24092668

15. Liu S, Yang C. Machine learning design for high-entropy alloys: Models and algorithms. *Metals*. 2024;14(2):235.

doi: 10.3390/met14020235

16. Ng WL, Goh GL, Goh GD, Ten JSJ, Yeong WY. Progress and opportunities for machine learning in materials and processes of additive manufacturing. *Adv Mater.* 2024;36(34):2310006.

doi: 10.1002/adma.202310006

17. Fahimi K, Amirabadi M. Constructing the organizational excellence model using technique for order of preference by similarity to ideal solution and Analytic hierarchy process. *Int J Hum Capital Urban Manag*. 2024;9:157-176.

doi: 10.22034/IJHCUM.2024.01.11

18. Galal A, Elawady H, Mostafa NA. An integrated framework for third party logistic evaluation by using fuzzy analytical hierarchy process and technique for order preference by similarity to ideal solution. *Int J Logist Syst Manag.* 2025;50(3):361-385.

doi: 10.1504/IJLSM.2025.144680

19. Prasetyo DE, Nurfaizal H, Effendi A. Comparative analysis of the analytical hierarchy process (ahp) and technique for order preference by similarity to ideal solution (topsis) methods in selecting majors for new students: A case study at smks binong permai an-nurmaniyah. J *Inform Utama*. 2024;2(1):43-49.

20. Hanafi AM, Moawed MA, Abdellatif OE. Advancing sustainable energy management: A comprehensive review of artificial intelligence techniques in building. *Eng Res J (Shoubra)*. 2024;53(2):26-46.

doi: 10.21608/erjsh.2023.226854.1196

21. Ukoba K, Olatunji KO, Adeoye E, Jen TC, Madyira DM. Optimizing renewable energy systems through artificial intelligence: Review and future prospects. *Energy Environ*. 2024;35(7):3833-3879.

doi: 10.1177/0958305X241256293

22. Rojek I, Mikołajewski D, Mroziński A, Macko M. Green energy management in manufacturing based on demand prediction by artificial intelligence-a review. *Electronics*. 2024;13(16):3338.

doi: 10.3390/electronics13163338

23. Sarkar C, Das B, Rawat VS, *et al*. Artificial intelligence and machine learning technology driven modern drug discovery and development. *Int J Mol Sci.* 2023;24(3):2026.

doi: 10.3390/ijms24032026

24. Babu SS, Mourad AHI, Harib KH, Vijayavenkataraman S. Recent developments in the application of machine-learning towards accelerated predictive multiscale design and additive manufacturing. *Virtual Phys Prototy.* 2023;18(1):e2141653.

doi: 10.1080/17452759.2022.2141653

25. Yousuf M, Alsuwian T, Amin AA, Fareed S, Hamza M. IoT-based health monitoring and fault detection of industrial AC induction motor for efficient predictive maintenance. *Measure Control*. 2024;57(8):1146-1160.

    doi: 10.1177/002029402412314

26. Moscol-Albañil I, Solórzano-Requejo W, Rodriguez C, Ojeda C, Lantada AD. Innovative AI-driven design of patient-specific short femoral stems in primary hip arthroplasty. *Mater Design*. 2024;240:112868.

    doi: 10.1016/j.matdes.2024.112868

27. Westphal E, Seitz H. Generative artificial intelligence: Analyzing its future applications in additive manufacturing. *Big Data Cogn Comput.* 2024;8(7):74.

    doi: 10.3390/bdcc8070074

28. Zhang Y, Song C. A novel design of centrifugal pump impeller for hydropower station management based on multi-objective inverse optimization. *Processes*. 2023;11(12):3335.

    doi: 10.3390/pr11123335

29. Pinto RN, Afzal A, D'Souza LV, Ansari Z, Mohammed Samee A. Computational fluid dynamics in turbomachinery: A review of state of the art. *Arch Computat Methods Eng*. 2017;24(3):467-479.

    doi: 10.1007/s11831-016-9175-2

30. Cao S, Peng G, Yu Z. Hydrodynamic design of rotodynamic pump impeller for multiphase pumping by combined approach of inverse design and CFD analysis. *J Fluids Eng*. 2005;127:330-338.

    doi: 10.1115/1.1881697

31. Raja S, Praveenkumar V, Rusho MA, Yishak S. Optimizing additive manufacturing parameters for graphene-reinforced PETG impeller production: A fuzzy AHP-TOPSIS approach. *Results Eng.* 2024;24:103018.

    doi: 10.1016/j.rineng.2024.103018

32. Mushtaq RT, Wang Y, Rehman M, *et al*. Investigation of the mechanical properties, surface quality, and energy efficiency of a fused filament fabrication for PA6. *Rev Adv Mater Sci.* 2023;62(1):20220332.

    doi: 10.1515/rams-2022-0332

33. Raja S, Jayalakshmi M, Rusho MA, *et al*. Fused deposition modeling process parameter optimization on the development of graphene enhanced polyethylene terephthalate glycol. *Sci Rep.* 2024;14(1):30744.

    doi: 10.1038/s41598-024-80376-4

34. Borah J, Chandrasekaran M. Development of ANN model for predicting mechanical properties of 3D printed PEEK polymer using FDM and optimization of process parameters for better mechanical properties. *Phys Scripta*. 2024;99(11):116005.

    doi: 10.1088/1402-4896/ad7f0f

35. Villegas AI, Garcia JP, Carillo J, Espalin D. *Bead-Weaved Layered Prints for Improved Interlayer Adhesion in Additive Manufacturing*. United States: University of Texas at Austin; 2024.

    doi: 10.26153/tsw/58049

36. Alharbi A, Alosaimi W, Alyami H, *et al*. Selection of data analytic techniques by using fuzzy AHP TOPSIS from a healthcare perspective. *BMC Med Inform Decis Mak*. 2024;24(1):240.

    doi: 10.1186/s12911-024-02651-8

37. Lambiase F, Liparoti S, Pace F, Scipioni SI, Paoletti A. A multidisciplinary approach to investigate the influence of process parameters on interlayer adhesion in material extrusion additive manufacturing. *Int J Adv Manuf Technol.* 2024;133(11):5553-5570.

    doi: 10.1007/s00170-024-14079-5

38. Kumar MS, Farooq MU, Ross NS, Yang CH, Kavimani V, Adediran AA. Achieving effective interlayer bonding of PLA parts during the material extrusion process with enhanced mechanical properties. *Sci Rep.* 2023;13(1):6800.

    doi: 10.1038/s41598-023-33510-7

39. Altıparmak SC, Yardley VA, Shi Z, Lin J. Extrusion-based additive manufacturing technologies: State of the art and future perspectives. *J Manuf Process*. 2022;83:607-636.

    doi: 10.1016/j.jmapro.2022.09.032

40. Polo-Triana S, Gutierrez JC, Leon-Becerra J. Integration of machine learning in the supply chain for decision making: A systematic literature review. *J Ind Eng Manag.* 2024;17(2):344-372.

    doi: 10.3926/jiem.6403

41. Mishra A, Linh NTD, Bhardwaj M, Pinto CM, editors. *Multi-criteria Decision Models in Software Reliability: Methods and Applications*. CRC Press; 2022. Available from: https://books.google.co.in/books?hl=en&lr=&id=lqcveaaaqbaj&oi=fnd&pg=pp1&dq=%5b41%5d.%09mishra,+a.,+linh,+n.+t.+d.,+bhardwaj,+m.,+%26+pinto,+c.+m.+(eds.).+(2022).+multi/criteria+decision+models+in+software+reliability:+methods+and+applications.+crc+press.&ots=hrepmhkbj6&sig=wlxd5kraczllcgqu3vvkrdhr0vw&redir_esc=y#v=on epage&q&f=false [Last accessed on 2025 Jul 22].

42. Sæterbø M. *A Decision Support Framework for Metal Additive Manufacturing Adoption in Small and Medium-Sized Enterprises*; 2024. Available from: https://www.hdl.handle.net/10037/35740 [Last accessed on 2025 Jul 22].

43. Getachew MT, Shiferaw MZ, Ayele BS. Recent advances of additive manufacturing for aerospace industries: Methods, materials, challenges, and future outlooks. In: *Solomon*

Workneh Fanta Mesfin Wogayehu Tenagashaw Muluken Temsgen Tigabu. 2025. p47.

doi: 10.1007/978-3-031-77339-6_4

44. Li Z, Chang L. Development of wear-resistant polymeric materials using fused deposition modelling (FDM) technologies: A review. *Lubricants*. 2025;13(3):98.

doi: 10.3390/lubricants13030098

45. Klenam D, Asumadu T, Bodunrin M, *et al*. Toward sustainable industrialization in Africa: The potential of additive manufacturing-an overview. *Front Manuf Technol*. 2025;4:1410653.

doi: 10.3389/fmtec.2024.1410653

46. Al-Sammak KA, Al-Gburi SH, Marghescu I, *et al*. Optimizing IoT energy efficiency: Real-time adaptive algorithms for smart meters with LoRaWAN and NB-IoT. *Energies*. 2025;18(4):987.

doi: 10.3390/en18040987

47. Glogar M, Petrak S, Mahnić Naglić M. Digital technologies in the sustainable design and development of textiles and clothing-a literature review. *Sustainability*. 2025;17(4):1371.

doi: 10.3390/su17041371

48. Yan Z, Guo X, Hui J, Lv J, Xu Z. Optimization of energy consumption and dimensional accuracy for fused deposition modeling processes through a hybrid method. *Int J Adv Manuf Technol*. 2025;137:2335-2354.

doi: 10.1007/s00170-025-15294-4

49. Ghaith K. Integrating eco-innovation with AI: Reimagining non-heritage cultural product design through sustainable technological interventions. *J Next Gener Rese*. 2025;1:1-12.

doi: 10.70792/jngr5.0.v1i2.58

50. Natarajan M, Pasupuleti T, Kumar V, Kiruthika J, Katta LN, Silambarasan R. *Development of AI Prediction Tool for Fused Deposition Modeling of ABS Material for Automobile Applications* (No. 2025-28-0127). SAE Technical Paper; 2025.

doi: 10.4271/2025-28-0127

51. Łach Ł, Svyetlichnyy D. Advances in numerical modeling for heat transfer and thermal management: A review of computational approaches and environmental impacts. *Energies*. 2025;18(5):1302.

doi: 10.3390/en18051302

52. Fan H, Liu C, Bian S, *et al*. New era towards autonomous additive manufacturing: A review of recent trends and future perspectives. *Int J Extrem Manuf*. 2025;7:032006.

doi: 10.1088/2631-7990/ada8e4

53. Jalasri M, Panchal SM, Mahalingam K, Venkatasubramanian R, Hemalatha R, Boopathi S. Ai-powered smart energy management for optimizing energy efficiency in high-performance computing systems. In: *Future of Digital Technology and AI in Social Sectors*. United States: IGI Global; 2025. p. 329-366.

doi: 10.4018/979-8-3693-5533-6.ch012

ACCSCIENCE PUBLISHING

Materials Science in Additive Manufacturing

ORIGINAL RESEARCH ARTICLE

Performance evaluation of artificial hip joints 3D-printed through stereolithography using dental resin reinforced with titanium dioxide nanoparticles

Bhre Wangsa Lenggana[1]*, Rony Akbar Majid[2], Ubaidillah[2]*, and Joko Triyono[2]

[1]Department of Mechanical Engineering, Faculty of Engineering, Universitas Jenderal Soedirman, Purwokerto, Central Java, Indonesia

[2]Department of Mechanical Engineering, Faculty of Engineering, Universitas Sebelas Maret, Surakarta, Central Java, Indonesia

Abstract

Hip osteoarthritis is a degenerative joint disease commonly associated with aging. One effective treatment to restore patients' quality of life is total hip arthroplasty, in which the damaged hip joint is replaced with a prosthetic implant. Currently, there is a growing demand for customized artificial hip joints tailored to individual anatomical dimensions. However, the conventional casting method generally used to fabricate these implants is often considered ineffective. Additive manufacturing technology, also known as 3D printing, has emerged as a promising alternative. This technology enables the fabrication of complex designs with high accuracy and customizable geometries and sizes without altering the physical components of the 3D printing machine. This study aims to develop a 3D-printed artificial hip joint prosthesis using a dental photopolymer resin reinforced with titanium dioxide (TiO_2) nanoparticles. The mechanical performance of the prostheses was evaluated through both experimental and simulated compression testing. Four concentrations of TiO_2 nanoparticles were tested, namely 0%, 1%, 3%, and 5%. The results showed that the prosthesis reinforced with 3% TiO_2 nanoparticles exhibited the highest strength (717.2 N), while the one with 5% TiO_2 nanoparticles exhibited the lowest strength (241.8 N).

Keywords: Additive manufacturing; 3D printing; Titanium oxide nanoparticles; Hip joint prosthesis; Stereolithography

***Corresponding authors:**
Bhre Wangsa Lenggana (bhre.lenggana@unsoed.ac.id)
Ubaidillah (ubaidillah_ft@staff.uns.ac.id)

Citation: Lenggana BW, Majid RA, Ubaidillah, Triyono J. Performance evaluation of artificial hip joints 3D-printed through stereolithography using dental resin reinforced with titanium dioxide nanoparticles. *Mater Sci Add Manuf*. 2025;4(3):025200032. doi: 10.36922/MSAM025200032

Received: May 14, 2025

1st revised: June 20, 2025

2nd revised: June 30, 2025

Accepted: June 30, 2025

Published online: August 1, 2025

1. Introduction

Osteoarthritis of the hip joint is commonly associated with aging and often results in difficulty performing activities such as walking or running. Other contributing factors include obesity and injuries to the hip joint.[1] To improve the quality of life of patients with hip osteoarthritis, total hip replacement surgery–a clinically and cost-effective procedure–is often recommended. According to a study conducted in the United States, over 300,000 patients with hip osteoarthritis undergo hip replacement surgery annually.[2]

During the procedure, the damaged joint of osteoarthritis patients is replaced with an artificial hip prosthesis, which typically consists of several components, including the acetabular cup, acetabular liner, femoral head, and femoral stem. The acetabular cup, femoral head, and femoral stem are generally fabricated from metal alloys, while the acetabular liner is composed of a polymer material.[3]

Casting is the conventional manufacturing process for artificial hip joint components such as the femoral stem and femoral head. Among the various casting methods, investment casting is widely used due to its ability to produce components in large quantities with uniform dimensions, complex geometries, and good surface finishes.[4] However, the demand for customized artificial hip joints tailored to individual patient anatomy is increasing. Conventional casting methods are considered ineffective for this purpose because customized implants require patient-specific dimensions, making casting less efficient in terms of production time and costs.[5] Additive manufacturing technology, also known as 3D printing, has emerged to fabricate parts with complex designs, diverse geometries, and varying sizes with high precision without requiring modifications to the physical hardware of the printing machine. The fundamental mechanism of this technology involves converting a 3D computer-aided design model into a physical object by sequentially arranging layers of materials.[6] There are several types of 3D printing technology, including selective laser sintering, fused deposition modeling (FDM), selective laser melting (SLM), and stereolithography (SLA).[7] SLA 3D printing uses ultraviolet light to solidify a photopolymer resin into precise, detailed objects.

Several studies have investigated the fabrication of artificial hip joint components using 3D printing technology. For instance, Wang *et al.*[3] investigated the fabrication of acetabular cup components using the SLM 3D printing method with Ti_6Al_4V alloy. In a separate study, Kang *et al.*[5] fabricated acetabular cup components from titanium alloy using the PBF 3D printing method. In contrast, the current study focuses on the fabrication of femoral stem and femoral head components of artificial hip joints using the SLA 3D printing method. The material used in this study was a dental photopolymer resin reinforced with titanium dioxide (TiO_2) nanoparticles. Before conducting this research, the mechanical properties of the materials used in this study had been obtained for the simulation test. This research aims to evaluate the performance of the fabricated artificial hip joint prostheses through finite element analysis and experimental compression testing.

2. Materials and methods

2.1. Experimental setup and fabrication

In this study, the artificial hip joint design was created using Fusion 360 software (Autodesk, Inc., United States) based on the previous research design conducted by Ishihara.[8] Figure 1 shows the design created with the software.

The fabrication of prostheses began with the preparation of composite materials. The composite materials were prepared by mixing photopolymer resin and TiO_2 nanoparticles (Jiangsu Xfnano Materials Tech Co., Ltd., China). The photopolymer resin used was a dental resin-type photopolymer resin (Esun Dental Model Resin, Shenzhen Esun Industrial Co., Ltd., China). Dental resin was chosen because it is commonly used in the medical field, namely, dental care and repair by dentists.[9,10] Three variations of TiO_2 concentration (1%, 3%, and 5% weight) were added to the resin. The materials were measured using a digital scale (TN-Series, TN Lab, USA) with a capacity of 100 g and an accuracy of 0.001 g. The composite materials were then mixed using a magnetic stirrer (MSH-A, Daihan, South Korea) for 30 minu, followed by an ultrasonic mixer (Krisbow 10250184, Indonesia) for 90 min for all variations. The mixed TiO_2 nanoparticle composite material was then used for the artificial hip joint printing process using 3D printing SLA with a 3D printer (Creality Halot Sky Cl-89 SLA, Shenzhen Creality 3D Technology Co., Ltd., China). The setup parameters used were 70 s bottom exposure time, 4 s light off delay, 1 mm/s motor speed, 6 mm bottom lighting distance, and 3 s exposure time. Figure 2 shows the fabrication process of an artificial hip joint.

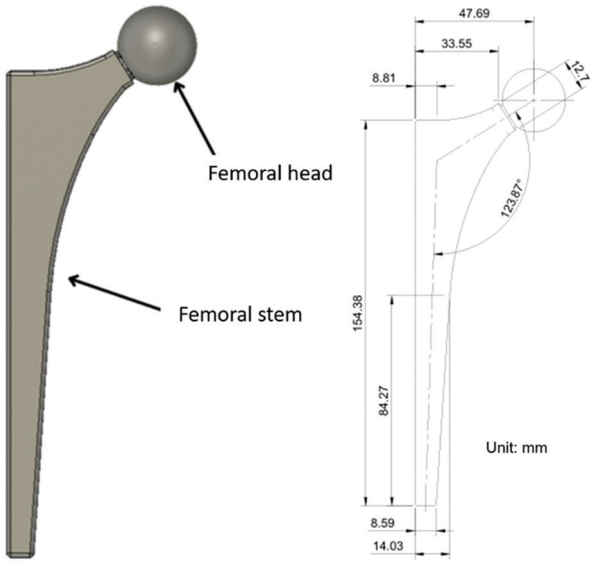

Figure 1. The design and dimensions of the artificial hip joint prosthesis

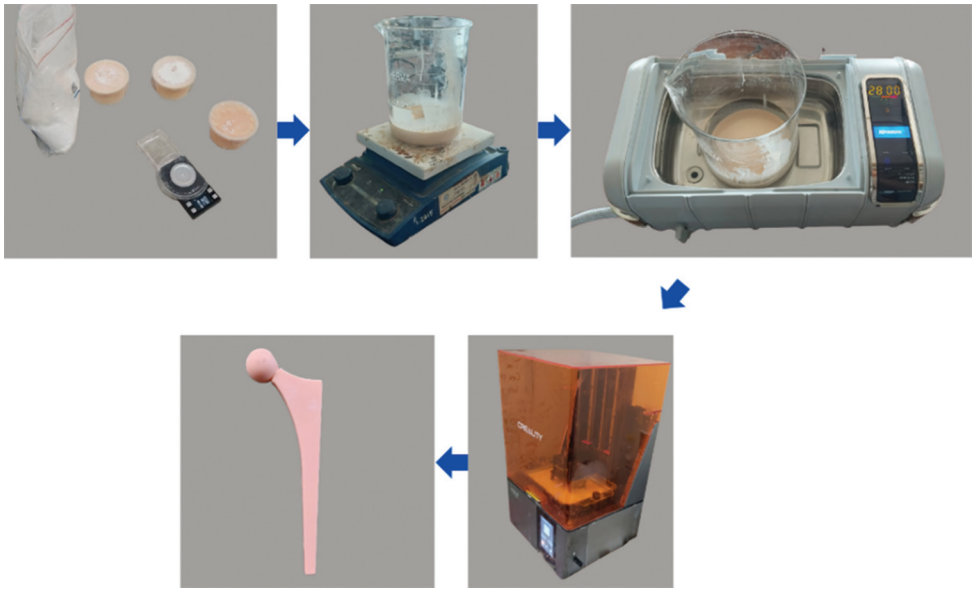

Figure 2. Fabrication process of an artificial hip joint

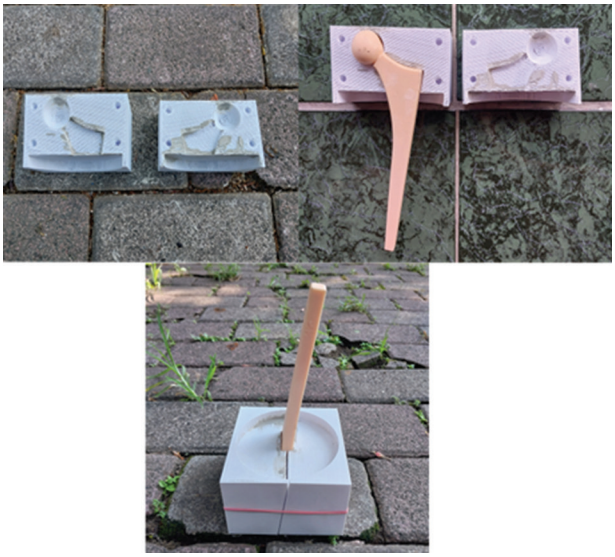

Figure 3. Template installation for the artificial hip joint bracket

The artificial hip joint samples were then subjected to a compression test using the universal testing machine (JTMS510, J.T.M. Technology Co., Ltd., China). The compression test was performed until the artificial hip joint was deformed or damaged. The standard used in this test was ISO 7206-6.[11] To install the artificial hip joint on the bracket according to the standard provisions, a template was created using FDM 3D printing (Figure 3). After creating the template, the next step was to lock the position of the artificial hip joint with a bracket. The bracket was constructed using a 3-inch diameter polyvinyl chloride pipe, which was then cast with a cement mixture

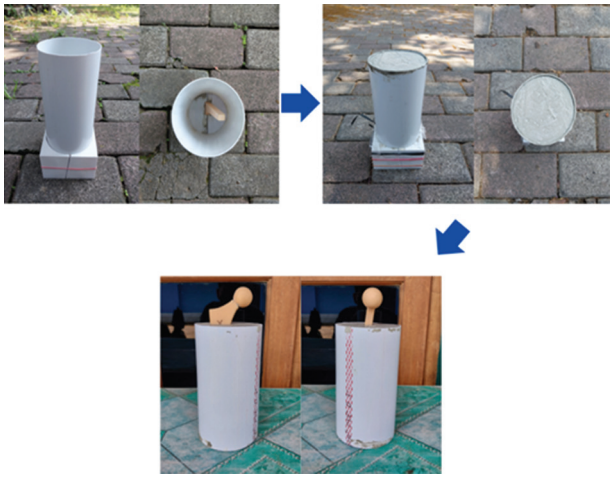

Figure 4. Fabrication of a bracket for the artificial hip joint compression test

(Figure 4). The compression test was then performed according to the scheme as shown in Figure 5.

2.2. Materials used in 3D printing

Photopolymer resins are commonly used in photopolymerization-based processes such as SLA and digital light processing. Photopolymerization involves the use of monomers or oligomers in a liquid state, along with a photoinitiator, which converts light energy into reactive species and initiates the polymerization process. The photopolymer resin was mixed with the TiO_2 nanoparticles–chemicals in the form of white solid granules–to strengthen the resin matrix. This material is considered technologically important due to several

properties, including ease of synthesis, good tensile strength, adequate biocompatibility, and low toxicity, as well as antibacterial and photocatalytic activity. These nanoparticles are widely used as catalyst supports in biomedicine, water and air purification, pigments, cosmetics, solar cells, and tissue engineering.[12,13] The TiO_2 nanoparticles used in this study were nanoparticles with an average particle diameter of 10 nm.

2.3. Numerical simulation

Before conducting a finite element analysis, the mechanical properties of the material were determined for simulation purposes. These properties were derived from experimental engineering stress–strain data, which were subsequently converted into actual stress–strain data and input into the finite element analysis software. The material used in the simulation was a composite consisting of dental photopolymer resin reinforced with TiO_2 nanoparticles. The engineering stress–strain behavior of this composite has been previously characterized. Curve fitting was performed based on the experimental engineering stress–strain graph data, and the fitting process was refined until an R^2 value of ≥0.95 was achieved. The resulting mechanical properties of the composites obtained from the study are shown in Table 1.

2.4. Sample characterization

The mechanical properties of TiO_2 nanoparticle composites were validated by conducting tensile test simulations using ANSYS software (Ansys, Inc., United States). The simulations were performed on specimens conforming to ASTM D638-14 type V standards. The dimensions of the specimens are shown in Figure 6. The boundary conditions applied were fixed support on side A and a velocity of 1 mm/min moving upward parallel to the Y-axis on side B (Figure 7). The tensile test simulation was set up following the experimental setup. The results of the tensile test simulation were compared with the experimental test, as shown in Figure 8. The mechanical properties of TiO_2 nanoparticle composites were considered valid if the difference or error between the two tests was ≤5%. This standard was also applied to the simulation process to validate consistency between the experiment and simulation. The tensile test sample was fabricated using the same 3D printing tool as the fabrication of compression test samples, as explained in the methodology section. We used a speed of 1 mm/min and provided details of the specimen dimensions in tensile testing. While in compression testing, we applied the ISO 7206-6 standard. This standard provides information on the position of the artificial hip joint placement, including both the installation depth and angle of the artificial hip joint to the bracket. The compression speed in this test was 2 mm/min.

Table 1. Mechanical properties of dental photopolymer resin with varying concentration of TiO_2 nanoparticle reinforcement

Mechanical properties	Value			
	0% TiO_2	1% TiO_2	3% TiO_2	5% TiO_2
Density (g/cm3)	1.13	1.15	1.19	1.20
Young's modulus (MPa)	201	232	317	365
Poisson's ratio	0.43	0.43	0.43	0.43
Yield tensile strength (MPa)	17.99	22.80	28.29	21.62
Ultimate tensile strength (MPa)	38.44	40.32	43.90	34.83

Abbreviation: TiO_2: Titanium dioxide.

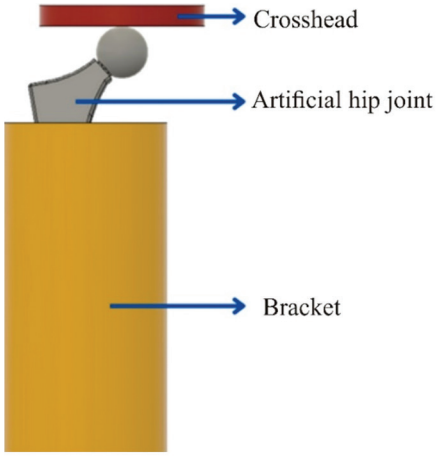

Figure 5. Schematic illustration of the artificial hip joint compression test

This setting was also used in the simulation process, with boundary conditions set according to the ISO standard.

A finite element study simulates the compression test to be performed on the artificial hip joint. Finite element simulation testing was performed using Ansys software based on the ISO 7206-6 test standard. This standard provides information on the placement position of the artificial hip joint, including both the depth and angle of installation of the artificial hip joint to the bracket.[11] According to the ISO 7206-6 standard, the angle of installation of the artificial hip joint must be $\alpha = 10°$ and $\beta = 9°$, with a depth of installation to the bracket as in the real case of total or partial hip joint replacement, as shown in Figure 9A.

To shorten the simulation time, the bracket geometry was excluded from the simulation process. Instead, the boundary conditions were set, namely, the femoral stem section was defined as a fixed support following the ISO 7206-6 standard. Then, the crosshead geometry that pressed the artificial hip joint was defined as moving downward in the Y-axis direction at a speed of 2 mm/min, as shown

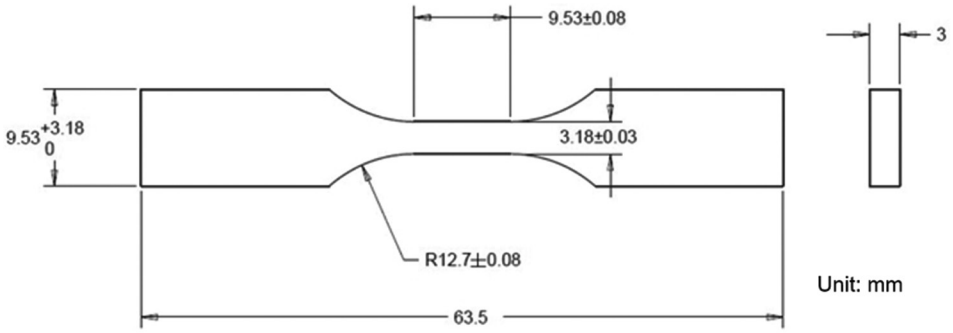

Figure 6. Specimen dimensions for tensile testing based on ASTM D638-14 type V standards

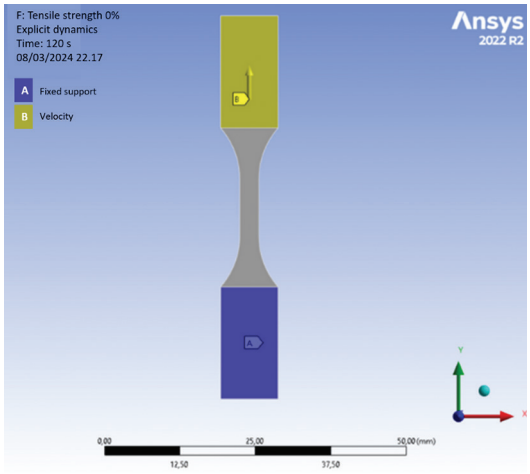

Figure 7. Boundary condition setup for tensile simulation

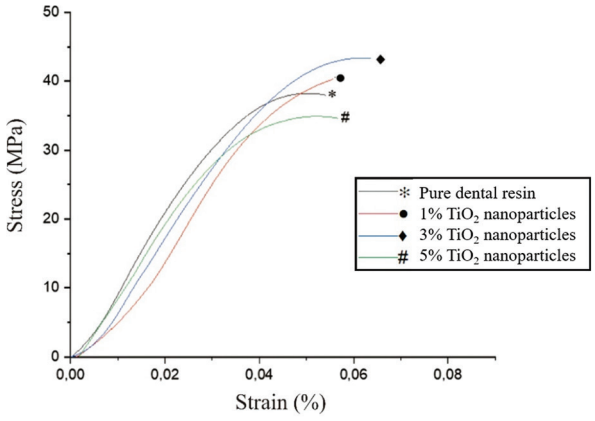

Figure 8. Experimental result of the tensile test

in Figure 9B. Figure 9C shows the mesh settings. For the artificial hip joint, a mesh setting with a size of 7.079 mm was applied, which went through a mesh convergence test process. For the crosshead geometry, a body sizing mesh setting with a size of 20 mm was applied. Finally, a contact sizing mesh setting was applied between the artificial hip joint geometry and the crosshead with a size of 3 mm.

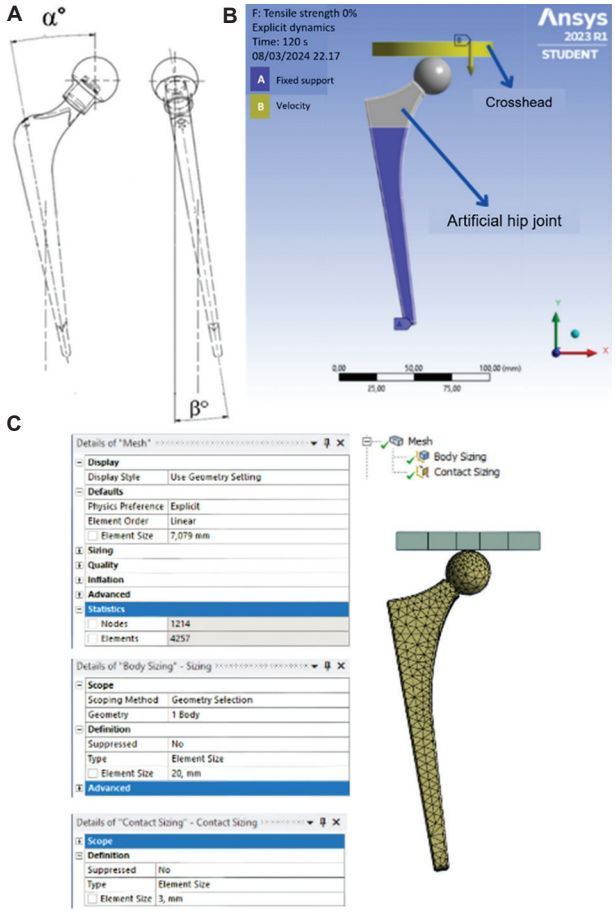

Figure 9. Simulation setup (A) Installation angle of artificial hip joint bracket. (B) Boundary condition setup for compression test simulation. (C) Meshing process setup for compression test simulation

3. Results and discussion

3.1. Validation of mechanical properties of TiO_2 nanoparticle composites

The mechanical properties of TiO_2 nanoparticle composites were validated by comparing the tensile strength at break values of the experimental tensile test with the

simulated tensile strength obtained using Ansys software. A threshold difference or error limit of 5% was set between the experimental and simulated tensile test results. The test results are shown in Figure 10. The average difference or error obtained at this stage was 0.96% (Table 2). The results indicate that the mechanical properties of the TiO_2 nanoparticle composite used to conduct the simulation were valid. The mechanical properties of the TiO_2 nanoparticle composite were then used to perform artificial hip joint compression test simulations.

3.2. Experimental results and simulation of artificial hip joint compression testing

The maximum load and displacement data of the artificial hip joint were obtained from the compression test. Maximum load data were defined as the maximum load received by the artificial hip joint before it was deformed or damaged. Displacement data were the amount of crosshead movement or deformation at maximum load on the artificial hip joint. In the experimental test, the highest maximum load and displacement values were obtained with 3% TiO_2, at 717.2 N and 3.56 mm, respectively. In contrast, the lowest maximum load and displacement values were obtained with 5% TiO_2, at 241.8 N and 2.32 mm, respectively. In the simulation test, the highest maximum load and displacement values were also obtained with 3% TiO_2, at 698.42 N and 4.43 mm, respectively. Similarly, the lowest maximum load and displacement values were also obtained with 5% TiO_2, at 241.07 N and 1.64 mm, respectively (Figures 11 and 12).

Table 2. Comparison of experimental and simulated tensile test results

Tensile strength at break	Experiment (MPa)	Simulation (MPa)	Error (%)
0% TiO_2 nanoparticles	38.4	38	1.04
1% TiO_2 nanoparticles	40.3	40.9	1.48
3% TiO_2 nanoparticles	43.9	44.1	0.45
5% TiO_2 nanoparticles	34.8	34.5	0.86
Average error			0.96

Abbreviation: TiO_2: Titanium dioxide.

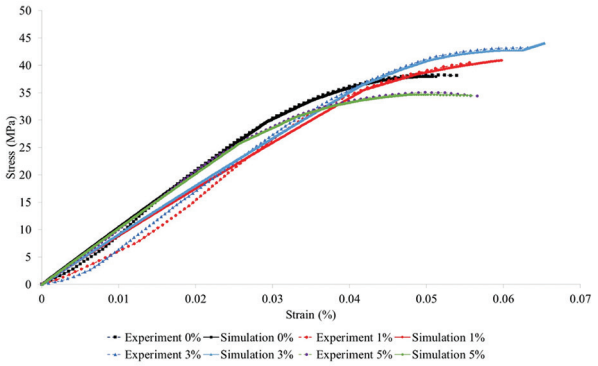

Figure 10. Comparison between experimental and simulated results of the tensile test

Figure 10 shows a similar trend between the experimental test graph and the simulation test graph, with only a slight difference in the curves between the two tests. Similarly, Figures 11 and 12 also displays a similar trend between the experimental test graph and the simulation test graph. However, there are remarkable differences in the results for variations in TiO_2 concentrations of 1%, 3%, and 5%. This may be due to the use of tensile test data for simulation, as the experimental test performed on the artificial hip joint was a compression test. This may result in differences between the experimental and simulated results of the artificial hip joint displacement. Based on the trends from Figures 11 and 12, the results of the experimental and simulated tests are acceptable.

Figure 11 shows that the addition of TiO_2 nanoparticles up to a concentration of 3% increased the maximum load of artificial hip joints. However, the addition of TiO_2

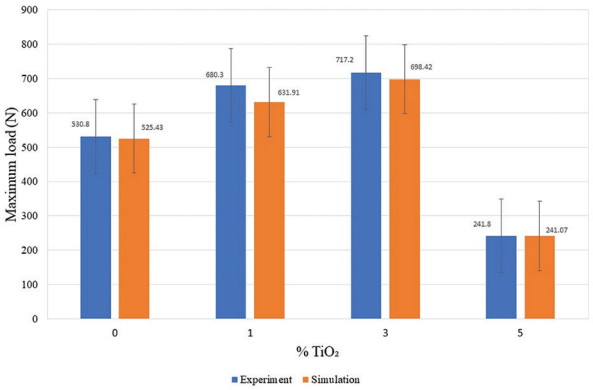

Figure 11. Maximum load data from experimental and simulated results

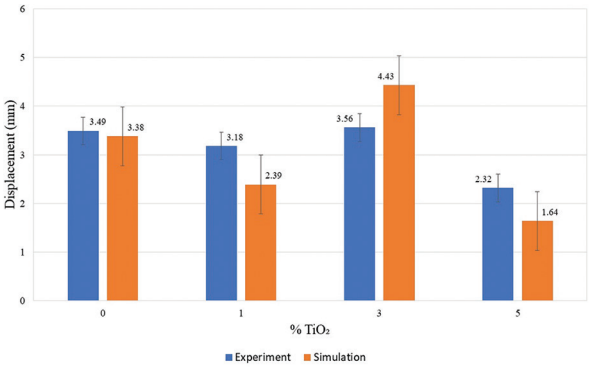

Figure 12. Displacement data from experimental and simulated results

nanoparticles beyond 3% reduces the maximum load of artificial hip joints. A similar phenomenon is found in the tensile test results. The initial increase in strength is attributed to enhanced intermolecular interactions. TiO_2 nanoparticles possess a high surface area-to-volume ratio, and when uniformly dispersed within the resin matrix, they significantly increase the surface area available for bonding. This promotes stronger interactions between the nanoparticles and the surrounding resin, improving internal adhesion and ultimately enhancing the mechanical strength of the composite material. In addition, the increase in strength is also attributed to the nanoscale reinforcement. Nanoparticles are effective reinforcing materials that can interact with polymer chains in the resin, restricting their mobility and thereby increasing stiffness and resistance to deformation of the overall structure. This interaction significantly enhances the stiffness, tensile strength, and compressive strength of the resulting composite material.[14] However, when the concentration of TiO_2 nanoparticles exceeds a certain threshold, agglomeration may occur. The formation of nanoparticle clusters disrupts the uniform dispersion within the resin matrix, leading to stress concentrations and weakened interfacial bonding.[15] As a result, the mechanical strength of the dental photopolymer resin composite may decrease.

Figure 13 compares the behavior of the artificial hip joint prosthesis between the experimental and simulated compression tests. The figure shows similar behavior of the artificial hip joint prosthesis between the experimental and the simulated compression test, with only a slight difference in the fracture shape when the artificial hip joint prosthesis breaks.

3.3. Micrograph analysis

The results of scanning electron microscopy (SEM) indicate that the fracture surface of the specimen is smooth and neat in pure photopolymer as shown in Figure 14A. After the addition of nanoparticles, the specimen surface looks rougher. In Figure 14B-D, there are clumps indicated by arrows; the larger the TiO_2 nanoparticles used, the more clumping and voids appear. Roughness on the fracture surface indicates an increase in the mechanical strength of the specimen. When combining SLA resin with TiO_2 nanoparticles, several characteristic features are expected from the SEM images. SEM imaging provides detailed surface information, revealing the distribution, morphology, and interaction of nanoparticles within the resin matrix. A uniform dispersion of TiO_2 nanoparticles throughout the resin matrix should be observed in the SEM images, indicating a uniform dispersion and successful incorporation of the nanoparticles into the resin. This uniform dispersion signifies good interaction between the nanoparticles and the resin, which is crucial for enhancing the mechanical strength of the composite.

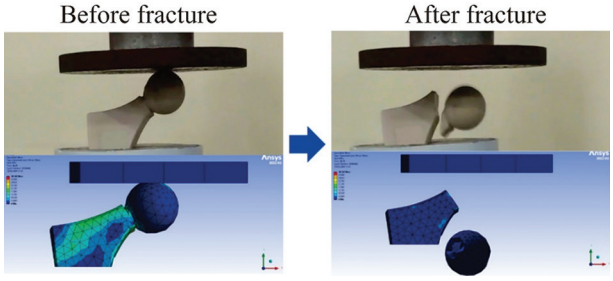

Figure 13. In-frame comparison of the experiment with simulation

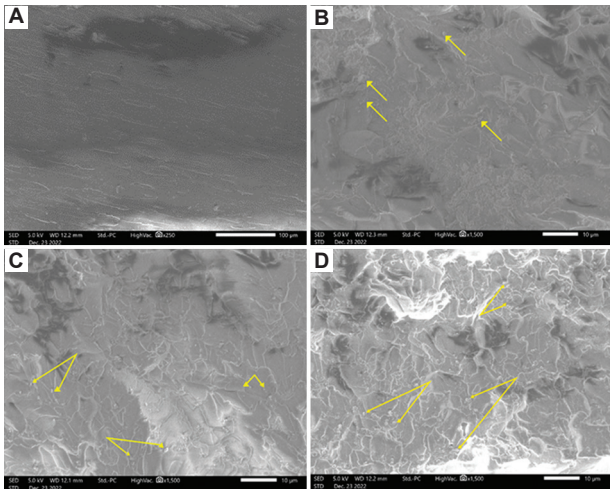

Figure 14. Scanning electron microscopy images of the fracture surface. (A) Pure resin at ×250 magnification with 100 µm scale bar. (B) 1% weight TiO_2 at ×1,500 magnification with 10 µm scale bar. (C) 3% weight TiO_2 at ×1,500 × magnification with 10 µm scale bar. (D) 5% weight TiO_2 at ×1,500 magnification with 10 µm scale bar

Individual TiO_2 nanoparticles should be visible as distinct entities in the SEM images, indicating proper dispersion with minimal agglomeration. The presence of individual nanoparticles contributes to strengthening the composite and enhancing various functional properties. Although small aggregates of TiO_2 nanoparticles form when nanoparticles come into proximity and may be present in the SEM images, these aggregates do not form large clusters or lumps. These aggregates offer improved mechanical and functional properties comparable to individual nanoparticles. Besides, an adequate surface coverage of TiO_2 nanoparticles on the resin matrix should also be observed in the SEM images. The nanoparticles should be evenly distributed across the resin's surface, creating a continuous or semi-continuous layer. This surface coverage ensures effective reinforcement and desired functional properties, such as increased strength, improved thermal stability, or enhanced optical properties.

In addition to nanoparticle distribution, SEM images can also reveal the morphological characteristics of the TiO_2 nanoparticles. The nanoparticles may exhibit various shapes, such as spherical, rod-like, or irregular structures, depending on their synthesis method and properties. Observing the morphology of the nanoparticles provides insights into their behavior and interaction within the resin matrix.

The presence of lumps in SEM images of SLA resin reinforced with TiO_2 nanoparticles can be attributed to several factors, including the resin composition, nanoparticle dispersion, processing conditions, and sample preparation. One of the primary causes of lump formation is the agglomeration of nanoparticles. During the fabrication process, TiO_2 nanoparticles may agglomerate due to interparticle forces such as van der Waals forces or electrostatic interactions, resulting in the formation of larger clusters or lumps. Additionally, inadequate dispersion of nanoparticles within the resin matrix can also contribute to the formation of lumps. Therefore, a homogeneous distribution of nanoparticles is crucial. Factors such as insufficient mixing, improper choice of dispersants, or high viscosity of the resin can restrict the effective dispersion of nanoparticles. Moreover, the curing or drying process of the SLA resin can also contribute to the formation of lumps. As SLA resins undergo a curing or drying process to solidify the material, the resin may not solidify uniformly if the curing conditions, such as temperature or curing time, are not properly controlled. This non-uniform solidification can result in the formation of lumps or irregularities on the resin's surface. Sample preparation for SEM analysis is another critical aspect to consider. Improper sample preparation can introduce artifacts or contaminants that appear as lumps in the SEM images. For example, incomplete cleaning or inadequate drying of the sample can leave residues or moisture that form irregularities or lumps in the images. To address the issue of lump formation, several strategies can be employed. Optimizing the dispersion process during resin formulation or fabrication can help prevent agglomeration and ensure a uniform distribution of nanoparticles. Controlling the curing or drying conditions is also important in achieving consistent solidification of the resin. Finally, proper sample cleaning and drying techniques should be employed to minimize the introduction of artifacts during the SEM sample preparation.

3.4. Benchmarking

Da Costa *et al.*[11] conducted a study on the fabrication of artificial hip joints using polyurethane reinforced with glass fiber. The fabricated prosthesis has a modulus of elasticity comparable to the human femur. The strength test results based on the ISO 7206-6 standard of the fabricated prosthesis are shown in Table 3. Three variations of composites were utilized to fabricate the prosthesis in the study, namely polyurethane, polyurethane with 16 strands of glass fiber reinforcement, and a mixture of polyurethane and calcium carbonate with 16 strands of glass fiber reinforcement (PUCa16G). Of the three variations, the PUCa16G variation results in the highest maximum load of 1,739.73 N. In addition, the PUCa16G variation has a modulus of elasticity similar to the human femur.[11]

Figure 15 shows the comparison of compression test results between the study by Da Costa *et al.*[11] and the present study. It can be seen that the strength of the artificial hip joint fabricated with TiO_2 nanoparticle composite is significantly lower than PUCa16G composite. This is mainly due to the difference in the reinforcing materials used, where two reinforcing materials, calcium carbonate and glass fiber, were utilized by Da Costa *et al.*[11] In addition, the maximum load of the artificial hip joint fabricated with TiO_2 nanoparticle composite is also remarkably low compared to the one fabricated using PUCa16G composite, as the strength of the dental photopolymer resin matrix is weaker than the polyurethane matrix. The results of the

Table 3. Result from the study by Da Costa *et al.*,[11] based on ISO 7206-6

Materials	Maximum load (N)	Displacement (mm)
PU	911.90±82.01	4.67±0.71
PU16G	1043.84±132.57	8.34±1.56
PUCa16G	1739.73±79.68	5.07±1.12
Nanoparticle TiO_2	717.2	3.56

Abbreviations: PU: Polyurethane; PU16G: Polyurethane with 16 strands of glass fiber reinforcement; PUCa16G: A mixture of polyurethane and calcium carbonate with 16 strands of glass fiber reinforcement.

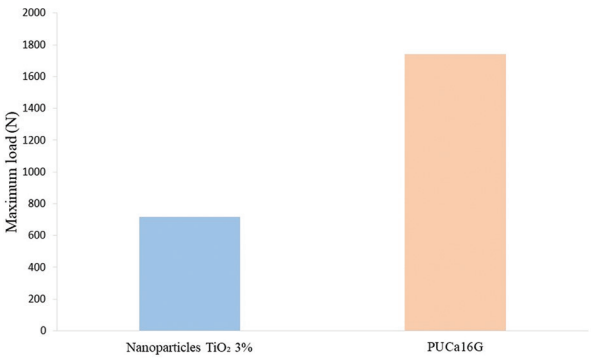

Figure 15. Comparison of the maximum load of the artificial hip joints between Da Costa *et al.*[11] and the present study
Abbreviation: PUCa16G: A mixture of polyurethane and calcium carbonate with 16 strands of glass fiber reinforcement

present study are not comparable to the study of Da Costa *et al.*[11] due to the significant difference in material strength. These results were compared because the same prototypes were fabricated, both of which were artificial hip joint prosthesis prototypes. Despite the significant difference in the strength of the artificial hip joint prosthesis, the fabrication of prostheses using the 3D printing or additive manufacturing method is still promising for further research considering the advantages of this method, such as being able to fabricate complex designs with high accuracy and customizable geometries without altering the physical components to the 3D printing machine.

4. Conclusion

The performance of artificial hip joint prosthesis fabricated using dental photopolymer resin reinforced with varying concentration (0%, 1%, 3%, and 5% weight) of TiO_2 nanoparticles using a 3D printing method was investigated. A simulated compression test of the artificial hip joint has been conducted, which shows that the 3% TiO_2 exhibits the highest maximum load value among all variations. This is in accordance with the experimental compression testing performed in this study. In contrast, the lowest values are reported at 5% weight TiO_2. Based on the analysis conducted, the simulation results closely correspond to the experimental results. However, the performance of the hip joint prosthesis fabricated in the present study is weaker compared to previous research utilizing stronger materials. Despite the limitation in performance, the SLA 3D printing method remains a viable approach for further research due to its ability to fabricate a wide range of prostheses without requiring modifications to the 3D printer.

Acknowledgments

We would like to acknowledge the Universitas Sebelas Maret for providing the materials/equipments/etc., for this study.

Funding

This research was supported by the Laboratory of Vibration and Additive Manufacturing of Universitas Sebelas Maret.

Conflict of interest

The authors declare no competing interests.

Author contributions

Conceptualization: Ubaidillah, Joko Triyono
Formal analysis: Ubaidillah, Joko Triyono
Investigation: Bhre Wangsa Lenggana, Rony Akbar Majid
Methodology: Rony Akbar Majid, Bhre Wangsa Lenggana, Ubaidillah
Writing – original draft: Bhre Wangsa Lenggana
Writing – review & editing: Bhre Wangsa Lenggana, Rony Akbar Majid

Ethics approval and consent to participate

Not applicable.

Consent for publication

Not applicable.

Availability of data

No datasets were generated or analyzed during the current study.

References

1. Gross JB, Guillaume C, Gégout-Pottie P, Mainard D, Presle N. Synovial fluid levels of adipokines in osteoarthritis: Association with local factors of inflammation and cartilage maintenance. *Biomed Mater Eng*. 2014;24(S1):17-25.

   doi: 10.3233/bme-140970

2. Kurtz SM, Ong KL, Lau E, Bozic KJ. Impact of the economic downturn on total joint replacement demand in the United States. *J Bone Joint Surg*. 2014;96(8):624-630.

   doi: 10.2106/jbjs.m.00285

3. Wang C, Sun B, Zhang Y, Wang C, Yang G. Design of a novel trabecular acetabular cup and selective laser melting fabrication. *Materials*. 2022;15(17):6142.

   doi: 10.3390/ma15176142

4. Ismail R, Bayuseno AP, Fitriyana DF, *et al*. Mechanical properties characterization of Ti6Al4V for artificial hip joint materials prepared by investment casting. *IOP Conf Ser Earth Environ Sci*. 2022;969(1):012001.

   doi: 10.1088/1755-1315/969/1/012001

5. Kang Y, Sun DH, Park JC, Kim J. Shape suitability and mechanical safety of customised hip implants: Three-dimensional printed acetabular cup for hip arthroplasty. *J Orthop*. 2022;34:166-172.

   doi: 10.1016/j.jor.2022.08.011

6. Guo N, Leu MC. Additive manufacturing: technology, applications and research needs. *Front Mech Eng*. 2013;8(3):215-243.

   doi: 10.1007/s11465-013-0248-8

7. Grygier D, Kujawa M, Kowalewski P. Deposition of biocompatible polymers by 3D printing (FDM) on titanium alloy. *Polymers*. 2022;14(2):235.

   doi: 10.3390/polym14020235

8. Ishihara K. Highly lubricated polymer interfaces for advanced artificial hip joints through biomimetic design.

Polym J. 2015;47(9):585-597.

doi: 10.1038/pj.2015.45

9. Liqcreate. *Digital Dentistry and Dental Resin 3D-Printing*. Available from: https://www.liqcreate.com/supportarticles/digital-dentistry-and-dental-resin-3d-printing [Last accessed on 2023 Aug 04].

10. Esun. *Dental Resin*. Available from: https://www.esun3d.com/dental-resin/?gad_source=1&gclid=cj0kcqjwxeyxbhc7arisac7ds38iy-mpxesejk3hae1sh_yjox-m6bjfpr3ecyc6-kqwdopvify0k1oaao7_ealw_wcb [Last accessed on 2024 May 21].

11. Da Costa RR, De Almeida FR, Da Silva AA, Domiciano SM, Vieira AF. Design of a polymeric composite material femoral stem for hip joint implant. *Polímeros*. 2019;29(4):354.

doi: 10.1590/0104-1428.02119

12. Alrahlah A, Khan R, Vohra F, *et al*. Influence of the physical inclusion of ZRO2/TIO2 nanoparticles on physical, mechanical, and morphological characteristics of PMMA-Based interim restorative material. *Biomed Res Int*. 2022;2022:1743019.

doi: 10.1155/2022/1743019

13. Bukichev YS, Bogdanova LM, Lesnichaya VA, Chukanov NV, Golubeva ND, Dzhardimalieva GI. Mechanical and thermophysical properties of epoxy nanocomposites with titanium dioxide nanoparticles. *Appl Sci*. 2023;13(7):4488.

doi: 10.3390/app13074488

14. Sun J, Watson SS, Allsopp DA, Stanley D, Skrtic D. Tuning photo-catalytic activities of TiO2 nanoparticles using dimethacrylate resins. *Dent Mater*. 2016;32(3):363-372.

doi: 10.1016/j.dental.2015.11.021

15. Hada T, Kanazawa M, Miyamoto N, *et al*. Effect of different filler contents and printing directions on the mechanical properties for photopolymer resins. *Int J Mol Sci*. 2022;23(4):2296.

doi: 10.3390/ijms23042296

ACCSCIENCE PUBLISHING

Materials Science in Additive Manufacturing

ORIGINAL RESEARCH ARTICLE

Sunflower-inspired composite metastructure for broadband microwave absorption fabricated via fused deposition modeling

Pengfei Fang[1,2], Fei Wang[1,2]*, Zhe Zhang[1,2], Kaiyong Jiang[1,2], and Peifeng Li[3]*

[1]Fujian Key Laboratory of Special Energy Manufacturing, Huaqiao University, Xiamen, Fujian, China
[2]Xiamen Key Laboratory of Digital Vision Measurement, Huaqiao University, Xiamen, Fujian, China
[3]James Watt School of Engineering, University of Glasgow, Glasgow, United Kingdom

Abstract

Microwave-absorbing structures are increasingly vital for applications such as electromagnetic protection, stealth technology, and wireless communications. However, their broader adoption is often limited by drawbacks such as excessive thickness, narrow absorption bandwidth, and high manufacturing costs. This study presents the design, fabrication, and evaluation of a sunflower-inspired metastructure for broadband microwave absorption, achieved via fused deposition modeling three-dimensional printing. The metastructure, inspired by the spiral geometry of sunflower seed arrangements, integrates multi-layered, gradient spiral elements composed of carbon black-carbonyl iron powder/polylactic acid (CB-CIP/PLA) composites. Electromagnetic simulations were employed to systematically optimize key structural parameters, including the gradient impedance increment and individual layer thicknesses, to maximize absorption efficiency. Both simulated and experimental results demonstrate that the absorber achieves an effective absorption bandwidth of 12.13 GHz (5.87 – 18.00 GHz) with reflection loss below 10 dB, covering the C, X, and Ku frequency bands. The performance is attributed to the synergistic effects of interfacial polarization and natural magnetic resonance within the CB-CIP/PLA composite. The metastructure also exhibits stable, wide-angle absorption properties, maintaining bandwidths exceeding 10 GHz for incident angles up to 50° under both transverse electric and transverse magnetic polarizations. The proposed sunflower-inspired design demonstrates significant advantages in bandwidth-to-thickness ratio, fabrication efficiency, and polarization insensitivity compared to conventional biomimetic absorbers. These findings highlight the promise of bio-inspired design strategies for developing lightweight, efficient, broadband microwave absorbers, providing valuable reference for future advancements in the field.

Keywords: Sunflower-inspired metastructure; Broadband microwave absorption; Composite metamaterial; 3D printing; Gradient impedance; Wide-angle absorption; Bio-inspired design

***Corresponding authors:**
Fei Wang
(wangfei@hqu.edu.cn)
Peifeng Li
(peifeng.li@glasgow.ac.uk)

Citation: Fang P, Wang F, Zhang Z, Jiang K, Li P. Sunflower-inspired composite metastructure for broadband microwave absorption fabricated via fused deposition modeling. *Mater Sci Add Manuf.* 2025;4(3):025220048. doi: 10.36922/MSAM025220048

Received: May 31, 2025

Revised: June 16, 2025

Accepted: June 23, 2025

Published Online: August 1, 2025

1. Introduction

With the rapid advancement of electronic information technology and the widespread proliferation of electronic devices, electromagnetic radiation has emerged as a significant source of environmental pollution. Such radiation poses substantial risks in critical areas, including personal health care, military stealth, wireless communication, and environmental safety.[1-3] To mitigate these harmful effects, substantial research efforts have been directed toward developing effective microwave-absorbing materials. These materials typically include dielectric loss materials (e.g., MXene[4] and silicon nitride[5]), magnetic loss materials (e.g., ferrites[6] and metallic powders[7]), and conductive loss materials (e.g., carbon black,[8,9] graphene,[10] and carbon nanotubes[11]).

Traditional absorbing coatings exhibit strong adhesion to object surfaces; however, their intrinsic absorption properties are insufficient to achieve broadband electromagnetic wave absorption.[12-14] Consequently, it remains a significant challenge to develop absorbers simultaneously characterized by a broad bandwidth, lightweight, thin profile, and high structural strength. Achieving these attributes is essential for effectively reducing the reflection and scattering of electromagnetic waves across a broad frequency range.

To address these challenges, biomimetic approaches have become increasingly attractive by leveraging structural and functional inspirations from nature. Many organisms have evolved intricate surface microstructures capable of manipulating electromagnetic waves, offering potential solutions for advanced absorber designs.[15] Examples include algae,[16] bamboos,[17] moth eyes,[18] honeycombs,[19] butterfly wings (e.g., *Pachliopta aristolochiae*),[20] and corals.[21] Through detailed examination of these natural structures, researchers have successfully translated biological principles into effective microwave-absorbing metastructures. For example, inspired by the gyroidal microstructures on butterfly wings, An *et al.*[22] designed a bionic metastructure, achieving ultra-wide absorption bandwidth and exhibiting stable microwave absorption even at an incident angle of 60°, despite the total thickness reaching 15 mm. Similarly, Chen *et al.*[23] fabricated a moth-eye-inspired microwave absorber using conductive graphite powder, resulting in an effective absorption bandwidth (EAB) of 13 GHz across the C, X, and Ku bands. However, this design required a relatively thick structure of 20 mm. Plant-inspired designs have also been explored. For example, Chen *et al.*[24] developed a layered aerogel based on liquid metal MXene, drawing inspiration from plant structures. This design achieved a maximum reflection loss (RL) of −73.2 dB at a density of 4.4 mg/cm^3, although with an EAB of only 7 GHz. Despite these advancements, considerable room remains for optimizing designs to achieve broader bandwidths, lighter weight, and thinner structures.

Among numerous biological templates, the sunflower exhibits a particularly promising structural geometry for bio-inspired engineering applications. Sunflower petals have inspired novel solar collectors integrating pulsating heat pipes into flat-plate designs.[25] Besides, sunflower stem pith is identified as an ultra-lightweight porous structure exhibiting exceptional mechanical properties and energy absorption capabilities.[26] In addition, the spiral arrangement of sunflower heads has informed the design of efficient deployable structures utilizing flat-folded isogonal spiral patterns.[27]

Motivated by these unique characteristics, this study proposes a novel sunflower-inspired microwave-absorbing metastructure, fabricated from a carbon black-carbonyl iron powder/polylactic acid (CB-CIP/PLA) composite via fused deposition modeling (FDM). By mimicking the sunflower disk's spiral pattern, the proposed metastructure aims to achieve enhanced broadband microwave absorption performance, reduced structural thickness, and a simplified fabrication process. Experimental analyses and electromagnetic simulations confirmed excellent microwave absorption under wide-angle and varying polarization conditions. The insights gained from this research are expected to significantly advance the development and practical application of broadband microwave absorption materials, particularly in military stealth technology and wireless communication systems.

2. Methodology

2.1. Design of sunflower-inspired metastructure and electromagnetic simulation

The sunflower is characterized by a unique spiral arrangement of seeds in its flower head. The sunflower head exhibits two distinct sets of constant-velocity spirals, one rotating clockwise and the other counterclockwise, interwoven with each other (Figure 1A). This arrangement positions sunflower seeds at intersections of spirals, enabling dense packing with minimal spacing. Consequently, the sunflower head achieves stable and smooth growth from bracts to a large floral disk.

While sunflowers do not directly influence microwave absorption, their distinctive seed arrangement can inspire effective absorber designs. This seed pattern resembles a constant-velocity spiral (Figure 1B), which can be modeled in polar coordinates as follows:

$$R_i = k_i \times \theta_i \quad \text{(I)}$$

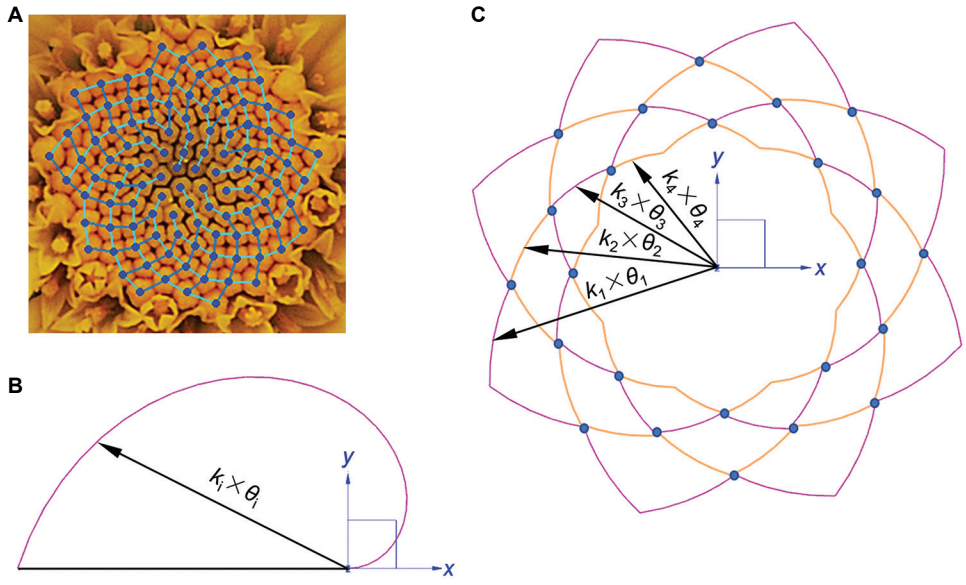

Figure 1. Modeling process for the sunflower-inspired metastructure. (A) Schematic representation of the spiral arrangement of seeds in a sunflower head, serving as the structural inspiration for the metastructure. (B) Outline of a single constant-velocity spiral. (C) Construction of mirrored and concentric spiral contours

where R_i represents the polar radius, θ_i is the polar angle, and k_i is the coefficient defining the spiral expansion rate. Figure 1C illustrates the modeling process of a sunflower-inspired spiral. Initially, the outermost spiral radius R_1 is determined by the periodic unit length L (equal to $2R$). Subsequent spirals are generated by performing mirror reflections (along the polar radius) and ring-array rotations (around the coordinate origin), progressively determining inner spiral intersections. This iterative process results in a gradient arrangement of spiral radii along the z-axis, producing a sunflower-like three-dimensional spiral structure in both clockwise and counterclockwise orientations.

A periodic array of these metastructure units is formed along the x and y directions (Figure 2A). Specific geometric parameters of the unit are detailed in Figure 2B. To achieve optimal electromagnetic performance, multiple spiral layers with distinct spiral coefficients (k_1, k_2, k_3, and k_4) are stacked vertically, creating a gradient distribution. Each spiral layer possesses an identical thickness (h_1=h_2=h_3=h_4). Electromagnetic simulations, including RL analysis and evaluations of electric, magnetic, and power loss field distributions, were performed using CST Studio Suite software (Dassault Systèmes, France).

2.2. Materials and fabrication

The raw materials used in this study included CB powder (surface area 55 – 70 m^2/g, resistivity 2.5 Ω·m) (Tianjin Zhengyuan Technology Co. Ltd., China), CIP powder (Hebei Lebo Metal Material Technology Co. Ltd., China),

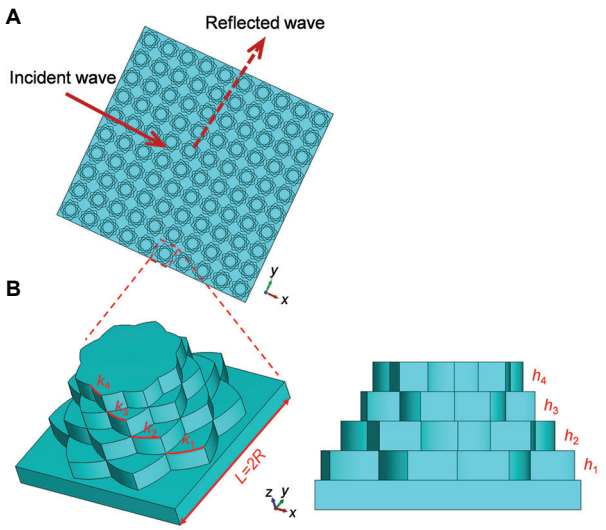

Figure 2. Structural characteristics of the sunflower-inspired metastructure. (A) Periodic array arrangement along the x and y axes. (B) A single metastructure unit cell illustrating key geometric parameters

and polymer matrix PLA powder (4032D) (Dongguan Huachuang Plastic Technology Co. Ltd., China). The sunflower-inspired metastructure was fabricated using FDM 3D printing (Figure 3). Before printing, CB-CIP/PLA composite filaments were prepared. First, CB and PLA were dried at 80°C for 6 h to remove residual moisture. Subsequently, PLA was mixed with 1.5 wt.% aluminate coupling agent, followed by the addition of 20 wt.% CB and 30 wt.% CIP. Note that the weight percentages here are relative to the PLA matrix mass. This mixture was

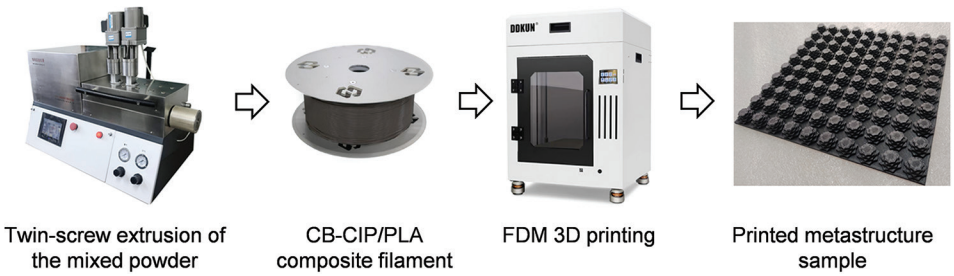

Figure 3. Fabrication of CB-CIP/PLA composite filaments and 3D printing process of the sunflower-inspired metastructure sample for microwave absorption testing
Abbreviations: CB-CIP/PLA: Carbon black-carbonyl iron powder/polylactic acid; FDM: Fused deposition modeling

homogenized using a dual-motion high-energy mixer (Zhengzhou Gold Co-Powder Technology Co. Ltd., China) with cylinder and blade speeds set at 28 rpm and 17 rpm, respectively, for 1 h. The uniformly mixed material was then fed into a micro twin-screw extruder (Wuhan Ruiming Experimental Instrument Manufacturing Co. Ltd., China) to produce filaments with a diameter of 1.75 ± 0.10 mm. The composite filaments were subsequently used to fabricate the designed metastructure through an FDM 3D printer (DDKUNT3040, Creative 3D Technology Co., Ltd., China) using the processing parameters as listed in Table 1. The printed metastructure sample (180 mm × 180 mm), composed of an array of 10 × 10 units, was finally prepared for microwave absorption testing.

2.3. Characterization and measurement

The microstructure of the fabricated composite was characterized using scanning electron microscopy (SEM). Electromagnetic parameters were measured in the frequency range of 2 – 18 GHz using a vector network analyzer (Keysight, USA) and adopting a coaxial transmission line method. Test specimens used for parameter measurements had an outer diameter of 7.00 mm, an inner diameter of 3.04 mm, and a thickness of 2.00 mm.

The microwave absorption performance of the printed metastructure was evaluated via a modified bow-shaped measurement method (Figure 4). Unlike the conventional bow-shaped method, where horn antennas and the sample are placed horizontally, this modified approach positions the horn antennas horizontally and the test sample vertically. Incident electromagnetic waves, transmitted from one horn antenna, are partially reflected off the sample surface. The reflected waves are either captured by the receiving antenna or absorbed by corner foam absorbers. This configuration enables precise measurement and analysis of microwave absorption performance across different incident angles and polarization states.

Table 1. Processing parameters in fused deposition modeling 3D printing

Parameter	Value
Printing speed (mm/s)	40
Layer height (mm)	0.2
Nozzle temperature (°C)	210
Bed temperature (°C)	50
Filling density (%)	100

3. Results and discussion

3.1. Morphology and electromagnetic properties of CB-CIP/PLA composite filaments

Figure 5A demonstrates the SEM image of the CB-CIP/PLA composite. The CB and CIP particles are largely uniformly dispersed within the PLA matrix, facilitated by high-temperature extrusion and frictional shear during twin-screw processing. However, due to the high specific surface area and surface energy of CB, agglomeration is observed. These CB agglomerates contribute to the formation of conductive networks, thereby enhancing the electrical conductivity and dielectric constant of the composite. Similarly, CIP particles, characterized by high surface activity, also show signs of localized agglomeration during the melting or molding process (as highlighted in Figure 5A). These CIP agglomerates increase local eddy current losses and suppress natural resonance behavior.[28] Note that the CB and CIP contents influence the microwave absorption performance of the filaments, with the combination of 20 wt.% CB and 30 wt.% CIP yielding the optimal absorption properties.[28] The electromagnetic parameters of the composite were characterized in the frequency range of 2 – 18 GHz. As shown in Figure 5B, the real and imaginary parts of the complex permittivity remain relatively stable across the measured frequency range. In contrast, both the real and imaginary components of the complex permeability exhibit a decreasing trend with increasing frequency.

To evaluate the microwave absorption performance of the composite, the RL was calculated for the composite absorber plate of varying thickness as follows:[29]

$$RL = 20\log\left|\frac{Z_{in} - Z_0}{Z_{in} + Z_0}\right| \quad \text{(II)}$$

$$Z_{in} = Z_0\sqrt{\frac{\mu}{\varepsilon}}\tanh\left[j\left(\frac{2\pi fd}{c}\right)\sqrt{\mu E}\right] \quad \text{(III)}$$

where Z_0, with a value of 377 Ω, is the impedance of free space, Z_{in} is the input impedance of the material, ε and μ are the relative complex permittivity and permeability, respectively, f is the frequency of the incident microwave, d is the thickness of the absorbing plate, and c, with a value of 3×10^8 m/s, is the speed of electromagnetic wave in free space.

Figure 6A and B present the RL curves and corresponding 3D plots, respectively, for composites of different thicknesses over the 2 – 18 GHz frequency range. As the thickness increases, the minimum RL (absorption peak) initially decreases and then increases, whereas the corresponding peak frequency shifts toward lower frequencies. This behavior is consistent with the quarter-wavelength ($\lambda/4$) matching condition,[30,31] which describes the relationship between matching thickness (d_m) and the peak matching frequency (f_m) as:

$$d_m = \frac{n\lambda}{4} = \frac{nc}{4f_m\sqrt{|\mu\varepsilon|}} \quad (n = 1,3,5,\ldots) \quad \text{(IV)}$$

where λ is the electromagnetic wavelength in the material.

Figure 6C demonstrates the experimental relationship between d_m and f_m. The red pentagrams denote the experimental matching points, which align closely with the theoretical $\lambda/4$ curve. This confirms the validity of the $\lambda/4$ model for the composite. However, the experimental points lie slightly above the theoretical curve, indicating that the absorption peaks occur at higher frequencies than predicted for a given thickness. This deviation is attributed to the intrinsic absorption properties of the material, which shift the peak absorption frequency. Meanwhile, Figure 6D illustrates the EABs (defined as RL < −10 dB) for thicknesses ranging from 1.5 to 4.0 mm. The widest EAB is achieved at a thickness of 2.0 mm, indicating that the absorption performance of the composite can be effectively tuned by adjusting the absorber plate thickness.

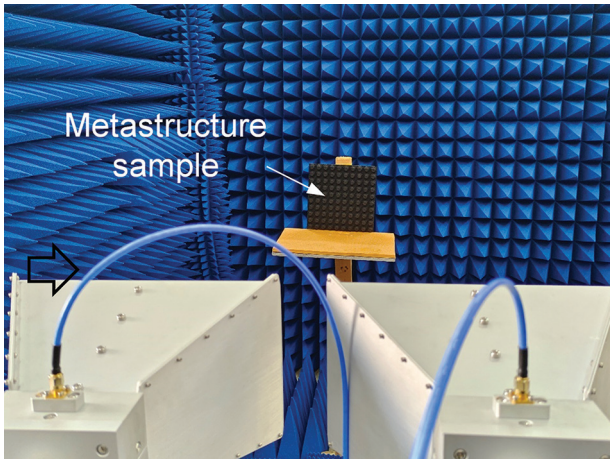

Figure 4. Experimental setup for microwave absorption measurements using the bow-shaped method, depicting the arrangement of the horn antennas and the sample positioning for reflection loss evaluation

3.2. Geometric optimization of the sunflower-inspired metastructure

3.2.1. Determination of spiral parameters

To achieve broadband microwave absorption, the geometric parameters of the sunflower-inspired metastructure were carefully investigated and optimized

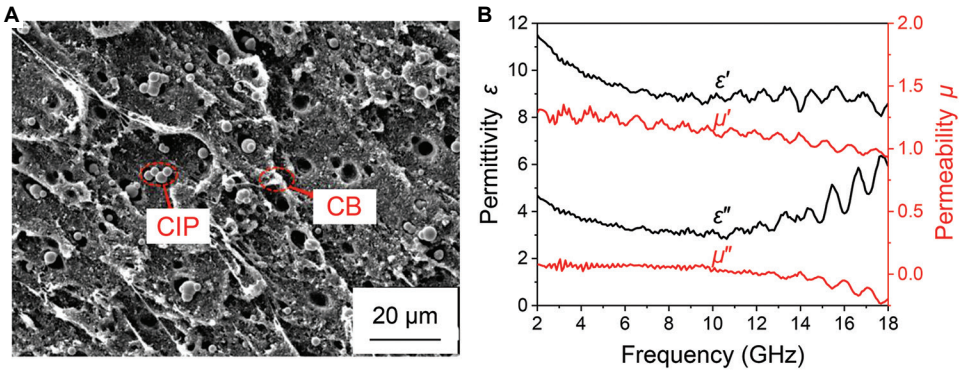

Figure 5. Morphology and electromagnetic properties of CB-CIP/PLA composite filaments. (A) SEM image of the composite, showing the dispersion and agglomeration of CB and CIP particles within the PLA matrix (scale bar: 20 μm; magnification: 1000×). (B) Real and imaginary parts of the composite's complex permittivity and permeability

Abbreviations: CB-CIP/PLA: Carbon black-carbonyl iron powder/polylactic acid; SEM: Scanning electron microscopy

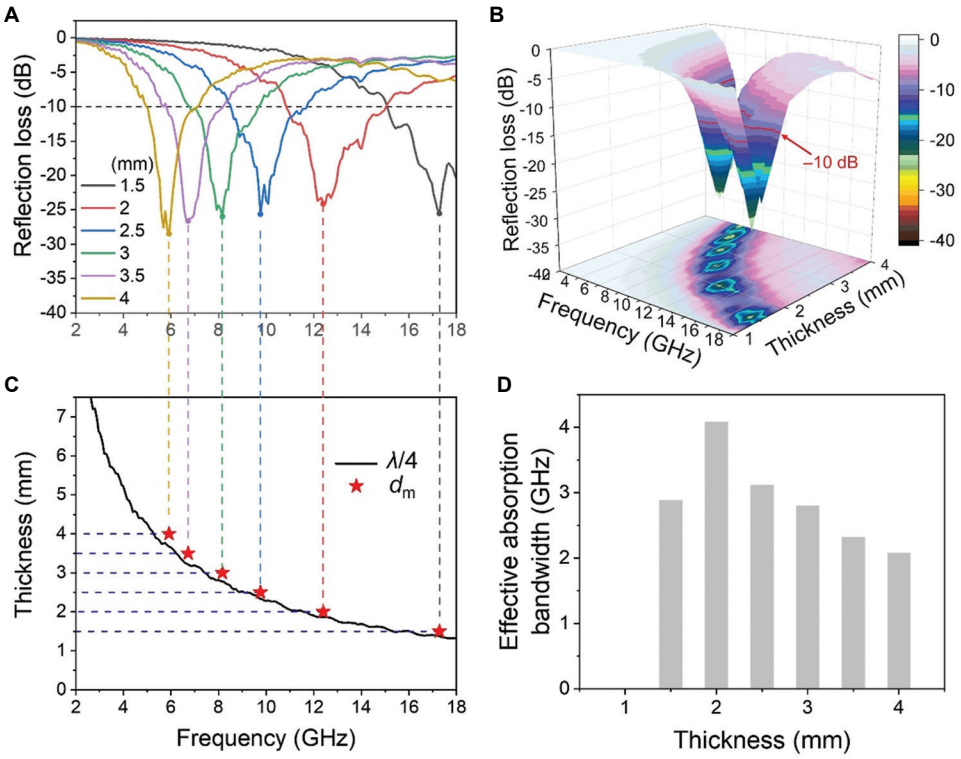

Figure 6. Microwave absorption performance of the CB-CIP/PLA composite. (A) Reflection loss curves for the composite at varying thicknesses over the 2 – 18 GHz frequency range. (B) A 3D representation of reflection loss versus frequency and sample thickness. (C) Relationship between matching thickness (d_m) and frequency (f_m), comparing the experimental data with the theoretical $\lambda/4$ model. (D) Effective absorption bandwidth as a function of sample thickness (1.0 – 4.0 mm)
Abbreviation: CB-CIP/PLA: Carbon black-carbonyl iron powder/polylactic acid

using electromagnetic simulations. The metastructure unit length (L) was set to 18 mm, and the polar radius of the constant-velocity spiral was thus determined as half the unit length (i.e., R = 9 mm) (Figure 2B). Based on the desired gradient characteristic impedance distribution, the parameters k (spiral coefficient) and θ (polar angle) of the constant-velocity spirals were calculated for each layer. The spiral layer thickness was fixed at $h_1 = h_2 = h_3 = h_4 = 2$ mm.

To ensure a smooth impedance gradient across the layers and achieve broadband impedance matching, the gradient impedance increment (ΔZ) between adjacent layers was varied systematically from 18 Ω to 28 Ω in steps of 2 Ω. The equivalent characteristic impedance (Z_i) of each layer was first calculated as follows:

$$Z_i = Z_0 \left| \sqrt{\frac{\mu_{eff}' - \mu_{eff}''}{\varepsilon_{eff}' - \varepsilon_{eff}''}} \right| \quad \text{(V)}$$

$$\Delta Z = Z_{i+1} - Z_i \quad \text{(VI)}$$

where ε_{eff} is the effective permittivity and μ_{eff} is the effective permeability. The impedance of the adjacent layer (Z_{i+1}) was then determined by controlling the ΔZ. The layers were sequentially stacked from bottom (closest to the metallic backplane) to top (closest to the air) in ascending order of impedance (Z_i). The bottom-most square layer featured a fixed characteristic impedance (Z) of 127.8 Ω. Next, the volume fraction f_c of each layer composed of constant-velocity spirals was calculated using the effective permittivity (ε_{eff}) and permeability (μ_{eff}):

$$\varepsilon_{eff} = \varepsilon_c f_c + (1 - f_c)\varepsilon_0 \quad \text{(VII)}$$

$$\mu_{eff} = \mu_c f_c + (1 - f_c)\mu_0 \quad \text{(VIII)}$$

where ε_c and μ_c represent the relative complex permittivity and permeability of the composite material, respectively, but ε_0 and μ_0 denote the respective values for air. The disk area S_i of each spiral layer was then obtained using the volume fraction f_c in Equation IX, and the spiral coefficient k_i for each layer was calculated using Equation X.

$$f_c = \frac{S_i}{L^2} \quad \text{(IX)}$$

$$S_i = 16 \times \int_{\frac{R_i}{k_i} - \frac{\pi}{8}}^{\frac{R_i}{k_i}} \frac{1}{2} k_i^2 \theta^2 d\theta \quad \text{(X)}$$

Figure 7 illustrates how the ΔZ influences the microwave absorption performance. With increasing ΔZ, the EAB for RL below −10 dB gradually decreases, whereas the EAB for RL below −15 dB initially increases and then decreases. Notably, when ΔZ reaches 24 Ω, the metastructure achieves an effective −10 dB absorption bandwidth of 14.07 GHz (3.93 – 18 GHz), covering the entire C, X, and Ku bands. In addition, the −15 dB absorption bandwidth reaches 11.54 GHz (4.25 – 5.15 GHz and 7.36 – 18 GHz). This enhanced performance at ΔZ of 24 Ω can be attributed to the reduced spiral coefficients (k_i), which intensify resonance interactions between adjacent layers, thus enabling efficient dissipation of microwave energy across a broad frequency range. However, further increasing ΔZ beyond 24 Ω (e.g., to 28 Ω) results in a narrowing of the EAB. Based on a comprehensive comparison of absorption bandwidth and RL performance, the optimal ΔZ was determined to be 24 Ω, with corresponding spiral coefficients k_1 of 4.39, k_2 of 2.80, k_3 of 2.74, and k_4 of 1.69.

3.2.2. Determination of layer thicknesses

Initially, the four gradient layers of the sunflower-inspired metastructure were equally divided without considering the influence of layer thickness on microwave absorption performance. To optimize the metastructure systematically, the individual thicknesses (h_1, h_2, h_3, and h_4) of each layer were analyzed separately using parametric sweeps in the CST software. During these sweeps, each layer thickness was varied independently from 1 to 3 mm in 0.5 mm increments, whereas the remaining layers were fixed at a baseline value of 2 mm.

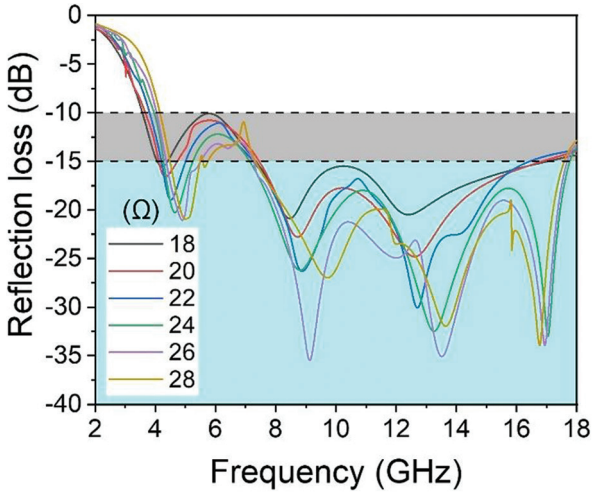

Figure 7. Effect of the gradient characteristic impedance increment (ΔZ) between adjacent layers on the absorption bandwidth and reflection loss of the sunflower-inspired metastructure

Figure 8 demonstrates how varying the thickness of each layer influences the metastructure's microwave absorption performance. Increasing either h_1 or h_2 shifts the low- and mid-frequency absorption peaks toward lower frequencies, while slightly shifting the high-frequency peak toward higher frequencies. In contrast, increasing h_3 or h_4 shifts low- and mid-frequency peaks to lower frequencies but does not notably affect the high-frequency peak position. Although these adjustments slightly broaden the EAB, the overall effect on bandwidth is limited. For example, increasing h_1 from 1 mm to 3 mm only expands the EAB from 13.71 GHz to 14.32 GHz, an increment of just 0.61 GHz.

Nonetheless, layer thickness variations significantly affected absorption peak intensity, and these influences differed among layers (Figure 8). Specifically, increasing h_1 consistently reduces the overall peak RL. For h_2, the absorption peaks at low and high frequencies gradually decrease, whereas the mid-frequency absorption peak initially intensifies and then weakens, reaching a maximum absorption of −50.96 dB at a h_2 of 3 mm. The layer thickness h_3 exhibits its strongest absorption peak (−59.65 dB) at the intermediate frequency when set to 2.5 mm. Finally, when h_4 was set to 2.5 mm, the metastructure achieves a maximum peak absorption of −57.78 dB in the mid-to-high frequency range.

In summary, adjusting individual layer thicknesses primarily impacts the absorption peak positions and intensities rather than significantly altering the total effective bandwidth. Therefore, precise tuning of h_1 through h_4 is vital for optimizing the metastructure's microwave absorption performance across the desired frequency bands.

3.3. Microwave absorption mechanisms of the sunflower-inspired metastructure

The previous analysis revealed that increasing the ΔZ between adjacent layers narrows the EAB at lower frequencies (Figure 7). This is primarily attributed to local impedance mismatches introduced by the centrosymmetric configuration of the sunflower-inspired metastructure unit. To quantitatively analyze this effect, the effective input impedance (Z_{eff}) was calculated as follows:[32,33]

$$Z_{eff} = \sqrt{\frac{(1+S_{11})^2 - S_{21}^2}{(1-S_{11})^2 - S_{21}^2}} \quad \text{(XI)}$$

where S_{11} is the reflection coefficient and S_{21} is the transmission coefficient. Due to the presence of a copper foil backplane, transmission is suppressed ($S_{21} = 0$). Using the optimal structural parameters identified in Section 3.2, the computed real and imaginary parts of Z_{eff} are shown in

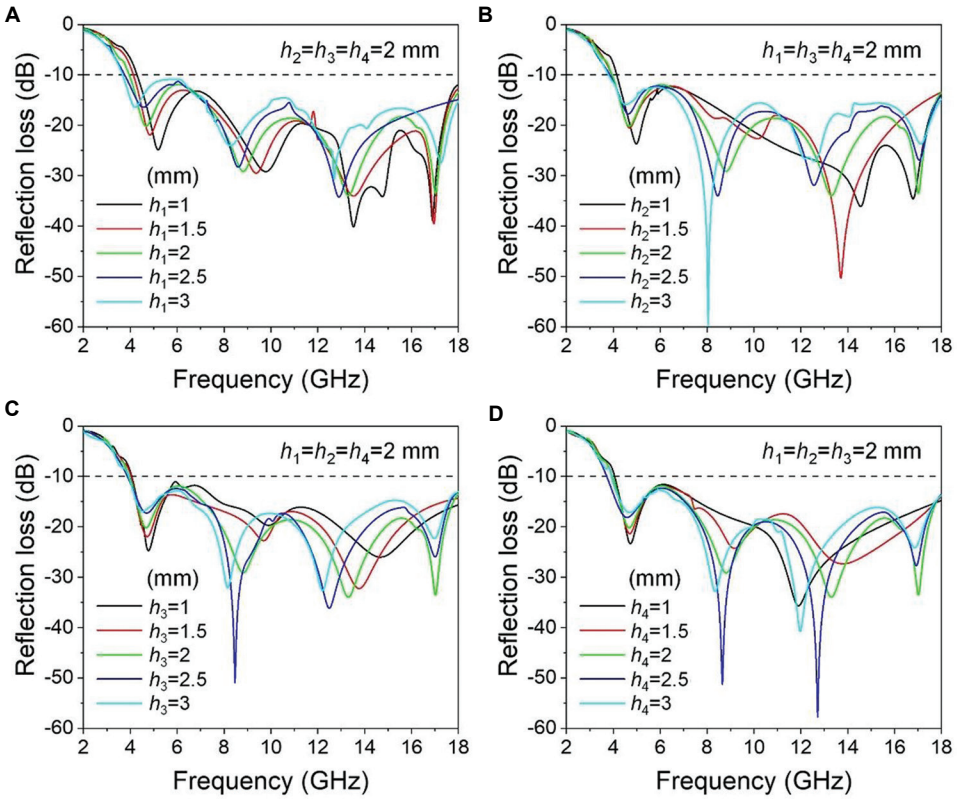

Figure 8. Effects of individual layer thickness on the absorption performance of the sunflower-inspired metastructure: (A) h_1, (B) h_2, (C) h_3, and (D) h_4

Figure 9. For effective absorption, Z_{eff} should closely match the impedance of free space, i.e., the real part should be close to 1, and the imaginary part close to 0. This condition is generally met above 3.93 GHz. However, in the 2 – 3.93 GHz range, both the real and imaginary parts fluctuate, indicating impedance mismatch and reduced absorption efficiency at low frequencies.

To further explore the metastructure's angular and polarization stabilities, RL was simulated under varying incident angles for both transverse electric (TE) and transverse magnetic (TM) polarizations. As shown in Figure 10, the metastructure maintains robust absorption performance across a range of incident angles. Under TE polarization, the EAB (RL < −10 dB) remains nearly unchanged up to 33°, due to enhanced multiple reflections and edge scattering between adjacent units.[34,35] Beyond 33°, the bandwidth gradually decreases as more waves are reflected at higher incident angles. TM polarization demonstrates greater angular stability. Even at 50°, the EABs for TE and TM waves remain as high as 10.63 GHz and 13.70 GHz, respectively. The centrosymmetric design of the metastructure unit also ensures polarization insensitivity, as confirmed by the consistent response at various polarization angles ranging from 0° (TE mode) to 90° (TM mode) in Figure 11.

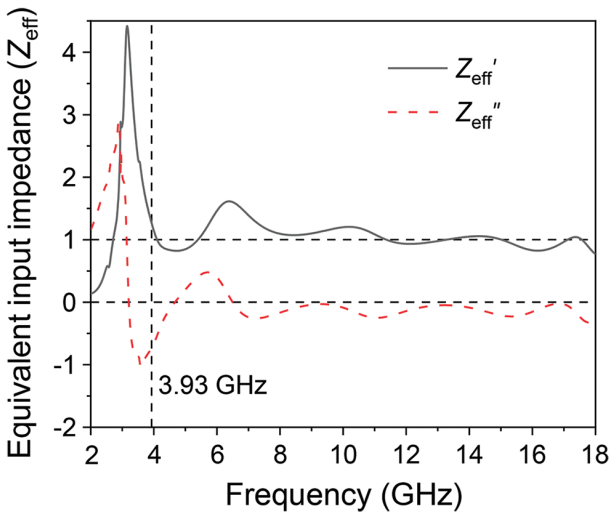

Figure 9. Real (Z_{eff}') and imaginary (Z_{eff}") parts of the equivalent input impedance (Z_{eff}) for the sunflower-inspired metastructure as a function of frequency, illustrating the impedance matching behavior with free space

To elucidate the absorption mechanisms, electric and magnetic field distributions were simulated at four characteristic peak frequencies: 4.66 GHz, 8.80 GHz, 13.25 GHz, and 17.04 GHz (Figure 12). At the first

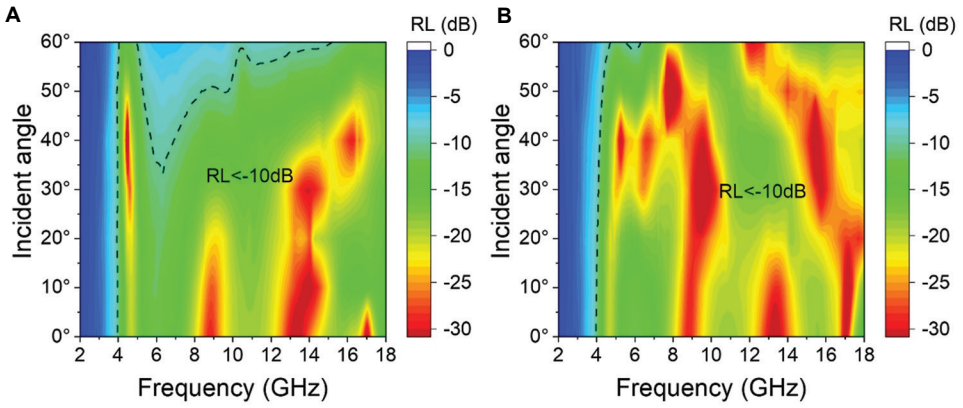

Figure 10. Absorption spectra of the sunflower-inspired metastructure under various incident angles and polarization states. (A) Reflection loss (RL) under transverse electric polarization for incident angles 0 – 60°. (B) RL under transverse magnetic polarization

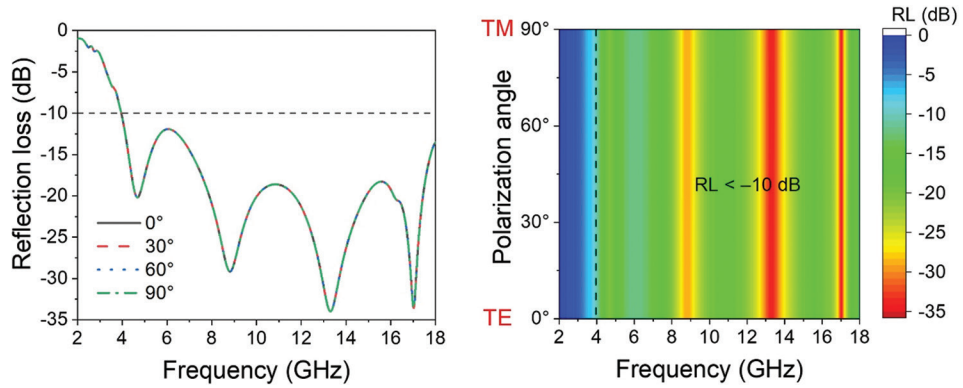

Figure 11. Polarization dependence of the sunflower-inspired metastructure, showing RL as a function of polarization angle and demonstrating polarization insensitivity
Abbreviations: TE: Transverse electric; TM: Transverse magnetic; RL: Reflection loss

peak frequency (4.66 GHz), the electric field mainly concentrates on the upper edges and inter-unit gaps, whereas the magnetic field localizes near the bottom metal plane, demonstrating a classic $\lambda/4$ resonance behavior.[36-38] At the second peak (8.80 GHz), the electric field extends to the top structure and across interlayer gaps, whereas the magnetic field shifts to the middle and lower sections of the absorber. By the third peak (13.25 GHz), a strong structural resonance appears between adjacent units, and the magnetic field shifts toward the top center. At the fourth peak (17.04 GHz), both electric and magnetic fields are concentrated near the top edge, exhibiting pronounced edge diffraction effects.[39,40]

Figure 13 presents the power loss density distributions at the same frequencies. At 4.66 GHz, energy loss is concentrated in the central region of the metastructure. As frequency increases, the loss region gradually shifts toward the top and eventually to the top edge. The loss culminates at the top edge by 17.04 GHz with strong energy dissipation at the structure's boundary, consistent with high-frequency edge diffraction effects.

In summary, the sunflower-inspired metastructure achieved microwave attenuation through multiple mechanisms:

- Low frequencies: $\lambda/4$ resonance induced by magnetic losses near the metal backplane;
- Intermediate frequencies: structural resonance between adjacent spiral layers;
- High frequencies: edge diffraction and strong field localization at the structure's periphery.

The correlation between the magnetic field and power loss distributions at high frequencies also suggests that magnetic losses, such as those caused by domain wall motion and hysteresis between adjacent structural units, are significant contributors to microwave absorption in the designed metastructure.

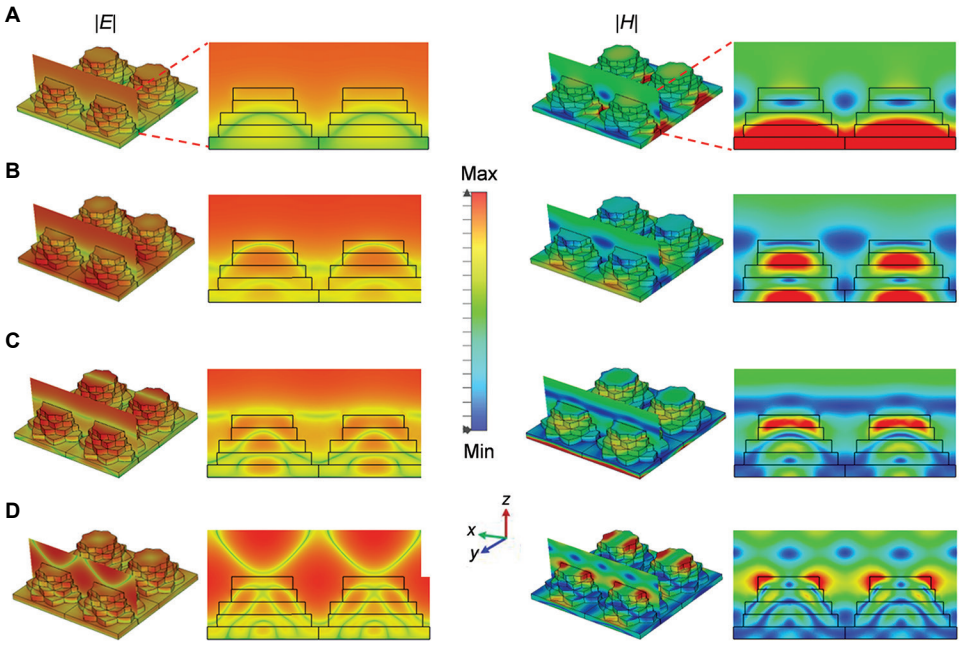

Figure 12. Simulated electric field (|*E*|, left) and magnetic field (|*H*|, right) distributions of the sunflower-inspired metastructure at absorption peak frequencies: (A) 4.66 GHz, (B) 8.80 GHz, (C) 13.25 GHz, and (D) 17.04 GHz, illustrating the evolution of the field localization and resonance behavior

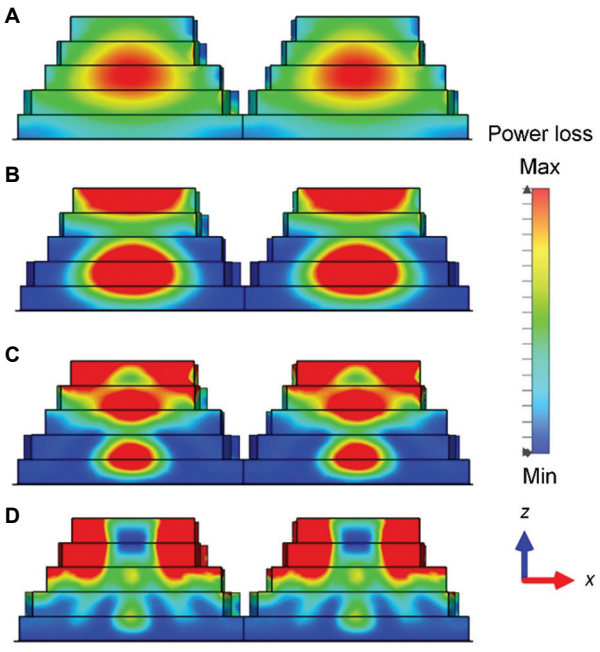

Figure 13. Simulated power loss density distributions of the metastructure at varying absorption peak frequencies: (A) 4.66 GHz, (B) 8.80 GHz, (C) 13.25 GHz, and (D) 17.04 GHz, showing the shift of energy dissipation from the structure's center to its top edge at higher frequencies

3.4. Experimental verification

To validate the accuracy and reliability of the simulation results, the sunflower-inspired metastructure was fabricated using FDM 3D printing, as shown in Figure 3. The simulated and experimentally measured RL curves at the incident angle of 0° under TE polarization are compared in Figure 14. Overall, the measured results exhibit a trend consistent with the simulations, confirming the validity of the electromagnetic modeling approach. However, minor discrepancies are observed between the measured and simulated data. These deviations are primarily attributed to several factors: the small unit size, dimensional inaccuracies, slight warping at the base of the printed sample, and surface roughness caused by the step effect inherent to the FDM process. These imperfections can lead to additional electromagnetic wave scattering and, consequently, diminished absorption efficiency.

The measured EAB (12.13 GHz) spans from 5.87 to 18 GHz, which is slightly narrower than the simulated bandwidth. In the 2 – 5.87 GHz range, the measured RL does not reach −10 dB, unlike in simulations (Figure 14). This discrepancy is potentially due to differences in the incident angle. While simulations assumed normal incidence, the experimental setup employed side-by-side horn antennas, resulting in a non-zero incident angle and reduced absorption. Nonetheless, the metastructure still demonstrates strong performance, maintaining over 80% absorptivity (i.e., RL < −7 dB) in the 3.16 – 5.87 GHz band.

In summary, the experimental findings validated the sunflower-inspired metastructure's excellent broadband microwave absorption performance. In addition, Table 2 compares the performance of this metastructure with

Table 2. Comparison of microwave absorption performance parameters between the sunflower-inspired metastructure and previously reported biomimetic microwave absorbers

Material	Structure	Thickness (mm)	Absorption bandwidth (GHz)	References
ABS	Bio-inspired gyroid	15	2.3 – 40	22
PEEK/FCIPs	Bamboo	15	3.2 – 40	17
Resistance patch+PLA	Honeycomb	15.51	3.53 – 24	19
Graphite powder/epoxy resin	Bio-inspired moth eye	20	5 – 18	23
CB-CIP/PLA	Sunflower-inspired metastructure	10	5.87 – 18	This study

Abbreviations: ABS: Acrylonitrile butadiene styrene; CB-CIP/PLA: Carbon black-carbonyl iron powder/polylactic acid; PEEK/FCIPs: Polyether ether ketone/flaky carbonyl iron powder.

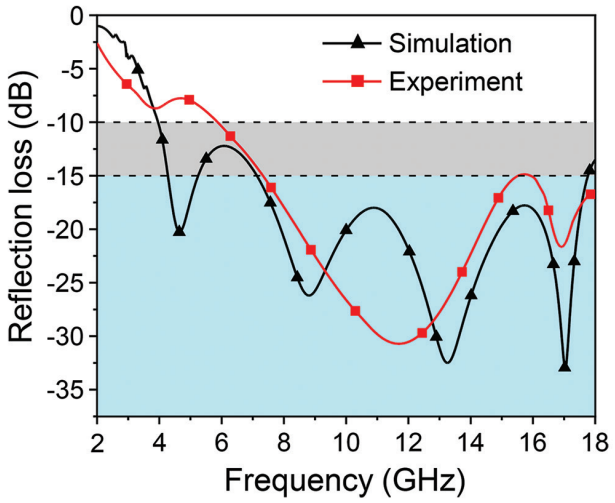

Figure 14. Comparison of simulated and experimentally measured reflection loss for the sunflower-inspired metastructure, demonstrating the consistency between simulation and measurement results

previously reported biomimetic absorbers. The present design achieves competitive absorption performance while maintaining a thinner profile. Compared to other structures, this metastructure benefits from reduced thickness and optimized material selection, demonstrating significant advantages in practical application. Finally, the metastructure is based on a periodic array of identical unit cells, which can be readily expanded or reduced to accommodate different application requirements.

4. Conclusion

This work presents a bio-inspired metastructure based on the spiral geometry of sunflower seed arrangements, developed for broadband microwave absorption. The metastructure integrates a CB-CIP/PLA composite and a multi-layered spiral gradient configuration to achieve both structural simplicity and enhanced electromagnetic performance. By optimizing structural parameters, particularly the gradient impedance increments between adjacent layers, a low-cost metastructure absorber was successfully fabricated using FDM 3D printing. Experimental results confirmed that the metastructure achieves an EAB of 12.13 GHz (5.87 – 18 GHz), with absorption rates exceeding 90% (RL < −10 dB), effectively covering the C, X, and Ku frequency bands.

In the CB-CIP/PLA composites used in this study, the interfacial polarization between CB and CIP improves the dielectric loss, while natural resonance enhances magnetic loss. These synergistic effects contribute to the efficient microwave attenuation observed. In addition, the metastructure absorber exhibits stable, wide-angle performance: for both TE and TM polarization states, the absorption bandwidths exceeding 10 GHz are maintained at incident angles up to 50°. Electric and magnetic field simulations, along with power loss density distributions, further confirmed the absorption mechanisms across different frequency bands, namely, $\lambda/4$ resonance at low frequencies, inter-layer structural resonance at intermediate frequencies, and edge diffraction at high frequencies. The findings demonstrate that combining biological inspiration with additive manufacturing offers a promising route for developing lightweight, efficient, and broadband microwave-absorbing materials.

Acknowledgments

None.

Funding

This study was funded by the Fuzhou–Xiamen–Quanzhou National Independent Innovation Demonstration Zone Collaborative Innovation Platform Project (3502ZCQXT2024003) and the Fujian Province Industry–University Cooperation Plan (2023H6015).

Conflicts of interest

The authors declare they have no competing interests.

Author's contributions

Conceptualization: Fei Wang, Kaiyong Jiang, Peifeng Li
Formal analysis: Pengfei Fang, Zhe Zhang

Funding acquisition: Fei Wang, Kaiyong Jiang
Investigation: Pengfei Fang, Fei Wang, Zhe Zhang
Methodology: Fei Wang, Kaiyong Jiang, Peifeng Li
Resources: Kaiyong Jiang
Validation: Fei Wang, Kaiyong Jiang, Peifeng Li
Writing–original draft: Pengfei Fang, Fei Wang
Writing–review & editing: Peifeng Li

Ethics approval and consent to participate

Not applicable.

Consent for publication

Not applicable.

Availability of data

The raw/processed data required to reproduce these findings cannot be shared at this time, as the data are part of an ongoing study.

References

1. Abdalla I, Cai JY, Lu W, Yu JY, Li ZL, Ding B. Recent progress on electromagnetic wave absorption materials enabled by electrospun carbon nanofibers. *Carbon.* 2023;213:118300.

   doi: 10.1016/j.carbon.2023.118300

2. Chen XT, Wu Y, Gu WH, *et al.* Research progress on nanostructure design and composition regulation of carbon spheres for the microwave absorption. *Carbon.* 2022;189:617-633.

   doi: 10.1016/j.carbon.2021.12.100

3. Li B, Liu M, Zhong W, *et al.* Partially contacted NixSy@N, S-codoped carbon yolk-shelled structures for efficient microwave absorption. *Carbon.* 2021;182:276-286.

   doi: 10.1016/j.carbon.2021.05.057

4. Guan X, Yang Z, Zhou M, *et al.* 2D MXene nanomaterials: Synthesis, mechanism, and multifunctional applications in microwave absorption. *Small Struct.* 2022;3(10):2200102.

   doi: 10.1002/sstr.202200102

5. Zhou W, Long L, Bu G, Li Y. Mechanical and microwave-absorption properties of Si3N4 ceramic with SiCNFs fillers. *Adv Eng Mater.* 2019;21(5):1800665.

   doi: 10.1002/adem.201800665

6. Houbi A, Aldashevich ZA, Atassi Y, Telmanovna ZB, Saule M, Kubanych K. Microwave absorbing properties of ferrites and their composites: A review. *J Magn Magn Mater.* 2021;529:167839.

   doi: 10.1016/j.jmmm.2021.167839

7. Jang W, Mallesh S, Lee S, Kim KH. Microwave absorption properties of core-shell structured FeCoNi@PMMA filled in composites. *Curr Appl Phys.* 2020;20(4):525-530.

   doi: 10.1016/j.cap.2020.01.019

8. Wang F, Zhou Q, Zhang Z, He P, Zhang J, Jiang K. Microwave absorption performance of carbon black/polylactic acid composite for fused filament fabrication. *Appl Sci Basel.* 2022;12(24):12747.

   doi: 10.3390/app122412747

9. Wang F, Zhou Q, Liu H, Fang P, Jiang K, Li P. Wide-angle broadband metamaterial absorber with carbon black-carbonyl iron/polylactic acid composites fabricated by fused filament fabrication. *Mater Sci Addit Manuf.* 2024;3(3):4158.

   doi: 10.36922/msam.4158

10. Ding GX, Chen CX, Tai HX, *et al*. Structural characterization and microwave absorbing performance of CuFe2O4/RGO composites. *J Solid State Chem.* 2021;297:22051.

    doi: 10.1016/j.jssc.2021.122051

11. Zhang K, Gao X, Zhang Q, Chen H, Chen X. Fe3O4 nanoparticles decorated MWCNTs @ C ferrite nanocomposites and their enhanced microwave absorption properties. *J Magn Magn Mater.* 2018;452:55-63.

    doi: 10.1016/j.jmmm.2017.12.039

12. Ding DH, Luo F, Zhou WC, Shi YM, Zhou L. Research status and outlook of high temperature radar absorbing materials. *J Inorg Mater.* 2014;29(5):461-469.

    doi: 10.3724/sp.J.1077.2014.13471

13. Tang XJ, Li XB, Sun HG. Preparation and Properties of an Anti-Friction and Anti-Corrosive Radar Absorbing Material with Periodic Intermediate Coating. In: *Paper Presented at: 6th Annual International Conference on Material Science and Environmental Engineering (MSEE),* Chongqing, PR China; 2018.

    doi: 10.1088/1757-899x/472/1/012012

14. Wang YM, Pan M, Liang XY, Li BJ, Zhang S. Electromagnetic wave absorption coating material with self-healing properties. *Macromol Rapid Commun.* 2017;38(23):1700447.

    doi: 10.1002/marc.201700447

15. Li AB, Zhao XG, Duan GW, Anderson S, Zhang X. Diatom frustule-inspired metamaterial absorbers: The effect of hierarchical pattern arrays. *Adv Funct Mater.* 2019;29(22):1809029.

    doi: 10.1002/adfm.201809029

16. Lopez-Garcia M, Masters N, O'Brien HE, *et al*. Light-induced dynamic structural color by intracellular 3D photonic crystals in brown algae. *Sci Adv.* 2018;4(4):eaan8917.

    doi: 10.1126/sciadv.aan8917

17. Duan Y, Liang Q, Yang Z, *et al*. Bamboo-inspired composite metastructure for broadband microwave absorption and

load bearing. *Mater Res Bull.* 2023;166:112368.

doi: 10.1016/j.materresbull.2023.112368

18. Huang L, Duan Y, Dai X, *et al*. Bioinspired metamaterials: Multibands electromagnetic wave adaptability and hydrophobic characteristics. *Small.* 2019;15(40):1902730.

doi: 10.1002/smll.201902730

19. Jiang W, Yan LL, Ma H, *et al*. Electromagnetic wave absorption and compressive behavior of a three-dimensional metamaterial absorber based on 3D printed honeycomb. *Sci Rep.* 2018;8:4817.

doi: 10.1038/s41598-018-23286-6

20. Huang L, Duan Y, Liu J, *et al*. Bionic composite metamaterials for harvesting of microwave and integration of multifunctionality. *Compos Sci Technol.* 2021;204:108640.

doi: 10.1016/j.compscitech.2020.108640

21. Wu W, Xu R, Zhou Y, *et al*. Biomimetic 3D coral reef-like GO@TiO2 composite framework inlaid with TiO2-C for low-frequency electromagnetic wave absorption. *Carbon.* 2021;178:144-156.

doi: 10.1016/j.carbon.2020.11.085

22. An Q, Li DW, Liao WH, *et al.* A novel ultra-wideband electromagnetic-wave-absorbing metastructure inspired by bionic gyroid structures. *Adv Mater.* 2023;35(26):2300659.

doi: 10.1002/adma.202300659

23. Chen ZM, Zhang Y, Wang ZD, *et al.* Bioinspired moth-eye multi-mechanism composite ultra-wideband microwave absorber based on the graphite powder. *Carbon.* 2023;201:542-548.

doi: 10.1016/j.carbon.2022.09.035

24. Chen X, Li YL, Cheng SY, *et al.* Liquid metal-MXene-based hierarchical aerogel with radar-infrared compatible camouflage. *Adv Funct Mater.* 2024;34(10):2308274.

doi: 10.1002/adfm.202308274

25. Chen Y, He YQ, Zhu XQ. Flower-type pulsating heat pipe for a solar collector. *Int J Energy Res.* 2020;44(9):7734-7745.

doi: 10.1002/er.5505

26. Xu YC, Huang YZ, Yan H, *et al*. Sunflower-pith-inspired anisotropic auxetic mechanics from dual-gradient cellular structures. *Matter.* 2023;6(5):1569-1584.

doi: 10.1016/j.matt.2023.03.010

27. Yu SQ, Liu JG, Zhao PY, Tang YY. A flat-foldable equiangular spiral folding pattern inspired by sunflowers for deployable structures. *Chin J Aeronaut.* 2024;37(6):425-438.

doi: 10.1016/j.cja.2023.10.004

28. Wang F, Zhou QF, Zhang Z, Gu YH, Zhang JL, Jiang KY. Microwave absorption properties of carbon black-carbonyl iron/polylactic acid composite filament for fused deposition modeling. *Materials.* 2022;15(15):5455.

doi: 10.3390/ma15155455

29. Feng MF, Zhang KF, Xiao JJ, *et al.* Material-structure collaborative design for broadband microwave absorption metamaterial with low density and thin thickness. *Compos Pt B-Eng.* 2023;263:110862.

doi: 10.1016/j.compositesb.2023.110862

30. Lei L, Yao ZJ, Zhou JT, Wei B, Fan HY. 3D printing of carbon black/polypropylene composites with excellent microwave absorption performance. *Compos Sci Technol.* 2020;200:108479.

doi: 10.1016/j.compscitech.2020.108479

31. Ye XC, Yang C, He EY, *et al.* Electromagnetic wave absorption properties of the FeSiAl/PLA and FeSiAl-MoS2-Graphene/PLA double-layer absorber formed by fused deposition modeling. *J Magn Magn Mater.* 2023;565:170280.

doi: 10.1016/j.jmmm.2022.170280

32. Baqir MA, Latif H, Altintas O, *et al*. Fractal metamaterial based multiband absorber operating in 5G regime. *Optik.* 2022;266:169626.

doi: 10.1016/j.ijleo.2022.169626

33. Zhang Z, Wang F, Zhang JL, Li PF, Jiang KY. Ultra-broadband and wide-angle metamaterial absorber with carbon black/carbonyl iron composites fabricated by direct-ink-write 3D printing. *Adv Eng Mater.* 2023;25(6):2201236.

doi: 10.1002/adem.202201236

34. Min DD, Zhou WC, Qing YC, Luo F, Zhu DM. Single-layer and double-layer microwave absorbers based on graphene nanosheets/epoxy resin composite. *Nano.* 2017;12(7):1750089.

doi: 10.1142/s1793292017500898

35. Zhou Q, Yin XW, Ye F, Liu XF, Cheng LF, Zhang LT. A novel two-layer periodic stepped structure for effective broadband radar electromagnetic absorption. *Mater Des.* 2017;123:46-53.

doi: 10.1016/j.matdes.2017.03.044

36. Duan YB, Liang QX, Yang Z, et al. A wide-angle broadband electromagnetic absorbing metastructure using 3D printing technology. *Mater Des.* 2021;208:109900. doi: 10.1016/j.matdes.2021.109900

37. Huang YX, Song WL, Wang CX, *et al*. Multi-scale design of electromagnetic composite metamaterials for broadband microwave absorption. *Compos Sci Technol.* 2018;162:206-214.

doi: 10.1016/j.compscitech.2018.04.028

38. Wang BC, Wei JQ, Yang Y, Wang T, Li FS. Investigation on peak frequency of the microwave absorption for carbonyl iron/epoxy resin composite. *J Magn Magn Mater.* 2011;323(8):1101-1103.

doi: 10.1016/j.jmmm.2010.12.028

39. Fan QF, Huang YX, Chen MJ, Li Y, Song WL, Fang DN. Integrated design of component and configuration for a flexible and ultrabroadband radar absorbing composite. *Compos Sci Technol.* 2019;176:81-89.

doi: 10.1016/j.compscitech.2019.04.008

40. Ning J, Dong SF, Luo XY, *et al.* Ultra-broadband microwave absorption by ultra-thin metamaterial with stepped structure induced multi-resonances. *Results Phys.* 2020;18:103320.

doi: 10.1016/j.rinp.2020.103320

ACCSCIENCE PUBLISHING

Materials Science in Additive Manufacturing

ORIGINAL RESEARCH ARTICLE

Microstructural evolution and mechanical properties of laser-powder bed fusion-fabricated Ti-10Ta-2Nb-2Zr alloy as a potential orthopedic implant material

Igor Polozov*, Victoria Nefyodova, Anton Zolotarev, and Anatoly Popovich

Scientific and Educational Center, Structural and Functional Materials, Institute of Mechanical Engineering, Materials, and Transport, Peter the Great Saint Petersburg Polytechnic University, Saint Petersburg, Russia

(This article belongs to the *Special Issue: Advances in Tailoring of Microstructure, Materials, and Design with Additive Manufacturing*)

Abstract

Titanium alloys are gaining attention for their potential to improve implant performance in biomedical applications. This study investigates the Ti-10Ta-2Nb-2Zr alloy fabricated using laser-powder bed fusion (L-PBF) for potential biomedical applications. The research aims to examine the influence of processing parameters on material structure and properties, and to develop porous structures based on triply periodic minimal surfaces (TPMS) to reduce elastic modulus and improve mechanical compatibility with bone tissue. Spherical Ti-10Ta-2Nb-2Zr powder was processed using L-PBF with varying laser power (250 – 280 W), scanning speed (500 – 1000 mm/s), and hatch spacing (80 – 100 μm). Maximum relative density of 99.91% was achieved at volumetric energy density of 70 J/mm^3. Differential scanning calorimetry revealed the β-transus temperature at 862°C. Microstructural analysis showed the formation of martensitic α'-phase in the as-built condition with acicular morphology. Heat treatment at 900°C resulted in the formation of a lamellar α + β structure. Mechanical properties in the as-built condition were characterized by yield strength of 551.8 MPa, ultimate tensile strength of 641.2 MPa, elongation of 19.0%, and elastic modulus of 89.0 GPa. After heat treatment, strength characteristics decreased by 15 – 18%, whereas elastic modulus reduced to 86.0 GPa. TPMS porous structures (gyroid, Schwarz, and split) with 50% porosity demonstrated an elastic modulus of 9.2 – 9.7 GPa, representing approximately 18% of the solid material value. These results demonstrate the potential of Ti-10Ta-2Nb-2Zr as a promising alternative to conventional Ti-6Al-4V for orthopedic applications, offering enhanced mechanical properties and reduced stress shielding due to its lower elastic modulus and tailored porous architectures.

Keywords: Titanium alloy; Laser powder bed fusion; Biomaterials; Triply periodic minimal surfaces; Mechanical properties; Microstructure

***Corresponding author:**
Igor Polozov
(polozov_ia@spbstu.ru)

Citation: Polozov I, Nefyodova V, Zolotarev A, Popovich A. Microstructural evolution and mechanical properties of laser-powder bed fusion-fabricated Ti-10Ta-2Nb-2Zr alloy as a potential orthopedic implant material. *Mater Sci Add Manuf.* 2025;4(3):025220044. doi: 10.36922/MSAM025220044

Received: May 30, 2025

Revised: July 7, 2025

Accepted: July 9, 2025

Published online: August 12, 2025

1. Introduction

Titanium (Ti) and its alloys have gained widespread recognition as biomaterials due to their unique combination of high specific strength, excellent corrosion resistance, and superior biocompatibility.[1,2] However, the traditional Ti-6Al-4V alloy, which dominates biomedical applications, has two significant limitations: a relatively high elastic modulus (~110 – 120 GPa) compared to human bone tissue (10 – 30 GPa for cortical bone), and concerns regarding the potential long-term toxicity of aluminum (Al) and vanadium (V) ions released into surrounding tissues.[3,4] These limitations have stimulated extensive research efforts aimed at developing novel Ti alloys specifically designed for biomedical applications, with particular emphasis on reducing the elastic modulus to minimize stress shielding effects while maintaining adequate mechanical strength and biocompatibility.

Stress shielding represents a critical clinical problem in orthopedic implants, arising from a significant mismatch between the elastic moduli of the implant material and surrounding bone tissue. This mechanical incompatibility results in the stiffer implant bearing a greater portion of applied loads, leading to reduced mechanical stimulation of adjacent bone. Consequently, bone remodeling is disrupted, resulting in bone resorption, osteoporosis, and potential implant loosening over time.[4,5] The risk of stress shielding increases proportionally with the difference between implant and bone elastic moduli, making the development of low-modulus implants a paramount objective in orthopedic biomaterial research.

Beyond developing new alloys, researchers have paid significant attention to a structural approach for addressing elastic modulus mismatch through the application of lattice structures based on triply periodic minimal surfaces (TPMS).[6] These biomimetic structures enable a significant reduction in the effective elastic modulus of implants to values comparable to those of bone tissue, regardless of the base material.[7] A key advantage of TPMS structures is the ability to control mechanical properties through variation of parameters such as relative density, unit cell type (gyroid, Schwarz, split, etc.), and their geometric characteristics. Moreover, the porous architecture of lattice structures promotes enhanced osteointegration by providing optimal pore sizes for bone tissue ingrowth and efficient nutrient transport.[8,9]

Beta-Ti alloys have emerged as promising candidates for addressing these issues due to their inherently lower elastic modulus compared to α and α + β Ti alloys. The β-phase has a body-centered cubic (BCC) crystal structure, which fundamentally exhibits lower stiffness than the hexagonal close-packed (HCP) structure of the α-phase.[10] This characteristic makes β-Ti alloys particularly attractive for load-bearing orthopedic applications where modulus matching with bone tissue is critical. Recent advances in β-Ti alloys have enabled the development of compositions with elastic moduli as low as 40 – 80 GPa, which is substantially closer to natural bone properties compared to traditional implant alloys.[11,12]

Several β-stabilizing elements, including niobium (Nb), tantalum (Ta), molybdenum (Mo), and zirconium (Zr), have been thoroughly investigated for biomedical Ti alloys due to their superior biocompatibility and ability to reduce elastic modulus while maintaining adequate mechanical strength.[13] Among these elements, Ta has attracted significant attention due to its exceptional biocompatibility, outstanding corrosion resistance, and strong tendency to stabilize the β-phase in Ti.[14-16] When alloyed with Ti, even at relatively modest concentrations, Ta promotes the formation of the BCC crystal structure, which exhibits a lower elastic modulus than the HCP structure of pure Ti or predominantly α-alloys.

Notable developments in this field include the Ti-Nb alloy family, with compositions such as Ti-35Nb-7Zr-5Ta demonstrating promising combinations of low elastic modulus and good biocompatibility.[17,18] Similarly, Ti-24Nb-4Zr-8Sn has shown excellent superelasticity with an elastic modulus of only 53 GPa.[19] Other β-alloys, such as Ti-29Nb-13Ta-4.6Zr and Ti-35Nb-5Ta-7Zr, have also demonstrated favorable combinations of mechanical properties and biocompatibility for orthopedic implants.[20,21] However, many of these compositions contain relatively high concentrations of expensive elements, such as Nb and Ta, potentially limiting their widespread clinical application.

Binary Ti-Ta alloys, particularly those containing 20 – 40 wt.% of Ta, have demonstrated promising combinations of relatively low elastic modulus (65 – 70 GPa) and good biocompatibility.[22] However, these binary alloys often suffer from processing issues due to the high melting point of Ta (3,017°C) and its significant density difference compared to Ti. In addition, the high cost of Ta makes high-Ta content alloys economically less attractive for widespread clinical application. To address these limitations while retaining the beneficial properties of Ta, the development of multi-component Ti-Ta alloys with reduced Ta content and the addition of other β-stabilizing elements has attracted attention.[23,24]

The Ti-10Ta-2Nb-2Zr alloy represents a strategic design approach that utilizes synergistic effects between different alloying elements.[25] Ta provides primary β-stabilization and biocompatibility, while Nb contributes additional β-stabilization and may enhance mechanical properties through solid solution strengthening. Zr, as a

neutral alloying element, can improve strength without significantly affecting phase stability and has been reported to enhance the corrosion resistance of Ti alloys. The reduced Ta content (10 wt.%) offers substantial economic advantages compared to higher Ta content alloys while potentially retaining most of the beneficial properties associated with Ta addition. The significance of this alloy lies in its elimination of potentially toxic elements (Al, V) present in conventional Ti-6Al-4V, making it more suitable for long-term biomedical applications. Furthermore, the combination of optimized chemical composition with advanced manufacturing techniques, such as laser powder bed fusion (L-PBF), enables the development of complex porous architectures that can achieve elastic modulus values approaching those of natural bone tissue. This dual approach of compositional design and structural engineering represents a promising strategy for next-generation orthopedic implants with enhanced mechanical compatibility.

Traditional manufacturing methods for Ti-Ta alloys include casting, forging, and powder metallurgy approaches, each presenting specific challenges in utilizing Ta due to its high melting point, segregation issues, and difficulties in achieving homogeneous microstructures.[26,27] L-PBF, an additive manufacturing method, offers distinct advantages for processing these alloys, including the ability to create complex, patient-specific geometries, reduced material waste, and potentially improved microstructural control through rapid solidification conditions.[14,16] However, processing Ti-Ta-based alloys using L-PBF introduces challenges, including the need to optimize processing parameters to achieve high density, desired microstructures, and stable mechanical properties.

Previous studies of L-PBF Ti alloys containing Ta and other β-stabilizers have demonstrated the feasibility of achieving high-density components with promising mechanical properties. However, the influence of specific L-PBF processing parameters on densification behavior, microstructural evolution, and mechanical properties of the Ti-10Ta-2Nb-2Zr alloy has not been systematically investigated. Furthermore, the effect of thermal treatments on phase transformations, microstructural stabilization, and mechanical behavior of this alloy remains largely unexplored.

The present study aims to address these research gaps by:

(i) Systematically investigating the influence of L-PBF processing parameters on density, microstructure, and mechanical properties of the Ti-10Ta-2Nb-2Zr alloy;
(ii) Studying phase transformation behavior and microstructural evolution during thermal treatments;
(iii) Establishing correlations between processing parameters, microstructural features, and resulting mechanical properties, particularly regarding elastic modulus reduction, which is critical for biomedical applications;
(iv) Determining optimal processing windows and thermal treatment regimes to achieve the best combination of properties for orthopedic implants;
(v) Designing and evaluating the influence of TPMS lattice structures made from Ti-10Ta-2Nb-2Zr alloy on mechanical properties.

Through this comprehensive investigation, we aim to advance the understanding of process–structure–property relationships in this promising biomedical alloy and contribute to the development of improved Ti implants with enhanced biomechanical compatibility.

2. Materials and methods

2.1. Starting materials

The primary material used in this investigation was pre-alloyed Ti-10Ta-2Nb-2Zr powder (Guangzhou Sailong Additive Manufacturing Co., Ltd., China). The powder particles exhibited predominantly spherical morphology with satellite particles occasionally present on larger spheres (Figure 1A). Particle size distribution analysis performed using a laser analyzer (Fritsch Analysette 22, NanoTec plus, Germany) showed a size distribution with d_{10} = 11.3 μm, d_{50} = 29.1 μm, and d_{90} = 61.7 μm (Figure 1B).

Scanning electron microscopy (SEM) examination of the powder particles revealed surface morphology characterized by fine dendritic structures typical of rapid solidification during gas atomization (Figure 1C). Cross-sectional analysis combined with energy-dispersive X-ray spectroscopy (EDS) mapping confirmed uniform distribution of Ti, Ta, Nb, and Zr elements within individual particles, demonstrating good compositional homogeneity (Figure 1D). Chemical analysis of the powder showed the following composition (wt.%): Ti: Balance; Ta: 9.85 ± 0.18%; Nb: 1.95 ± 0.12%; Zr: 1.92 ± 0.10%.

2.2. L-PBF

Samples were fabricated using an L-PBF system (MINI, 3DLAM, Russia) equipped with a fiber laser IPG Photonics, USA) with a maximum power of 300 W and a beam diameter of 70 μm. Processing was conducted in a high-purity argon atmosphere (O_2 < 100 ppm) on a Ti build platform without pre-heating. The building strategy featured a linear scanning pattern with 90° rotation between consecutive layers for bulk volumes.

The selection of processing parameters was based on our previous experience with similar Ti alloys, where

high-density components were successfully manufactured within similar parameter ranges (Table 1). The processing parameters were systematically varied to investigate their influence on densification behavior and microstructural evolution. The volumetric energy density (E) was calculated using Equation I.

$$E = \frac{P}{V \cdot h \cdot t} \quad (I)$$

where P is laser power (W); V is scanning speed (mm/s); h is hatch spacing (μm); and t is layer thickness (μm).

Cubic samples (10 × 10 × 10 mm^3) were fabricated for density measurements and microstructural characterization. For mechanical testing, cylindrical tensile specimens were produced according to the American Society for Testing and Materials (ASTM) E8/E8M standard with a gauge length of 15 mm and a diameter of 3 mm.

2.3. Heat treatments

The selected specimens were heat-treated using the following parameters: vacuum annealing at 900°C for 1 h, followed by furnace cooling. The samples were heated at a rate of 10°C/min to the target temperature in a vacuum furnace (Carbolite Gero, UK) at a vacuum level of 10^{-5} mbar.

The selection of heat treatment temperature was based on differential scanning calorimetry (DSC) analysis, which identified the β-transus temperature range for the Ti-10Ta-2Nb-2Zr alloy. The annealing temperature of 900°C was

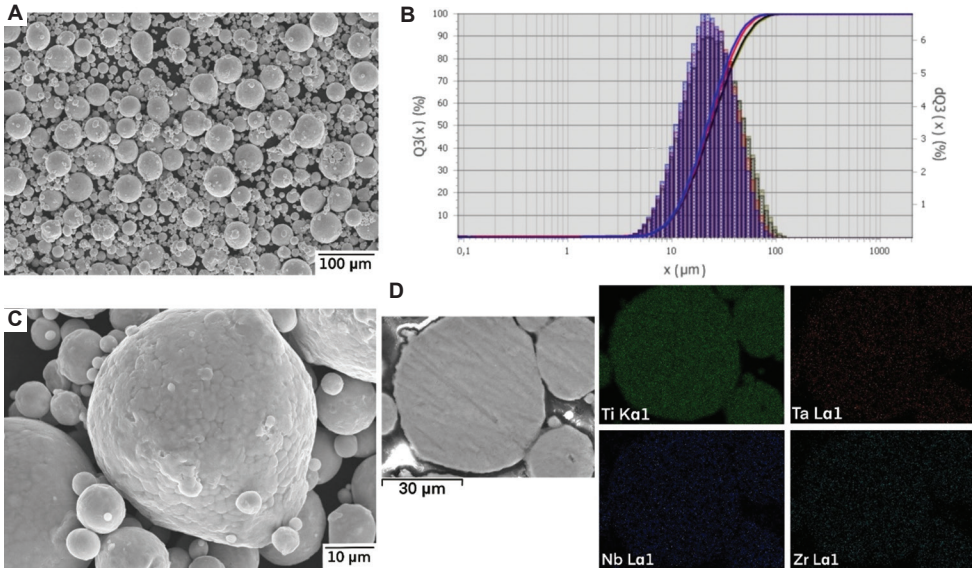

Figure 1. Characterization of Ti-10Ta-2Nb-2Zr powder. (A) Scanning electron micrograph shows general morphology of powder particles, scale bar: 100 μm; magnification: ×150; (B) Particle size distribution histogram with cumulative curve; (C) High-magnification SEM image of individual particle surface morphology, scale bar: 10 μm; magnification: ×1000; (D) cross-sectional scanning electron microscopic image with corresponding energy-dispersive X-ray spectroscopy mapping showing uniform Ti, Ta, Nb and Zr distribution, scale bar: 30 μm; magnification: ×1000

Table 1. Processing parameters used for laser-powder bed fusion of Ti-10Ta-2Nb-2Zr alloy

Regime	Power (P), W	Scanning speed (V), mm/s	Layer thickness (t), μm	Hatch spacing (h), μm	Energy density, J/mm^3
1	250	800	50	100	62.5
2	280	500	50	100	112.0
3	280	800	50	100	70.0
4	250	600	50	100	83.3
5	250	1,000	50	100	50.0
6	280	600	50	100	93.3
7	280	600	50	80	116.7
8	250	800	50	80	78.1
9	280	800	50	80	87.5

chosen to ensure complete transformation to the β-phase field, as it is approximately 40°C above the measured β-transus finish temperature (862°C). This temperature was selected to promote full recrystallization of the as-built microstructure while minimizing grain growth. Furnace cooling was selected to promote the formation of a stable lamellar α + β microstructure, balancing strength and ductility, which is critical for load-bearing orthopedic implants.

2.4. TPMS structures

As part of the investigation into the effects of cellular structures on the mechanical properties of alloys, experimental samples with three different TPMS architecture types were designed and fabricated: Schwarz, gyroid, and split (Figure 2). Computer-aided design of the TPMS architectures was performed using nTopology software (Version 3.0, nTopology Inc., USA). To ensure an optimal balance between mechanical characteristics and L-PBF manufacturing capabilities, a unit cell size of 1.5 mm was established for all architecture types. Adjustment of the wall thickness was performed to achieve the target volumetric porosity of 50%. For mechanical compression testing, cylindrical specimens with TPMS architecture were constructed with dimensions of 6 mm in diameter and 12 mm in height. During manufacturing, the samples were positioned so that the longitudinal axis of the cylinder aligned with the build direction.

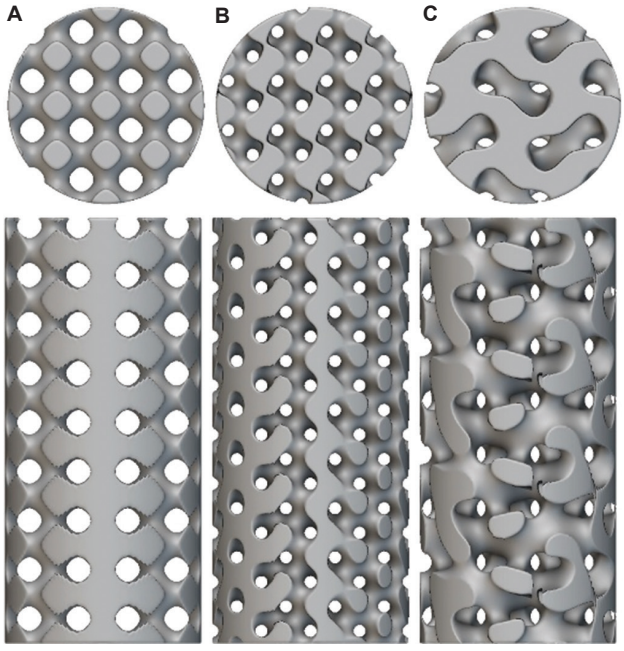

Figure 2. Designs of triply periodic minimal surface samples. (A) Schwarz; (B) gyroid; (C) split

The design of TPMS architectures took into consideration the technological limitations and capabilities of the L-PBF process. The sample dimensions were selected according to the work of Soro *et al.*,[28] whereas the unit cell size was adapted to account for the technical specifications of the printer used. The chosen parameters ensure that key structural elements comply with the minimum permissible dimensions for our L-PBF equipment while maintaining the required mechanical properties. The selected TPMS architecture types (Schwarz, gyroid, and split) represent designs whose feasibility in L-PBF processes has been confirmed by previous studies.[29,30] Nevertheless, the geometric features of these structures lead to variations in manufacturing accuracy. Among the considered variants, the split structure, characterized by the smallest constructive elements, demonstrates an increased susceptibility to manufacturing imperfections compared to gyroid and Schwarz structures, which is reflected in the variability of mechanical properties. To ensure uniformity in production conditions and resulting mechanical characteristics, all experimental samples were manufactured with the longitudinal axis of the cylinder oriented along the build direction. The positioning strategy and technological parameters were optimized based on published data on the successful fabrication of TPMS structures from Ti alloys. In addition, an investigation of the printed gyroid lattice structure was conducted to evaluate the influence of lattice geometry on the resulting microstructure, which established a relationship between the topological features of the cellular construction and microstructural parameters in various regions of the Ti-10Ta-2Nb-2Zr alloy specimen.

2.5. Characterization methods

2.5.1. Density analysis

The density of the fabricated samples was measured using the Archimedes method (hydrostatic weighing) with an analytical balance (XS205, Mettler Toledo, Switzerland) equipped with a density measurement kit. Distilled water was used as the immersion medium, and measurements were conducted at 22 ± 0.5°C. Four measurements were taken for each sample to ensure statistical reliability.

The theoretical density of the Ti-10Ta-2Nb-2Zr alloy was calculated using thermodynamic calculations in JMatPro 11 software (11.0, Sente Software Ltd., United Kingdom), which provides accurate density predictions based on the chemical composition and phase equilibria of the alloy system.

The relative density was determined as the ratio of the measured density (obtained using Archimedes' method) to the theoretical density (calculated using JMatPro 11).

2.5.2. Microstructural analysis

Samples for microstructural analysis were prepared using standard metallographic procedures. After grinding and polishing as described above, the specimens were etched using Kroll's reagent (2 mL HF, 6 mL HNO_3, and 92 mL H_2O) for 15 – 20 s at room temperature to reveal microstructural features.

Microstructural examination was performed using a SEM (MIRA 3, TESCAN, Czech Republic) equipped with an EDS detector for compositional analysis. Imaging was conducted at accelerating voltages between 15 and 20 kV using secondary electron and backscattered electron detectors to optimize contrast between different phases.

Phase analysis was performed using an X-ray diffractometer (D8 Advance, Bruker, Germany) with CuK-α radiation (λ = 1.5418 Å) operated at 40 kV and 40 mA. X-ray diffraction (XRD) patterns were recorded in the 2θ range of 30 – 90° with a step size of 0.02° and a counting time of 2 s per step. Phase identification was performed using the International Centre of Diffraction Data PDF-4 + database.

2.5.3. Mechanical testing

Vickers microhardness measurements were conducted using a hardness tester (Wilson VH1202, Buehler, USA) under a load of 500 g ($HV_{0.5}$) with a dwell time of 15 s. At least 10 indentations were made on each sample to ensure statistical significance, with indentation sites selected to avoid proximity to pores or sample edges.

Tensile tests were conducted on a universal testing machine (Zwick/Roell Z100, ZwickRoell GmbH & Co., Germany) at room temperature with a strain rate of 0.001 s^{-1} according to ASTM E8/E8M standard. A minimum of five specimens were tested for each processing condition to ensure reproducibility. The elastic modulus was determined using an extensometer attached to the gauge section during initial loading.

2.5.4. Thermal analysis

DSC was carried out using a simultaneous thermal analyzer (STA409, Netzch-Gerätebau GmbH, Germany) at a heating rate of 10°C/min under high-purity argon flow (50 mL/min). Samples with a mass of approximately 50 mg were placed in alumina crucibles and subjected to heating/cooling cycles between room temperature and 1,000°C to investigate phase transformation behavior. The temperature and heat flow calibrations were performed using high-purity standards before the measurements.

3. Results and discussion

3.1. Effect of L-PBF parameters on the relative density of Ti-10Ta-2Nb-2Zr alloy

Table 2 presents the density values obtained using the hydrostatic weighing method. The theoretical density of Ti-10Ta-2Nb-2Zr alloy calculated using JMatPro 11 thermodynamic software was 4.9400 g/cm³. Hydrostatic weighing revealed absolute density values ranging from 4.9153 to 4.9355 g/cm³, with the highest value of 4.9355 ± 0.0015 g/cm³ achieved at energy densities of 70 J/mm³ (laser power P = 280 W, scanning speed V = 800 mm/s).

The lowest relative density of 99.49 ± 0.21% was recorded at an energy density of 116.7 J/mm³ (P = 280 W, V = 600 mm/s, h = 50 μm), which may indicate the formation of keyhole porosity defects due to excessive energy input, consistent with findings for similar Ti-based alloys.[31] At the minimum energy density of 50.0 J/mm³ (P = 250 W, V = 1000 mm/s, h = 50 μm), the relative density reached 4.9212 ± 0.0054, demonstrating sufficient material melting.

The dependence of relative density on volumetric energy density (Figure 3) demonstrates a non-monotonic behavior. The highest density values were achieved in the range of 60 – 90 J/mm³, with a peak value of 99.91% at 70 J/mm³. Lower energy densities (<60 J/mm³) resulted in insufficient melting and increased porosity, while excessive energy input (>90 J/mm³) led to the formation of keyhole defects. The optimal energy density window appears to be broader than typically reported for binary Ti-Ta alloys,[14,16] suggesting enhanced processability of the quaternary composition.

These results underscore the importance of optimizing L-PBF parameters to achieve near-full densification (>99.85%) for biomedical implants, where high density

Table 2. Densities of the samples obtained using the hydrostatic weighing method and metallographic analysis

Regime	Measured density (g/cm³)	Relative density (%)
1	4.9326±0.0040	99.85±0.08
2	4.9153±0.0084	99.54±0.17
3	4.9355±0.0015	99.91±0.03
4	4.9192±0.0069	99.58±0.14
5	4.9212±0.0054	99.62±0.11
6	4.9282±0.0030	99.72±0.06
7	4.9153±0.0094	99.46±0.19
8	4.9207±0.0044	99.61±0.09
9	4.9242±0.0074	99.64±0.15

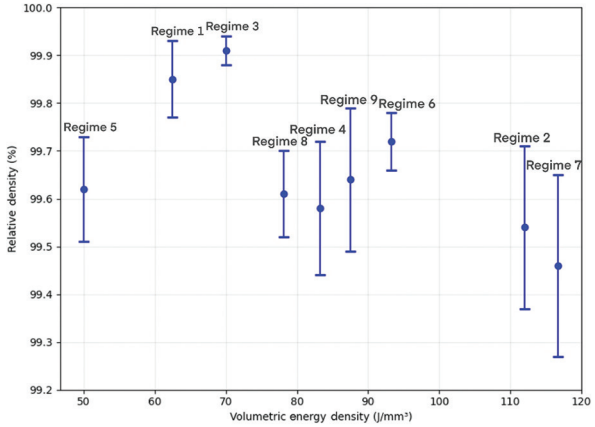

Figure 3. The influence of volumetric energy density on the relative density of the Ti-10Ta-2Nb-2Zr alloy

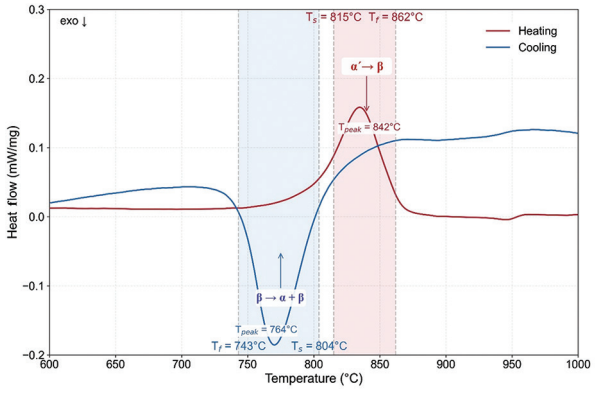

Figure 4. Differential scanning calorimetry curves of the Ti-10Ta-2Nb-2Zr alloy show phase transformations during heating and cooling at 20 K/min. The heating curve (red) exhibits an endothermic peak corresponding to α' → β transformation (T_s = 815°C, T_{peak} = 842°C, T_f = 862°C), while the cooling curve (blue) shows an exothermic peak associated with β → α + β transformation (T_s = 804°C, T_{peak} = 764°C, T_f = 743°C). Shaded regions indicate the temperature ranges of phase transformations

ensures mechanical integrity and corrosion resistance in physiological environments.[32] The composition of Ti-10Ta-2Nb-2Zr alloy that is free of toxic elements, such as Al and V, combined with its low elastic modulus (~75 GPa), based on similar β-stabilized alloys,[33] positions it as a promising alternative to Ti-6Al-4V for long-term implantation. The identified processing window (p=250 – 280 W, V = 600 – 800 mm/s, h = 80 – 100 μm, E = 62.5 – 83.3 J/mm^3) provides a robust foundation for fabricating defect-free, biocompatible implants with complex geometries.

3.2. DSC analysis

The thermal behavior of the Ti-10Ta-2Nb-2Zr alloy was investigated using DSC during heating and cooling cycles at a rate of 10 K/min, covering a temperature range from 600°C to 1,000°C. This analysis was performed to determine the β-transus temperature and understand phase transformation behavior, which is essential for optimizing heat treatment parameters and predicting microstructural evolution during thermal processing.

The DSC curves (Figure 4) reveal distinct phase transformation events characteristic of Ti alloys with β-stabilizing elements (Ta and Nb) and α-stabilizing elements (Zr). It should be noted that the as-built condition after L-PBF processing contains metastable α'-phase (martensite) due to the rapid cooling rates inherent in the additive manufacturing process, as confirmed by subsequent microstructural and XRD analyses (sections 3.3.1 and 3.3.3).

During heating, an endothermic peak at 842°C, with a starting temperature T_s of 815°C and a finishing temperature T_f of 862°C, indicates the α' → β phase transformation, where the metastable martensitic structure transforms into a single β-phase structure.[34] The exothermic nature of the cooling curve, with a peak at 764°C and boundaries at T_s = 804°C and T_f = 743°C, corresponds to the equilibrium β → α + β transformation, reflecting the precipitation of the α-phase within the β matrix under controlled cooling conditions.[13] These transformations are typical for near-β or β-Ti alloys and are influenced by the alloy composition and cooling rate.[35]

The observed phase transformation temperatures and their thermal signatures align with the expected behavior of Ti-based alloys with Ta, Nb, and Zr additions, which enhance β-phase stability and lower the martensitic transformation temperatures compared to pure Ti.[36] The hysteresis between heating and cooling curves (approximately 40 – 50°C) suggests a diffusion-controlled transformation mechanism during the equilibrium cooling process, which is common in Ti alloys under similar thermal conditions.[37]

These findings provide critical insights into the thermal stability and phase evolution of Ti-10Ta-2Nb-2Zr, enabling the optimization of heat treatment protocols to achieve desired microstructural and mechanical properties for biomedical applications.[38]

3.3. Microstructural analysis of as-built Ti-10Ta-2Nb-2Zr alloy

3.3.1. General microstructural features

The microstructure of as-built Ti-10Ta-2Nb-2Zr samples produced via L-PBF was characterized to understand the correlation between processing conditions and resulting material properties. Figure 5 presents SEM micrographs of the as-built microstructure at different magnifications.

The microstructure of the Ti-10Ta-2Nb-2Zr alloy fabricated with L-PBF is characterized by a pronounced acicular morphology. In Figure 5A, fine needle-like features are observed, organized into groups with predominantly parallel orientation. The needles intersect at angles of approximately 60 – 120°, forming a characteristic pattern of martensitic transformation.

At higher magnification Figure 5B, the morphology reveals more detail. The structure consists of needles 50 – 400 nm in width, densely packed with varying orientations. A high degree of structural refinement is observed, with no presence of large grains.

The acicular morphology with characteristic crystallographic relationships indicates the dominance of the α' martensitic phase. The presence of α' martensite is also possible.[14] The fine acicular α'-martensitic structure observed in the as-built condition is a direct result of the high cooling rates (10^5 – 10^6 K/s) inherent to the L-PBF process. These rapid cooling rates suppress diffusional transformations, stabilizing the metastable martensitic phase and contributing to the high strength of the alloy in the as-built state, which is advantageous for load-bearing applications.

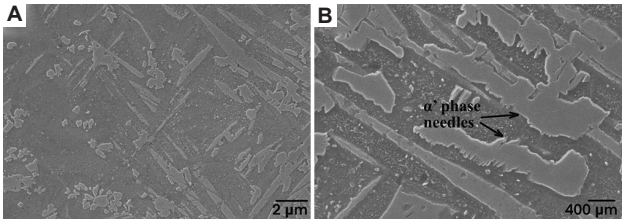

Figure 5. Scanning electron micrographs of as-built Ti-10Ta-2Nb-2Zr alloy. (A) Microstructure with intersecting needle-like features, characteristic of martensitic transformation, scale bar: 2 µm; magnification: ×5000; (B) High-magnification image showing densely packed needles with varied orientations and refined structure, scale bar: 400 nm; magnification: ×20000

3.3.2. Elemental distribution analysis

Elemental mapping using EDX was performed to evaluate the distribution of alloying elements within the as-built microstructure. Figure 6A presents an SEM micrograph of the analyzed region, whereas Figure 6B-E shows the corresponding elemental maps for Ti, Ta, Nb, and Zr, respectively.

The EDX mapping reveals a remarkably uniform distribution of all alloying elements throughout the microstructure, despite the rapid solidification conditions of the L-PBF process. Ti, as the matrix element, shows high and consistent concentration across the entire mapped area (Figure 6B). Notably, Ta (Figure 6C), Nb (Figure 6D), and Zr (Figure 6E) exhibit homogeneous distributions without significant segregation or clustering, which is particularly remarkable considering the high melting point of Ta (3,017°C) and its significant density difference compared to Ti.

This chemical homogeneity can be attributed to several factors: the pre-alloyed powder composition that provides a uniform starting distribution of elements; complete melting achieved with the selected laser parameters; the restricted time available for element diffusion and segregation during rapid solidification; and potential multiple remelting of preceding layers during the layer-by-layer building process.

3.3.3. Phase composition analysis

XRD analysis was conducted to identify the phase composition of the Ti-10Ta-2Nb-2Zr alloy in the as-built and heat-treated conditions. Figure 7 presents the XRD

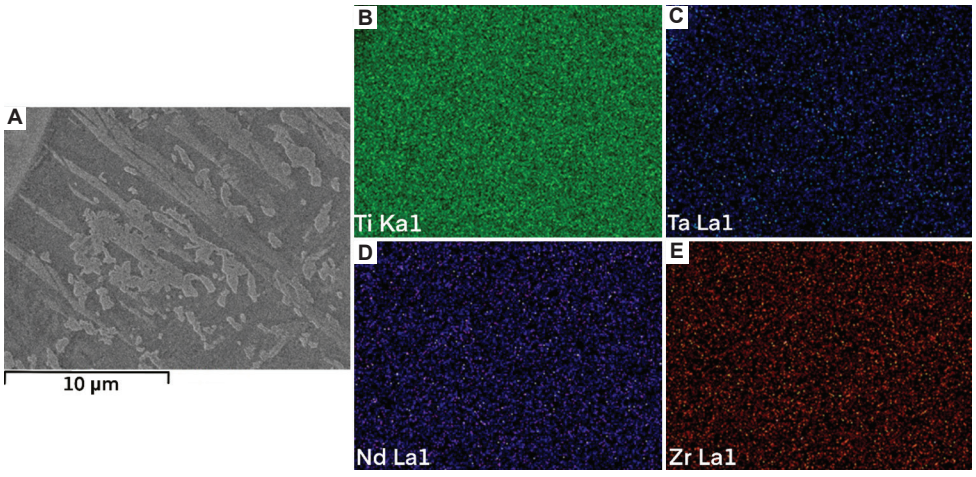

Figure 6. Elemental distribution in as-built Ti-10Ta-2Nb-2Zr alloy. (A) Scanning electron micrograph of analyzed region, scale bar: 10 µm; magnification: ×4000; elemental distribution maps of (B) Titanium; (C) Tantalum; (D) Niobium; (E) Zirconium

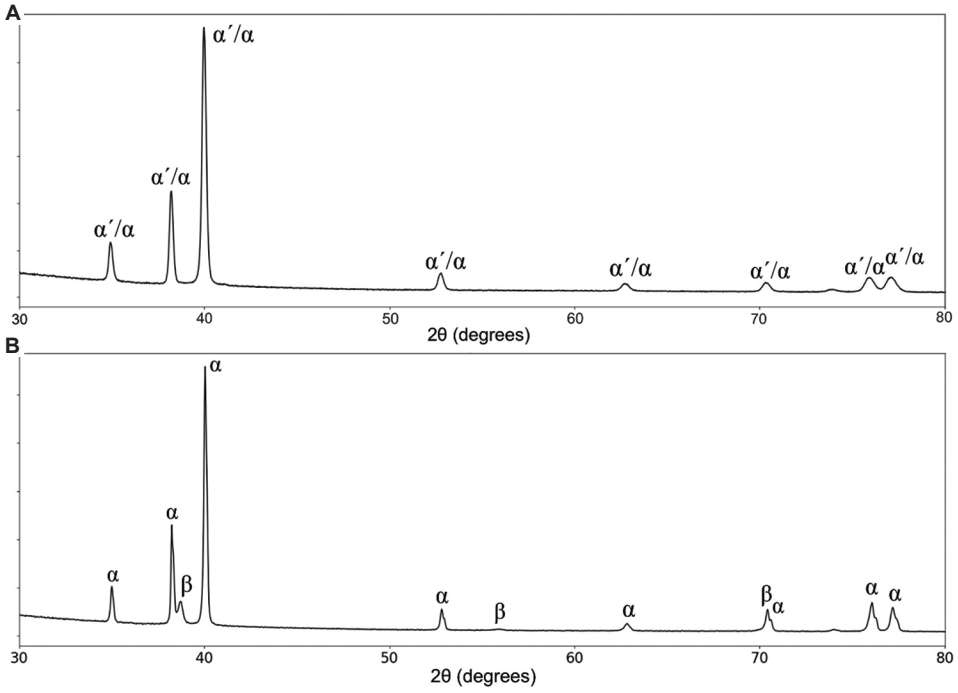

Figure 7. X-ray diffraction patterns of the Ti-10Ta-2Nb-2Zr alloy. (A) As-built condition; (B) After heat treatment

patterns obtained from the samples: Figure 7A corresponds to the as-built condition, while Figure 7B shows the results after heat treatment.

The XRD pattern reveals that the as-built microstructure consists predominantly of α' martensitic phase with HCP crystal structure. The most intense diffraction peak appears at approximately 40° (2θ), corresponding to the α-Ti (101) plane. Other characteristic α-Ti reflections are observed at approximately 35° (100), 38° (002), 53°, 63°, 70°, and 76 – 77° (doublet). The peaks exhibit some broadening, indicative of high levels of internal stress and small crystallite size typical of rapid solidification during L-PBF.

No distinct peaks associated with β-phase BCC are visible in the pattern, suggesting that the high cooling rates during L-PBF processing promoted almost complete transformation to α' martensite. The slight shifts in peak positions compared to pure Ti result from lattice distortion caused by the incorporation of alloying elements (Ta, Nb, Zr).

These XRD results align with the SEM observations of acicular microstructure characteristic of martensitic transformation. The dominant martensitic structure is consistent with the phase transformation behavior identified in the DSC analysis (Section 3.2), where the $\beta \rightarrow \alpha + \beta$ transformation during cooling was detected in the temperature range of 804 – 743°C. During L-PBF processing, the cooling rates far exceed those used in DSC analysis, further promoting the formation of a non-equilibrium martensitic phase instead of the equilibrium $\alpha + \beta$ structure.

3.4. Mechanical properties of Ti-10Ta-2Nb-2Zr alloy

3.4.1. Tensile properties

The tensile properties of the Ti-10Ta-2Nb-2Zr alloy in the as-built condition and after heat treatment are summarized in Table 3. Each value represents the average of multiple specimens, with standard deviations provided to indicate the variability of the measurements.

The as-built Ti-10Ta-2Nb-2Zr specimens exhibited high strength characteristics of a yield strength of 551.8 ± 8.4 MPa and an ultimate tensile strength of 641.2 ± 5.7 MPa, combined with a good ductility indicated by an elongation of 19.0 ± 1.8% and a reduction in area of 58.0 ± 2.3%. The elastic modulus in the as-built condition was 89.0 ± 2.4 GPa, which is significantly lower than that typically reported for conventional Ti alloys such as Ti-6Al-4V (110 – 120 GPa).

The application of heat treatment (vacuum annealing at 900°C for 1 h) resulted in a notable decrease in strength properties (Figure 8), with the yield strength reduced by 18.0% – 452.3 ± 14.7 MPa and the ultimate tensile strength reduced by 15.0% – 545.0 ± 3.6 MPa. Interestingly, the elongation slightly increased to 20.2 ± 3.6%, while the

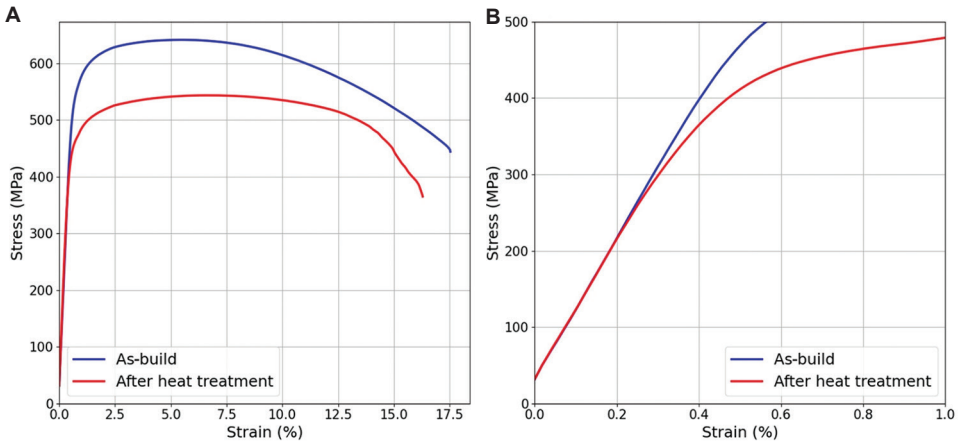

Figure 8. Comparison of strength properties between as-built and annealed Ti-10Ta-2Nb-2Zr. (A) Representative engineering stress-strain curves for Ti-10Ta-2Nb-2Zr alloy in as-built condition and after heat treatment; (B) Enlarged view of the elastic region

Table 3. Tensile properties of Ti-10Ta-2Nb-2Zr alloy and their comparison with other biomedical alloys in different conditions

Alloy condition	Elastic modulus (GPa)	Yield strength (MPa)	Tensile strength (MPa)	Elongation (%)	Reduction in area (%)	References
Ti-10Ta-2Nb-2Zr, as-built	89.0±2.4	551.8±8.4	641.2±5.7	19.0±1.8	58.0±2.3	Current study
Ti-10Ta-2Nb-2Zr, after annealing	86.0±2.2	452.3±14.7	545.0±3.6	20.2±3.6	45.8±15.5	Current study
Ti-6Al-4V	110 – 120	-	~900 – 1000	~10 – 15%	-	39,40
Ti-35Nb-7Zr-5Ta	81	-	630	15	-	18

reduction in area decreased to 45.8 ± 15.5%. The elastic modulus after annealing decreased to approximately 86.0 GPa, representing a 3.4% reduction compared to the as-built condition.

3.4.2. Microhardness measurements

Microhardness measurements were performed on samples fabricated using different L-PBF processing regimes. The results are presented in Table 4.

The microhardness of the Ti-10Ta-2Nb-2Zr alloy exhibited relatively consistent values across different L-PBF processing regimes, with an average of 224 $HV_{0.5}$ and standard deviations within a narrow range. The variation in hardness values did not show a strong correlation with processing parameters, indicating that the mechanical properties of the alloy remain stable across the investigated processing window. The highest hardness value of 231 $HV_{0.5}$ was observed in Regime 7 (with the highest energy density of 116.7 J/mm^3), while the lowest hardness value of 216 $HV_{0.5}$ was measured in Regime 3. This relatively narrow range of hardness values (216 – 231 $HV_{0.5}$) suggests good process stability for the Ti-10Ta-2Nb-2Zr alloy during L-PBF manufacturing.

Table 4. Microhardness of Ti-10Ta-2Nb-2Zr alloy fabricated using different L-PBF processing regimes

Regime	Energy density (J/mm^3)	Microhardness ($HV_{0.5}$)
1	62.5	227±7
2	112.0	222±4
3	70.0	216±6
4	83.3	225±7
5	50.0	223±5
6	93.3	216±5
7	116.7	231±6
8	78.1	229±8
9	87.5	223±6
Mean	–	224±6

3.5. Effects of heat treatment on microstructure and mechanical properties

3.5.1. Microstructural evolution after heat treatment

To evaluate the influence of post-processing treatments on the Ti-10Ta-2Nb-2Zr alloy, samples produced under optimal L-PBF conditions (Regime 3) were subjected to vacuum

annealing at 900°C for 1 h, followed by furnace cooling. This temperature was selected based on the DSC analysis results (Section 3.2), which identified a β-transus finish temperature of 862°C, ensuring complete transformation to the β-phase during the annealing process. The annealing temperature of 900°C was chosen to be approximately 40°C above the measured β-transus to guarantee complete transformation while minimizing grain growth.

The microstructural evolution resulting from heat treatment is illustrated in Figure 9, which presents SEM micrographs at different magnifications of the alloy after heat treatment.

As evident in Figure 9A, the heat treatment resulted in complete recrystallization of the as-built microstructure, with elimination of the directional features and melt pool boundaries that were characteristic of the L-PBF process. The previous fine acicular martensitic structure has been transformed into a well-defined lamellar arrangement of α + β phases. The microstructure exhibits a classical Widmanstätten or "basket-weave" pattern consisting of α-plates within prior β grains.

At higher magnification (Figure 9B), the structure reveals colonies of parallel α-plates, significantly coarser than the fine martensitic features observed in the as-built condition. The α-plates are arranged in multiple crystallographic orientations within individual prior β grains, which exhibit sizes of approximately 50 – 200 μm. Thin regions of retained β-phase are present between the α-plates, creating the characteristic lamellar structure.

The observed microstructural transformation can be attributed to the following mechanism: during heating above the β-transus temperature (862°C), the martensitic α' structure completely transforms to a single-phase β structure; subsequently, during the slow furnace cooling, α-phase nucleates preferentially at prior β grain boundaries and grows into the grains as parallel plates along specific crystallographic planes of the parent β-phase.

3.5.2. Phase composition changes

XRD analysis was performed to confirm the phase transformation resulting from heat treatment. Figure 7 presents a comparison of the XRD patterns for the as-built and heat-treated conditions.

The XRD pattern of the heat-treated alloy reveals significant differences compared to the as-built condition. While the as-built sample exhibited predominantly α' martensitic phase with peak broadening characteristic of high internal stresses, the heat-treated sample shows distinct peaks corresponding to both α and β phases. The presence of β-phase peaks, most notably at $2\theta \approx 38 - 39°$ (110) β, confirms the formation of a dual-phase structure during heat treatment.

In addition, the α-phase peaks in the heat-treated condition appear sharper and more defined compared to the as-built condition, indicating reduced internal stresses and increased crystallinity resulting from the annealing process. The peak positions also show slight shifts, reflecting compositional redistribution between α and β phases during the controlled cooling process.

3.5.3. Effects on mechanical properties

The microstructural evolution resulting from heat treatment had a significant impact on the mechanical properties of

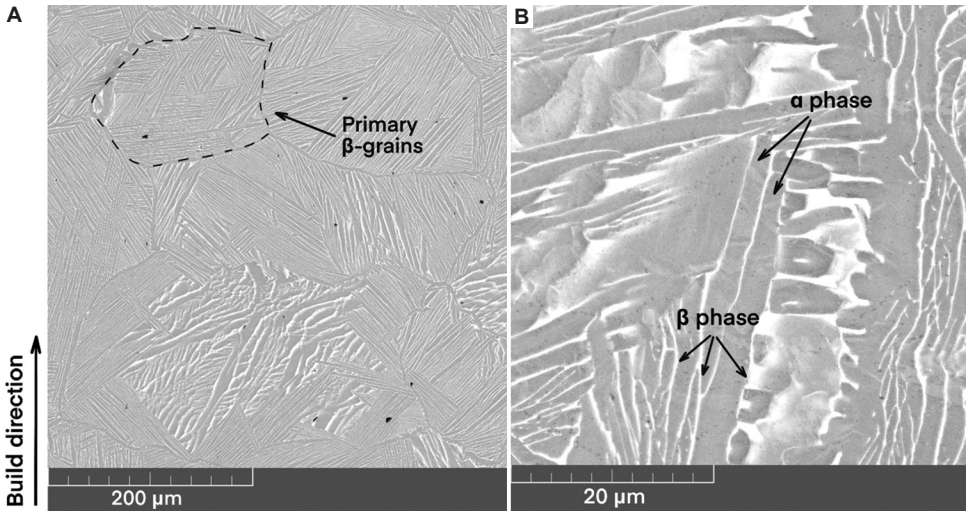

Figure 9. Scanning electron micrographs of Ti-10Ta-2Nb-2Zr alloy after heat treatment (vacuum annealing at 900°C for 1 h, furnace cooled). (A) Low magnification shows complete recrystallization and elimination of L-PBF-induced directional features, scale bar: 200 μm; magnification: ×500; (B) Higher magnification revealing characteristic lamellar α + β microstructure, scale bar: 20 μm; magnification: ×5000

the Ti-10Ta-2Nb-2Zr alloy. Table 3 summarizes the tensile properties before and after heat treatment.

The heat treatment had a significant impact on the mechanical properties of the Ti-10Ta-2Nb-2Zr alloy, as previously presented in Section 3.4. Heat treatment resulted in a notable reduction in strength properties, with yield strength decreasing from 551.8 ± 8.4 MPa to 452.3 ± 14.7 MPa (approximately 18% reduction) and ultimate tensile strength decreasing from 641.2 ± 5.7 MPa to 545.0 ± 3.6 MPa (approximately 15% reduction).

Heat treatment resulted in a notable reduction in strength properties, with yield strength decreasing by 18.0% and ultimate tensile strength by 15.0%. This strength reduction is directly attributable to the replacement of the fine martensitic structure with a coarser lamellar $\alpha + \beta$ microstructure, which offers fewer barriers to dislocation movement.

Interestingly, the elastic modulus decreased slightly from 89.0 GPa to 86.0 GPa (−3.4%) after heat treatment. This reduction, while modest, is beneficial for biomedical applications as it brings the material's stiffness closer to that of bone, potentially reducing stress-shielding effects in orthopedic implants.

The effect on ductility parameters was mixed: elongation increased from 19.0% to 20.2% (+6.3%), indicating improved uniform deformation capacity, while reduction in area decreased from 58.0% to 45.8% (−21.0%), suggesting a reduced localized necking ability. The greater variability in ductility measurements after heat treatment (standard deviations of 3.6% for elongation and 15.5% for reduction in area) indicates less consistent fracture behavior compared to the as-built condition.

The stress-strain curves confirm the reduced strength and slightly enhanced elongation after heat treatment (Figure 8). The heat-treated sample exhibits a more gradual transition from elastic to plastic deformation compared to the sharper yield point of the as-built condition, consistent with the more homogeneous, recrystallized microstructure with reduced internal stresses.

3.6. TPMS structures

Figure 10 presents experimental cylindrical specimens (6 mm diameter, 12 mm height) with different types of TPMS architectures fabricated using L-PBF with Ti-10Ta-2Nb-2Zr alloy. (A) Schwarz structure, (B) gyroid structure, and (C) split structure. All samples are characterized by 50% volumetric porosity and 1.5 mm unit cell size. The manufacturing quality of all structures confirms the technological capabilities of the L-PBF process for reproducing complex biomimetic architectures.

3.6.1. Compression mechanical properties

The results of compressive testing of Ti-10Ta-2Nb-2Zr lattice structures (Table 5) report characteristic features determined by their architecture and L-PBF process. The elastic modulus of all investigated lattice structures lies within a narrow range of 9.2 – 9.7 GPa, which represents approximately 18% of the solid material value (52.2 GPa). Such a significant reduction in stiffness is typical for porous structures and is attributed to the decreased volume fraction of material in the lattice.

The yield strength of lattice structures varies depending on their topology: the Schwarz structure shows the highest values (207.9 MPa), followed by gyroid (198.4 MPa) and split (193.6 MPa). These differences may be associated with the specific stress distribution patterns in different lattice topologies under compression.

Notably, the gyroid structure demonstrates the lowest scatter of experimental data among all investigated lattice types. The standard deviation is 2 – 3 times smaller compared to other structures (Figure 11). Such high reproducibility of results is attributed to the geometric

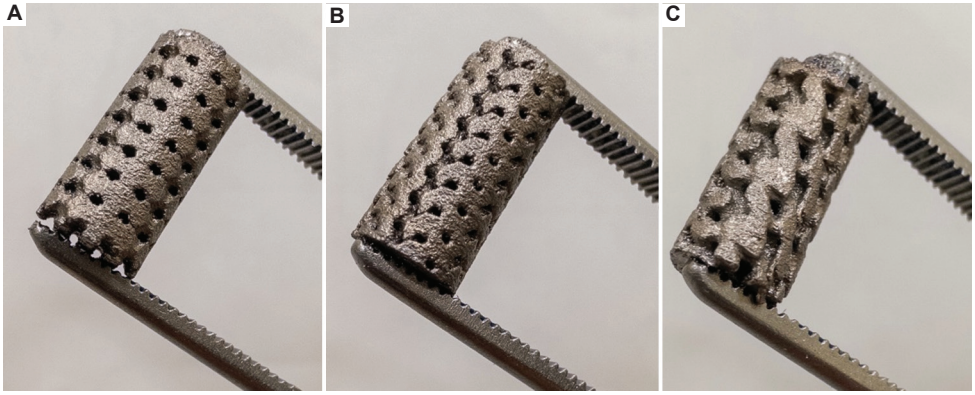

Figure 10. As-built cylindrical specimens with different types of triply periodic minimal surface. (A) Schwarz; (B) Gyroid; (C) Split

features of the gyroid lattice. The gyroid represents a triply periodic minimal surface with constant mean curvature, which provides the most uniform material distribution in space and eliminates sharp angles or abrupt cross-sectional changes characteristic of other topologies. This leads to more stable heat transfer conditions during the L-PBF process, minimization of stress concentrators, and consequently, enhanced reproducibility of mechanical properties among different specimens.

Table 5. Compression mechanical properties of lattice and solid structures

Structure	Elastic modulus (GPa)	Yield strength (MPa)
Schwarz	9.2±1.1	207.9±4.8
Gyroid	9.2±0.5	198.4±2.1
Split	9.7±0.4	193.6±5.9
Solid	52.2±8.4	539.3±23.3

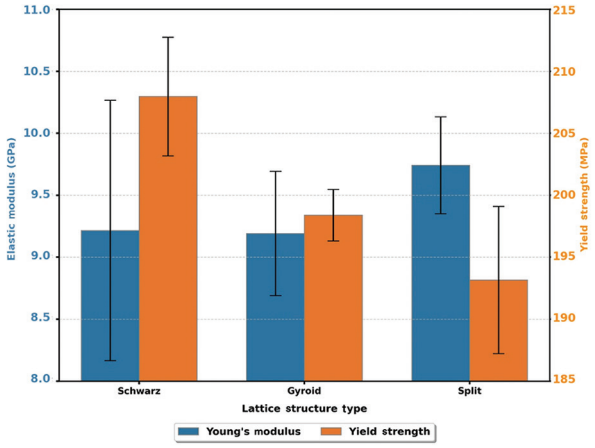

Figure 11. Compression mechanical properties of lattice structures

3.6.2. Triply periodic minimal surface microstructure analysis

Microstructural analysis of the etched surface of the gyroid structure revealed a characteristic microstructural gradient from the periphery to the center of lattice elements (Figure 12). The observed transition from fine acicular structure at the edges to coarser lamellar structure in the central regions reflects differences in crystallization conditions during L-PBF. Peripheral regions in contact with pores are characterized by higher cooling rates due to efficient heat dissipation through the gaseous medium and surrounding powder, which leads to the formation of fine acicular α'-martensitic structure. In the central regions of lattice elements, where heat dissipation is less intensive, slower cooling occurs, promoting the growth of coarser α' plates.

The observed microstructural gradient in TPMS struts reflects the complex thermal conditions during L-PBF processing of thin structural elements. Peripheral regions experience higher cooling rates due to efficient heat dissipation through the surrounding pore space and

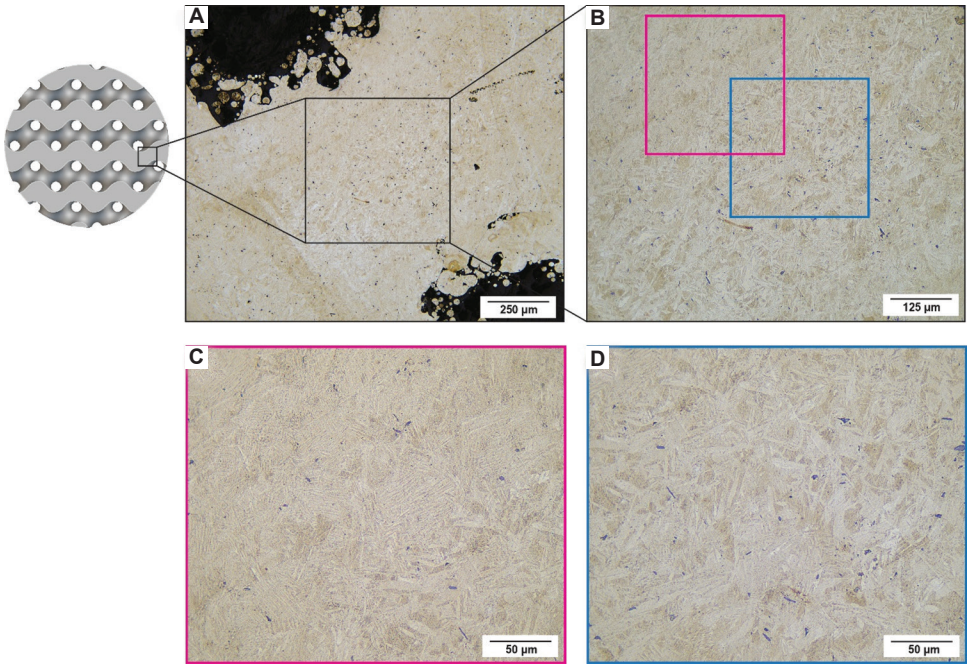

Figure 12. Optical microscope images of a gyroid-type structure. (A) AAA, scale bar: 250 µm; magnification: ×10; (B) BBB, scale bar: 250 µm; magnification: ×20; (C) CCC, scale bar: 50 µm; magnification: ×50; (D) DDD, scale bar: 50 µm; magnification: ×50

powder bed, resulting in finer microstructural features, while central regions undergo slower cooling due to thermal mass effects, producing coarser microstructural elements. This thermal gradient creates variations in residual stress distribution, phase constitution, and dislocation density throughout the strut cross-section. However, the mechanical behavior of lattice structures is governed by the overall microstructural homogeneity achieved through optimized L-PBF parameters rather than local microstructural variations. The consistent yield strength values of 194 – 208 MPa across different TPMS types demonstrate that the Ti-10Ta-2Nb-2Zr alloy maintains stable mechanical properties regardless of local thermal gradients. The excellent reproducibility observed, particularly in gyroid structures, indicates that the microstructural quality achieved through the optimized processing window ensures reliable mechanical performance of complex geometries.

4. Conclusion

A comprehensive investigation of Ti-10Ta-2Nb-2Zr alloy fabricated using L-PBF enabled the establishment of optimal processing regimes and characterization of structural-phase state and mechanical properties for biomedical applications.

(i) Systematic variation of L-PBF parameters revealed an optimal processing window: Laser power 250 – 280 W, scanning speed 600 – 800 mm/s, corresponding to volumetric energy density of 62.5 – 93.3 J/mm^3. Within this range, a maximum relative density of 99.91% was achieved, ensuring high mechanical integrity of components. Exceeding these energy parameters leads to keyhole porosity formation, reducing material density.

(ii) Microstructural analysis showed the formation of predominantly martensitic α'-phase in the as-built condition with characteristic acicular morphology due to high cooling rates during L-PBF. DSC determined β-transus temperature at 862°C. Heat treatment at 900°C provides complete recrystallization with the formation of equilibrium lamellar α + β structure, confirmed by XRD analyses.

(iii) Mechanical properties of Ti-10Ta-2Nb-2Zr alloy in as-built condition are characterized by high strength characteristics: yield strength 551.8 MPa, ultimate tensile strength 641.2 MPa, with elongation of 19.0% and elastic modulus of 89.0 GPa. Heat treatment reduces strength properties by 15 – 18% but decreases elastic modulus to 86.0 GPa, bringing it closer to the properties of bone tissue.

(iv) Developed porous structures based on TPMS (gyroid, Schwarz, and split) with 50% volumetric porosity demonstrate an elastic modulus of 9.2 – 9.7 GPa, representing approximately 18% of the solid material value. Among the investigated topologies, the gyroid structure showed the best reproducibility of mechanical properties due to uniform stress distribution. Microstructural analysis of porous elements revealed a gradient from fine acicular structure at the periphery to coarser lamellar structure in central regions, providing an optimal combination of strength and ductility.

The obtained results confirm the high potential of the Ti-10Ta-2Nb-2Zr alloy for the additive manufacturing of orthopedic implants using the L-PBF process.

Acknowledgments

None.

Funding

This research was supported by the Ministry of Science and Higher Education of the Russian Federation (agreement No. 075-15-2024-562).

Conflicts of interest

The authors declare they have no competing interests.

Author contributions

Conceptualization: Igor Polozov, Anatoly Popovich
Formal analysis: Igor Polozov, Victoria Nefyodova, Anton Zolotarev
Investigation: Igor Polozov, Anton Zolotarev, Victoria Nefyodova
Methodology: Igor Polozov, Anatoly Popovich
Project administration: Igor Polozov
Resources: Anatoly Popovich
Supervision: Anatoly Popovich
Writing – original draft: Igor Polozov
Writing – review & editing: Anatoly Popovich, Victoria Nefyodova

Ethics approval and consent to participate

Not applicable.

Consent for publication

Not applicable.

Availability of data

The datasets used and/or analyzed during the current study are available from the corresponding author on reasonable request. Raw data files for mechanical testing, microstructural analysis, and selective laser melting

processing parameters can be obtained by contacting the corresponding author.

References

1. Wu H, Chen X, Kong L, Liu P. Mechanical and biological properties of Ti and its alloys for oral implant with preparation techniques: A review. *Materials (Basel)*. 2023;16(21):6860.

   doi: 10.3390/ma16216860

2. Khorasani AM, Goldberg M, Doeven EH, Littlefair G. Titanium in biomedical applications-properties and fabrication: A review. *J Biomater Tissue Eng*. 2015;5(8):593-619.

   doi: 10.1166/jbt.2015.1361

3. Zhang Y, Xiu P, Jia Z, *et al*. Effect of vanadium released from micro-arc oxidized porous Ti6Al4V on biocompatibility in orthopedic applications. *Colloids Surf B Biointerfaces*. 2018;169:366-374.

   doi: 10.1016/j.colsurfb.2018.05.044

4. Abdel-Hady Gepreel M, Niinomi M. Biocompatibility of Ti-alloys for long-term implantation. *J Mech Behav Biomed Mater*. 2013;20:407-415.

   doi: 10.1016/j.jmbbm.2012.11.014

5. Laheurte P, Prima F, Eberhardt A, Gloriant T, Wary M, Patoor E. Mechanical properties of low modulus β titanium alloys designed from the electronic approach. *J Mech Behav Biomed Mater*. 2010;3(8):565-573.

   doi: 10.1016/j.jmbbm.2010.07.001

6. Han L, Che S. An overview of materials with triply periodic minimal surfaces and related geometry: From biological structures to self-assembled systems. *Adv Mater*. 2018;30(17):e1705708.

   doi: 10.1002/adma.201705708

7. Learmonth ID, Young C, Rorabeck C. The operation of the century: Total hip replacement. *Lancet*. 2007;370(9597):1508-1519.

   doi: 10.1016/S0140-6736(07)60457-7

8. khan B, Kumar S. *Implementation of Triply Periodic Minimal Surface (TPMS) Structure in Mesenchymal Stem Cell Differentiation*. United States: Research Square; 2022.

   doi: 10.21203/rs.3.rs-2156625/v1

9. Castro APG, Pires T, Santos JE, Gouveia BP, Fernandes PR. Permeability versus design in TPMS scaffolds. *Materials (Basel)*. 2019;12(8):1313.

   doi: 10.3390/ma12081313

10. Chen LY, Cui YW, Zhang LC. Recent development in beta titanium alloys for biomedical applications. *Metals (Basel)*. 2020;10(9):1139.

    doi: 10.3390/met10091139

11. Niinomi M, Boehlert CJ. Titanium alloys for biomedical applications. In: *Advances in Metallic Biometerials*. Berlin: Springer; 2015. p. 179-213.

    doi: 10.1007/978-3-662-46836-4_8

12. Bahl S, Suwas S, Chatterjee K. Comprehensive review on alloy design, processing, and performance of β Titanium alloys as biomedical materials. *Int Mater Rev*. 2021;66(2):114-139.

    doi: 10.1080/09506608.2020.1735829

13. Niinomi M. Mechanical biocompatibilities of titanium alloys for biomedical applications. *J Mech Behav Biomed Mater*. 2008;1(1):30-42.

    doi: 10.1016/j.jmbbm.2007.07.001

14. Huang S, Sing SL, De Looze G, Wilson R, Yeong WY. Laser powder bed fusion of titanium-tantalum alloys: Compositions and designs for biomedical applications. *J Mech Behav Biomed Mater*. 2020;108:103775.

    doi: 10.1016/j.jmbbm.2020.103775

15. Fuerst J, Medlin D, Carter M, Sears J, Vander Voort G. LASER additive manufacturing of titanium-tantalum alloy structured interfaces for modular orthopedic devices. *JOM*. 2015;67(4):775-780.

    doi: 10.1007/s11837-015-1345-4

16. Sing SL, Yeong WY, Wiria FE. Selective laser melting of titanium alloy with 50 wt% tantalum: Microstructure and mechanical properties. *J Alloys Compd*. 2016;660:461-470.

    doi: 10.1016/j.jallcom.2015.11.141

17. Plaine AH, Silva MR, Bolfarini C. Effect of thermo-mechanical treatments on the microstructure and mechanical properties of the metastable β-type Ti-35Nb-7Zr-5Ta alloy. *Mater Res*. 2018;22(1):e20180462.

    doi: 10.1590/1980-5373-mr-2018-0462

18. Ummethala R, Karamched PS, Rathinavelu S, *et al*. Selective laser melting of high-strength, low-modulus Ti–35Nb–7Zr–5Ta alloy. *Materialia*. 2020;14:100941.

    doi: 10.1016/j.mtla.2020.100941

19. Zhang LC, Klemm D, Eckert J, Hao YL, Sercombe TB. Manufacture by selective laser melting and mechanical behavior of a biomedical Ti-24Nb-4Zr-8Sn alloy. *Scrip Mater*. 2011;65(1):21-24.

    doi: 10.1016/j.scriptamat.2011.03.024

20. Hao YL, Yang R, Niinomi M, *et al*. Young's modulus and mechanical properties of Ti-29Nb-13Ta-4.6Zr in relation to α" martensite. *Metall Mater Trans A*. 2002;33(10):3137-3144.

    doi: 10.1007/s11661-002-0299-7

21. Yang K, Wang J, Tang H, Li Y. Additive manufacturing of in-situ reinforced Ti-35Nb-5Ta-7Zr (TNTZ) alloy by selective electron beam melting (SEBM). *J Alloys Compd*. 2020;826:154178.

doi: 10.1016/j.jallcom.2020.154178

22. Brodie EG, Medvedev AE, Frith JE, Dargusch MS, Fraser HL, Molotnikov A. Remelt processing and microstructure of selective laser melted Ti25Ta. *J Alloys Compd*. 2020;820:153082.

doi: 10.1016/j.jallcom.2019.153082

23. Ji G, Zhou Z, Meng F, *et al*. Effect of Zr addition on the local structure and mechanical properties of Ti-Ta-Nb-Zr refractory high-entropy alloys. *J Mater Res Technol*. 2022;19:4428-4438.

doi: 10.1016/j.jmrt.2022.06.160

24. Biesiekierski A, Lin J, Li Y, Ping D, Yamabe-Mitarai Y, Wen C. Investigations into Ti-(Nb,Ta)-Fe alloys for biomedical applications. *Acta Biomater*. 2016;32:336-347.

doi: 10.1016/j.actbio.2015.12.010

25. Zhenhuan W, Yu D, Junsi L, *et al*. Physiochemical and biological evaluation of SLM-manufactured Ti-10Ta-2Nb-2Zr alloy for biomedical implant applications. *Biomed Mater*. 2020;15(4):045017.

doi: 10.1088/1748-605X/ab7ff4

26. Morita A, Fukui H, Tadano H, Hayashi S, Hasegawa J, Niinomi M. Alloying titanium and tantalum by cold crucible levitation melting (CCLM) furnace. *Mater Sci Eng A*. 2000;280(1):208-213.

doi: 10.1016/S0921-5093(99)00668-1

27. Zhao D, Han C, Li Y, *et al*. Improvement on mechanical properties and corrosion resistance of titanium-tantalum alloys *in-situ* fabricated via selective laser melting. *J Alloys Compd*. 2019;804:288-298.

doi: 10.1016/j.jallcom.2019.06.307

28. Soro N, Brodie EG, Abdal-hay A, Alali AQ, Kent D, Dargusch MS. Additive manufacturing of biomimetic titanium-tantalum lattices for biomedical implant applications. *Mater Des*. 2022;218:110688.

doi: 10.1016/j.matdes.2022.110688

29. Yoo DJ. Computer-aided porous scaffold design for tissue engineering using triply periodic minimal surfaces. *Int J Precis Eng Manuf*. 2011;12(1):61-71.

doi: 10.1007/s12541-011-0008-9

30. Yoo DJ. Porous scaffold design using the distance field and triply periodic minimal surface models. *Biomaterials*. 2011;32(31):7741-7754.

doi: 10.1016/j.biomaterials.2011.07.019

31. Dilip JJS, Zhang S, Teng C, *et al*. Influence of processing parameters on the evolution of melt pool, porosity, and microstructures in Ti-6Al-4V alloy parts fabricated by selective laser melting. *Prog Addit Manuf*. 2017;2(3):157-167.

doi: 10.1007/s40964-017-0030-2

32. Xiang S, Yuan Y, Zhang C, Chen J. Effects of process parameters on the corrosion resistance and biocompatibility of Ti6Al4V parts fabricated by selective laser melting. *ACS Omega*. 2022;7(7):5954-5961.

doi: 10.1021/acsomega.1c06246

33. Pesode P, Barve S. A review-metastable β titanium alloy for biomedical applications. *J Eng Appl Sci*. 2023;70(1):25.

doi: 10.1186/s44147-023-00196-7

34. Liu CC, Li YHZ, Gu J, Song M. Phase transformation in titanium alloys: A review. *Trans Nonferrous Metals Soc China*. 2024;34(10):3093-3117.

doi: 10.1016/S1003-6326(24)66597-0

35. Banerjee D, Williams JC. Perspectives on titanium science and technology. *Acta Mater*. 2013;61(3):844-879.

doi: 10.1016/j.actamat.2012.10.043

36. Ahmed T, Rack HJ. Phase transformations during cooling in α+β titanium alloys. *Mater Sci Eng A*. 1998;243(1-2):206-211.

doi: 10.1016/S0921-5093(97)00802-2

37. Bania PJ. Beta titanium alloys and their role in the titanium industry. *JOM*. 1994;46(7):16-19.

doi: 10.1007/BF03220742

38. Geetha M, Singh AK, Asokamani R, Gogia AK. Ti based biomaterials, the ultimate choice for orthopaedic implants - A review. *Prog Mater Sci*. 2009;54(3):397-425.

doi: 10.1016/j.pmatsci.2008.06.004

39. Jamshidi P, Aristizabal M, Kong W, *et al*. Selective laser melting of Ti-6Al-4V: The impact of post-processing on the tensile, fatigue and biological properties for medical implant applications. *Materials*. 2020;13(12):2813.

doi: 10.3390/ma13122813

40. Cho JY, Xu W, Brandt M, Qian M. Selective laser melting-fabricated Ti-6Al-4V alloy: Microstructural inhomogeneity, consequent variations in elastic modulus and implications. *Opt Laser Technol*. 2019;111:664-670.

doi: 10.1016/j.optlastec.2018.08.052

Our Journals

International Journal of Bioprinting is an international journal covering the technology, science and clinical application of the broadly defined field of Bioprinting. Bioprinting is defined as the use of 3D printing technology with materials that incorporate viable living cells or biological elements to produce tissue or biotechnological products. We are interested in the scientific topics spanning all stages of bioprinting process from concept creation to fabrication and beyond. Knowledge generated in these researches must be related to bioprinting. *IJB* covers subject areas, including but not limited to the following:

- Information technologies and basic research
- Materials and formulation
- Cell source and biotechnology for additive manufacturing
- 3D Bioprinting technologies
- New design and fabrication paradigm
- Applied research purpose & evaluation of 3D printed products
- Associated social implications

International Journal of AI for Materials and Design is an international, peer-reviewed open-access journal that aims to bridge the cutting-edge research between AI and materials, AI and design. In recent years, the tremendous progress in AI is leading a radical shift of AI research from a mainly academic endeavor to a much broader field with increasing industrial and governmental investments. The maturation of AI technology brings about a step change in the scientific research of various domains, especially in the world of materials and design. Machine learning (ML) algorithms enable researchers to analyze extensive datasets on material properties and accurately predict their behavior in different conditions. This subsequently impact the industry to leverage on big data and advanced analytics to build scientific strategies, scale operational performance of processes and drive innovation. In addition, AI and ML are uniquely positioned to enable advanced manufacturing technologies across the value chain of different industries. Integration of multiple and complementary AI techniques, such as ML, search, reasoning, planning, and knowledge representation, will further accelerate advances in scientific discoveries, engineering excellence and the future of cyber-physical systems manufacturing.

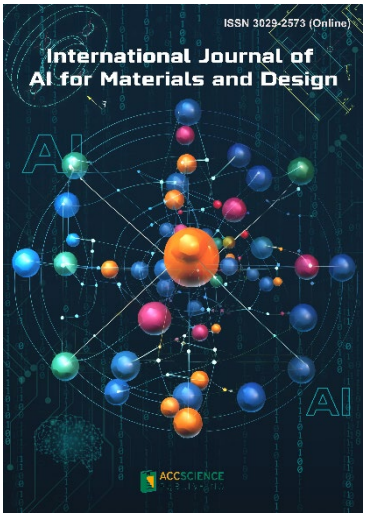

International Journal of AI for Materials and Design covers the following topics: AI or machine learning for material discovery, AI for process optimization, AI and data-driven approaches for product or systems design, application of AI in advanced manufacturing processes such as additive manufacturing, IoT, sensors, robotics, cloud-based manufacturing, intelligent manufacturing for various applications, autonomous experiments, material intelligence, energy intelligence, and AI-linked decarbonization technologies.

Start a new journal

Write to us via email if you are interested to start a new journal with AccScience Publishing. Please attach your CV, professional profile page and a brief pitch proposal in your email. We shall inform you of our decision whether we are interested to collaborate in starting a new journal.

Contact: info@accscience.com

https://accscience.com/journal/MSAM

Access Science Without Barriers

Contact

www.accscience.com
9 Raffles Place, Republic Plaza 1 #06-00 Singapore 048619
E-mail: editorial@accscience.com
Phone: +65 8182 1586